Mechanisms and kinetics of alkenes isomerization and cracking in chabazite zeolite quantified by constrained ab initio molecular dynamics

Jérôme Rey

To cite this version:

Jérôme Rey. Mechanisms and kinetics of alkenes isomerization and cracking in chabazite zeolite quantified by constrained ab initio molecular dynamics. Theoretical and/or physical chemistry. Université de Lyon, 2019. English. NNT : 2019LYSEN049 . tel-03510141

HAL Id: tel-03510141
https://theses.hal.science/tel-03510141

Submitted on 4 Jan 2022

Numéro National de Thèse : 2019LYSEN049

THESE de DOCTORAT DE L'UNIVERSITE DE LYON

opérée par

l'Ecole Normale Supérieure de Lyon

Ecole Doctorale N° 206
Ecole Doctorale de Chimie (Chimie, Procédés, Environnement)

Discipline : Chimie

Soutenue publiquement le 20/09/2019, par :

Jérôme REY

Mechanisms and kinetics of alkenes isomerization and cracking in chabazite zeolite quantified by constrained *ab initio* molecular dynamics

Mécanismes et cinétique de l'isomérisation et du craquage d'alcènes dans la zéolithe chabazite quantifiés par dynamique moléculaire *ab initio* contrainte

---

Devant le jury composé de :

STUDT, Felix	Professeur IKFT-KIT Karlsruhe	Rapporteur
FLEURAT-LESSARD, Paul	Professeur CMUB Bourgogne	Rapporteur
MICHEL, Carine	Chargée de recherche CNRS ENS de Lyon	Examinatrice
SAUER, Joachim	Professeur Humbolt Universität, Berlin	Examinateur
TRAVERT, Arnaud	Professeur LCS ENSICAEN	Examinateur
BUCKO, Tomáš	Professeur associé Comenius University, Bratislava	Examinateur
CHIZALLET, Céline	Ingénieure de recherche IFP Energies nouvelles	Examinatrice
RAYBAUD, Pascal	Ingénieur de recherche IFP Energies nouvelles	Directeur de thèse

Acknowledgements

This thesis being unusually late, I have to thank a lot of people who helped to make possible this adventure.

First of all, I would like to thank people from IFPEN (Céline Chizallet, Pascal Raybaud, Tivadar Cseri and Denis Guillaume) who welcomed me for my come back to research and computational chemistry in 2014-2015, after a long period of teaching in “classes préparatoires aux grandes écoles”. The « fondation de la maison de la chimie », the « inspection générale de sciences physiques » and Jean-Pierre Foulon made this first scientific stay possible. This year was so instructive and fruitful for me that it finally contributed to the change of direction of my career.

After one more year of teaching, I came back to IFPEN for a PhD thesis in September 2016, with the same people and Jean-Marc Schweitzer. It was a difficult decision to take, but I was confident to work with the same team at IFPEN and actually I have never regretted my choice. Thank you Celine and Pascal for these opportunities to work with you and for your constant enthusiasm, availability, and help during this 4 years of common work. PhD students are really fortunate when they find such supervisors.

In addition to the constant support in the work and in the everyday life at IFPEN, I thank Celine and Pascal for the opportunity of a very nice trip to an international conference at Rio de Janeiro in 2017. It was an unexpected consequence of our first collaboration.

This computational thesis is related to catalytic tests performed at IFPEN, which was the opportunity of insightful exchanges with this experimental team, especially Christophe Bouchy, who always provided great advice on all aspects of reactivity in zeolites.

I am really grateful to these people at IFPEN, and to the current director of R06 group, Luc Nougier, to have tried the experience and to have entrust a PhD student of my status.

The methodological aspects of this thesis, with advanced Molecular Dynamics, contributed to my decision to start this thesis work. Tomàš Bučko, from Comenius University in Bratislava, was the expert involved in that part of the project and I would like to thank him warmly for his huge involvement – both scientific and human – in all the aspects of this work. We exchanged thousands of emails and spent a lot of time in videoconferences, which helped me to understand the theoretical basis of MD and to make progress in the understanding of our mechanistic difficulties, and to support me in the difficult moments where work seems to move backwards. I will keep memorable souvenirs of Tomàš’s greeting in Bratislava, slipping on the snow of January, or seeking for some freshness in a pub with view on the Danube in June, and always with enthusiastic theoretical discussions and huge progress in this thesis. Thank you Tomas, I am indebted to you and I hope that we will continue to work together.

I also want to thank my young PhD and post-doctoral colleagues of the molecular modeling group and of R06 department. I cannot be exhaustive, but I cite the names of the ones with whom I shared years of presence : Wei Zhao, Laureline Treps, Elsy el Hayek and Ester Gutierez Acebo. With Ester, we worked on some difficult cases of reluctant protonated cyclopropanes and it's a pleasure to have a common publication. It was also a pleasure to speak with Manuel Corral-Valero in the molecular modeling corridor of IFPEN: MD and CV, scripting problems… it was always instructive.

I am very grateful to the interns who worked with me: Axel Gomez for a short but fruitful stay in summer 2018, and Charles Bignaud, for a 6 months collaboration, from January to June 2019. The last chapter on the cracking reactions owes him a lot.

Aside from having accepted to evaluate this work, I thank Pr. Joachim Sauer for fruitful discussions in Berlin and Rio de Janeiro. In Berlin, I had the opportunity to work with Marcin Rybicki. I thank warmly Marcin and I regret that this collaboration did not go further because of lack of time. I hope that it will be possible in the future.

I thank also the other members of the jury for having accepted to evaluate this work: Carine Michel from ENS de Lyon (I also have to thank Carine for an upcoming Molecular Dynamics collaboration), Paul Fleurat-Lessart from university of Bourgogne (it is an uncommon way of seeing each other a couple of decades after our DEA of physical and theoretical chemistry at Orsay), Felix Studt of Karlsruhe Institute of Technology and Arnaud Travert, from Laboratoire Catalyse & Spectrochimie of Université de Caen.

Andreas Savin and François Colonna have been my first mentors in DFT at the Laboratoire de Chimie Théorique of Université Paris VI. Even if, at that time, our work did not come to its conclusion, their teaching and their example was profitable and proved very useful for me more than twenty years later.

And, of course, nothing would have been possible without the comprehensive support of my wife Marie-Pierre, this adventure involving the whole family. It's not always comfortable to have an husband who leaves his job to become a student again. My children have also been involved indirectly, and I also thank them. It's always a pleasure to speak with Lucas on scientific points (refreshment of some mathematical tools or of some theorems of statistical physics). Eglantine has been briefly a young and smiling colleague here at IFPEN. And my younger son Pablo, who is a passionate of programming and algorithmic researches was extremely helpful for writing post-processing scripts and for an efficient informatics assistance.

Contents

Résumé **5**

Summary **6**

Introduction **7**

Section I. State of the art **9**
- I.1. Hydroconversion of hydrocarbons 9
  - I.1.1. General mechanism 9
  - I.1.2. Ideal hydrocracking 10
  - I.1.3. Hydrogenation–dehydrogenation function 10
  - I.1.4. Products distribution and selectivity 11
- I.2. Zeolites 13
  - I.2.1. General features 13
  - I.2.2. Chabazite zeolite 14
- I.3. Nature of the reaction intermediates in zeolites 15
  - I.3.1. General features 15
  - I.3.2. Experimental observations 16
  - I.3.3. Theoretical results 18
  - I.3.4. Conclusion 23
- I.4. Reactions involved in hydrocracking 23
  - I.4.1. Isomerization step 23
  - I.4.2. Cracking 29
  - I.4.3. Shape selectivity 31
- I.5. Conclusion and strategy of the thesis 32
- References 34

Section II. Methodology **37**
- II.1) Wavefunction methods 37
- II.2) Density Functional Theory (DFT) 38
  - II.2.1) Basic Principles of DFT 38
  - II.2.2) Exchange-correlation energy 40
  - II.2.3) DFT based dispersion methods 41
- II.3) Codes employed in the present work 42
- II.4) Static approach 42
  - II.4.1) Introduction 42
  - II.4.2) Identification of potential energy minima 43

II.4.3) Searching for saddle points 43
II.4.4) Intrinsic reaction coordinate (IRC) 45
II.4.5) Line minimization procedure 45
II.4.6) Thermodynamic calculations 47
II.4.7) Rate constants from static calculations 49
II.5) Molecular dynamics 49
II.5.1) Standard molecular dynamics in the canonical ensemble 50
II.5.2) Simulating rare events: free energy methods 55
II.5.3. Free energies of activation $\Delta_r A^{\ddagger}$ and of reaction $\Delta_r A_{R \rightarrow P}$ 63
II.5.4) Free-energy partitioning 66
II.5.5) Andersen thermostat 67
II.6) Computational section 68
II.7) Conclusions 68
Annexes 70
A.II.1) Jarzynski's identity 70
A.II.2) Statistical errors tests in molecular dynamics. 70
A.II.3) Committor distribution 74
References 75

Section III. On the origin of the difference between type A and type B skeletal isomerization of alkenes catalyzed by zeolites: the crucial input of ab initio molecular dynamics 78
III.1. Introduction 78
III.2. Methodology 80
III.2.1. Total energy calculations 80
III.2.2. Transition state search through the static approach 81
III.2.3. Molecular dynamics simulations 81
III.2.4. Structural Model 83
III.3. Results and discussion 84
III.3.1. Isomerization mechanisms and question of the reactant / product rotamers: static approach applied to gas phase reactions 84
III.3.2. Static approach applied to reactions in zeolite 88
III.3.3. Molecular Dynamics of type B isomerization in zeolite 91
III.3.4. Free energy calculations for type A isomerization reaction 97
III.3.5. On the atomic origin of the different kinetics of type A versus type B isomerization reactions in zeolites 99
III.4. Conclusion 102
References 104
Supporting Information* 107

Section IV. Competition of secondary versus tertiary carbenium Routes for the type B Isomerization of Alkenes over Acid Zeolites Quantified by AIMD Simulations 131
IV.1. Introduction 131
IV.2. Methodology 135

IV.3. Results 137
  IV.3.1. Characterization of the reactant state 137
  IV.3.2. Mechanism I 140
  IV.3.3. Mechanism II 144
IV.4. Discussion 147
  IV.4.1. Thermal variation of the overall free energy profiles 147
  IV.4.2. Comparison of structure and stability of the transition states for the 1,3 hydride shift and type B isomerization 149
  IV.4.3. Implication for the kinetic modeling of isomerization reaction networks 152
IV.5. Conclusion 156
References 158
Supporting Information* 162

Section V. Relevant cracking intermediates and transition states for β-scission reactions of alkenes over acid zeolites revealed by AIMD simulations 183
V.1. Introduction 183
V.2. Methodology 186
V.3. Results and discussion 188
  V.3.1. Type B_1 β-scission 188
  V.3.2. Type B_2 β-scission of 2-4-dimethyl-penten-2-ium 201
V.4. Conclusion 204
References 206
Supporting Information* 208

Conclusion and perspectives 220

---

* Tables of contents of Supporting Information are reported at the beginning of the corresponding sections.

« Hélas ! la vie n’est pas une thèse de doctorat qu’on puisse fignoler à volonté, allant et venant librement sans tenir compte de l’irréversible ni de l’irrévocable ».

« Sadly, life is not a doctoral thesis you can tinker around with as much you wish, freely going back and forth without considering what is irreversible or irrevocable » [personal translation].

Vladimir Jankélévitch, *L’irréversible et la nostalgie.*
Nostalgia and the Irreversible.

Résumé

Les catalyseurs d'hydrocraquage et d'hydroisomérization sont bifonctionnels, avec une fonction hydro-déshydrogénante et une fonction acide, une zéolithe protonée, pour isomériser et craquer les alcènes. Par dynamique moléculaire *ab initio* avancée, et avec prise en compte explicite des effets thermiques (300 – 500 K), nous avons étudié les mécanismes d'isomérisation et de craquage d'alcènes C_7 dans la zéolithe chabazite dans le but d'obtenir des constantes de vitesse fiables et d'interpréter la distribution des produits.

Par la méthode blue moon, nous avons établi les premiers profils d'énergie libre d'isomérisations d'alcènes C_7, avec des carbocations intermédiaires (et des états de transition cyclopropanes protonés, PCP), reliant des isomères di- à tri- et mono- à di-branchés (Sections III et IV). Nos simulations démontrent que les effets dynamiques et l'échantillonnage correct des rotamères jouent un rôle crucial sur la stabilité des intermédiaires et des états de transition. Ces effets ne pouvaient pas être décrits par les précédentes études de DFT statiques. Les barrières bien plus basses pour l'isomérisation de type A sont ainsi retrouvées, et expliquées par un état de transition mou, alors que l'état de transition de l'isomérisation de type B est contraint, à cause de la formation d'un edge PCP. L'étude des réactions de craquage avec les mêmes méthodes (Section V) éclaircit le rôle des cations secondaires. Pour la première fois, nous identifions les états de transitions des β−scission. Nous déduisons de cette analyse des constantes de vitesse *ab initio* qui pourront être utilisées dans un modèle cinétique pour prédire l'activité et la sélectivité du catalyseur.

Summary

Hydrocracking and hydroisomerization catalysts are bifunctional, with a hydro-dehydrogenation function and an acidic function, typically an acid zeolite, to isomerize and crack alkenes. With advanced *ab initio* molecular dynamics approach, and explicit simulation of the effects of temperature (300 – 500 K), we investigate the mechanisms of isomerization and cracking reactions of C_7 alkenes within the chabazite zeolite in order to provide reliable rate constants and explain the observed products distribution.

By blue moon sampling, we established for the first time, the free energy profiles for the isomerization of C_7 alkenes in zeolites, with carbenium ions as intermediates (and protonated cyclopropane (PCP) as transition states), connecting di- to tri-branched, and mono- to di-branched alkene isomers (Sections III and IV). We demonstrate that the dynamic effects with the correct sampling of rotational conformers play an important role to quantify the stability of the key intermediates and transition states. These effects could not be captured by previous static DFT simulations. The much lower barriers for type A isomerization mechanisms are thus recovered, and assigned to a loose transition state, while the transition state of type B isomerization is tighter, due to the formation of an edge PCP. The study of cracking reactions (Section V) with the same methods, unravel the role of secondary cations. For the first time, we identify the structures of transition states involved in the β–scission mechanisms. From this analysis, we deduce the *ab initio*- rate constants that could be used in future kinetic modeling to predict activity and selectivity of the catalyst.

Introduction

Hydrocracking consists in the isomerization and shortening of the chain size of long chain hydrocarbons obtained from heavy cuts of crude oils, utilized at industrial scales mainly for valorization as diesel and jet fuels.[1] Hydrocracking is also used for the heaviest parts of hydrocarbons, obtained via the Fischer-Tropsch process, from different feedstocks (coal, biomass or gas) and for very heavy unconventional crudes (tar sands, shale oils, etc.).[2,3] Moreover, the specific hydroisomerization process of C_7 and C_8 linear alkanes enables the increase of octane number of hydrocarbon molecules incorporated in gasoline fuel.

Hydrocracking and hydroisomerization catalysts combine two functions: a hydrogenation/dehydrogenation function on a noble metal or a metallic sulfide and an acidic function of the Brønsted type (zeolites or amorphous silica-aluminas).[3] The reaction begins by the dehydrogenation of long chain alkanes into alkenes. These alkenes are afterwards protonated on the acidic function. Intermediate carbocations are formed and these species evolve by isomerization (through proton or alkyl transfer or through more complicated reactions involving non-classical carbonium ions such as protonated cyclopropane) and β-scission. The resulting shorter and isomerized alkenes are hydrogenated to form alkanes, which are eventually desorbed.[3,4]

Zeolites are commonly chosen as acidic catalysts. They are non-corrosive, non-toxic solids, and they can resist high temperatures. They are microporous and possibly mesoporous solids, with a large variety of structures. The selectivity of the isomerization and cracking reactions can be tuned by confinement near the acid sites and by diffusion limitations.[2,5] Kinetic modeling is a valuable tool to predict the behavior of hydrocracking catalysts, but a debate remains about the features of the most relevant steps, namely isomerization and β-scission [6–10]. Density functional theory (DFT) calculations are useful to unravel the reaction mechanisms and quantify rate constants at an atomic scale level. These investigations are usually done within the frame of the "static approach", with only approximate inclusion of thermal and entropic effects, and of the flexibility of the framework.[11–13] The quality of such an approach for reactions in zeolites is questionable, in particular when carbenium species are involved.[11,14,15,16]

In the present work, we employ *ab initio* calculations to investigate relevant reactions occurring at the acid phase during hydroconversion of n-heptane. This molecule is generally used as a model molecule for probing hydrocracking catalysts at laboratory scale but it is also industrially converted into isomerized C_7 molecules added in the gasoline pool. The methodological objective of this thesis is to go beyond the static approach and to investigate molecular mechanisms of the isomerization and cracking reactions with advanced *ab initio* molecular dynamics methods. In practical terms, the aim is to calculate accurate rate constants for each kind of elementary steps, that will further be used to build a predictive multi-scale kinetic model to be compared with experiments performed at IFPEN.

The present thesis manuscript is organized as follows. It first reports an overview of the state of the art (Section I), highlighting the key challenges for the present study. It is followed by the methodological aspects relevant to the work (Section II). The results are presented and discussed in the next sections. In Sections III, type A and B isomerization reaction starting from a dibranched tertiary carbenium ion are investigated, and different theoretical methods (static calculations versus *ab initio* Molecular Dynamics –AIMD– simulations) are compared. In Section IV, two mechanisms of type B isomerization reaction of monobranched cations, involving secondary and tertiary carbenium ions, are considered by AIMD simulations. In Section V, mechanistic insights for cracking reactions are given, before conclusions and perspectives, in particular in terms of kinetic modeling, are proposed.

Section I. State of the art

I.1. Hydroconversion of hydrocarbons

I.1.1. General mechanism

In Europe, hydrocracking is mainly employed in the conversion of heavy feedstocks in middle distillates for the production of diesel fuel (a mixture of hydrocarbons with around 16 carbon atoms). Hydrocracking is a very versatile process in refining. It can deal with different petroleum fractions to deliver good quality products. Its only drawback is the cost associated to the overall process and the need of high hydrogen pressure requiring a special unit to produce hydrogen.[17]

The general scheme for the hydroisomerization and hydrocracking of a linear hydrocarbon (or normal paraffin) on a bifunctional catalyst is depicted in Figure I- 1.

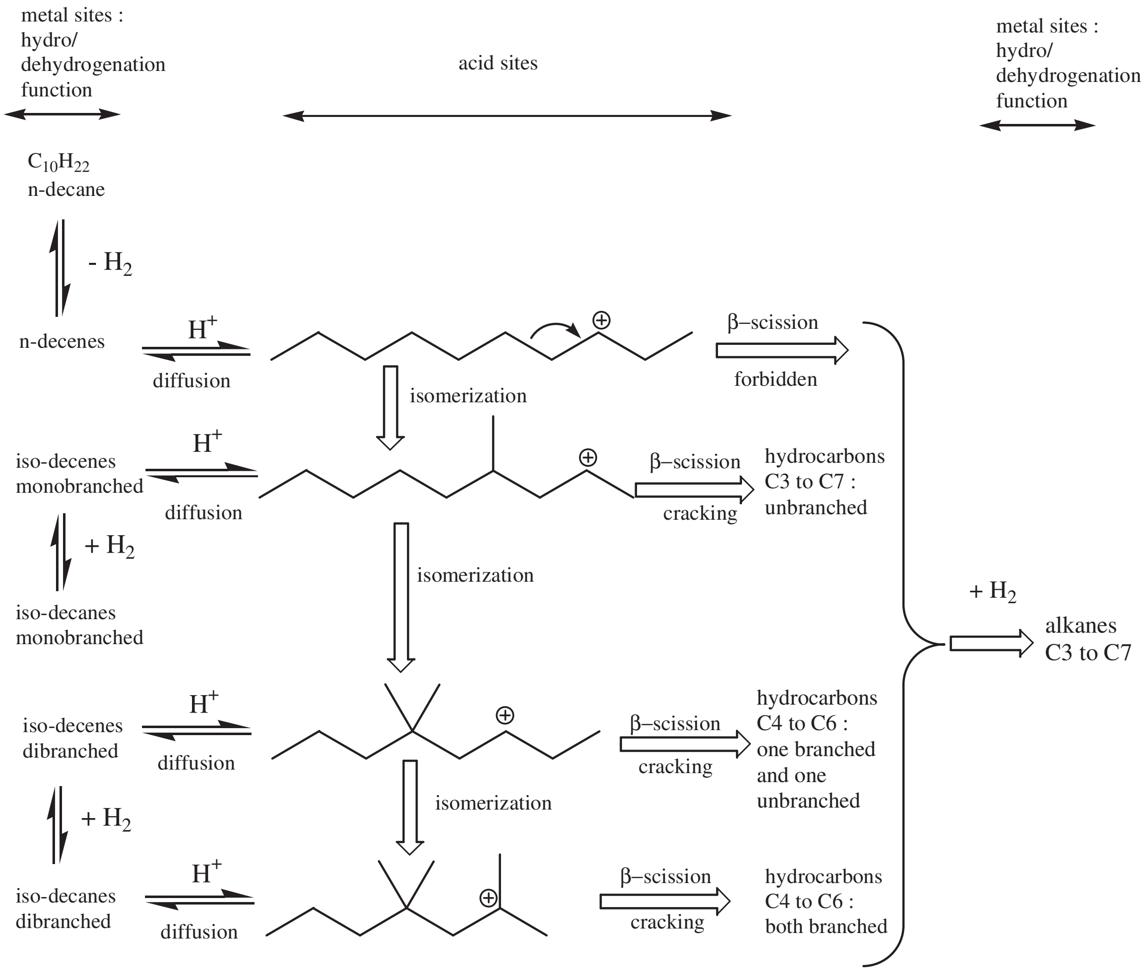

Figure I- 1. General scheme for reactions involved in hydrocracking, illustrated on the example of the hydroconversion of n-decane. Adapted from ref[3,4]

After adsorption on the active site for hydrogenation/dehydrogenation, the linear alkane is dehydrogenated to form a linear alkene (or n-olefin). The alkene diffuses towards the Brønsted acid site where it is protonated. The resulting carbenium ions can be isomerized into various isomers, increasing such the degree of branching of the chain. All these cations can be cracked into lighter cations, subsequently forming lighter olefins.

After deprotonation, the alkenes diffuse back to the hydrogenation/dehydrogenation site where they are hydrogenated into alkanes. After desorption shorter alkanes formed as products are released. Our main focus is put on the reaction at the acid phase, which is usually a zeolite.

I.1.2. Ideal hydrocracking

Ideally, the conversion of long hydrocarbons into shorter molecules should be selective, without over-cracking: the hydrocracked products should be desorbed before a second carbon-carbon bond cleavage (which is called pure primary cracking). The isomerized middle distillates (with high branching degree) should also be favored to improve the cold flow properties of the fuels.[3,4]

In ideal hydrocracking, according to Weitkamp's terminology[4], the following conditions must be satisfied:

- Olefin diffusion between the two catalytic functions should not limit the reaction rate: the two functions must be close enough. This refers to the Weisz criterion of minimal distance between the two functions of a bi-functional catalyst.[18] This concept still leads to some debate in the recent literature (with nanometric investigations, it is shown that "the closer the better" notion of intimacy is not always the most relevant).[19]
- The hydrogenation/dehydrogenation steps should not limit the reaction rate. These steps are quasi-equilibrated and the acid function is fed with long alkenes whereas primary cracked alkenes must be quickly hydrogenated and desorbed.
- The limiting steps occur on the acid sites and branched iso-alkanes are favored.

The yields in branched isomers are maximal with ideal hydrocracking conditions. Under non-ideal hydrocracking conditions, higher cracked products are expected to be formed at high abundance.

I.1.3. Hydrogenation–dehydrogenation function

During hydrocracking, the partial pressure of H_2 is high (more than 100 bars[2]) and the temperature is moderate, around 250 °C. The products are fully hydrogenated (no alkenes in the outlet).The rate determining steps occur on the acidic function of the catalyst if the hydrogenation function is active enough (with a sufficient amount and dispersion of the metal sites).[3,4] Typically, for the hydrocracking of n-heptane on the bifunctional catalyst Pt/H-Y (with Y belonging to the faujasite family, structural type FAU), the hydrogenation-dehydrogenation function is no more limiting from 0.5% of Pt in weight, with a good dispersion of platinum.[17] In our *ab initio* calculations we shall consider the conditions of ideal hydrocracking,[4] which implies that we can focus on the kinetics of the reactions taking place in the zeolite, without explicit simulation of the mechanism occurring on the metal phase, which is not kinetically relevant in these conditions.

I.1.4. Products distribution and selectivity

I.1.4.1. Number of atoms in the products

Starting from a C_n alkane, C_1 and C_2 (methane and ethane) are unlikely to be obtained: they would require a too difficult type D β-scission between a secondary carbenium and a very unstable primary carbenium. The main products are in the range C_3 to C_{n-3}. Within the ideal hydrocracking conditions, the molar distribution curves of the product are "bell-shaped" (or "volcano-shaped") and symmetric, centered around n/2.[3,4,17] The results for ideal hydrocracking of dodecane on Pt/US-Y (ultra-stable Y zeolite) are shown in Figure I- 2 (left), for a total conversion around 55%.

With a non-ideal catalyst or with an ideal one at higher conversion, the distribution curve is not symmetric anymore, with a predominance of shorter molecules resulting from successive cracking reactions. The results for hydrocracking of heptadecane over ideal bifunctional catalyst Pt/US-Y are shown in Figure I- 2 (right). With increasing conversions, the maximum of the distribution of cracked products is observed at smaller carbon numbers.

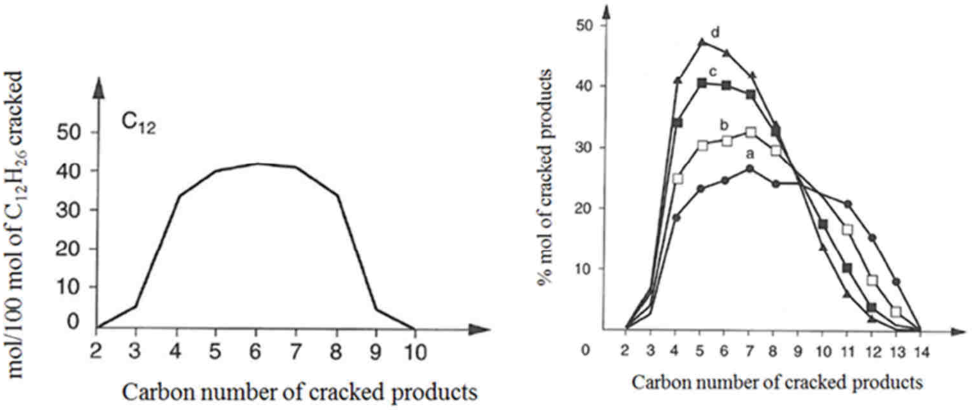

Figure I- 2. Left: molar distribution curves for products of ideal hydrocracking of dodecane. Right: products distribution curves for non-ideal hydrocracking with increasing conversions (from *a* to *d*; *a*: 20%; *b*: 83%; *c*: 93%; *d*: 97%) over bifunctional catalyst Pt/US-Y[17].

I.1.4.2. Structure of the products: degree of branching

Pour point and cetane number are important parameters to measure the quality of a diesel fuel and these parameters are related to the branching degree of hydrocarbons. The cetane number describes the ignition quality of a diesel fuel. It is high for normal and iso-paraffins (linear and monobranched alkanes).

The value of pour point lies between –18°C and –30°C for diesel fuels in Europe. The pour point and the melting point of alkanes increase with the branching degree of hydrocarbons. Isomerization and branching are necessary to fulfill this criterion.[17]

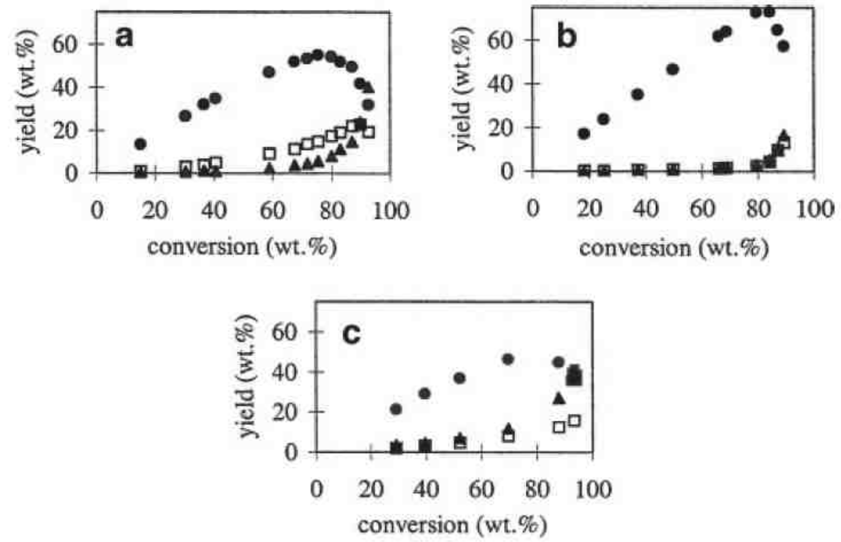

Figure I- 3. Yield in monobranched isomers (●), mutibranched isomers (▲), and cracked products (□) obtained on (a) Pt/H-BEA zeolite (210°C), (b) Pt/H-ZSM-22 or 23 at 240°C, and Pt/H-EU-1 at 220°C. Reprinted from ref.[5] with permission from Elsevier.

Fisher-Tropsch waxes contain mainly linear alkanes: they must be isomerized into branched alkanes to increase their pour point for transformation in diesel fuel or lubricant base oil.[3,17]

Mono, di and tribranched cations appear successively. Multibranched cations can undergo cracking by β-scission. The cations can be converted into alkenes on the acid sites. After hydrogenation, branched alkanes are released. For instance, for the linear heptane studied in this thesis, seven different C_7 alkane isomers are formed by type B isomerization: 2 monobranched, 4 dibranched and 1 tribranched (see later Figure I- 17).

From the results displayed in Figure I- 3, we can see that the yield in monobranched products initially increases with increasing conversion, while the same quantity decreases at the higher conversions. The multibranched and cracked products appear successively. The shapes of the curves depend on the tested zeolites (a: Pt/H-BEA, b: Pt/H-ZSM-22, c: Pt/H-EU-1) which means that there is a shape selectivity, depending on the topology of the zeolites (see Section I.4.3).

I.2. Zeolites

I.2.1. General features

Zeolites are microporous crystalline aluminosilicates. Natural zeolites were discovered in the 18th century but industrial applications began in the 1950s, after synthesis of zeolites of commercial interest.[20] These solids are widely used in catalysis (which is their economically most important application and includes redox catalysis or acid catalysis in cracking of hydrocarbons) and in exchange and separation processes.[21,22]

Zeolites are built out of SiO_4 and AlO_4 tetrahedra. They can be described as a purely siliceous network in which a part of Si atoms are substituted by Al. Electro-neutrality requires that the substitution of a Si^{4+} ion by an Al^{3+} ion must be counterbalanced by an extra-framework cation, typically an alkali metal, an alkali earth metal or lighter ions such as proton or ammonium cation. The general chemical formula of zeolites is $M^{n+}_{\frac{x}{n}}Al_xSi_{1-x}O_2.yX$, with M^{n+} being the counterion and X a possible neutral molecule included in the structure. It is well known that bridging Si-(OH)-Al groups are Brønsted acid sites of these solids[23] (Figure I- 4).

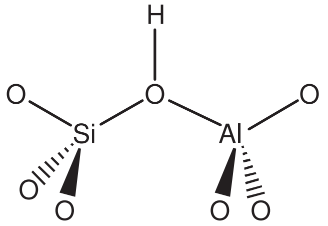

Figure I- 4. Bridging Si-(OH)-Al Brønsted acid site in an acid zeolite

The strong Brønsted acidity of these bridging sites and the shape selectivity of these solids (due to the pore size and the confinement effect[24,25]) are responsible for the excellent catalytic activity of acid zeolites.

The SiO_4 and AlO_4 tetrahedra are the elementary building units of all zeolite structures. The secondary structure is made up of chains, rings, channels, and cages. Zeolites are classified by the size and connectivity of their network of interconnecting pores. A channel is characterized by the size of the ring limiting its opening (i.e. the number of T-atoms of this limiting ring). The 8MR, 10MR and 12MR channels (with respectively 8, 10 and 12 tetrahedral cations in their opening ring) are considered as small, medium and large pores.[20]

There is an infinite number of 3-periodic 4-connected nets and 2.6 million zeolite frameworks have been generated via computer simulation.[22] A total of 232 frameworks are identified by the International Zeolite Association at the present time.[26] Some twenty of them are used in industrial applications.[2] The flexibility of the framework is important for the synthesis process[22] and also for reactivity where a large configurational space and vibrational entropies are key factors.[27] These frameworks exhibit a high stability of a kinetic nature. Indeed, zeolites are metastable with respect to more dense polymorphs of SiO_2 such as quartz and their framework collapse at very high temperatures (1200–1300 K). This very high temperature required for the phase transition allows to use zeolites in refinery conditions, with operating temperatures of up to 800°C.[2,22] Apart from this thermal stability, zeolites have several other properties, which are advantageous in practical applications in catalysis:

- they are non-corrosive and non-toxic
- they are easy to process and separate
- their structures are tunable via:
    - a wide range of composition (with different ratio Si/Al, T atoms (Ti, Ga, Ge…) or extra framework cations)
    - a wide variety of crystalline structures and pore sizes which allow to adjust the shape selectivity. The notion of shape selectivity in hydrocracking reactions is described in Section I.4.3.
    - a wide range of crystal sizes. In catalysis, the crystal size is usually around one micrometer. For crystals between 0.1 and 5 µm, the internal surface of micropores is in the range 300 to 700 $m^2.g^{-1}$ and the external surface in the range 10 to 40 $m^2.g^{-1}$.[2] With nanocrystals of catalysts, the catalytic activity can be higher, especially if the reaction occurs mainly at the external surface (for instance, for dealkylation on faujasite).[28]

For computational reasons explained hereafter, our study will be devoted to zeolite chabazite.

I.2.2. Chabazite zeolite

Chabazite (framework type CHA) is a small pore zeolite which has been initially used in separation and adsorption.[2] As a catalyst, chabazite converts methanol into olefins (MTO process).[2,22,29] Chabazite is also used in the selective catalytic reduction of NO_x in Cu-SSZ-13 (a Cu^{2+} ion-exchanged zeolite SSZ-13 with CHA structure).[30] Due to the small primitive cell, chabazite is often used in simulations or for benchmark purposes, e.g. in comparisons of the dispersion correction for the adsorption of alkanes in chabazite.[31] More recently, SSZ-13 was also experimentally evaluated at IFPEN laboratories (experiments supervised by C. Bouchy and JM Schweitzer) for the hydroconversion of C_7 molecules and it exhibits relevant isomerization and cracking performances compared to other zeolites previously studied.[5]

The small pore structure of CHA is built up of double six membered-rings forming large ellipsoidal cavities (Figure I- 5).

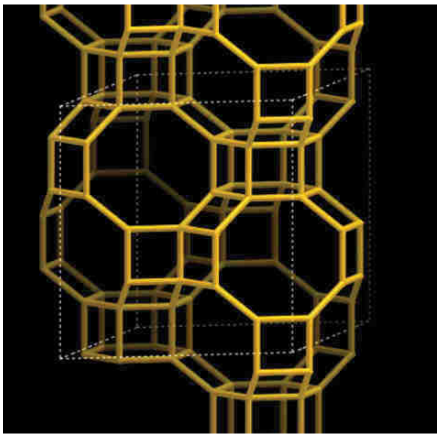

Figure I- 5. Silicon framework of CHA (from IZA website[26])

The large cages are connected in three directions by small 8MR pores.[32] All the tetrahedral sites are symmetry equivalent. The conventional crystallographic unit cell of purely siliceous CHA is trigonal, with lattice constants $\alpha = \beta = 90°$, $\gamma = 120°$, $a = b = 13.6750$ Å, and $c = 14.7670$ Å and it contains 108 atoms (i.e. 36 SiO_2 units). The maximal diameter of a sphere that can be included in a pore is 7.37 Å, which is larger than the maximal allowed size of adsorbate in BEA (6.68 Å) for example. The dimensions of the 8MR channels are 3.8×3.8 Å (smaller than BEA). This last diameter is variable because the framework exhibits a very large flexibility.[26] In order to reduce the computational cost, a unit cell with 24 SiO_2 units can be used in simulations (Sections III to V).

I.3. Nature of the reaction intermediates in zeolites

I.3.1. General features

Alkenes (obtained upon alkane dehydrogenation) diffuse within the microporosity and then they are adsorbed on acid sites to yield reactive intermediates, and finally, the products. Alkenes are very reactive in acid zeolites, even at low temperatures, and they are very difficult to detect experimentally, suggesting that they are short-lived intermediates.[33,34] Alkenes are first physisorbed as van der Waals complexes in the cavity of the zeolites and then as π-complexes on the acid sites. Upon chemisorption, accompanied by a proton transfer, carbenium ions and alkoxides can be formed (Figure I- 6). The nature of these chemisorbed intermediates is crucial for understanding of the mechanisms of isomerization and cracking of alkenes. The exact nature of these intermediates is still a matter of debate, and experiments alone probably cannot answer this question because the lifetime of these species is too short.[3,4,7,14,22,33,34]

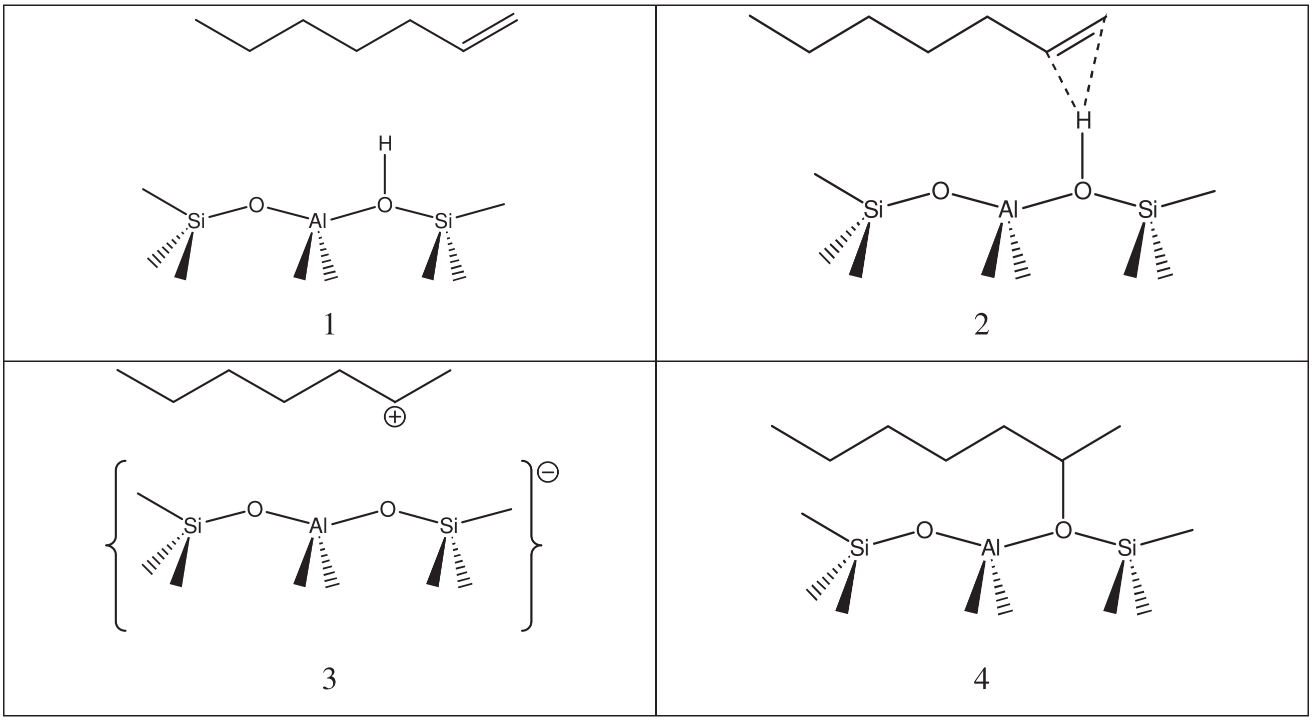

Figure I- 6. Assumed adsorption states of 1-heptene on the acid site of a zeolite: 1: van der Waals complex; 2: π-complex; 3: carbenium ion; 4: alkoxide.

By analogy with conventional organic chemistry,[35,36] the reactive intermediates were traditionally assumed to be carbenium ions, and carbenium or carbonium ions.[37] In textbooks[17] or review articles[3,4], general mechanisms are written with carbenium ions as reactive intermediates and with carbonium ions playing role of transition states (Sections I.1 and I.4).

I.3.2. Experimental observations

Carbenium ions detected experimentally in zeolites are highly resonant and branched species (cyclic alkenyl or aromatic carbenium ions, Figure I- 7).[38]

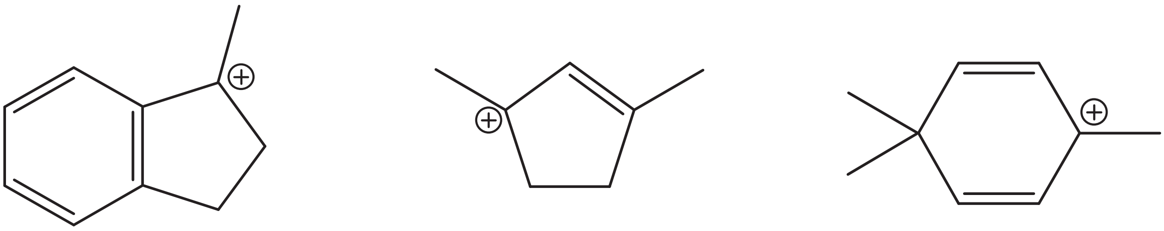

Figure I- 7. Aromatic and cyclic alkenyl carbenium ions observed in zeolites.[38]

The parent alkenes of these cations are Brønsted bases that are strong enough to capture the proton from the zeolite while the corresponding alkoxides are unstable because of their steric hindrance. On basis of experimental and theoretical data, Nicholas and Haw concluded that carbenium ions can be observed by NMR if the proton affinity of the parent alkene is higher than 875 kJ.mol^{-1} (close to the value measured for NH_3).[38]

Ivanova and Kolyagin[34] reviewed the impact of in situ MAS NMR techniques on understanding the mechanisms of zeolite catalyzed reactions. Starting from small alkenes or alcohol, simple carbenium ions are not observed and the formation of alkoxides is detected. Persistent carbenium ions are observed as secondary products of oligomerisation with longer and more branched species. Indirect evidence of the formation of transient carbenium ions are reported for longer alkenes. For instance, the ^{13}C scrambling of 1-octene is consistent with the mechanism that includes carbenium ions as reactive intermediates and protonated cyclopropanes (PCP) as transition states (Figure I- 8).

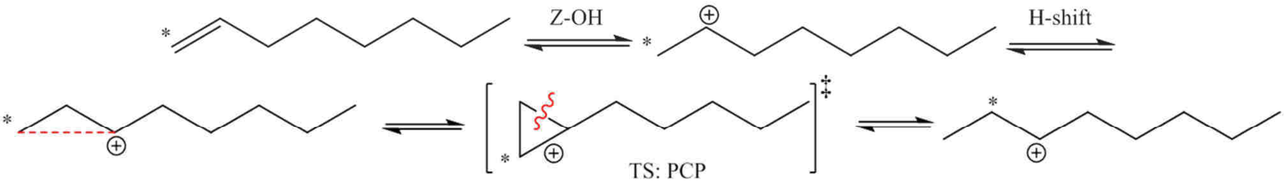

Figure I- 8. ^{13}C scrambling of 1-octene. Adapted from ref[34,39]. ^{13}C is spotted C*.

This ^{13}C scrambling over the whole skeleton of the molecule is typical of the behavior of carbenium ions in superacidic solutions. At this stage, a similar mechanism with alkoxides instead of carbenium ions as intermediates, cannot be excluded. Another indirect evidence of the existence of carbenium ions is the interaction of carbenium ions with carbon monoxide, the resulting oxo-carbenium ion yielding carboxylic acid in presence of water, which is the same reaction as in solutions of strong acids.[39] Simultaneously, the signal from the adsorbed alkoxides disappears suggesting that alkoxides are transformed into carboxylic acids via carbenium and then oxocarbenium ions. With these observations, the authors conclude that unstable carbenium ions are certainly in equilibrium with alkoxides when the original reactants are octene, isobutene, *tert*-butyl, isobutyl and n-butyl alcohols.[39]

Based on these results, Ivanova and Kolyagin conclude that acid zeolites can stabilize highly resonant or long chain cations (such as the examples of Figure I- 7, or cations obtained from triphenylmethanol or from oligomerisation of shorter species) but not the simple short cations (ethyl, propyl). There is indirect evidence for the longer or more branched simple cations (obtained from octene, *n*-butene isobutene or *tert*-butyl alcohol with CO adsorption or ^{13}C scrambling).[34]

Other indirect evidence in favor of carbenium ions comes from kinetic studies of hydrocracking of C_6-C_9 alkanes on zeolites of different compositions with varying ratios Si/Al. Similar kinetic constants are found for different ratios Si/Al, which is consistent with a reaction route involving free carbenium ions rather than with the mechanism involving transition states not completely separated from the acid sites (which would be the case for reactions starting and ending with alkoxides according to the authors).[40] One may wonder, however, if carbenium transition states, separated from the framework could not also exist with alkoxides as intermediates.

The first more direct evidence of the existence of the tert-butyl cation was reported very recently.[41] In zeolite H-ZSM-5, the isobutenium cation was captured with ammonia and the resulting ammonium ion (Figure I- 9) was identified by MAS NMR spectroscopy (by comparison with DFT calculations, with the non-local BEEF-vdW functional). A direct substitution of ammonia on the alkoxide can still be considered but the authors explained that the signal of the *tert*-butylammonium ion can only be observed if gaseous isobutene and ammonia are introduced simultaneously. If ammonia is introduced after isobutene adsorption, the signal of the *tert*-butylammonium is not detected, because of too short lifetime of the isobutenium cation.[41] This conclusion has been confirmed in a subsequent work starting with ^{13}C labeled *tert*-butanol.[42]

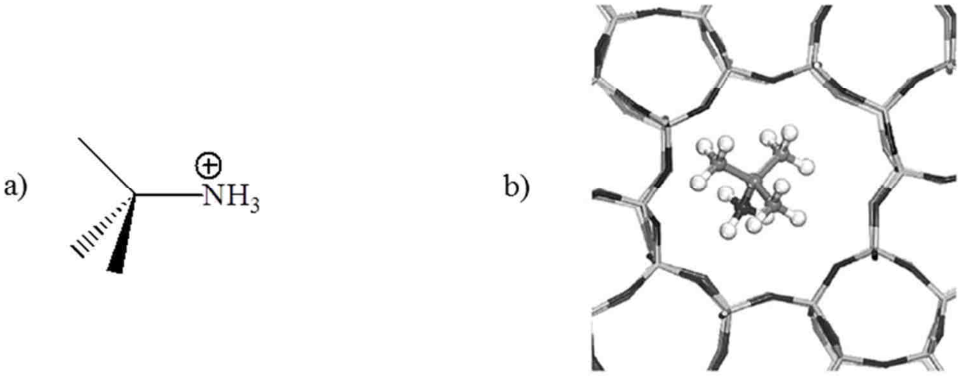

Figure I- 9. Schematic drawing of tert-butyl ammonium (a) and the same cation created in H-ZSM-5 (b). Adapted from ref.[41]

I.3.3. Theoretical results

I.3.3.1. Early theoretical results

Computational studies have considered the issue of the nature of the reactive intermediates in hydroconversion in zeolites since the end of the eighties. The conclusions have changed over time with the level of theory used in the simulations. Early quantum chemical calculations concluded that alkoxides were stable and that carbenium ions were only transition states in zeolites. On this basis, some authors denied the existence of carbenium ions (even tertiary ones) as possible intermediates in zeolites.

The pioneering calculations were performed by Kazansky and Senchenya.[43] They performed semi-empirical and non-empirical calculations (SCF LCAO with a minimal basis set STO-3G) using small clusters representing a zeolite framework (one, two, or three silicon and alumina-oxygen tetrahedral units), with dangling bonds saturated by hydrogen atoms and alkoxides obtained from short alcohols: methanol, ethanol and isopropanol. They concluded that alkoxides were stable and that carbenium ions were transition states.

Similarly, van Santen[44] et al. addressed these questions with Hartree-Fock and DFT (B3LYP) calculations of small clusters (one or three tetrahedral sites) in the context of cracking of butene and pentene.[44] They proposed the mechanism shown in Figure I- 10, with alkoxides as stable intermediates at the beginning and at the end (a and d), an intermediate cyclopropane (b) and a transition state (a complex of a carbocation in strong interaction with the cluster) (c). They also concluded that the stable intermediates were alkoxides and that carbenium ions were high-energy transition states with energy barriers as high as 250 to 300 kJ.mol^{-1} (depending on the level of theory, the size of the cluster and the mechanism).

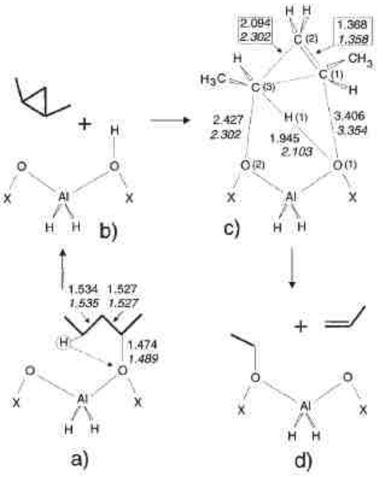

Figure I- 10. Two-steps of β-scission of pent-2-oxy. Distances are in Ångströms (standard font is used for X = H, small cluster and italics for X = SiH_3, the bigger cluster). Reprinted with permission from ref[44]. Copyright (1998) American Chemical Society.

Because of the limited computational power available at the time, these early calculations were carried out using small clusters which were not able to describe the microporosity of a zeolite and hence they necessarily underestimated the steric hindrance (mainly for alkoxides). All these early calculations have been performed without inclusion of long-range dispersion corrections. Later, the conclusions of these studies have been reevaluated using more advanced simulation methods and more realistic structural models.

I.3.3.2. Improvement of the description of long range effect

The first *ab initio* study of an isomerization reaction in a zeolite with periodic boundary conditions was done by Demuth et al. in 2003.[11] They explored the isomerization of pent-2-ene by means of the DFT simulations (with the GGA functional PW91, without correction for missing long-range dispersion interactions). They also proposed mechanisms with stable alkoxides as intermediates and carbenium ions as high energy transition states. They found the potential energy barriers of around 100 kJ.mol^{-1}.

At around the same time, some computational studies with periodic DFT or embedded clusters showed that depending on the position and on the zeolite framework, the stability of iso-butoxide becomes comparable to the corresponding transition state carbenium ion and that the *tert*-butyl carbenium can be chemisorbed to form *tert*-butoxide.[45,46] The stability of alkoxides in different zeolites was studied by Marin and coworkers with embedded clusters and finite temperature corrections leading to estimates of enthalpy: the chemisorption of 1-alkenes in alkoxide is framework dependent and becomes increasingly more favorable when the catalyst is altered in the following order H-FAU < H-MOR < H-BEA < H-ZSM-5.[47] Corma and coworkers investigated some mechanisms of acid-catalyzed reactions of alkenes (C_2 to C_4) (scrambling and skeletal isomerization of butene, for instance), with embedded clusters. They concluded that the *tert*-butyl cation can exist as an intermediate and that the alkoxides can be destabilized depending on the position on the framework. Non classical carbonium ions may also exist as intermediates if the positive charge is inaccessible to framework oxygen atoms.[46,48]

I.3.3.3. Static thermal effects

Tuma and Sauer performed calculations with zero-point vibration energies, entropic effects, and finite temperature corrections.[49] Their results obtained using the DFT (PBE) method without correction for the long-range dispersion interactions and in the harmonic approximation for vibrations showed that the *tert*-butyl cation becomes more stable (in terms of free energy) than the alkoxides in the acid ferrierite H-FER at temperatures higher than 120 K. The additional covalent bond present in the alkoxides limits their mobility and hence it must lower their entropy. At this level of theory, only the π–complex is more stable than the gas phase isobutene.

Using DFT with periodic boundary conditions (and Tkatchenko-Scheffler van der Waals correction[50]) and embedded cluster calculation, Ferguson and coworkers[51] investigated the stability of the C_4 carbenium ions in H-ZSM-5 taking into account the thermal excitations of vibrational degrees of freedom: at 500K, secondary butyl cation can be present at small amounts (< 1% of alkoxide), and the *tert*-butyl cation is the only cation that may exist in significant quantities. Primary cations are never found as minima. The authors conclude that mechanisms involving tertiary and secondary cations are relevant at high temperatures.

Recently, it was shown that anharmonic corrections for vibrational frequencies make possible the calculation of thermodynamic properties and rate constants within chemical accuracy (± 4.2 kJ/mol with reference data) for adsorption of alkanes in zeolites[52] and for chemical reactions such as conversion of methanol to olefins[53] and for proton exchange barriers for alkanes[54] in acid zeolites.

I.3.3.4. Higher levels of theory

Tuma and Sauer included dispersion interactions at the MP2 level for a cluster embedded in a periodic model, with extrapolation of the MP2 energy to the complete basis set limit and further extrapolation of the MP2 reaction energy to the full periodic structure.[55] Within this hybrid method, the adsorbed species are stabilized compared to the isobutene in gas phase, and the authors concluded that the *tert*-butyl cation is less stable than the alkoxides at 298 K. In a more recent work employing hybrid MP2:DFT calculation, Tuma, Kerber and Sauer also calculated the potential energy barriers for reactions involving different adsorbed species.[56] They showed that the *tert*-butyl cation is a local minimum of potential energy although it is less stable than the corresponding alkoxides. With finite temperature corrections, they estimated the life-time of the carbenium to be 60 μs at 298 K with an uncertainty of order of tens of μs. The dispersion correction increases the barriers separating the carbenium from the alkoxides and π-complex.

Altogether, according to high level calculations (hybrid calculations, beyond DFT and up to post-Hartree-Fock methods, with entropic and thermal effects), the relative stability of the carbenium ions is reinforced in comparison with the earlier theoretical studies.

The nature of isolated secondary cations, classical or non-classical with hydrido-bridged structures (Figure I- 11) has been debated.[57,58] An accurate treatment of the electronic correlation by wave-functions methods is required for the proper description of the potential energy surface of secondary cations. An hydrido-bridged structure of the 2-3dimethyl-buten-2-ium secondary cation in gas phase has been described as a shallow local minimum of potential energy surface at the MP2 level.[57] Recently, it was shown that the hydrido-bridged structure and the classical one (being strongly constrained in a PCP-like structure) of the buten-2-ium cation are nearly degenerate, at the MP2, CCSD(T) or B3LYP levels.[58] These differences in energy are very small and the experimental evidence of the corresponding structures can only be obtained at very low temperature (the buten-2-ium cation giving spontaneously the tertiobutyl cation at -40°C in superacid solutions). Similarly, non-classical structures of tertiary cations (corner protonated cyclopropanes) have also been identified as local minima with MP2 calculations in gas phase but cannot be detected by ^{13}C NMR above -108°C,[59] which tempers the need of high level calculation at temperatures such as 300 or 500 K.

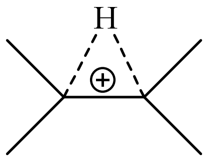

Figure I- 11. Hydrido-bridged structure of a carbocation.

I.3.3.5. Ab initio Molecular dynamics

In very recent studies, using *ab initio* molecular dynamics simulations, van Speybroeck and coworkers investigated the stability of intermediates obtained from pentene in H-ZSM-5 and concluded that the stability of alkoxides had been overestimated in the early studies, mainly at high T (> 573 K).[14,15,33] *Ab initio* molecular dynamics accounts for the mobility of adsorbates and for entropic effects without using the harmonic approximation for the vibrations. Static calculations tend to overestimate the stability of adsorbed species (which is due to the use of geometries optimized at T = 0 K), yielding too high adsorption enthalpies, as shown by Göltl and co-workers for adsorption of alkanes in chabazite.[31]

With straightforward *ab initio* molecular dynamics (at the rev-PBE-D3 level of theory), starting from π-complex and alkoxides of linear pentene in H-ZSM-5, van Speybroeck and coworkers did not obtain any carbenium ion, indicating that the transformation in carbenium ion is a rare event. Advanced methods are necessary to sample rare events in molecular dynamics. The authors used Metadynamics (a biased molecular dynamics method designed to study rare events) to obtain a free-energy profile from the π-complex to the carbenium and the alkoxide at T = 323 K. The results are qualitative due to the limited simulation time but the secondary carbenium ions obtained from pentenes appeared as local minima of free energy (see Figure I- 12 for pent-1-ene), with π-complex and alkoxide of a similar stability. The activation free-energy for transformation of the π-complex into the carbenium ion is at least 32 kJ.mol^{-1} and the secondary carbenium ion appears as a transient species.[14]

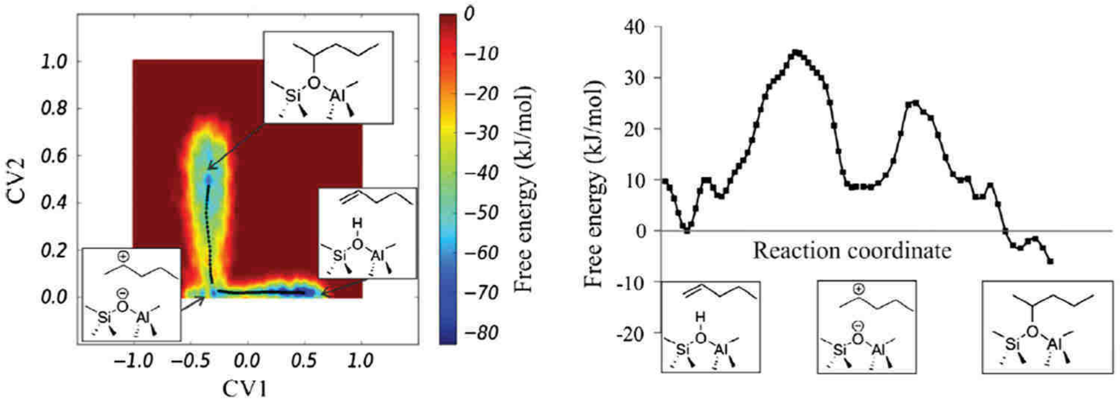

Figure I- 12. Left: 2D free energy surface for the formation of 2-pentoxide from a 1-pentene π-complex. Right: corresponding 1D free energy profile. Reprinted from ref. [14] with permission from Elsevier.

In their subsequent paper, van Speybroeck and coworkers investigated the effect of temperature and branching on the adsorption of alkenes with 4 or 5 carbons. Temperatures of 323, 523 and 773 K (temperature of cracking) were considered. They concluded that static calculations are not appropriate (they underestimate the stability of carbenium ions) and that secondary and tertiary alkoxides are disadvantaged at high temperature (773 K) (Figure I- 13). Tertiary carbenium ions are stable at 773 K whereas secondary cations are metastable.[33]

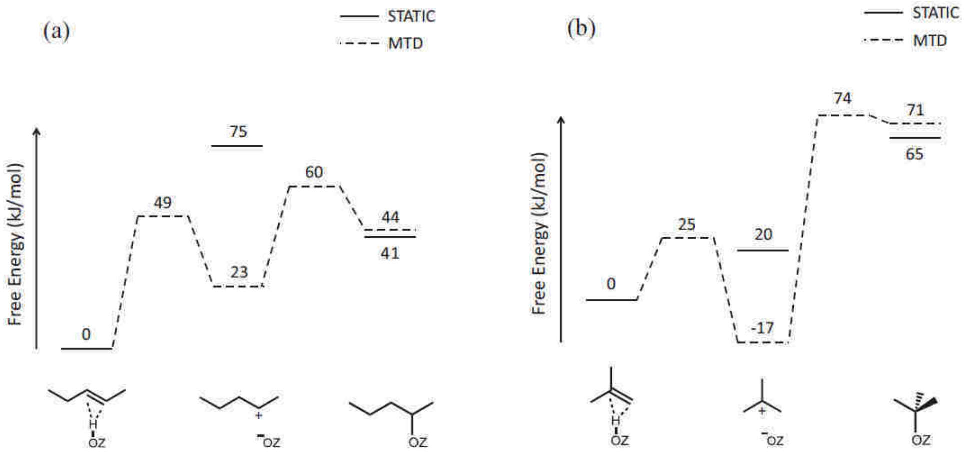

Figure I- 13. Free energy profiles in kJ.mol^{-1} at 773 K for (a) the formation of 2-pentoxide from 2-pentene and (b) the formation of *tert*-butoxide from isobutene from metadynamics (MTD) simulations and static calculations.[33]

I.3.4. Conclusion

The theoretical predictions of the stability of the reactive intermediates have clearly evolved over time. With the more realistic simulations, accounting for finite temperature effects, the existence of the carbenium ions has been re-evaluated. In particular biased *ab initio* molecular dynamics simulations reveal that the stability of carbenium ions was underestimated while that of alkoxides was overestimated in the previous theoretical static calculations.

I.4. Reactions involved in hydrocracking

In this section, we will describe the mechanisms and selectivity of hydrocracking in terms of carbenium ions transformations, as depicted in the general scheme of Figure I- 1.

I.4.1. Isomerization step

I.4.1.1. General mechanisms

There are two types of mechanism for the isomerization:[3,4]

- Type A isomerization: the carbocation (or classical carbenium ion) undergoes an alkyl shift (R = CH_3 for instance) or hydride shift (R = H). The branching degree of the chain is not modified (Figure I- 14).

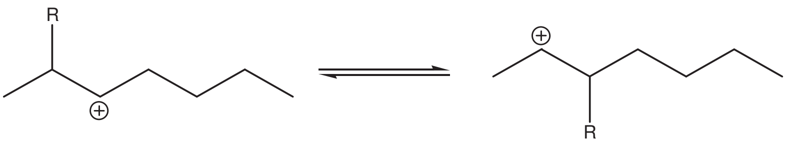

Figure I- 14. Type A isomerization without modification of the branching degree.

The reaction rate of 1,2 hydride shift decreases in the following order, depending on the nature of the initial and final carbenium ions: secondary-secondary > tertiary-tertiary > tertiary-secondary.[36] Alkyl shifts are slower and 1,2 methyl shifts are the easiest. The reaction rate decreases in the order tertiary-tertiary > tertiary-secondary.[36] The 1,2 hydride shifts were believed to be dominant over 1,3 shifts under refining conditions.[60] However, it was also demonstrated by experiments[36] and *ab initio* calculations[57] (in gas phase, at the MP2-MP4 level of theory) that in some cases, the 1,3 hydride shift is easier than two successive 1,2 hydride shifts.

Transition states for these type A isomerization reactions are supposed to be non-classical carbonium ions, protonated cyclopropanes (PCP): edge protonated cyclopropanes (or EPCP) for 1,3 hydride shifts,[36,57,60,61] and corner protonated cyclopropanes (or CPCP) for 1,2 methyl shifts.[59,60]

Figure I- 15. a) Edge protonated cyclopropane (EPCP). b) Corner protonated cyclopropane (CPCP, or methyl-bridged structure).[36,60]

- Type B isomerization: the branching degree of the chain is modified. The reaction proceeds via non-classical carbonium ions: protonated cyclopropanes or PCP (Figure I- 16).[36,60]

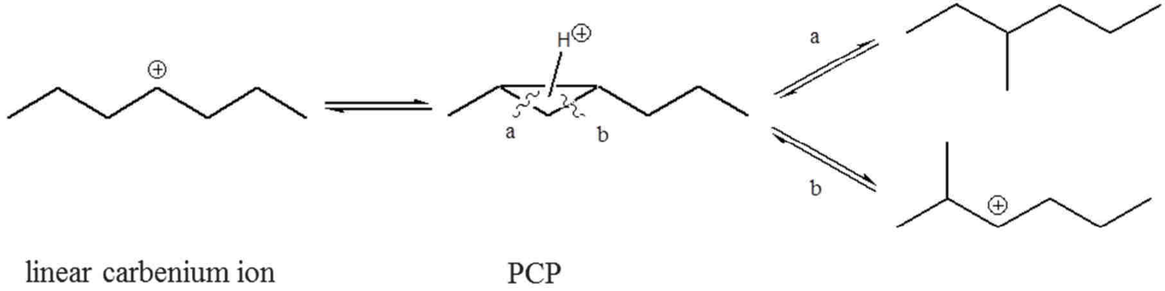

Figure I- 16. Type B isomerization with increase of the branching degree.

The exact nature of the PCP, reaction intermediate or transition state, is still unclear. According to the few DFT calculations devoted to the simulation of such ions, it depends on the location of the proton (corner protonated cyclopropane, CPCP, or edge protonated cyclopropane, EPCP).[11] Since, this question is still open and it will be investigated in the present PhD work with more advanced AIMD.

Type A isomerization is much faster than type B (about 1000 times[17], which represents a difference in activation energy of 20 kJ.mol^{-1} at T = 300 K). Without steric constraints induced by the catalyst, the positional isomers obtained by type A isomerization, may thus be at thermodynamic equilibrium between them, in conditions where type B isomerization can take place.[3,4]

The network of the type B isomerization reactions of C_7 alkanes has been established by Patrigeon et al[5] (Figure I- 17). We shall pay more attention to describe these reactions because they will be used as a case study for our theoretical investigation. Six different transition states (PCP) skeletons are necessary to describe all the transformations. Note that in Figure I- 17, the position of the proton on the PCP is not depicted, which may lead to several possibilities for each skeleton. It is noteworthy that the last isomer, with the skeleton of 2-ethyl-pentane can be obtained by type A isomerization, without change in the branching degree (Figure I- 18), and so it does not appear in the network of type B.

For short alkenes, for which it is not possible to obtain primary carbenium ions, the mechanisms for isomerization reactions are different. A mechanism of isomerization of cis-to trans butene has been proposed to proceed via an alkoxide route on the outer surface of H-ZSM-5.[62] The skeletal isomerization from linear butene to iso-butene has been investigated by quantum chemistry, whereby mono and bimolecular mechanisms have been discussed. It has been suggested that isobutene is mainly produced by the monomolecular mechanism (the bimolecular one giving mainly side products) and a mechanism via alkoxides and transition states (protonated cyclopropane and primary carbenium) has been proposed.[63] D. Gleeson compared the alkoxy and carbenium routes for this skeletal isomerization: the barriers are lower for reactions involving carbenium ions but the alkoxides are more stable. The bimolecular route appears more favorable, but non-selective in isobutene.[64]

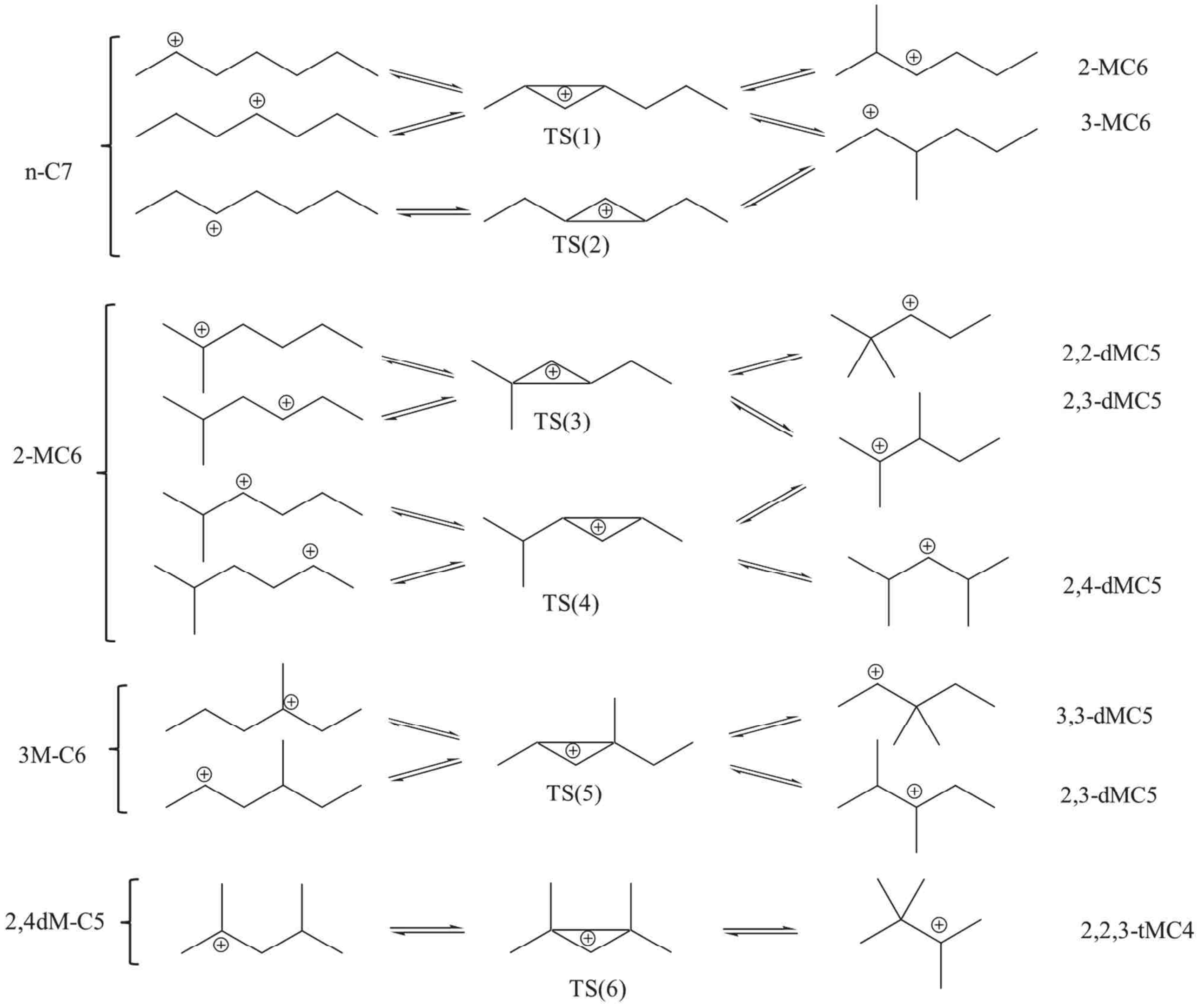

Figure I- 17. Type B isomerization reactions for C_7 alkanes. Adapted from ref.[5] with permission from Elsevier.

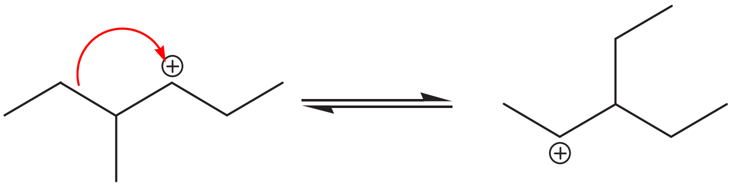

Figure I- 18. Type A isomerization leading to the 2-ethyl-pentane cation.

I.4.1.2. Energy barriers

In their DFT investigations of the isomerization of pent-2-ene in the zeolite H-ZSM-22, Demuth and coworkers[11] obtained two mechanisms, starting and finishing with alkoxides (Figure I- 19 and Figure I- 20). A pathway via an ethyl shift was discarded because of a too high energy barrier of 180 kJ.mol^{-1}. As transition states, carbenium ions were identified. These two pathways exhibit activations energy around 100 kJ.mol^{-1} (98 and 112 kJ.mol^{-1}). The easiest one (from the point of view of the electronic energy) proceeds via a neutral adsorbed cyclopropane (ads DMCP in Figure I- 19 and Figure I- 20) and it requires complex rotations. For that reason it is probably kinetically disfavoured with respect to the more direct one, proceeding via an intramolecular hydrogen shift (and an edge protonated cyclopropane EPCP). The authors were not able to address this question as their methodology was limited to zero temperature static calculations. The reported potential energy barrier around 100 kJ.mol^{-1} is in agreement with the experimental result for the n-hexane hydroisomerization in Pt/H-ZSM-22 (106 kJ.mol^{-1} at 240 °C).[65]

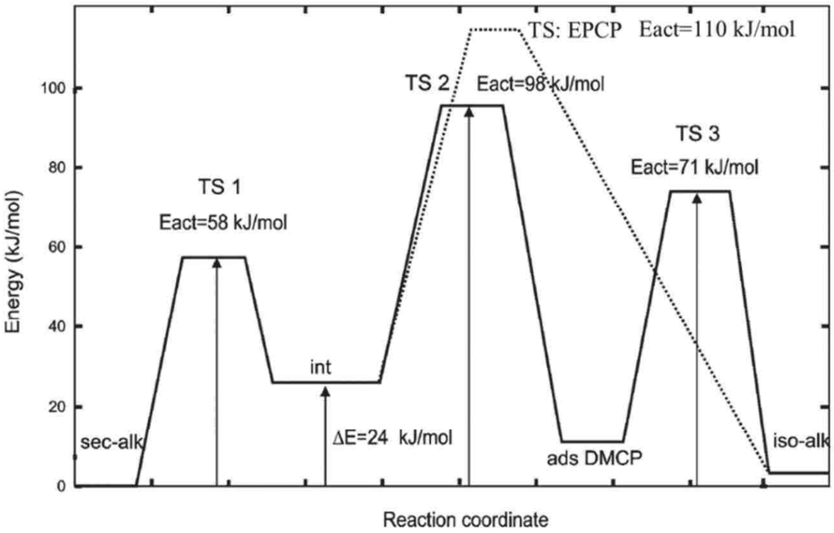

Figure I- 19. Electronic energy diagram for the isomerization of 2-pentene (see the structures in Figure I- 20). Solid line: isomerization via a DMCP intermediate; dashed line: via an intramolecular hydrogen shift. Reprinted from ref.[11] with permission from Elsevier.

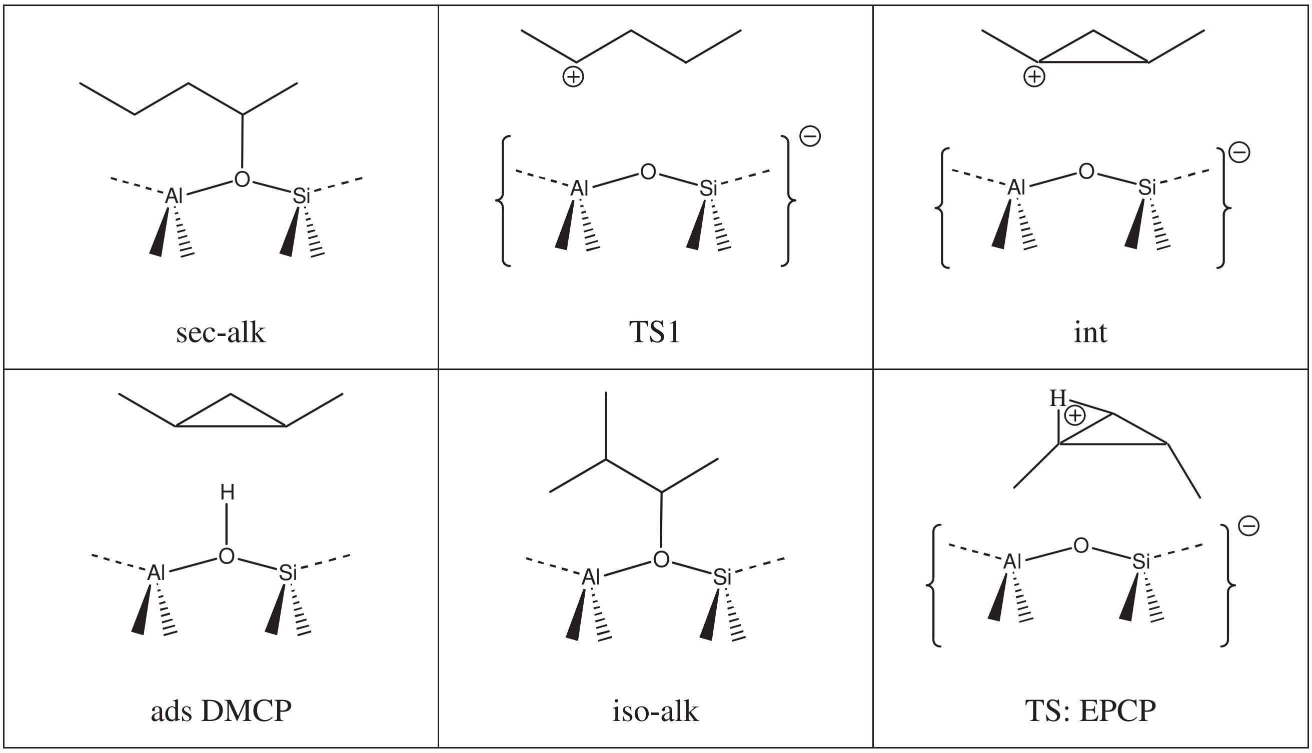

sec-alk | TS1 | int

ads DMCP | iso-alk | TS: EPCP

Figure I- 20. Structures of stationary states displayed in Figure I- 19. Adapted from ref.[11]

Kinetic information on hydrocracking have been obtained by the single-event kinetic modeling methodology. In the "single event" methodology, the reactivity of a molecule is linked to its geometry and to a few kinetic parameters depending on the nature of the molecule and of the relevant reaction. The global single event network is generated by an algorithm. Relumping techniques are used to reduce the reaction network and the number of differential equations to be solved: molecules are grouped by families of isomers (depending, for instance, on their degree of branching) considered to be in equilibrium.[66]

With single event kinetic modeling, fitted on experimental data for C_8 to C_{12} alkanes on Pt/USY catalysts, Martens and coworkers obtained intrinsic activation energies of about 100 $kJ.mol^{-1}$ for isomerization between carbenium ions, via protonated cyclopropanes (from 99 to 128 $kJ.mol^{-1}$ for secondary/secondary to tertiary/tertiary isomerizations) and intrinsic barriers from 74 to 105 $kJ.mol^{-1}$ for alkyl shifts.[6,7]

Thybaut and coworkers obtained results of the same order of magnitude in a recent single event kinetic modelling of isomerizations between carbenium ions (via protonated cyclopropane) for n-hexane hydroisomerization in Pt/H-ZSM-5[9] and for n-hexadecane hydrocracking on Pt/H-BEA[10]. They obtained activation enthalpies for isomerization reactions of values between 100 and 140 $kJ.mol^{-1}$ (depending on the cations) and between 75 and 100 $kJ.mol^{-1}$ for alkyl shifts.

I.4.2. Cracking

I.4.2.1. General mechanism

According to the nature of the carbenium ions involved in reaction (tertiary or *tert* in an abbreviated form, secondary or *sec*, primary or *prim*), five types of β-scission reactions can be written. They are referred to as type A, B_1, B_2, C and D according to the Weitkamp's terminology (Table I- 1). Their rate constants decrease from type A to type D as the stability of the carbenium ions (reactants and/or products) decreases.[3,4] As a consequence, a β-scission of a more branched carbon chain is more favorable .

Tribranched cations appear at higher conversion and even in ideal hydrocracking conditions they undergo cracking into a shorter alkene and a shorter tertiary cation since the type A (*tert* → *tert*) or B_2 (*tert* → *sec*) cracking reactions are fast.[4,17]

Type	Minimal number of C atoms	carbeniums involved	Example
A	≥ 8	*tert* → *tert*	
B_1	≥ 7	*sec* → *tert*	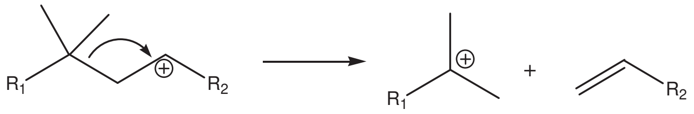
B_2	≥ 7	*tert* → *sec*	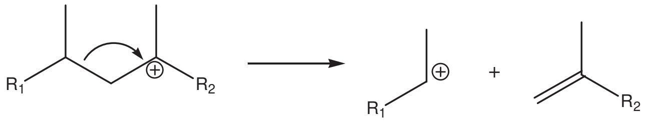
C	≥ 6	*sec* → *sec*	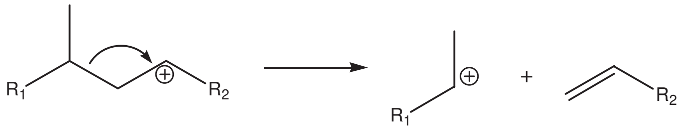
D	≥ 5	*sec* → *prim*	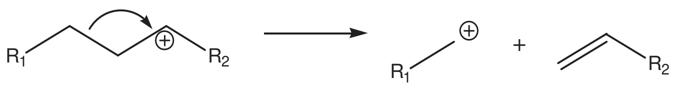

Table I- 1 Terminology of the different types of isomerization reactions. Adapted from ref.[17]

In hydrocracking conditions, no methane nor ethane are obtained: the type D β-scission, involving a primary carbenium ion, is considered as forbidden.

The network of cracking reactions for the C_7 alkanes that will be investigated in this thesis has been established by Patrigeon et al. (Figure I- 21).[5] The forbidden type D β-scissions are not involved in his scheme and it is noteworthy that the tribranched cation cannot undergo a β-scission in this specific case.

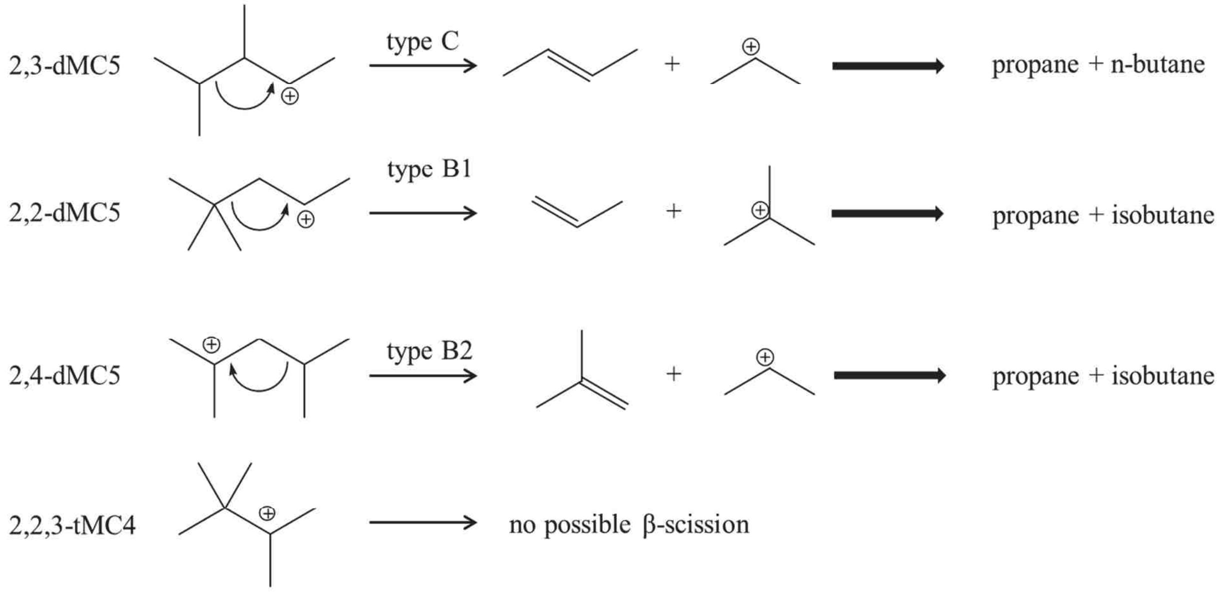

Figure I- 21. β-scissions for C_7 alkanes. Reprinted from ref.[5] with permission from Elsevier.

I.4.2.2. Energy barriers

Experiments in superacid liquid phase[36] or in zeolite[67] demonstrated that type A cracking is faster than type B isomerization reactions, and that type B1 and B2 cracking reactions are slower.

A single-event kinetic model (starting from carbenium ions) for 1-pentene cracking in H-ZSM-5 predicts the activation energy of around 200 kJ.mol^{-1} (around 170 kJ.mol^{-1} for the transformation from tertiary to secondary cations).[68] With a single-events microkinetics model of the shape selectivity effects for the hydrocracking of n-hexane on Pt/H-ZSM-5, Vandegehuchte et al. obtained a cracking barrier of 143 kJ.mol^{-1} for the reaction linking two secondary carbenium ions.[9] They obtained enthalpy barriers ranging between 118 (secondary to tertiary carbenium ions) and 152 kJ.mol^{-1} (tertiary to secondary carbenium ions) for the n-hexadecane hydrocracking on Pt/H-beta.[10] The uncertainty in these models is large, due to the fitting of numerous parameters and to the models describing the adsorption and protonation of the reactant alkenes.

As for the isomerization reactions, barriers for cracking (β-scission) of olefins were usually evaluated in the framework of static DFT calculations assuming alkoxides as the initial state. With periodic DFT calculations and experiments, potential energy barriers from 100 to more than 200 kJ.mol^{-1} (depending on the substitution of the initial species) were obtained for the β-scission of C_6 and C_8 olefins, starting mainly from alkoxides or carbenium ions.[8,12] Similar high potential energy barriers were calculated for the cracking of butene and octene, starting from alkoxides, on different zeolites.[13] For C_7[69] and C_6[70] alkenes, potential energy barriers above 100 kJ/mol were found with static calculations, starting with π-complexes or alkoxides. The static approach is highly questionable because a large dispersion of the barriers is observed: 89 and 171 kJ/mol for instance, for the same B_2 cracking reaction, depending on the conformation of the reactant,[12] and 90 to 167 kJ/mol for different configurations of the transition state of a B_2 cracking reaction of C_8 alkenes.[15] In contrast with experimental results, the barriers previously estimated by kinetic modeling and static DFT appear to be higher than those for type B isomerization reactions. They are questionable because of the wide range of values due to uncertainties inherent to the models used in simulations. Recent studies demonstrated that dynamics effects must be taken into account for the cracking of alkanes in zeolites,[71] and in a very recent biased Molecular Dynamics study for C_8 alkenes in H-ZSM5, van Speybroeck and coworkers computed lower free energy barriers for the cracking of C_8 alkenes, from 53 to 112 kJ/mol, for type A to E_2 (i.e. tertiary to primary cations) cracking reactions at 773 K. This suggests that in this case, again, advanced Molecular Dynamics methods are required.

I.4.3. Shape selectivity

Confinement effect in zeolites can be at the origin of shape selectivity for hydrocracking reactions as demonstrated by previous force fields simulations.[25] Shape selectivity can be determining at three different steps: diffusion of the reactants, steric hindrance for the transition states, and diffusion of the products.[72] Reactants which are too bulky to diffuse in the zeolite porosity cannot be transformed or should react at the external surface.[73] Similarly, too bulky products (often because of branching) cannot diffuse out of the zeolite. Transition states for type B isomerization (protonated cyclopropanes), with the increase of the branching degree, are constrained and bulky structures, and they may be destabilized in the microporosity of some zeolites.[3,5] In large pore zeolites, tribranched isomers with at least 8 carbon atoms can be formed and they undergo a very fast type A β-scission.[4]

Patrigeon et al. performed catalytic tests on n-heptane hydroisomerisation catalyzed by various zeolites (Figure I- 3).[5] At high conversions, more multibranched and cracked products are obtained in large pore zeolites (such as Beta or Y zeolite) than in smaller pore zeolites (such as ZSM-22 and ZSM-23) where monobranched products predominate even at high conversions. With force fields calculations, this result was explained by the absence of steric hindrance in the transition states and by the easy diffusion of products within the large pore zeolites.

In contrast, it was found in another study dealing with longer alkanes (n-C_{10}, nC_{14} and nC_{16}) that the large pore Beta zeolite exhibits greater yields in monobranched isomers than smaller pore zeolites (MCM-22 and ZSM-5) which was attributed to a fast diffusion of the products in the network of large pores of the Beta zeolite.[74] However, significant amounts of cracking and multibranched side products are observed in the Beta zeolite. Reducing the agglomeration of zeolite nanocrystals, the residence time of the products in the zeolite decrease and the yield in monobranched isomers is increased.[75]

These two latter results seem to be contradictory but they definitely indicate that shape selectivity results from too many subtle topologic effects and that the diameter of the pores is not the only relevant parameter. Moreover, the molecular size and pore-mouth catalysis for long molecules may also play some role.

Shape selectivity can also occur within monobranched or dibranched products. Patrigeon et al.[5] showed that in comparison with large pore zeolites (Beta and Y), the concentration of products 2,2- and 3,3-dimethyl-pentane are much lower than the concentration of 2,3 and 2,4-dimethyl-pentane (except at the highest conversions) in the small pores (10 member rings) zeolites ZSM-22 and ZSM-23. The former products are disadvantaged by high diffusion barriers and also by bulky transition states. In ZSM-22, the concentration of 2,3-dimethyl-pentane is negligible, with a molar fraction of 0.4 % at high conversion because of a diffusion barrier higher than for 2,4-dimethyl-pentane. 2,3 dimethyl-pentane can be cracked to form propane and butane or it can be transformed by methyl shift into the carbenium ion 2,4-dimethyl-pentenium (Figure I- 22).

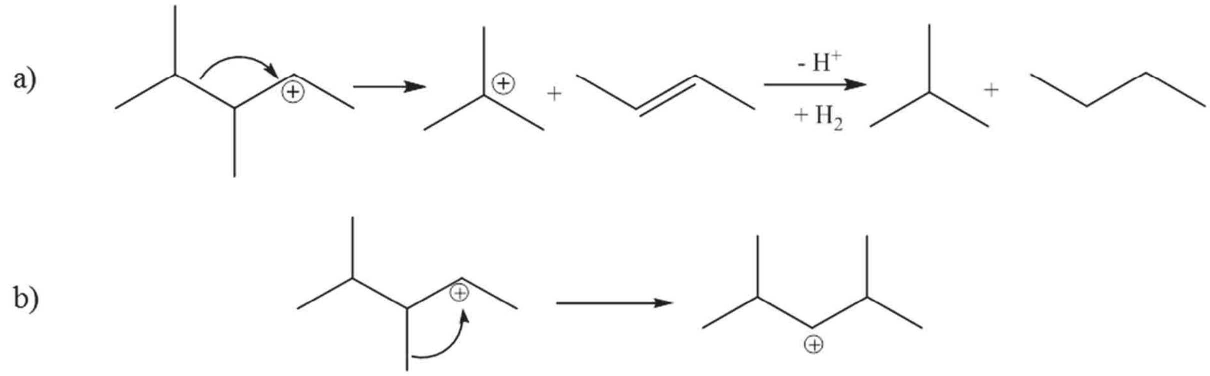

Figure I- 22. a) cracking reaction and b) methyl shift of a carbenium ion with the 2,3 dimethyl-pentane skeleton.

Similarly, in the zeolites ZSM-22 and ZSM-23, the product 2-methyl-hexane dominates over 3-methylhexane, which is attributed to a higher diffusion barrier of the latter. In larger pore zeolites, the ratio of concentrations of the aforementioned products is close to 1.

This concept justifies that it is crucial to get a more refined description of transition state involved in isomerization and cracking reactions in order to better quantify such transition state shape selectivity effects that are likely to impact the selectivity of the catalyst.

I.5. Conclusion and strategy of the thesis

According to the results published in the literature, the questions of the nature and stability of the reaction intermediates involved in hydrocracking/ reactions and the question of the accurate determination of energy barriers are still open. The more recent theoretical calculations, with higher levels of theory, with effect of temperature and/or dynamic effects tend to favor the carbenium ions rather than alkoxides (Section I.3.3). As a consequence, we have started our investigations with carbenium ions as reactive intermediates. The difficult question of the stability or metastability of the carbenium ions (and especially for the secondary ones) will be addressed in this work (Sections IV and V).

For isomerization reactions, some energy barriers have been published but only with potential energy calculations, and in some cases with approximate thermal corrections and β-scission. The necessity of *ab initio* molecular dynamics calculations was demonstrated for the estimation of the stability of relevant intermediates in zeolites (Section I.3.3), but to the best of our knowledge, no free energy barriers obtained from molecular dynamics simulation have ever been published so far for the isomerization reactions. For cracking reactions, most published results have been obtained with static calculations. A very recent study[15] proposed some free energy barriers from molecular dynamics for the cracking of C_8 alkenes in H-ZSM5 (Section I.4.2.2), in the case where reaction intermediates are tertiary carbenium ions. Moreover, no precise TS structure is reported. Obtaining accurate and consistent structural and energetic data that allow a quantitative comparison between isomerization and cracking reactions is needed in that context. We propose to investigate prototypical isomerization and cracking reactions for C_7 molecules, in chabazite (for computational reasons explained in Section II), employing advanced molecular simulation techniques.

Within the objectives of the thesis (see Introduction), we will start our investigations with isomerization reaction involving carbenium ions as reactive intermediates. With advanced *ab initio* molecular dynamics, we aim at understanding the molecular mechanism of the isomerization reactions of linear heptane, and in particular at providing reliable free energies of activation for the reactions of isomerization and β-scission. These results will be compared with static calculations at the PBE-D2 level. For reactions involving C_7 alkanes, the single event networks involves a large number of different reactions. We have started our investigations with two isomerization reactions leading to increase of the branching degree, from di to tribranched isomers and mono to dibranched isomers (Section III and IV). The theoretical methods are described in Section II and the results of our simulations in Sections III to V, where the more specialized bibliographic and methodological points will be discussed.

References

[1] C. Marcilly, *J. Catal.* **2003**, *216*, 47–62.

[2] W. Vermeiren, J.-P. Gilson, *Top. Catal.* **2009**, *52*, 1131–1161.

[3] C. Bouchy, G. Hastoy, E. Guillon, J. A. Martens, *Oil Gas Sci. Technol. – Rev. IFP Energies nouvelles* **2009**, *64*, 91–112.

[4] J. Weitkamp, *ChemCatChem* **2012**, *4*, 292–306.

[5] P. Raybaud, A. Patrigeon, H. Toulhoat, *J. Catal.* **2001**, *197*, 98–112.

[6] G. G. Martens, G. B. Marin, J. A. Martens, P. A. Jacobs, G. V. Baron, *J. Catal.* **2000**, *195*, 253–267.

[7] J. W. Thybaut, L. C. S. Narasimhan, G. B. Marin, J. F.M. Denayer, G. V. Baron, P. A. Jacobs, J. A. Martens, *Catal. Lett.* **2004**, *94*, 81–88.

[8] C.-J. Chen, S. Rangarajan, I. M. Hill, A. Bhan, *ACS Catal.* **2014**, *4*, 2319–2327.

[9] B. D. Vandegehuchte, J. W. Thybaut, G. B. Marin, *Ind. Eng. Chem. Res.* **2014**, *53*, 15333–15347.

[10] B. D. Vandegehuchte, J. W. Thybaut, A. Martínez, M. A. Arribas, G. B. Marin, *Appl. Catal. A-Gen.* **2012**, *441-442*, 10–20.

[11] T. Demuth, X. Rozanska, Benco, L.: Hafner, J., R. A. van Santen, H. Toulhoat, *J. Catal.* **2003**, *214*, 68–77.

[12] M. N. Mazar, S. Al-Hashimi, M. Cococcioni, A. Bhan, *J. Phys. Chem. C* **2013**, *117*.

[13] Y.-X. Sun, J. Yang, L.-F. Zhao, J.-X. Dai, H. Sun, *J. Phys. Chem. C* **2010**, *114*, 5975–5984.

[14] J. Hajek, J. van der Mynsbrugge, K. de Wispelaere, P. Cnudde, L. Vanduyfhuys, M. Waroquier, V. van Speybroeck, *J. Catal.* **2016**, *340*, 227–235.

[15] P. Cnudde, K. de Wispelaere, L. Vanduyfhuys, R. Demuynck, J. van der Mynsbrugge, M. Waroquier, V. van Speybroeck, *ACS Catal.* **2018**, *8*, 9579–9595.

[16] a) T. Bučko, L. Benco, J. Hafner, J. G. Ángyán, *J. Catal.* **2011**, *279*, 220–228; b) J. Rey, A. Gomez, P. Raybaud, C. Chizallet, T. Bučko, *J. Catal.* **2019**, *373*, 361–373;

[17] C. Marcilly, *Catalyse acido-basique. Application au raffinage et à la pétrochimie*, Technip, Paris, **2003**.

[18] P. B. Weisz, *Adv. Catal.* **1962**, *13*, 137–190.

[19] J. Zečević, G. Vanbutsele, K. P. de Jong, J. A. Martens, *Nature* **2015**, *528*, 245–248.

[20] C. Martinez, J. Pérez-Pariente (Eds.) *Zeolites and ordered porous solids. Fundamentals and applications*, 3rd FEZA shool on zeolites. Universitat Politècnica de València, **2011**.

[21] G. Busca, *Chem. Rev.* **2007**, *107*, 5366–5410.

[22] V. van Speybroeck, K. Hemelsoet, L. Joos, M. Waroquier, R. G. Bell, C. R. A. Catlow, *Chem. Soc. Rev.* **2015**, *44*, 7044–7111.

[23] a) W. O. Haag, R. M. Lago, P. B. Weisz, *Nature* **1984**, *309*, 589–591; b) W. J. Mortier, J. Sauer, J. A. Lercher, H. Noller, *J. Phys. Chem.* **1984**, *88*, 905–912;

[24] E. G. Derouane, Andre, J-M., Lucas, A. A., *J. Catal.* **1988**, *110*, 58–73.

[25] H. Toulhoat, P. Raybaud, E. Benazzi, *J. Catal.* **2004**, *221*, 500–509.

[26] C. Baerlocher, J. K. McCusker, "International Zeolite Association", to be found under http://www.iza-structure.org/databases/, **2017**.

[27] T. Bučko, J. Hafner, *J. Catal.* **2015**, *329*, 32–48.

[28] H. Awala, J.-P. Gilson, R. Retoux, P. Boullay, J.-M. Goupil, V. Valtchev, S. Mintova, *Nat. Mater.* **2015**, *14*, 447–451.

[29] U. Olsbye, S. Svelle, M. Bjørgen, P. Beato, T. V. W. Janssens, F. Joensen, S. Bordiga, K. P. Lillerud, *Angew. Chem. Int. Edit.* **2012**, *51*, 5810–5831.

[30] J. H. Kwak, R. G. Tonkyn, D. H. Kim, J. Szanyi, C. H.F. Peden, *J. Catal.* **2010**, *275*, 187–190.

[31] F. Goltl, A. Gruneis, T. Bucko, J. Hafner, *J. Chem. Phys.* **2012**, *137*, 114111.

[32] L. S. Dent, J. V. Smith, *Nature* **1958**, *181*, 1794–1796.

[33] P. Cnudde, K. de Wispelaere, J. van der Mynsbrugge, M. Waroquier, V. van Speybroeck, *J. Catal.* **2017**, *345*, 53–69.

[34] I. I. Ivanova, Y. G. Kolyagin, *Chem. Soc. Rev.* **2010**, *39*, 5018–5050.

[35] a) G. A. Olah, *Science* **1970**, *168*, 1298–1311; b) G. A. Olah, *J. Am. Chem. Soc.* **1972**, *94*, 808–820;

[36] D. M. Brouwer, Hogeven H., *Prog. Phys. Org. Chem.* **1972**, *9*, 179–240.

[37] Wojciechowski, B. W. and Corma, A., *Catalytic Cracking, Catalysis, Chemistry, and Kinetics.*, Marcel Dekker, **1987**, *Vol. 33*.

[38] J. B. Nicholas, J. F. Haw, *J. Am. Chem. Soc.* **1998**, *120*, 11804–11805.

[39] A. G. Stepanov, M. V. Luzgin, V. N. Romannikov, V. N. Sidelnikov, E. A. Paukshtis, *J. Catal.* **1998**, *178*, 466–477.

[40] J. F. Denayer, G. V. Baron, G. Vanbutsele, P. A. Jacobs, J. A. Martens, *J. Catal.* **2000**, *190*.

[41] W. Dai, C. Wang, X. Yi, A. Zheng, L. Li, G. Wu, N. Guan, Z. Xie, M. Dyballa, M. Hunger, *Angew. Chem. Int. Edit.* **2015**, *54*, 8783–8786.

[42] M. Huang, Q. Wang, X. Yi, Y. Chu, W. Dai, L. Li, A. Zheng, F. Deng, *Chem. Commun.* **2016**, *52*, 10606–10608.

[43] V. B. Kazansky, I. N. Senchenya, *J. Catal.* **1989**, *119*, 108–120.

[44] M. V. Frash, V. B. Kazansky, R. A. Rigby, R. A. van Santen, *J. Phys. Chem. B* **1998**, *102*, 2232–2238.

[45] X. Rozanska, R. A. van Santen, T. Demuth, F. Hutschka, J. Hafner, *J. Phys. Chem. B* **2003**, *107*, 1309–1315.

[46] M. Boronat, P. M. Viruela, A. Corma, *J. Am. Chem. Soc.* **2004**, *126*, 3300–3309.

[47] Cuong M. Nguyen, Bart A. De Moor, Marie-Françoise Reyniers, and Guy B. Marin, *J. Phys. Chem. C* **2011**, *115*, 23831–23847.

[48] M. Boronat, A. Corma, *Appl. Catal. A-Gen.* **2008**, *336*, 2–10.

[49] C. Tuma, J. Sauer, *Angew. Chem. Int. Edit.* **2005**, *44*, 4769–4771.

[50] A. Tkatchenko, M. Scheffler, *Phys. Rev. Lett.* **2009**, *102*, 73005.

[51] G. A. Ferguson, L. Cheng, L. Bu, S. Kim, D. J. Robichaud, M. R. Nimlos, L. A. Curtiss, G. T. Beckham, *J.Phys.Chem. A* **2015**, *119*, 11397–11405.

[52] a) G. Piccini, J. Sauer, *J. Chem. Theory Comput.* **2014**, *10*, 2479–2487; b) G. Piccini, J. Sauer, *J. Chem. Theory Comput.* **2013**, *9*, 5038–5045; c) G. Piccini, M. Alessio, J. Sauer, Y. Zhi, Y. Liu, R. Kolvenbach, A. Jentys, J. A. Lercher, *J. Phys. Chem. C* **2015**, 6128–6137;

[53] G. Piccini, M. Alessio, J. Sauer, *Angew. Chem. Int. Ed.* **2016**, *55*, 5235–5237.

[54] M. Rybicki, J. Sauer, *J. Am. Chem. Soc.* **2018**, *140*, 18151–18161.

[55] C. Tuma, J. Sauer, *Phys. Chem. Chem. Phys.* **2006**, *8*, 3955–3965.

[56] C. Tuma, T. Kerber, J. Sauer, *Angew. Chem. Int. Edit.* **2010**, *49*, 4678–4680.

[57] I. V. Vrček, V. Vrček, H.-U. Siehl, *J. Phys. Chem. A* **2002**, *106*, 1604–1611.

[58] G. Rasul, G. K. S. Prakash, G. A. Olah, *J.Phys.Chem. A* **2015**, *119*, 5762–5769.

[59] G. A. Olah, G. K. S. Prakash, G. Rasul, *J. Comput. Chem* **2016**, *37*, 70–77.

[60] C. Marcilly, *Acido-Basic Catalysis. Application to Refining and Petrochemistry*, Technip, **2005**.

[61] a) D. M. Brouwer, J. M. Oelderik, *Recl. Trav. Chim. Pays-Bas* **1968**, *87*, 721–736; b) C. J. Collins, *Chem. Rev.* **1969**, *69*, 543–550; c) J. A. Martens, D. Verboekend, K. Thomas, G. Vanbutsele, J.-P. Gilson, J. Pérez-Ramírez, *ChemSusChem* **2013**, *6*, 421–425;

[62] F. Ferrante, T. Rubino, D. Duca, *J. Phys. Chem. C* **2011**, 14862–14868.

[63] C. Wattanakit, S. Nokbin, B. Boekfa, P. Pantu, J. Limtrakul, *J. Phys. Chem. C* **2012**, *116*, 5654–5663.

[64] a) D. Gleeson, *J.Phys.Chem. A* **2011**, *115*, 14629–14636; b) D. Gleeson, *J. Mol. Catal. A-Chem.* **2013**, *368-369*, 107–111;

[65] A. Corma, F. V. Melo, S. Mendioroz, J. L. G. Fierro (Eds.) *Studies in Surface Science and Catalysis. Acidity in zeolite catalysis*, Elsevier B.V, **2000**, *130A*.

[66] L. P. de Oliveira, D. Hudebine, D. Guillaume, J. J. Verstraete, J. F. Joly, *Oil Gas Sci. Technol. – Rev. IFP Energies nouvelles* **2016**, *71*, 45.

[67] J. A. Martens, P. A. Jacobs, J. Weitkamp, *Appl. Catal.* **1986**, *20*, 239–281.

[68] T. von Aretin, S. Schallmoser, S. Standl, M. Tonigold, J. A. Lercher, O. Hinrichsen, *Ind. Eng. Chem. Res.* **2015**, *54*, 11792–11803.

[69] C.-M. Wang, Y.-D. Wang, Z.-K. Xie, *J. Catal.* **2013**, *301*, 8–19.

[70] Y.-H. Guo, M. Pu, B.-H. Chen, F. Cao, *Appl. Catal. A-Gen.* **2013**, *455*, 65–70.

[71] a) P. M. Zimmerman, D. C. Tranca, J. Gomes, D. S. Lambrecht, M. Head-Gordon, A. T. Bell, *J. Am. Chem. Soc.* **2012**, *134*, 19468–19476; b) D. C. Tranca, J. Hanse, J. A. Swisher, B. Smit, F. J. Keil, *J. Phys. Chem. C* **2012**, *116*, 23408–23417;

[72] B. Smit, T. L. M. Maesen, *Chem. Rev.* **2008**, *108*, 4125–4184.

[73] a) J. A. Martens, W. Souverijns, W. Verrelst, Parton R., G. F. Froment, Jacobs P.A., *Angew. Chem. Int. Edit.* **1995**, *34*; b) J. A. Martens, G. Vanbutsele, P. A. Jacobs, J. Denayer, R. Ocakoglu, G. Baron, J. A. Muñoz Arroyo, J. Thybaut, G. B. Marin, *Catal. Today* **2001**, *65*, 111–116;

[74] A. Soualah, J. L. Lemberton, L. Pinard, M. Chater, P. Magnoux, K. Moljord, *Appl. Catal. A-Gen.* **2008**, *336*, 23–28.

[75] N. Batalha, S. Morisset, L. Pinard, I. Maupin, J. L. Lemberton, F. Lemos, Y. Pouilloux, *Micropor. Mesopor. Mat.* **2013**, *166*, 161–166.

Section II. Methodology

II.1) Wavefunction methods

In quantum chemistry, one has to find most often approximate solutions of the non-relativistic time-independent Schrödinger equation, to determine the electronic states of a many-body system (Equation II- 1):[1]

$$\boldsymbol{H}\,\psi = E\psi,$$

Equation II- 1

with $\boldsymbol{H}$ being the Hamiltonian operator (Equation II-2), ψ the wafunction and E the energy of the system.

In the Born-Oppenheimer approximation, the electronic motions are decoupled from the nuclear motions, the mass of an electron being about 2000 times smaller than the mass of a proton. The electronic wavefunction can be obtained separately for fixed nuclear positions $\{\mathbf{R_K}\}$. For a system with N electrons and M nuclei, the Hamiltonian (in atomic units) becomes:

$$\boldsymbol{H} = \sum_{i=1}^{N}\left[-\frac{1}{2}\nabla_i^2 + v_{ext}(\boldsymbol{r_i})\right] + \sum_{i>j>1}^{N}\frac{1}{\left|\boldsymbol{r_i}-\boldsymbol{r_j}\right|} + \sum_{K>L>1}^{M}\frac{\mathrm{Z}_K\mathrm{Z}_L}{\left|\boldsymbol{R_K}-\boldsymbol{R_L}\right|},$$

Equation II- 2

with the nuclear-electron attraction expressed as:

$$v_{ext}(\boldsymbol{r_i}) = \sum_{K}^{M}\frac{-Z_K}{\boldsymbol{r_{iK}}}.$$

Equation II- 3

The first term in Equation II- 2 is the operator for the kinetic energy of the electrons, the second for the Coulomb attraction between electron and nuclei, the third and fourth the repulsion between electrons and between nuclei. In the Born Oppenheimer approximation, the repulsion between the nuclei can be considered as constant and we have to solve the electronic equation for the given geometry, with the electronic Hamiltonian $\boldsymbol{H_{el}}$:

$$\boldsymbol{H_{el}}\,\psi_{el} = E_{el}\psi_{el},$$

$$\boldsymbol{H_{el}} = \sum_{i=1}^{N}\left[-\frac{1}{2}\nabla_i^2 + v_{ext}(\boldsymbol{r_i})\right] + \sum_{i>j>1}^{N}\frac{1}{\left|\boldsymbol{r_i}-\boldsymbol{r_j}\right|}.$$

Equation II- 4

The electronic energy and the electronic wavefunction depend parametrically on the nuclear coordinates $\{\mathbf{R_K}\}$. The total energy E_{tot} for fixed nuclei is:

$$E_{tot} = E_{el} + \sum_{K>L>1}^{M} \frac{Z_K Z_L}{|\boldsymbol{R_K} - \boldsymbol{R_L}|}. \qquad \text{Equation II- 5}$$

The electronic problem is defined by Equation II- 4 and Equation II- 5.

The total energy $E_{tot}(\{\boldsymbol{R_K}\})$ provides the potential for nuclear motion. The nuclear Schrödinger equation describes the movement of the nuclei, which can be decoupled into translations, vibrations and rotations. The solutions for these types of nuclear motions will be addressed in Section II.4.

For a *N*-electron system, the computational cost scales formally as N^4 for Hartree-Fock (HF) calculations (as *N* with most current methods), and N^5 to N^7 for post HF methods (second order Møller Plesset perturbation theory MP2 to coupled-cluster with full treatment of single and double and perturbative triple excitations CCSD(T)).[2] As a consequence, the computational cost becomes prohibitive for the large systems involved in heterogeneous catalysis.

Because of the inherent computational cost of wavefunction methods and the need of using *ab initio* molecular dynamics (Section II-5) in our investigations, we have used Density Functional Theory (Section II.2) in this work.

II.2) Density Functional Theory (DFT)

II.2.1) Basic Principles of DFT

In principle, the DFT is an exact theory where the electron density $\rho(\boldsymbol{r})$ plays the key role: all the observables of a system in its ground state are expressed as functionals of $\rho(\boldsymbol{r})$.[5] DFT becomes an accurate theory with the Hohenberg, Kohn and Sham publications of the early 60s. DFT scales as N^3 with the number of electrons. The VASP code scales roughly as $N^2 \ln N$[6] and codes in development scale as *N*.[7] The accuracy of DFT is due to the approximate exchange-correlation functionals) and is not as high as the higher level *ab initio* wavefunction methods. But DFT permits realistic simulations of systems up to few thousands of atoms. The impact of DFT has been tremendous. During the period 1980-2010, two of the three most cited physicists (Perdew and Becke) were theoreticians working on DFT.[8]

The electron density formula expressed in terms of the electronic wavefunction writes:

$$\rho(\boldsymbol{r}) = N \int \dots \int |\psi_{el}(\boldsymbol{r}, \boldsymbol{r}_2, \dots, \boldsymbol{r}_N)|^2 \, \mathrm{d}\boldsymbol{r}_2 \dots \mathrm{d}\boldsymbol{r}_N. \qquad \text{Equation II- 6}$$

The first Hohenkerg-Kohn theorem (1964)[5] states that for a system in its ground state, the external potential $v(\boldsymbol{r})$ is determined (up to irrelevant constant) by the electron density $\rho(\boldsymbol{r})$. It follows that $\rho(\boldsymbol{r})$ also determines the ground state wavefunction and all electronic properties. The energy E_v of the system associated to the external potential v can be written as a functional of the electron density $\rho(\boldsymbol{r})$:

$$E_v[\rho] = T[\rho] + V_{ee}[\rho] + V_{ext}[\rho]$$

$$E_v[\rho] = \int v_{ext}(\boldsymbol{r})\rho(\mathbf{r})\mathrm{d}\mathbf{r} + F_{HK}[\rho],$$ Equation II- 7

with:

$$F_{HK}[\rho] = T[\rho] + V_{ee}[\rho].$$ Equation II- 8

The second Hohenberg-Kohn theorem[5] provides the energy variational principle:

$$E_0 \leq E_v[\tilde{\rho}],$$ Equation II- 9

where $\tilde{\rho}$ is a trial density (which in turn determines its external potential and Hamiltonian). Equation II- 9 is analogous to the variational principle for the wavefunction of a ground state:

$$E_0 = \min_{\psi} E[\Psi].$$ Equation II- 10

$F_{HK}[\rho]$ is a universal functional (i.e. system independent). If we had an exact explicit form of $F_{HK}[\rho]$, the variational principle (Equation II-9) would give an exact equation for the ground state electron density. Unfortunately, the Hohenberg-Kohn theorems are existence theorems and do not provide a way to obtain $F_{HK}[\rho]$. In 1965, Kohn and Sham introduced an ingenious approach: they introduced orbitals convenient to compute the kinetic energy and to solve self-consistently the problem in a similar way as in the Hartree-Fock method.[5] It is possible to associate a single-determinental wavefunction ψ, describing a system of non-interacting electrons, to an electronic density ρ:

$$\psi = \frac{1}{\sqrt{N!}} det[\psi_1, \psi_2, \ldots, \psi_N]$$

$$\rho(\boldsymbol{r}) = \sum_{i=1}^{occ} |\psi_i(\boldsymbol{r})|^2.$$ Equation II- 11

The Kohn-Sham method associates a fictitious system, with N independent non-interacting electrons described by the orbitals ψ_i, to the real system with the **same ground state electron density**. The electronic energy can be rewritten:

$$E[\rho(\boldsymbol{r})] = T_s[\psi_i(\boldsymbol{r})] + E_{ext}[\rho(\boldsymbol{r})] + E_H[\rho(\boldsymbol{r})] + E_{xc}[\rho(\boldsymbol{r})],$$ Equation II- 12

with:

- T_s being the kinetic energy of the Kohn-Sham system of independent electrons:

$$T_s[\psi_i(\boldsymbol{r})] = \sum_{i=1}^{N} \langle \psi_i | \nabla_i^2 | \psi_i \rangle \qquad \text{Equation II- 13}$$

- E_H being the classical (Hartree) electronic repulsion energy:

$$E_H[\rho(\boldsymbol{r})] = \frac{1}{2} \iint \frac{\rho(\boldsymbol{r})\rho(\boldsymbol{r}')}{|\boldsymbol{r} - \boldsymbol{r}'|} d\boldsymbol{r} d\boldsymbol{r}' \qquad \text{Equation II- 14}$$

- E_{ext} is the energy associated to the external potential :

$$E_{ext}[\rho(\boldsymbol{r})] = \int \rho(\boldsymbol{r})\, v_{ext}(\boldsymbol{r}) d\boldsymbol{r} \qquad \text{Equation II- 15}$$

- E_{xc} is the exchange-correlation energy. It contains the difference, presumably small, between the exact kinetic energy T and T_S, and the non-classical part of the electronic repulsion.

Minimizing the energy with respect to the orbitals ψ_i leads to the Kohn-Sham equations:

$$\left[-\frac{1}{2} \nabla^2 + v_{eff} \right] \psi_i = \varepsilon_i \psi_i, \qquad \text{Equation II- 16}$$

with

$$v_{eff}(\boldsymbol{r}) = v_{ext}(\boldsymbol{r}) + \int \frac{\rho(\boldsymbol{r}')}{|\boldsymbol{r} - \boldsymbol{r}'|} d\boldsymbol{r}' + v_{xc}(\boldsymbol{r}), \qquad \text{Equation II- 17}$$

and the exchange-correlation potential $v_{xc}(\boldsymbol{r})$:

$$v_{xc}(\boldsymbol{r}) = \frac{\delta E_{xc}[\rho]}{\delta \rho(\boldsymbol{r})}. \qquad \text{Equation II- 18}$$

The Kohn-Sham equations are analogous to the Hartree equations but they include exchange and correlation. They have to be solved iteratively and their resolution is faster than the Hartree-Fock equations which contains a non-local exchange potential.[5,8]

The exact analytical expression of the exchange correlation functional is unknown. Some of the commonly used approximate functionals are introduced in the next section.

II.2.2) Exchange-correlation energy

Perdew has classified the approximations of the exchange-correlation energy as a functional of the electron density using the metaphor of “Jacob’s DFT ladder”.[9] $E_{xc}[\rho]$ is an explicit functional of $\rho(\boldsymbol{r})$ in the first two rungs (Local Density Approximation LDA and Generalized Gradient Approximation GGA). At the next level, meta-GGA functionals depend also on the Kohn-Sham kinetic energy T_S. The two successive levels, approaching the unattainable DFT heaven involve functionals of the occupied orbitals ψ_i (hybrid functionals) and of the unoccupied orbitals.

In the first level LDA, the exchange correlation-functional is formally written as follows:

$$E_{xc}^{LDA}[\rho(\boldsymbol{r})] = \int \rho(\boldsymbol{r})\, \varepsilon_{xc}(\rho) d\boldsymbol{r}, \qquad \text{Equation II- 19}$$

where $\varepsilon_{xc}(\rho)$ is the exchange-correlation energy of a uniform electron gas, with density ρ.

GGA and meta-GGA are corrections to LDA: GGA functionals also depend on $\nabla\rho(\boldsymbol{r})$, and meta-GGA on the Kohn-Sham kinetic energy T_S, i.e on $\langle\psi_i|\nabla_i^2|\psi_i\rangle$.

B3LYP, a hybrid functional is the most used in molecular chemistry and PBE, a GGA functional, in material science.[10]

We will use the PBE functional[11] in this work, with a correction to take into account the van der Waals dispersion forces (see Section II.2.3).

II.2.3) DFT based dispersion methods

DFT describes correctly short range electrostatic interactions (H bonds for instance) but standard exchange correlation functionals fail to describe long range dispersion interactions. The dispersion attractive interaction is the London term of the van der Waals forces. It originates in the instantaneous response of electrons in one region of space to instantaneous electron density fluctuations in another region. It gives rise to the London instantaneous dipole-induced dipole interaction with the $-1/r^6$ decay of the energy with the distance r.[12]

In analogy with the Jacob's ladder of the functionals, Klimeš and Michaelides introduced the "stairway to heaven" of dispersion correction schemes.[12] At ground level, the methods do not describe correctly the long range $-1/r^6$ decay (PBE functional[11] without correction for instance). Methods of steps 1 and 2 are termed "DFT-D". They are quite simple and their computational cost is modest, so they are very commonly used. A dispersion term, E_{disp}, is added to the energy calculated in DFT, E_{DFT}:

$$E_{tot} = E_{DFT} + E_{disp}, \qquad \text{Equation II- 20}$$

with

$$E_{disp} = -\frac{1}{2}\sum_{A,B} f(r_{AB}, A, B)\ \frac{C_6^{AB}}{r_{AB}^6}. \qquad \text{Equation II- 21}$$

C_6 constants are tabulated and f is a damping function which prevents the divergence of the interaction energy at small interatomic distances. Parameters of this function depend on the choice of the exchange-correlation functional. In the first level of correction, DFT-D2 method of Grimme[13], the C_6 coefficients are constant. At the second level (DFT-D3 method of Grimme[14]), the C_6 coefficients are environment dependent (depending on the coordination number and the oxidation number of the atoms). These methods are simple and efficient but they have some drawbacks: there is no direct relation between the C_6 coefficients and the experimental properties, higher order $1/r^8$ and $1/r^{10}$ terms are neglected (in DFT-D2 method) and the choice of the damping function is done empirically (it depends on the exchange-correlation functional and it can affect the energy more than the dispersion coefficients C_6 themselves).

At the next level of the "stairway to heaven", a non-local correction E_c^{nl} is added to E_{DFT}:

$$E_c^{nl} = \iint \rho(\vec{r_1})\, \varphi(\vec{r_1},\vec{r_2})\rho(\vec{r_2}) d\vec{r_1} d\vec{r_2}, \qquad \text{Equation II- 22}$$

where $\varphi(\vec{r_1},\vec{r_2})$ is an integration kernel with asymptotic behavior $O\left(\frac{1}{|\vec{r_1}-\vec{r_2}|^6}\right)$. The first of these method is the vdW-DF method.[15] It tends to be overbinding at large distances and it has been improved later (vdW-DF2 method).[16] At the last level the methods involve unoccupied orbitals (such as the Random Phase Approximation RPA) and their computational cost is very high, limiting their application in catalysis.[12]

Depending on the system, parametrized DFT-D methods can perform better than higher level corrections. For adsorption of alkanes in zeolites, the DFT-D2 method is a good choice at a reasonable computational cost.[17]

II.3) Codes employed in the present work

The DFT codes can be classified based on the basis set used to expand Kohn-Sham orbitals: plane waves or atomic localized functions (Gaussian-type orbitals for instance). For periodic solids, plane wave DFT is a popular choice.[18] In the work presented here, periodic DFT calculations were performed with the plane wave VASP code[6,19–21]. Electrons are described with PAW pseudo potentials.[22] We used the PBE functional[11] with DFT-D2 correction of Grimme[13] (Section II.2.3). The settings are detailed in Section II.6.

Some preliminary calculations have been performed with *ab initio* wavefunction methods using the molecular codes ORCA[23] and TURBOMOLE[24], within the hybrid scheme combining wavefunction and DFT methods of MonaLisa program.[25] These results are not presented in what follows.

II.4) Static approach

II.4.1) Introduction

Many theoretical studies of chemical reactions use a static approach to determine activation energy and rate constants of reaction. This approach is based on the analysis of potential energy surfaces at T = 0 K:[26]

- reactant, product, intermediate states and transition states are each represented by a single configuration, a stationary point on the potential energy surface (a saddle point for the transition states, a local minimum for the other species). The optimization of these species and of the minimum energy path connecting them is described in sections II.4.2 to II.4.5.

- Thermodynamic calculations are performed under the hypothesis that nuclear degrees of freedom of different types are fully decoupled and fall into one of the following categories: vibrations, rotations, or translations. Free energies and entropies at finite temperature are calculated within this frame (Section II.4.6) and the rate constants are calculated within the transition state theory (Section II.4.7).

This static approach is popular because it is computationally relatively inexpensive and it can provide a useful information about likely reaction paths.

II.4.2) Identification of potential energy minima

Starting from an initial guess, the structures of reactant, product and intermediate states are optimized after convergence of the electronic energy and forces. Forces $\boldsymbol{F}$ acting on atoms are computed using the gradients of potential energy E_p:

$$\boldsymbol{F}_i = -\frac{\partial E_p}{\partial \boldsymbol{r}_i}. \qquad \text{Equation II- 23}$$

In this work, the structural relaxations are performed using the conjugate gradient algorithm, as implemented in VASP. This algorithm is faster than a steepest descent algorithm: the first step is the same as a steepest descent step but the subsequent ones are performed along a direction which is a mixture of the previous direction and the direction of the current negative gradient.[27] The convergence is achieved when the forces on all atoms are smaller than a predefined (small) criterion (typically 0.005 eV/Å in this work).

Once the convergence is achieved, a vibrational analysis is performed to verify that the optimized configuration is a true potential energy minimum: all the frequencies must be real. If residual imaginary frequencies are found, a line minimization procedure is required (Section II.4.5).

II.4.3) Searching for saddle points

The activation energy of a reaction is defined as the energy difference between the transition state and the initial state. The determination of the transition state and of the activation energy is the key point in the computational investigation of a mechanism. Suitable algorithms are mandatory to determine transition states. The nudged elastic band method (NEB)[28,29,30] is a popular method to find a minimum energy path (MEP) between a reactant and a product. The MEP goes through a saddle point, the transition state. A discretized initial pathway connecting reactant and product is generated. The images are connected via spring forces (this is the “elastic band”). Typically we used the open source Opt’n Path[31] program by Paul Fleurat-Lessard which can use Cartesian coordinates or internal coordinates. Internal coordinates are necessary when complex movements including rotations occur during the transformation, which is the case with our reactions of C7 alkanes. The images are subject to the spring forces and the gradient of the intermolecular potential. During the relaxation, the initial pathway converge to the MEP (Figure II- 1). The NEB method is a constrained optimization of the initial pathway.

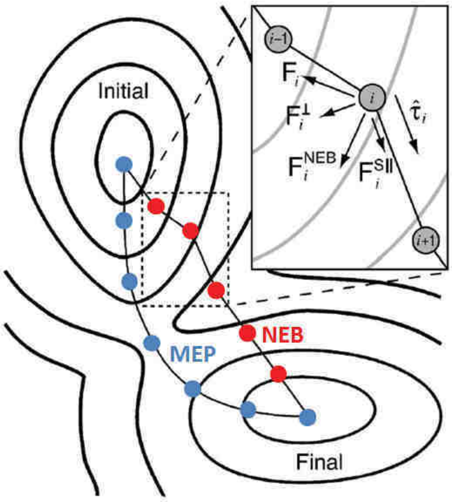

Figure II- 1. Initial string of configurations (NEB) and MEP between an initial and final state. Adapted from ref.[30]

In order to improve the determination of the saddle point, a CI-NEB (climbing image NEB) can be used: the highest energy structure is not connected by springs to its neighbors and can climb up to the saddle point.[29]

Usually, after a few tens of iterations giving a rough estimate of the MEP, the algorithm (NEB or CI-NEB) is stopped and a subsequent optimization of the structure with the maximum energy is performed. A quasi-newton algorithm, as implemented in VASP, can be used to find the point where the forces vanish (our tight convergence criterion for the forces is 0.005 eV/Å).

The determination of saddle point with these methods appeared to be a very difficult task in our reactions involving alkanes with 7 carbon atoms, with complex movements of torsion, and with some species (such as the carbenium) interacting only weekly with the zeolite framework. Quasi-newton and NEB optimization often did not converge and the dimer method[32,33] proved to be more efficient.

The dimer method can be performed after a 1st NEB or directly from a guess of the transition state. In some cases, the guess of the transition state was obtained from a constrained molecular dynamics simulation (Section II.5.2). This method is a fast mode following algorithm (the initial direction is provided by the user) requiring only first derivatives of the potential energy in the actual calculation. In this method, two different replicas of the same system are used. They are displaced by a small distance. The dimer is rotated along the lowest curvature mode (the reaction coordinate) along which the saddle point is a maximum and the saddle point search algorithm moves the dimer uphill towards the transition state.[32] We used the improved dimer method as implemented in VASP.[33]

After convergence, a vibrational analysis of the transition state is performed to ensure that the optimized configuration is a true saddle point: all but one frequency must be real, the only imaginary frequency corresponds to the unstable mode. Residual imaginary frequencies possibly occurring in the vibrational spectrum of the relaxed configuration are eliminated using a line minimization procedure (Section II.4.5).

II.4.4) Intrinsic reaction coordinate (IRC)

In the theoretical study of a chemical reaction, it is necessary to determine the stationary points (representing reactants, transition state and products) on the potential energy surface. Once a transition state has been determined, we have to check if it is connected to the expected reactant and product. The intrinsic reaction coordinate (IRC) approach allows to determine the reaction path connecting reactants, transition states and products on the potential energy surface. This concept has been introduced by Fukui.[34] The IRC is the steepest descent path, starting from the transition state in the direction of the transition vector (corresponding to the imaginary vibrational frequency which has to be determined e.g. via vibrational analysis). Once the minima linked with transition state via IRC have been determined, it is possible to calculate a rate constant using Eyring's transition state theory (Section II.4.7).

In this work, we used the damped velocity Verlet algorithm for the IRC determination[35] as implemented in VASP. This method generates a dynamic reaction path that approximates the IRC. With the damped velocity Verlet algorithm, the velocity is adjusted after each step (at a constant value) and the time step is adjusted to control the integration error and ensure that the path remains close to the IRC. This method is particularly advantageous for large systems.[35]

II.4.5) Line minimization procedure

This procedure allows to explore energy along a specific direction in the 3N dimensional configuration space. We employ this technique to eliminate the residual imaginary frequencies often remaining after the geometry optimizations. These imaginary frequencies are usually due to an incomplete energy minimization along one or more directions. This problem is often related to a relative flatness of potential energy landscape in some parts of the configuration space, hence even very tight convergence criteria used in atomic relaxations may not lead to elimination of all undesired imaginary frequencies.

For a periodic solid with *N* atoms, there are no global rotations and 3 global translations. The total momentum is taken to be zero in simulations, and there are 3*N* – 3 vibrational degrees of freedom.[36] Importantly, the potential energy of the system is translationally and rotationally invariant. In order to identify and efficiently eliminate the residual imaginary vibrations, the translational (and, in the case of the gas phase molecules, also rotational) degrees of freedom have to be decoupled from vibrations. As this is not done by the VASP code, we use a program developed for this purpose. The program reads the forces in the output file of the VASP calculation and computes and diagonalizes the Hesse and dynamical matrices in translationally and rotationally invariant internal coordinates. Translations (and rotations in the case of the gas phase molecules) are thus effectively decoupled from vibrations. In the next step, the energy landscape is sampled along the direction of the eigenvector with the largest undesired eigenvalue by a sequence of single point energy calculations (see Figure II- 2 for examples of successive sampling during the optimization of a transition state). The structure corresponding to the energy minimum is re-optimized and the vibrational frequencies are re-computed at each step. The procedure is repeated until the configuration with a correct vibrational spectrum is identified (typically 1 to 6 repeated cycles are needed).

This line minimization procedure has been successfully applied to all the static structures investigated in this thesis.

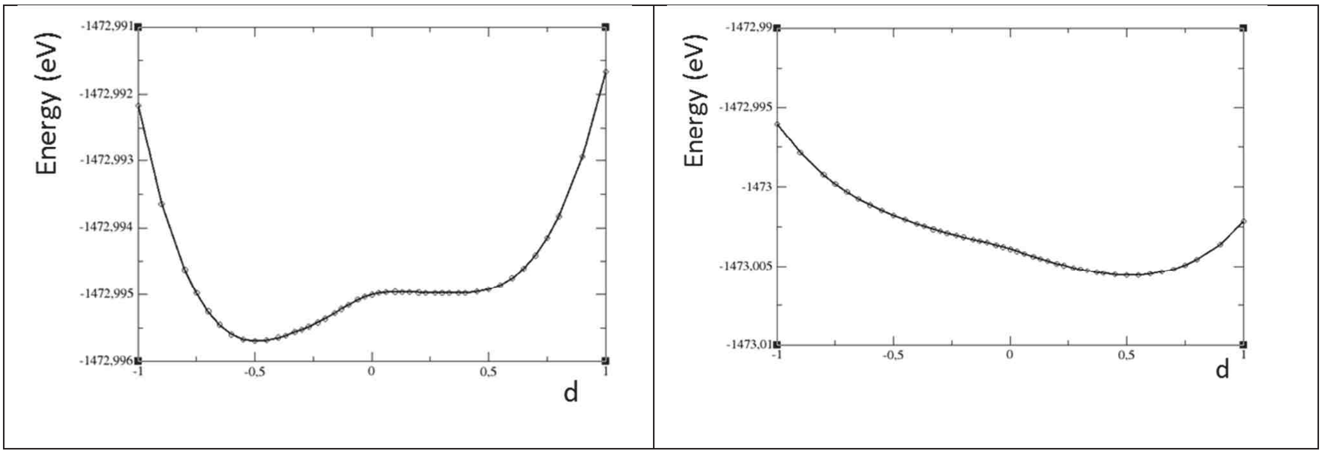

Figure II- 2. Successive sampling of the potential energy along Hesse matrix eigenvector with negative eigenvalue. d is a scaling dimensionless parameter for displacement. Two successive line minimizations for the same transition state are shown. Upon each line minimization, the structures with the lowest energy (for d = -0.55 (left) and d = 0.50 (right)) have been re-optimized and the Hesse matrix has been re-calculated. The procedure is stopped when the vibrational spectrum is correct.

II.4.6) Thermodynamic calculations

II.4.6.1) Statistical mechanics

After geometry optimization, quantum chemical calculations provide the electronic energy E_{el} (at T = 0 K). As described in Section II.4.1, the different degrees of freedom are assumed to be decoupled in the static approach. We can write the internal energy *U*(*T*) at finite temperature T:

$$U(T) = E_{el} + U_{trans}(T) + U_{rot}(T) + U_{vib}(T), \qquad \text{Equation II- 24}$$

and similarly for the entropy:

$$S(T) = S_{el} + S_{trans}(T) + S_{rot}(T) + S_{vib}(T). \qquad \text{Equation II- 25}$$

For a non-linear molecules with N atoms, there are 3 translational and 3 rotational degrees of freedom and $N_{vib} = 3N - 6$ vibrational degrees of freedom. For a periodic solid with *N* atoms, there are no global rotations and 3 global translations. The total momentum is often taken to be zero in simulations, and there are $N_{vib} = 3N - 3$ vibrational degrees of freedom. For a transition state, one normal mode corresponds to the reaction coordinate; its frequency is imaginary and it is not taken into account in the summations. Usually, the vibrational degrees of freedom are handled within the harmonic approximation (possibly with anharmonic corrections in advanced schemes[4,37]). Rotational degrees of freedom of gas phase molecules are treated within the rigid rotor approximation.

Statistical mechanics provides the following relations within the harmonic approximation:[38]

$$U_{vib}(T) = N_A \sum_{i=1}^{N_{vib}} h\nu_i \left(\frac{1}{2} + \frac{e^{-h\nu_i/k_B T}}{1 - e^{-h\nu_i/k_B T}}\right), \qquad \text{Equation II- 26}$$

with N_A the Avogadro constant and *U* in J.mol^{-1}.

The vibrational term at T = 0 K, $U_{vib}(0)$, is the quantum mechanical zero-point energy (ZPE):

$$U_{vib}(0) = \frac{1}{2} N_A \sum_{i=1}^{3N-6} h\nu_i, \qquad \text{Equation II- 27}$$

and for a non-linear gas-phase molecule:

$$U_{trans}(T) = \tfrac{3}{2}RT \text{ and } U_{rot}(T) = \tfrac{3}{2}RT. \qquad \text{Equation II- 28}$$

With a good approximation, the electronic energy E_{el} is considered as independent of *T* (unless the temperature is comparable to or higher than the Fermi temperature).

For entropy, the following vibrational contribution can be derived for a molecule or a periodic system:

$$S_{vib}(T) = R \sum_{i=1}^{N_{vib}} \left[\frac{h\nu_i}{k_B T} \frac{e^{-h\nu_i/k_B T}}{1 - e^{-h\nu_i/k_B T}} - ln\left(1 - e^{-h\nu_i/k_B T}\right) \right]. \qquad \text{Equation II- 29}$$

The translational and rotational contributions to the entropy of a non-linear gas-phase molecule (Sackur-Tetrode formulas, 1912) are as follows:

$$S_{trans}(T) = R \left[\frac{5}{2} + ln\left(\frac{RT}{P} \left(\frac{2\pi m k_B T}{h^2} \right)^{3/2} \right) \right], \qquad \text{Equation II- 30}$$

$$S_{rot}(T) = R \left[\frac{3}{2} + ln\left(\frac{\sqrt{\pi}}{\sigma} \left(\frac{8\pi^2 k_B T}{h^2} \right)^{3/2} (I_A I_B I_C)^{1/2} \right) \right], \qquad \text{Equation II- 31}$$

where P is the total pressure of the gas, m is its molecular mass, I_A, I_B and I_C are the principal moments of inertia and σ is the rotational symmetry number.

Finally the electronic contribution to entropy writes:

$$S_{el}(T) = Rln(g_0), \qquad \text{Equation II- 32}$$

where g_0 is the electronic degeneracy of the ground-state wavefunction. As the ground-state of all systems considered in this work is a singlet (g_0 = 1), the contribution of S_{el} to total entropy is zero.[27]

At constant N, V, and T, the Helmholtz free energy A is the determining thermodynamic potential. The free energy A can be deduced from U and S:

$$A = U - TS. \qquad \text{Equation II- 33}$$

It can be shown that within the harmonic approximation $H_{vib} = U_{vib}$ because the vibrational partition function does not depend on the volume.[27] Similarly, the vibrational Gibbs energy G is identical to the vibrational Helmholtz free energy A.

For a gas phase molecule, the only difference between H and U within the static approximation is due to the translational degrees of freedom: $H_{trans} = U_{trans} + RT$ (the translational partition function depends on the volume in this case). Hence the following relation holds for a gas phase molecule: $G = A + RT$.

We notice that the vibrational entropy diverges when a frequency ν_i approaches zero, whereas the contribution to the vibrational energy tends to zero. Flexible frameworks of zeolites give rise to many soft vibrational modes with low frequencies (ν_i < 50 cm^{-1}). The determination of these soft modes is relatively inaccurate with standard DFT calculations.[26] This is a critical point for the static calculation of vibrational entropies in zeolites.

II.4.6.2) Computation of the vibrational frequencies

The numerical calculation of the vibrational frequencies ν_i is the starting point for the thermodynamic calculations and for the validation of all stationary points as detailed in the previous sections. With the VASP code, the harmonic vibrational frequencies are computed by diagonalization of the dynamical matrix, closely related to the Hesse matrix of second derivatives $\frac{\partial^2 E}{\partial x_i \partial x_j}$ (it is the Hesse matrix for mass-weighted coordinates). Eigenvalues of the dynamical matrix are the frequencies and eigenvectors the vibrational normal modes. The Hesse matrix is calculated using finite differences in Cartesian coordinates. In this work we apply the central difference formula, whereby each atom is displaced in the three directions of each Cartesian coordinate by adding a small negative and positive displacement. The computational cost increases quickly with the size of the system because of the increasing number of force evaluations.

II.4.7) Rate constants from static calculations

In Eyring's transition state theory[39], kinetic constants k are calculated using the following approximations:

- a classical behavior of atomic nuclei, without tunneling effects.
- the activated complex (the structure with the geometry of the saddle point) is in equilibrium with reactants and products.
- once the activated complex is formed, it inevitably collapses to form products later in time, without recrossing of the barrier.

The Eyring-Polanyi equation states that:

$$k = \frac{k_B T}{h} e^{-\frac{\Delta A^{\#}}{k_B T}}. \qquad \text{Equation II- 34}$$

II.5) Molecular dynamics

In this thesis, we use molecular dynamics to overcome some of the limitations of the static approach (Section II.4.1). Molecular dynamics is a statistical mechanics method based on solving the equations of motion (according to the Newton's law) for atoms or molecules. It is a kind of "thought experiment" performed *in silico*, a computational fulfillment of statistical mechanics. In contrast to the static calculations detailed in the previous section, thermal and entropic effects are accurately taken into account. The laws of Newtonian mechanics cannot be solved analytically for more than two interacting bodies, thus computer simulations have to be used to deal with systems of many atoms and molecules which are relevant for material science or chemistry.[36]

The first computer simulations relevant to chemistry were performed on the Los Alamos MANIAC computer (Mathematical Analyzer, Numerical Integrator and Computer) in the early 1950s when computers became partially available for a nonmilitary use. Metropolis and coworkers performed the first simulation of a liquid in 1953, introducing the Metropolis Monte Carlo method. The first molecular dynamics simulation was reported in 1956 (the dynamics of hard spheres, by Alder and coworkers).[36]

The structural models tractable on computers are usually not macroscopic but they are large enough to enable the calculation of some macroscopic properties, provided the simulations are sufficiently long. Statistical mechanics provides a link between the microscopic laws of motion and the macroscopic, phenomenological, thermodynamics.[40]

The 1st subsection of this section will provide some basic expressions of statistical mechanics and the 2nd one will describe the advanced techniques used in this thesis to describe rare events such as chemical reactions.

II.5.1) Standard molecular dynamics in the canonical ensemble

II.5.1.1) Canonical ensemble

An ensemble is a collection of systems with the same microscopic interactions and the same macroscopic properties (e.g. the same total energy, volume and number of particles for instance). When macroscopic observables do not depend on time, these ensembles are called equilibrium ensemble. A macroscopic equilibrium observable O related to a microscopic phase space function $o(x)$ is obtained by an ensemble average, an average on the Z members of the ensemble (Equation II- 35):[40]

$$O = \frac{1}{Z}\sum_{i=0}^{Z} o(x_i) = \langle o \rangle \qquad \text{Equation II- 35}$$

The phase space is the space of all the microscopic states consistent with a set of macroscopic observables. The Liouville's theorem allows us to perform ensemble averages at any point in time. It states that for a collection of systems evolving according to Hamiltonian mechanics, a phase space volume element is constant during the time evolution. The phase space probability density remains normalized, there are no sources nor sinks in the phase space.[40]

In the canonical[1] (*NVT*) ensemble, each system is characterized by a constant particle number N, a constant volume V and a constant temperature T. Experiments are generally performed at constant pressure P rather than constant volume V but the *NVT* ensemble simulations can be more easily performed within the frame of plane-wave DFT where the basis set depends on the cell volume. In the canonical ensemble, the Helmholtz energy $A = U - TS$ (with U being the internal energy and S

---

[1] Canonical: according to a rule.

being the entropy) is the determining thermodynamic potential[2]. For large systems, the results obtained from the canonical ensemble do not differ much from results obtained from other ensembles.

In *ab initio* molecular dynamics (AIMD), the atomic motions are described by the classical mechanics whereby the forces are calculated at the quantum mechanics level.

II.5.1.2) Ergodic hypothesis

We have defined the average of the observable O in a static sense, over all the quantum states: it is called an ensemble average.

The **ergodic hypothesis** states that an observable O computed as a time average $\bar{O}$ over a sufficiently long time (the molecular dynamics approach) is equivalent to average $\langle O \rangle$ over the phase space with the conditions compatible with the values of the fixed macroscopic variables (which can be directly sampled via the Monte Carlo approach):

$$\bar{O} = \lim_{t \to \infty} \frac{1}{t} \int_0^t O(t) dt = \langle O \rangle \qquad \text{Equation II- 36}$$

It means that for a trajectory that is sufficiently long, the time average is independent of the initial conditions and that all points of the phase space are sampled with a correct statistical weights.

Ergodicity is very difficult to prove but it is strongly believed that the vast majority of many-body systems relevant to chemistry are ergodic. In contrast, some systems are known to be nonergodic (glasses, metastable systems). The ergodic hypothesis is applied to systems studied in computer simulations but the behavior of ergodic system during a too short AIMD simulation might turn out to be nonergodic. The ergodicity might be violated also when the phase space is not correctly sampled, e.g. because of the presence of energy barriers separating different parts of the phase space or if different volumes are connected by a narrow low-energy region (an entropy bottleneck). This phenomenon is called quasi-nonergodicity and it represents a problem commonly experienced when studying chemical reactions (for reactions with high barriers separating reactant and products or for reactions requiring very special conformations). In these cases, advanced techniques are needed.[36,41]

In the work presented in this thesis, we use some advanced techniques to study the hydro-isomerization reactions on alkenes containing 7 carbon atoms. These methods will be introduced in Section II.5.2.

---

[2] Following the recommendation of the IUPAC Green Book, we note A the Helmholtz energy $A = U - TS$ (from the German "Arbeit", also known as Helmholtz free energy or free energy; the letter F can also be used) and G the Gibbs energy $G = H - TS$ (also known as Gibbs free energy or free enthalpy).

II.5.1.3) Thermal average of an observable O

We consider a system whose properties are fully determined by the Hamiltonian $\boldsymbol{H}$ with eigenstates $|i\rangle$ and eigenenergies E_i. The Schrödinger equation is written as:

$$\boldsymbol{H}|i\rangle = E_i|i\rangle, \qquad \text{Equation II- 37}$$

with the Hamiltonian $\boldsymbol{H}$:

$$\boldsymbol{H} = \boldsymbol{K} + \boldsymbol{V} = \sum_i \frac{\boldsymbol{p}_i^2}{2m_i} + \boldsymbol{V}, \qquad \text{Equation II- 38}$$

where $\boldsymbol{K}$ is the kinetic energy operator and $\boldsymbol{V}$ the potential energy operator.

$\boldsymbol{O}$ is an operator associated with an observable o. The thermal average of $\boldsymbol{O}$ can be computed by:

$$\langle \boldsymbol{O} \rangle = \frac{\sum_i \exp(-\beta E_i)\langle i|\boldsymbol{O}|i\rangle}{\sum_j \exp(-\beta E_j)}, \qquad \text{Equation II- 39}$$

with $\beta = 1/k_B T$.

The Schrödinger equation is, in general, difficult to solve for a many-body system. For a macroscopic system with a number of quantum states of the order of magnitude of $\mathcal{O}(10^{23})$, such a calculation is unfeasible with the present day computer power. Within the classical limit, this expression becomes more tractable. It can be shown that the classical limit of the thermal average of O and of the canonical partition function $Q_{\text{classical}}$ can be written:[36,40]

$$\langle \boldsymbol{O} \rangle = \frac{\int exp(-\beta H)\, o(\boldsymbol{p}^N, \boldsymbol{r}^N) d\boldsymbol{p}^N d\boldsymbol{r}^N}{\int exp(-\beta H)\, d\boldsymbol{p}^N d\boldsymbol{r}^N} \qquad \text{Equation II- 40}$$

$$Q_{classical} = Tr\ exp(-\beta \boldsymbol{H}) \approx \frac{1}{h^{dN} N!} \int exp(-\beta H)\, d\boldsymbol{p}^N d\boldsymbol{r}^N \qquad \text{Equation II- 41}$$

with $\beta = 1/k_B T$ and d the dimensionality of the system. *N!* is added afterwards if the particles are indistinguishable; and $o(\boldsymbol{p}^N, \boldsymbol{r}^N)$ is the microscopic phase space function related to O.

The canonical partition function can be written as follows:

$$Q = M \int d\boldsymbol{p}^N \int d\boldsymbol{r}^N exp\big(-\beta H(\boldsymbol{p}^N, \boldsymbol{r}^N)\big), \qquad \text{Equation II- 42}$$

with M being a constant. In the canonical ensemble at a constant temperature T:

$$\int d\boldsymbol{p}^N exp\big(-\beta K(\boldsymbol{p}^N)\big) = cst, \qquad \text{Equation II- 43}$$

and the configurational part of the partition function is:

$$Z = \int d\boldsymbol{r}^N exp\big(-\beta V(\boldsymbol{r}^N)\big). \qquad \text{Equation II- 44}$$

If the function *o* depends only on the positions $\boldsymbol{r}$ (and not on the momenta $\boldsymbol{p}$) then Equation II- 40 can be written as follows:

$$\langle \boldsymbol{O} \rangle = \frac{\int dq\ o(\boldsymbol{r}^N) exp\big(-\beta V(\boldsymbol{r}^N)\big)}{Z} \qquad \text{Equation II- 45}$$

We can note here that the position-dependent quantity $\langle O \rangle$ is **independent of the atomic masses** m_i. In this sense, the atomic mass m_i is a parameter affecting the efficiency of sampling in molecular dynamics but not the result of a long simulation (provided the convergence has been achieved).

II.5.1.4) The workhorse equations of statistical thermodynamics

For a system at thermal equilibrium with a thermostat at temperature T, the probability P_i for this system to be in a state with energy E_i is given by the Boltzmann distribution:

$$P_i = \frac{\exp(-\beta E_i)}{\sum_j \exp\big(-\beta E_j\big)}. \qquad \text{Equation II- 46}$$

Using the probability defined in Equation II- 46, the average total energy of the system $\langle E \rangle$, corresponding by definition to its internal energy U is defined as follows:

$$U = \langle E \rangle = \sum_i E_i P_i. \qquad \text{Equation II- 47}$$

With the partition function $Q = \sum_j \exp\big(-\beta E_j\big)$, we obtain that:

$$\mathrm{U} = -\frac{\partial lnQ}{\partial \beta}. \qquad \text{Equation II- 48}$$

With the Gibbs-Helmholtz relation between the Helmholtz energy *A* and the energy *U*:

$$U = \frac{\partial \frac{A}{T}}{\partial \frac{1}{T}}, \qquad \text{Equation II- 49}$$

we obtain a very useful relation between the Helmholtz free energy *A* and the partition function *Q*:

$$A = -\frac{1}{\beta} \ln Q. \qquad \text{Equation II- 50}$$

Equation II- 48 and Equation II- 50 connect statistical mechanics and thermodynamics.[36,40]

The term *U* can be expressed as an ensemble average:

$$\mathrm{U} = \langle H(\boldsymbol{p}, \boldsymbol{r}) \rangle = \langle K(\boldsymbol{p}) \rangle + \langle V(\boldsymbol{r}) \rangle. \qquad \text{Equation II- 51}$$

Combining with the classical equipartition principle stating that every quadratic degree of freedom contributes $\frac{1}{2}k_BT$ to the total energy, we obtain for a system consisting of N_{at} atoms:

$$\langle K(\boldsymbol{p})\rangle = \frac{3}{2}N_{at}k_BT, \qquad \text{Equation II- 52}$$

and U is given by the ensemble average:

$$U = \frac{\int dq\, V(\boldsymbol{r})exp\big(-\beta V(\boldsymbol{r})\big)}{Z} + \frac{3}{2}N_{at}k_BT. \qquad \text{Equation II- 53}$$

Thus, U can be computed in a molecular dynamics simulation as a time average by means of the ergodic hypothesis.

The calculation of the free energy $A = -\frac{1}{\beta}\ln Q$ is less straightforward as this term is not expressible as an ensemble nor as a time average. In a direct application of Equation II- 50, calculation of Q is needed, which in turn requires a sampling of whole phase space. The same holds also for entropy S. It is the same problem in a “real experiment” in the “real word”: the absolute values of these thermal quantities (such as A or S) cannot be measured directly, one can only obtain derivatives of these thermal quantities. For instance, it is not possible to measure directly the free energy A in an experiment but it is possible to measure the pressure P which is a partial derivative of the free energy A:[36]

$$\left(\frac{\partial A}{\partial V}\right)_{N,T} = -P. \qquad \text{Equation II- 54}$$

II.5.1.5) Calculation of A: a binning procedure

The free energy A as a function of reaction coordinate ξ can be computed from the histograms of the visited conformations constructed by a binning procedure.[42] The relation between the free energy $A(\xi_i)$ and the probability density $P(\xi_i)$ can be derived as follows.[40]

For a general geometric parameter $\xi(\boldsymbol{r_1}, \ldots, \boldsymbol{r_N})$, the probability density is written as:

$$P(\xi_i\,) = \frac{1}{Z}\int \ldots \int d\boldsymbol{r}'_{\boldsymbol{1}} \ldots d\boldsymbol{r}'_{\boldsymbol{N}} exp\big(-\beta V(\boldsymbol{r_1}, \ldots, \boldsymbol{r_N}\,)\big)\delta(\xi - \xi_i). \qquad \text{Equation II- 55}$$

We recognize the ensemble average of $\delta(\xi - \xi_i)$:

$$P(\xi_i\,) = \langle\delta(\xi - \xi_i)\rangle = \frac{Z(\xi_i)}{Z}. \qquad \text{Equation II- 56}$$

And finally:

$$P(\xi_i) = \frac{Z(\xi_i)}{Z} = \frac{Q(\xi_i)}{Q}. \qquad \text{Equation II- 57}$$

Thus, the free energy A as a function of reaction coordinate can be written as follows:

$$A(\xi_i) = -k_B T \ln Q(\xi_i) = -\, k_B T \ln P(\xi_i) - k_B T ln\, Q, \qquad \text{Equation II- 58}$$

with the canonical partition function Q being a constant at the given T:

$$A(\xi_i) = -k_B T \ln P(\xi_i) + constant. \qquad \text{Equation II- 59}$$

Thus, the free energy difference between two states A and B defined via the value of ξ is:

$$\Delta A_{A \to B} = -k_B T \ln \frac{P(\xi_B)}{P(\xi_A)}. \qquad \text{Equation II- 60}$$

II.5.2) Simulating rare events: free energy methods

Nowadays, straightforward molecular dynamics can generate trajectories of length of a few nanoseconds when the forces are calculated at the quantum mechanics level (microseconds with force fields). This length might be sufficient for the sampling of reaction events with barriers of up to few multiples of the thermal energy $k_B T$ (2.5 kJ.mol^{-1} at 300K), such as the trans/gauche conformations of butane.[42] More sophisticated methods are necessary for the sampling of rare events, with energy barriers much larger than $k_B T$ (see Figure II- 3). As the free energy is a state function, the free energy differences between two states can be calculated along different physical or unphysical paths, which allows to use very different methods of calculations.[40,42] Consequently, the free energy of activation $\Delta A^{\ddagger}$ does not depend on the choice of parametrization of the reaction coordinate, provided this parametrization allows for a reversible transformation from reactant over transition state to product.

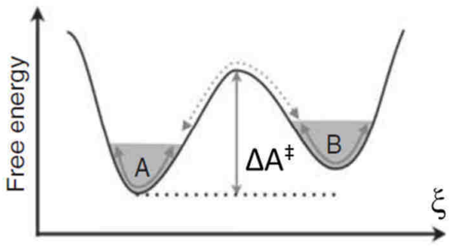

Figure II- 3. Example of a free energy profile for the transformation of A to B. Within a typical simulation time of MD, the system explores the grey shaded regions because of its thermal energy. Because the transition state receives a very low Boltzmann weight, it is very unlikely to be visited during a straightforward MD run.

II.5.2.1) The blue-moon[3] ensemble approach

This approach has been introduced by Carter and coworkers[43] and developed further by Sprik and Ciccotti[44]. A mechanical constraint is imposed on the parameter representing the reaction coordinate and the free energy difference is obtained by thermodynamic integration. A crucial ingredient of this method is the parameter ξ approximating the reaction coordinate (which is unique and characteristic of a reaction). The important requirement is that a reversible transformation is driven by variation of ξ. One needs an *a priori* knowledge of the mechanism to make a reasonable choice of this parameter ξ. This parameter ξ is sometimes termed "collective variable" or *CV* in molecular dynamics and we will use this term in the application part of this work (see Section III.5.2.3). Within this approach, it is possible to reduce the statistical errors by prolonging the simulation time at each point (giving a good sampling, notably at the transition state) and by adding as many points as necessary for the thermodynamic integration.[41,45]

Thermodynamic integration

The free energy difference ΔA is calculated by integration of the gradient of A over the parameter representing the reaction coordinate ξ evolving from ξ_1 to ξ_2 as follows:

$$\Delta A_{1\rightarrow 2} = \int_{\xi_1}^{\xi_2} \left(\frac{\partial A}{\partial \xi}\right) d\xi. \qquad \text{Equation II- 61}$$

By derivation of Equation II- 58, we obtain:

$$\left(\frac{\partial A}{\partial \xi}\right) = \langle \frac{\partial H(\boldsymbol{p},\boldsymbol{r})}{\partial \xi} \rangle_{\xi}. \qquad \text{Equation II- 62}$$

Hence the gradient of A can be expressed as an ensemble average computable from molecular dynamics. In the blue moon approach, the thermodynamic integration is performed along a discretized reaction path, i.e. the free-energy gradients are evaluated at selected fixed values ξ^* of ξ. From the second law of thermodynamics, the following relation holds for a reversible transformation:

$$\Delta A_{1\rightarrow 2} = W_{rev}, \qquad \text{Equation II- 63}$$

with W_{rev} being the non-expansion work performed during the transformation between the states 1 and 2, whereas, for an irreversible transformation, the following relation holds:

$$\Delta A_{1\rightarrow 2} < \mathrm{W}. \qquad \text{Equation II- 64}$$

---

[3] Rare events occur "once in a blue moon". A blue moon is the thirteenth full moon in a calendar year, it occurs roughly every 2.72 years.

The term $-\langle\frac{\partial H(\boldsymbol{p},\boldsymbol{q})}{\partial\xi}\rangle_{\xi^*}$ is analogous to a force and hence it is sometimes termed in literature as the mean force f_{rev} and the free energy is also called the potential of mean force:

$$\mathrm{d}A = \delta W_{rev} = -f_{rev}\, d\xi. \qquad \text{Equation II- 65}$$

We need to calculate *conditional* averages such as $\langle\frac{\partial H(\boldsymbol{p},\boldsymbol{q})}{\partial\xi}\rangle_{\xi^*}$ (see Equation II- 62): ξ is restricted to the constant value ξ^* but its conjugate momentum should be left unaffected. In the blue moon ensemble, both ξ^* and the associated momentum are fixed leading to a bias that must be corrected. For a velocity independent observable *O,* Carter and coworkers demonstrated that the relation between the *conditional* average $\langle O\rangle_{\xi^*}$ (with $\xi = \xi^*$ and $\left(\frac{d\xi}{dt}\right)_{\xi^*} \neq 0$) and the *constrained* average $\langle O\rangle_{\xi^*}^{constr}$ (with $\xi = \xi^*$ and $\left(\frac{d\xi}{dt}\right)_{\xi^*} = 0$) is as follows:[43]

$$\langle O\rangle_{\xi^*} = \frac{\langle OZ^{-\frac{1}{2}}\rangle_{\xi^*}^{constr}}{\langle Z^{-\frac{1}{2}}\rangle_{\xi^*}^{constr}}, \qquad \text{Equation II- 66}$$

with Z being the inverse mass metric tensor defined as follows:

$$Z = \sum_i \frac{1}{m_i}\left(\frac{\partial\xi}{\partial r_i}\right)^2. \qquad \text{Equation II- 67}$$

Equation II- 66 can be used to calculate the free energy gradient:[40,43,44]

$$\left(\frac{\partial A}{\partial\xi}\right)_{\xi^*} = \frac{1}{\langle Z^{-\frac{1}{2}}\rangle_{\xi^*}^{constr}}\langle Z^{-\frac{1}{2}}[-\lambda + k_B TG]\rangle_{\xi^*}^{constr}, \qquad \text{Equation II- 68}$$

with :

$$G = \frac{1}{Z^2}\sum_{i,j}\frac{1}{m_i}\frac{1}{m_j}\frac{\partial\xi}{\partial r_i}\frac{\partial^2\xi}{\partial r_i\partial r_j}\frac{\partial\xi}{\partial r_j}, \qquad \text{Equation II- 69}$$

and λ being the Lagrange multiplier associated with the constraint. In practice, λ is determined using the SHAKE algorithm[46] (see next section).

Equation II- 68 and Equation II- 69 were derived by Sprik and coworkers[44], transforming the corresponding equation of Carter and coworkers[43] into a form that is useful for practical applications. This method can be generalized for the use with multiple constraints.[47]

Constraints in the Lagrangian formalism; SHAKE algorithm

The Lagrange's equations of motion are formulated in term of generalized coordinates $\{q_i\}$ and the associated velocities $\{\dot{q}_i\}$, with the Lagrangian $L = K - V$:

$$-\frac{d}{dt}\frac{\partial L}{\partial \dot{q}_i}+\frac{\partial L}{\partial q_i}=0. \qquad \text{Equation II- 70}$$

In the Lagrangian formalism, constraints on the movements of the system can be introduced in a natural way.[36,40,48] If the constraints are expressible as equations connecting the coordinates of the particles (and possibly the time), the constraints are said to be holonomic:

$$\sigma_k(q_1, q_2, \dots, q_N, t)=0, \qquad \text{Equation II- 71}$$

for k = 1 to N_C (if there are N_C constraints). Non holonomic constraints depend also on the velocities.

For instance, if we want to impose a constraint on a distance d between the atoms A_i and A_j, we can define a function σ_1 which is equal to zero when $|\boldsymbol{r}_{ij}| = d$: $\sigma_1(\boldsymbol{r}_i, \boldsymbol{r}_j) = \boldsymbol{r}_{ij}^2 - d$.

With N_C constraints, $3N - N_C$ independent generalized coordinates are to be determined. With the method of Lagrange's multipliers, we solve the equations as if the 3N coordinates were independent, with N_c multipliers to be determined.

The constraints can be written in a differential formulation:

$$\sum_{\alpha=1}^{3N} a_{k\alpha} dq_\alpha + a_{kt} dt = 0 \qquad \text{Equation II- 72}$$

$$\sum_{\alpha=1}^{3N} a_{k\alpha} \dot{q}_\alpha + \frac{\partial \sigma_k}{\partial t} = 0, \qquad \text{Equation II- 73}$$

with $a_{k\alpha} = \nabla_i \sigma_k$ and $a_{kt} = \frac{\partial \sigma_k}{\partial t}$.

We introduce an extended Lagrangian L', which contains the constraints σ_k and the corresponding Lagrange multiplier λ_k:

$$L' = L - \sum_{k=1}^{N_C} \lambda_k \sigma_k. \qquad \text{Equation II- 74}$$

The $3N$ equations of motion become:

$$-\frac{d}{dt}\frac{\partial L'}{\partial \dot{q}_\alpha}+\frac{\partial L'}{\partial q_\alpha}=0 \qquad \text{Equation II- 75}$$

or

$$\frac{d}{dt}\frac{\partial L}{\partial \dot{q}_\alpha}=\frac{\partial L}{\partial q_\alpha}+\sum_{k=1}^{N_C} \lambda_k a_{k\alpha} \qquad \text{Equation II- 76}$$

or equivalently:

$$m_i\ddot{q}_i = -\frac{\partial V}{\partial q_i} - \sum_{k=1}^{N_C} \lambda_k a_{ki}$$

Equation II- 77

$$m_i\ddot{q}_i = F_i + \sum_{k=1}^{N_C} F_{ki}^c.$$

$F^c = \sum_{k=1}^{N_C} F_{ki}^c$ is the total constraint force or restoring force. The restoring force F_{ki}^c is proportional to the Lagrange multiplier λ_i.

The blue-moon approach can be used with multiple constraints[47], but we will use a single constraint on the reaction coordinate: $\xi(\boldsymbol{q}) = \xi^*$. For a set of initial configurations $\{\xi_i^*\}$ distributed along a transformation path, a constrained molecular dynamics run is performed at each value of ξ_i^*. The previous equations are solved iteratively with the SHAKE[46] algorithm as implemented in VASP. Starting from the usual leap-frog Verlet algorithm, with the forces associated to the constraints, the equations of motion are solved. The new positions and velocities are used to update the λ_k (and thus the restoring forces) and then velocities and positions. These steps are repeated until all convergence criteria are smaller than a predefined tolerance.

II.5.2.2) Slow growth method

This method represents a computationally less expensive albeit less accurate approximation to the blue moon sampling method.

The reaction coordinate ξ is not fixed but evaluated in time with a constant velocity $\dot{\xi}$. For a finite $\dot{\xi}$, the transformation is irreversible and the system is not able to sample the phase space exhaustively at each value of ξ.[41,49]

In this thesis, we used slow growth simulations (as implemented in VASP) mainly in qualitative tests to validate the choice of a reaction coordinate before starting a more accurate but also more time-consuming blue moon sampling,

From Equation II- 63 and Equation II- 64, we find that if the transformation is infinitesimally slow, with $\dot{\xi} \rightarrow 0$, it becomes reversible and then:

$$\Delta A_{A\rightarrow B} = W_{A\rightarrow B}^{rev} = \lim_{\dot{\xi}\rightarrow 0} \int_{t_1}^{t_2} dt\dot{\xi} \left(\frac{\partial H}{\partial \xi}\right)_{\xi=\xi(t)},$$

Equation II- 78

and for a finite $\dot{\xi}$:

$$\Delta A_{A\rightarrow B} \leq \langle W_{A\rightarrow B}\rangle,$$

Equation II- 79

with

$$W_{A\to B} = \int_{t_1}^{t_2} dt\dot{\xi}\left(\frac{\partial H}{\partial \xi}\right)_{\xi=\xi(t)}, \qquad \text{Equation II- 80}$$

and $\langle W_{A\to B}\rangle$ being an average over many repetitions starting from the configurations of the initial equilibrium ensemble.

In order to evaluate a free energy difference with the slow growth method, the transformation must be approximately reversible. A simple test of reversibility can be done by performing independent simulations for the forward and backward transformations. If the simulations are indeed performed in a reversible regime, the resulting free energy profile must be unchanged, i.e. without a significant hysteresis.[49]

Another closely related strategy is based on relation introduced by Jarzynski (Annex A.II.1).

II.5.2.3) Approximation to reaction coordinate (CV)

A small set of generalized coordinates is used to approximate the reaction coordinate. These coordinates are in literature referred to as the collective variables (*CV*), or as the order parameter. In this work we will adhere to the former term.

The expression of the *CV* can involve coordinates such as:

- **distances** between atoms; or a combination or a ratio of distances between atoms. For instance, for a proton transfer between an acidic zeolite and an alkene, we used the following *CV* (Figure II- 4).

$$CV = \frac{d(C^1 - H)}{d(O - H)}$$

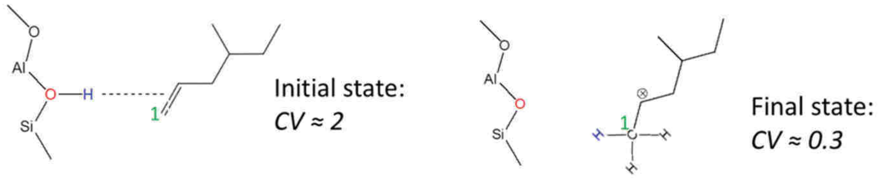

Figure II- 4. Collective variable for a proton transfer.

- **coordination number** *CN*,[50] or combination of *CN*. For a bond AB, the *CN* is defined in VASP as shown in Figure II- 5.

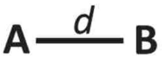

$$CN_i = \frac{1-\left(\frac{d}{d_{ref}}\right)^9}{1-\left(\frac{d}{d_{ref}}\right)^{14}}$$

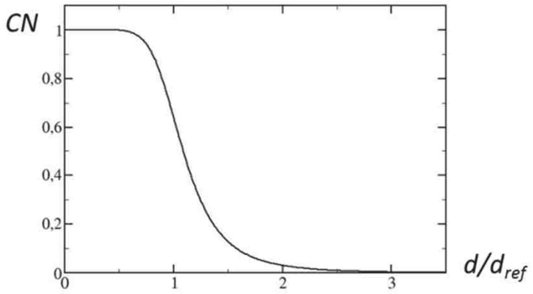

Figure II- 5. Coordination number CN used in definition of the collective variable *CV*.

d is the length of the bond and d_{ref} is a reference length. With such a definition, the *CN* increases continuously from long distances ($d >> d_{ref}$; CN → 0) to short distances ($d << d_{ref}$, CN → 1).

We used CN in the expression of the *CV* for isomerization reactions where coordination numbers change.

- **Torsion angles** α around a bond (Figure II- 6).

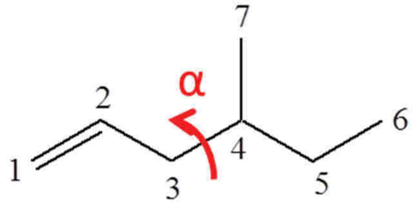

Figure II- 6. Torsion angles α around the C_3-C_4 bond.

We used a torsion angle to compare the free energy of rotamers of the 4-methyl hex-1-ene shown is illustrated by Figure II- 6.

- **Path based CV** Advanced CV has been developed to reduce the dimension of the CV space in metadynamics calculations. For complex reactions, different degrees of freedom evolve in a concerted manner and the CV is intrinsically multidimensional. In these cases, the free energy of the system can be investigated along a one-dimensional "reaction tube". For this purpose, we used a path-based collective variable (ξ), as introduced by Branduardi et al.[51], which is defined as follows:

$$\xi = \frac{1}{M-1}\frac{\sum_{i=1}^{M}(i-1)exp(-\lambda|\boldsymbol{q}-\tilde{\boldsymbol{q}}(i)|^2)}{\sum_{i=1}^{M}exp(-\lambda|\boldsymbol{q}-\tilde{\boldsymbol{q}}(i)|^2)}, \quad \text{Equation II- 81}$$

where $\boldsymbol{q}$ is a multidimensional vector whose components are primitive coordinates describing the changes in the structure of the system during the reaction, $\tilde{\boldsymbol{q}}(i)$ is the position vector (defined in the same primitive coordinate space as $\boldsymbol{q}$) of the i-th point of a discretized reaction path $\{\tilde{\boldsymbol{q}}(i); i = 1, \dots, M\}, M$ is the total number of points in $\{\tilde{\boldsymbol{q}}(i)\}$, and λ is an adjustable parameter. The neighboring points of $\{\tilde{\boldsymbol{q}}(i)\}$ should be approximately equidistant and the parameter λ should be chosen so as to correspond to the inverse of the average value of $|\tilde{\boldsymbol{q}}(i) - \tilde{\boldsymbol{q}}(i+1)|^2$.[42,51] By construction, the value of ξ ranges between 0 (reactant) and 1 (product).

Cartesian coordinates of a subset of atoms can be used as the primitive coordinates of the components of $\boldsymbol{q}$. Coordination numbers can also be convenient: explicit structures are not required and new mechanisms can be explored during the simulation.[52] We used such a path-based CV to study a type B isomerization reaction and in order to prevent the undesired subsequent fast type A isomerization reaction: the coordinate ξ has been defined so as to cover both subsequent isomerization reactions (Section III).

II.5.2.4) Transition path sampling

Transition path sampling (TPS) is used to overcome the difficulties of the investigation of rare events in complex systems, for which the investigation of a few stationary points is insufficient to describe an energy landscape with uncountable saddle points.[53,54] Notably, the reactive trajectories are not generated with some artificial bias but rather they are selected among all the trajectories sampled by the intrinsic dynamics of the system.[53] In this method, an ensemble of reactive trajectories is harvested by a Monte Carlo procedure. The prior knowledge of the mechanism and of a reaction coordinate is not required: more simply, the reactant and product states have only to be distinguished by a simpler low dimensional order parameter.[53,54]

An initial reactive trajectory is generated by integration of equations of motion forward and backward in time, starting from a transition state (optimized in the static approach, for instance) and with initial velocities of the same magnitude but the opposite sign, randomly generated according to the Maxwell-Boltzmann distribution. A new trial move is generated by “shooting” or “shifting” moves. In shooting moves, a state of the previous reactive trajectory is randomly chosen and the momenta are modified by addition of a small Maxwell-Boltzmann distributed noise (Figure II- 7 a). Then, the equations of motion are integrated forward and backward in time. In shifting moves, a typical state of the reactant (or product) region of the previous reactive trajectory is chosen. The states before (or after) this state are discarded and the trajectory is extended at the other end of the trajectory (Figure II- 7 b). All the trajectories have the same length. If the new trajectory is still reactive (connecting reactant and product, according to the order parameter chosen), it is accepted, and otherwise rejected. Free energies and rate calculations can be performed within this framework[53] but the computational cost is too high for *ab initio* MD calculations in zeolites and we used this method only qualitatively to get an insight into the relative statistics of the different pathways related to a single free energy transition state. Selected mechanisms can be further investigated by accurate free energy calculations, for instance with the blue moon ensemble approach.[26]

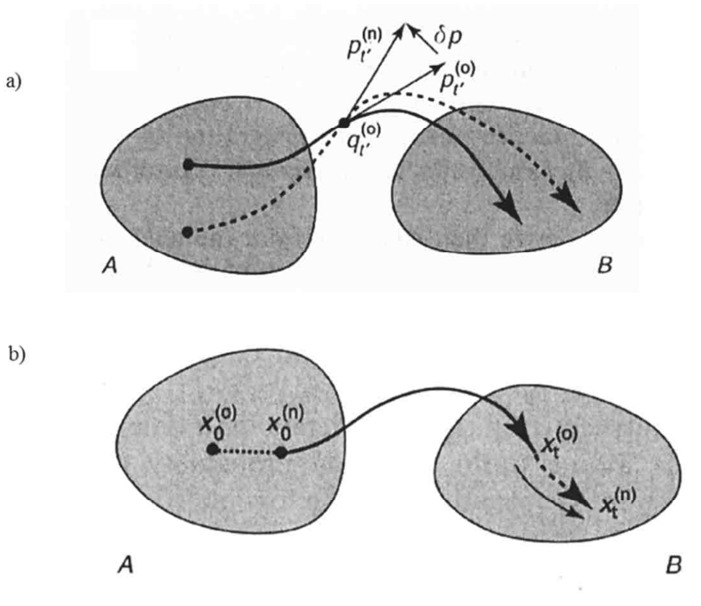

Figure II- 7. a) Shooting move where a new trial move (dash line) is generated by addition of a small Maxwell-Boltzmann distributed noise d*p* on the momenta on a randomly selected state of the old trajectory (solid line). b) In a shifting move a new trial move (dash line) is generated by removing a part of the trajectory (in the reactant region on this example) and by extension of the trajectory on the other side. Adapted from ref.[53]

II.5.3. Free energies of activation $\Delta_r A^{\ddagger}$ and of reaction $\Delta_r A_{R\to P}$

II.5.3.1. Derivation of the expressions

The free energy of activation $\Delta_r A^{\ddagger}$ can be computed from the free energy profile determined by an advanced molecular dynamics method and by comparison with the Eyring-Polanyi equation (Equation II- 82):[39,55]

$$k_{R\to P} = \frac{k_B T}{h} exp\left(-\frac{\Delta_r A^{\ddagger}}{k_B T}\right). \qquad \text{Equation II- 82.}$$

In Equation II- 82, $\Delta_r A^{\ddagger}$ is the phenomenological free energy of activation.

Within the Eyring's transition state theory, the rate constant for a transformation from a reactant *R* to a product *P* can be written as follows:[36],[56]

$$k_{R\to P} = \frac{\langle \dot{\xi}\delta\big(\xi^* - \xi(0)\big)\theta(\xi - \xi^*)\rangle}{\langle \theta(\xi^* - \xi)\rangle}, \qquad \text{Equation II- 83}$$

where:

- the product is identified with values of ξ such as $\xi > \xi^*$(and $\theta(\xi - \xi^*) = 1$) and the reactant with values of ξ such as $\xi < \xi^*$(and $\theta(\xi - \xi^*) = 0$)

- ξ^* is the reaction coordinate at the transition state
- $\dot{\xi}$ is the generalized velocity for configurations at transition state. $\dot{\xi}$ is obtained from the Cartesian velocities $\dot{x}_i$ as follows:

$$\dot{\xi} = \sum_i \frac{\partial \xi}{\partial x_i} \dot{x}_i \qquad \text{Equation II- 84}$$

- θ is the Heaviside step function and so
    - within the transition state theory and the *harmonic approximation*, the following equality holds: $\theta(\xi - \xi^*) = \theta(\dot{\xi})$. This term takes into account the contribution of molecules with positive generalized velocity, going from reactant to product
    - $\langle \theta(\xi^* - \xi) \rangle = \langle c_R \rangle$, probability of finding the system in the state *R*, i.e. the concentration in reactant *R*

Equation II- 83 can be rewritten as follows:

$$k_{R\to P} = \frac{\langle \dot{\xi}\delta\big(\xi^* - \xi(0)\big)\theta(\xi - \xi^*)\rangle}{\langle \delta(\xi^* - \xi)\rangle} \frac{\langle \delta\big(\xi_{ref,R} - \xi\big)\rangle}{\langle \theta(\xi^* - \xi)\rangle} \frac{\langle \delta(\xi^* - \xi)\rangle}{\langle \delta\big(\xi_{ref,R} - \xi\big)\rangle}, \qquad \text{Equation II- 85}$$

where:

- we choose $\xi_{ref,R}$ as a reference point near the reactant state. The probability density $P\big(\xi_{ref,R}\big)$ must be sufficiently high so that the configuration is well sampled in a regular, unconstrained, MD simulation.
- $\frac{\langle \delta(\xi_{ref,R} - \xi)\rangle}{\langle \theta(\xi^* - \xi)\rangle}$ is the probability density of finding the system at the reference point ξ_{ref} within the ensemble of all the reactant configurations *R*:

$$P\big(\xi_{ref,R}\big) = \frac{\langle \delta\big(\xi_{ref,R} - \xi\big)\rangle}{\langle \theta(\xi^* - \xi)\rangle} \qquad \text{Equation II- 86}$$

- $\frac{\langle \dot{\xi}\delta(\xi^* - \xi)\theta(\xi - \xi^*)\rangle}{\langle \delta(\xi^* - \xi)\rangle}$ is the conditional average of $\dot{\xi}$ given that $\xi = \xi^*$ and $\dot{\xi} > 0$ (the latter condition is just another formulation of the statement that transition state inevitably collapses into product before recrossing the barrier, which is one of the important assumptions used in the transition state theory). That means that it is the average velocity associated with a reaction coordinate for a trajectory starting at the TS and leading to a product P at t > 0.

$$\frac{\langle \dot{\xi}\delta(\xi^* - \xi)\theta(\xi - \xi^*)\rangle}{\langle \delta(\xi^* - \xi)\rangle} = \frac{1}{2}\langle |\dot{\xi}^*| \rangle \qquad \text{Equation II- 87}$$

- according to Equation II- 56 and Equation II- 58: $P(\xi_i) = \langle\delta(\xi_i - \xi)\rangle = C\; exp\left(-\frac{A(\xi_i)}{k_B T}\right)$ and the last term in Equation II- 85 can be rewritten:

$$\frac{\langle\delta(\xi^* - \xi)\rangle}{\langle\delta(\xi_{ref,R} - \xi)\rangle} = exp\left(-\frac{\Delta A_{\xi_{ref,R}\to\xi^*}}{k_B T}\right). \qquad \text{Equation II- 88}$$

Finally, with Equation II- 86 to Equation II- 88, the Equation II- 85 can be rewritten as follows:

$$k_{R\to P} = \frac{\langle|\dot{\xi}^*|\rangle}{2} P(\xi_{ref,R}) exp\left(-\frac{\Delta A_{\xi_{ref,R}\to\xi^*}}{k_B T}\right). \qquad \text{Equation II- 89}$$

We use the Equation II- 89 with:

- $\dot{\xi}$ calculated from the Cartesian velocities $\dot{x}_i$ (Equation II- 84) which are random-generated according to the Maxwell-Boltzmann distribution. 500 random velocities are typically generated for each $\dot{x}_i$ and the configurations with $\xi = \xi^*$ are taken in a constrained MD run at $\xi = \xi^*$. The unconstrained average for $|\dot{\xi}^*|$ is obtained using Equation II- 66:

$$\langle|\dot{\xi}^*|\rangle = \frac{\langle Z^{-\frac{1}{2}}|\dot{\xi}|\rangle_{\xi^*}}{\langle Z^{-\frac{1}{2}}\rangle_{\xi^*}}, \qquad \text{Equation II- 90}$$

  where $\langle\dots\rangle_{\xi^*}$ is the average in the constrained ensemble at $\xi = \xi^*$ and Z is the inverse mass metric tensor defined in Equation II- 67.
- $\Delta A_{\xi_{ref,R}\to\xi^*}$ is the free energy difference between the transition state and the reference *R*. In this work, this quantity is determined using the blue moon simulation as described in Section II.5.2.1.
- $P(\xi_{ref,R})$ is obtained from the unconstrained MD run for the reactant.

By identifying with the Eyring-Polanyi equation (Equation II- 82), we obtain the following expression for the phenomenological free-energy of activation $\Delta_r A^\ddagger$:

$$\Delta_r A^\ddagger = \Delta A_{\xi_{ref,R}\to\xi^*} - k_B T ln\left(\frac{h}{k_B T}\frac{\langle|\dot{\xi}^*(0)|\rangle}{2} P(\xi_{ref,R})\right). \qquad \text{Equation II- 91}$$

Combining Equation II- 91 with its analogue for the backward reaction, the following expression is obtained for the free energy of reaction $\Delta_r A_{R\to P}$:

$$\Delta_r A_{R\to P} = \Delta A_{\xi_{ref,R}\to\xi_{ref,P}} - k_B T ln\left(\frac{P(\xi_{ref,R})}{P(\xi_{ref,P})}\right), \qquad \text{Equation II- 92}$$

where $\Delta A_{\xi_{ref,R}\rightarrow\xi_{ref,P}}$ is the free energy difference between the reference states $\xi_{ref,R}$ and $\xi_{ref,P}$, and $P(\xi_{ref,P})$ is the probability density of the reference state $\xi_{ref,P}$ of the product among all product configurations.

II.5.3.2. Independence of the free energies of the choice of the approximation to reaction coordinate

The method developed in the previous subsection and derived of Bennett-Chandler method as described in Frenkel and Smit's textbook[36] is by design independent of the choice of the approximation to reaction coordinate ξ, provided this approximation drives the reaction, from reactant to product, reversibly. The blue moon sampling method used to compute $\Delta A_{\xi_{ref,R}\rightarrow\xi^*}$ in Equation II- 91 is exact in principle and should give the same result as other advanced MD methods (such as metadynamics or umbrella sampling). This result depends on the choice of ξ and the remaining term on the right hand side of Equation II- 91 $\left(k_BTln\left(\frac{h}{k_BT}\frac{\langle|\dot{\xi}^*(0)|\rangle}{2}P(\xi_{ref,R})\right)\right)$ ensures that the quantity $\Delta_rA^\ddagger$ is independent of ξ.

Invariance of the free energy with respect to the choice of the approximation to reaction coordinate ξ also implies that the results for different reactions with different reaction coordinates can be safely compared (different choices for ξ are necessary for reactions involving different atoms).

II.5.4) Free-energy partitioning

The free energy $A = U - TS$ can be partitioned into internal energy U and entropy S.

For reactants R and products P, the internal energy can be obtained as an ensemble average from a regular (unconstrained) molecular dynamics run. The internal energy of reaction $\Delta_rU_{R\rightarrow P}$ can be computed using Equation II- 93, and the entropy of reaction $\Delta_rS_{R\rightarrow P}$ using Equation II- 94.

$$\Delta\,_rU_{R\rightarrow P} = U_P - U_R = \langle E_P\rangle - \langle E_R\rangle, \qquad \text{Equation II- 93}$$

$$\Delta\,_rS_{R\rightarrow P} = \frac{\Delta\,_rU_{R\rightarrow P} - \Delta\,_rA_{R\rightarrow P}}{T}. \qquad \text{Equation II- 94}$$

The same method applies for the calculation of internal energy and entropy of activation, $\Delta_rU^\ddagger$ and $\Delta_rS^\ddagger$, but the energy of the transition state is obtained in a constrained molecular dynamics run and it has to be unbiased as it was shown in the blue moon ensemble approach (see part II.5.2.1).[43,56]

The internal energy of the transition state is obtained from Equation II- 95:

$$\langle E_{TS}\rangle = \frac{\langle Z^{-\frac{1}{2}}E_{TS}\rangle_{\xi^*}}{\langle Z^{-\frac{1}{2}}\rangle_{\xi^*}}, \qquad \text{Equation II- 95}$$

with Z being the mass metric tensor (Equation II- 67).

Finally, the internal energy and entropy of activation, $\Delta_r U^{\ddagger}$ and $\Delta_r S^{\ddagger}$ can be written as follows:

$$\Delta_r U^{\ddagger} = \langle E_{TS} \rangle - \langle E_R \rangle,$$

$$\Delta_r S^{\ddagger} = \frac{\Delta_r U^{\ddagger} - \Delta_r A^{\ddagger}}{T}.$$

Equation II- 96

In general, *U* is more difficult to converge than *A* because the former depends on the energy of all atoms in the cell (it is roughly proportional to the number of particles) and thus it is sensitive to errors in position and energy of each atom. ΔU is the small difference on two large numbers subject to large uncertainties. On the opposite, *A* is a more local quantity (*A* is deduced from its gradient which is linked to the restoring force acting on the atoms of the reactive molecule, and not on all the atoms of the cell). The uncertainty in ΔU can be one or two orders of magnitude larger than on ΔA. As standard errors decrease with the square root of number of samples, a 10^2 to 10^4 times longer sampling is required to achieve the same accuracy for ΔU than for ΔA, which is not realistic for large systems used in heterogeneous catalysis.[41,57]

We tried this free energy partitioning on the reactions investigated in Section III but the uncertainties on ΔU and consequently on ΔS proved to be too large to be reported.

II.5.5) Andersen thermostat

In computer simulations within the canonical *NVT* ensemble, we have used the Andersen's thermostat employing a stochastic heat bath imposing the desired temperature.[58]

At constant temperature T, the probability density of the velocities is given by the Maxwell-Boltzman distribution:[40]

$$f(v) = \left(\frac{m}{2\pi k_B T}\right)^{1/2} e^{-\frac{mv^2}{2k_B T}}.$$

Equation II- 97

The kinetic energy per particle is related to the simulation temperature T as follows: $k_B T = m\langle v_\alpha^2 \rangle$ (with v_α being the αth component of the velocity). It can be shown that in the canonical ensemble, the instantaneous temperature fluctuates. The relative variance of the instantaneous kinetic energy per particle and of the temperature decreases with the number *N* of particles as 1/*N*.[36]

With the Andersen thermostat, the system is coupled to the heat bath by stochastic collisions which reset the velocities of randomly selected particles (according to the Maxwell-Boltzmann distribution). Between these stochastic collisions, the system evolves according to the Newtonian laws of motion, conserving the total energy. Typically, we choose a probability of collision per atom and time step of 1%. Andersen showed that this combination of Newtonian dynamics and stochastic collisions generates a correct canonical distribution.[58]

II.6) Computational section

Periodic DFT calculations were performed with the VASP code[6,19–21], using the PBE exchange-correlation functional[11] with DFT-D2 dispersion correction of Grimme[13] and the projector-augmented-wave (PAW) method[22]. Brillouin-zone sampling was restricted to the Γ-point. The plane wave cutoff was set to 400 eV (800 eV for the optimization of the bulk cells of zeolites). The convergence criterion for the electronic self-consistency cycle was set to 10^{-7} eV. For geometry optimization, the convergence criterion on the forces was set to 0.005 eV/Å. Harmonic frequency calculations were performed with a displacement of ±0.02 Å around the equilibrium.

Molecular dynamics and free energy calculations have been performed in the NVT ensemble, with an integration step of 1 fs. The temperature was controlled with the Andersen thermostat[58] (with a collision frequency per atom of 0.01 fs^{-1}). The atomic mass of tritium has been chosen for H atoms in order to avoid numerical problems that would be likely to occur when a relatively large integration step is used in MD of a system containing light atoms.

We have used a unit cell of chabazite with 24 SiO_2 units (Sections III to V), which represents 94 atoms with the C_7 alkene. With this cell, we have estimated the total computational cost of a blue moon simulation (for 20 simulations of 50 ps) at around 100 000 hours of CPU time, approximately 100 times the computational cost of a static study. The computational cost of this advanced MD method is manageable for our cell of chabazite but becomes too high for the larger cells of other zeolites, such as the BEA zeolite.

II.7) Conclusions

The static approach is popular in the investigation of mechanisms. It is useful especially for potential energy dominated reactions. Nevertheless the application of this approach to reaction in zeolites is problematic.[26,59] For realistic structural models in heterogeneous catalysis, potential energy surfaces are complex and corrugated, with many local stationary points. Depending on the initial guess, it has been shown that for the cracking of propane in chabazite, the free energy of activation can differ by 20 $kJ.mol^{-1}$ at 800 K (which represents a ratio of 20 for the rate constants at this temperature).[26] However, error bars on energies of activation cannot be defined easily. This uncertainty is expected to be even more important for the C7 molecules investigated in this thesis. Moreover, the harmonic approximation is not realistic enough for a reacting system. The system has to stay near the same equilibrium configuration and a vibration cannot turn into a different type of motion.

Moreover, residual imaginary frequencies appear frequently as a consequence of incomplete energy minimization along one or more direction. They are handled with different unsatisfactory approximations (such as replacing them by a constant real frequency) or they need a time-consuming line-minimization procedure to be removed (section II.4.5).

As explained in the introduction of part I, the methodological objective of this thesis is to go beyond the static approach and to use advanced *ab initio* molecular dynamics methods to investigate mechanisms of the isomerization and cracking reactions of C_7 alkanes in zeolites.
As we have discussed in section II.5.1, molecular dynamics enables to calculate thermodynamic quantities such as entropy S and free energy A, without the approximations and limitations of the static approach. In molecular dynamics, reactant, product and transition states are not represented by a single configuration and the nuclear motions are not approximated by harmonic oscillator model. Molecular dynamics also enables to estimate and control the error bars (Annex A.II.2).

Annexes

A.II.1) Jarzynski's identity

Jarzynski has shown that the inequality in Equation II- 79 can be transformed into the following equality, the Jarzynski's identity:[60]

$$exp(-\beta \Delta A_{A\to B}) = \langle exp(-\beta W_{A\to B})\rangle. \qquad \text{Equation II- 98}$$

This identity represents a very surprising result: equilibrium free energy differences can be obtained from non-equilibrium simulations. However, "in science as in life, there is no such thing as a free lunch" and the problem is the statistical accuracy: the rare smaller contributions of W, which contribute largely to the average, are often insufficiently sampled. It is an issue mainly if the distribution of the work is much broader than $k_B T$.[36]

Jarzynski's identity can be used to obtain free energy differences from slow growth simulations. It is also used in steered molecular dynamics where a force is applied to induce the process of interest, an approach inspired by single molecule pulling experiments using atomic force microscopes. Steered molecular dynamics allows quantitative utilization of the slow growth method.

For instance, Park and coworkers[61] used steered molecular dynamics to study the helix-coil transition of deca-alanine. They concluded that with about ten irreversible realizations of the process of interest, a reliable estimate of the free energy difference can be obtained, which is much faster than a reversible transformation (100 to 1000 times faster) and comparable to an umbrella sampling (a biased sampling where a bias potential is added, with an accuracy depending on the choice of biasing potentials).[61]

A.II.2) Statistical errors tests in molecular dynamics.

Errors in statistical mechanics computer simulation originate in at least two sources: approximations and numerical noise in the representation of the system (system size, choice of a model, empirical force field or DFT calculations for forces…), and imperfect sampling due to limited simulation time. A systematic error is linked to the choice of the system whereas finite sampling errors can be decreased by performing better (longer) sampling or using more efficient sampling algorithms.[41]

We estimate error bars for the quantity $\left(\frac{\partial A}{\partial \xi}\right)_{\xi^*}$ (and then on the free energy $A(\xi)$ by integration) from the standard error calculated on the Lagrange multiplier λ.

Mean, standard deviation and standard error

Within the ergodic hypothesis, for a system at equilibrium, the mean value of $X(t)$ is equal to the ensemble average $\langle X\rangle$. A function $X(t)$ is characterized by its probability distribution $P(X)$. The first two moments of this distribution are the mean and the variance. At equilibrium, $P(X)$ is independent of time for all functions X. We need to know if the system is at equilibrium (if the equilibration time is long enough) and if the confidence limits on the mean are acceptable.[62]

If we have N independent data points X_i, $i = 1, 2, \ldots, N$, the best estimate of $\langle X \rangle$ is the sample mean $\bar{X}$:

$$\langle X \rangle \approx \bar{X} = \frac{1}{N}\sum_{i=1}^{N} X_i. \qquad \text{Equation II- 99}$$

And the variance v of the sampled values is defined by $v = \sigma^2$, with σ the standard deviation of the sample:[4]

$$v = \sigma^2 = \frac{1}{N}\sum_{i=1}^{N}(X_i - \bar{X})^2 = \frac{1}{N}\sum_{i=1}^{N} X_i^2 - \bar{X}^2. \qquad \text{Equation II- 100}$$

The standard deviation σ reflects the width of distribution and the standard error of the mean reflects the uncertainty in the mean value. The standard error of the mean $\sigma_{\bar{x}}$ is estimated on the sample by:

$$\sigma_{\bar{x}} = \frac{\sigma}{\sqrt{N}}. \qquad \text{Equation II- 101}$$

The variance is linked to fluctuations which are real physical properties. For instance, the heat capacity at constant volume is related to the energy fluctuations.[40,62]

For a normal (or Gaussian) distribution, 95% of the data points from a large set of independent measurements are from the interval $\langle X \rangle - 2\sigma$ and $\langle X \rangle + 2\sigma$.

For a system at equilibrium, after equilibration and without any trends or correlations, the mean value $\langle X \rangle$ is obtained according to the mean and the standard deviation of the sample:

$$\langle X \rangle = \bar{X} + \alpha_N \frac{\sigma}{\sqrt{N}}, \qquad \text{Equation II- 102}$$

where α_n is the chosen fractile (e.g. 0.975) of the Student's t-distribution. For $N \geq 24$, a condition largely verified in molecular dynamics, $\alpha_n \approx 2$.[62]

Block averaging

In molecular dynamics, raw data are not independent but highly correlated since each state is obtained by integration of equations of motion from the previous step. Standard formulas of statistics cannot be used directly to calculate mean and variance of a sample: the standard error of the mean (Equation II- 100) would be widely underestimated. One possible way to obtain data that

---

[4] To take into account the N – 1 degrees of freedom after calculation of the mean, an unbiased estimator of the sample variance is defined by $v = \sigma^2 = \frac{1}{N-1}\sum_{i=1}^{N}(X_i - \bar{X})^2$. In molecular dynamics, we have typically tens of thousands of data points, so the difference between N and $N - 1$ is negligible.

are approximately random distributed is to suitably coarse-grain the data e.g. via block averaging. This latter method allows for a faster and simpler evaluation of the error estimate of a time average than the other popular estimators based on correlation functions.[36,62,63] In the following text, the method is briefly described.

A block average is a time average over a finite time t_B:

$$\bar{X}_B = \frac{1}{t_B}\int_0^{t_B} dt\, X(t). \qquad \text{Equation II- 103}$$

For discrete data $X_i = X(i\Delta t)$, with Δt being the time step and $t_B = m\Delta t$, the block average is defined by:

$$\bar{X}_B = \frac{1}{m}\sum_{j=1}^{m} X_j. \qquad \text{Equation II- 104}$$

For small numbers of blocks (L), the data are correlated and the standard error increases with L. For too large values of L, there are too few samples and consequently large fluctuations in the standard error. On the plateau between these two limits, the “blocked” data are approximately independent of L and we can obtain a reliable estimate of the standard error of the mean.

An example of such an error estimation is shown in Figure A-II 2. For a molecular dynamics run of 70 ps (time step Δt = 1 fs) the temperature is plotted as a function of time in Figure A-II 1. The average temperature is $\bar{T} = 301.4\,\mathrm{K}$. Figure II.2 shows the standard error of the mean for the temperature as a function of the length of the block size. On the plateau previously defined, we can read off an estimate of the standard error of the mean: $\delta T = 1.15$ K. We can conclude that for this simulation, the temperature T is: $T = \bar{T} \pm 2\delta T = 301 \pm 3\,\mathrm{K}$, which is consistent with the temperature chosen for this simulation (300 K, imposed by the Andersen thermostat).

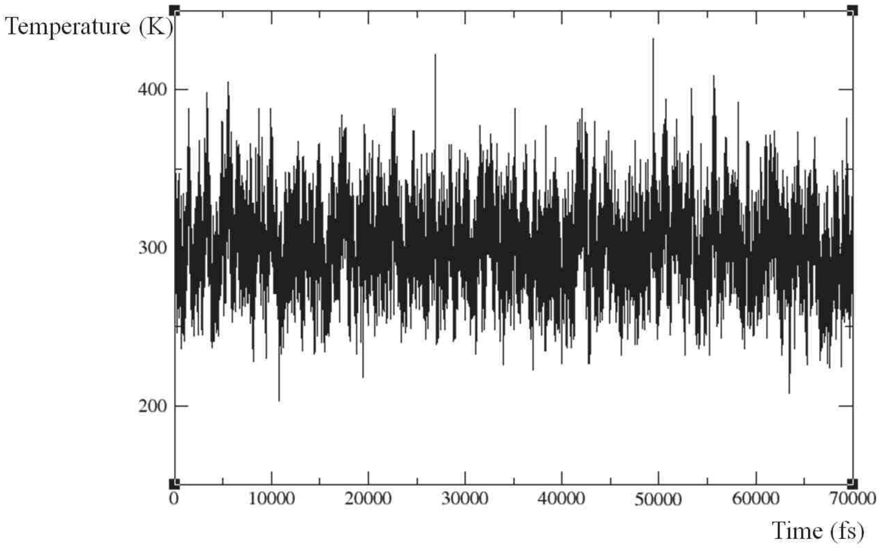

Figure A-II 1. Temperature as a function of time for a constrained run (see section II.5.2) of 4-methyl-pent-2-ene adsorbed (with a constrained skeletal angle) in acid chabazite.

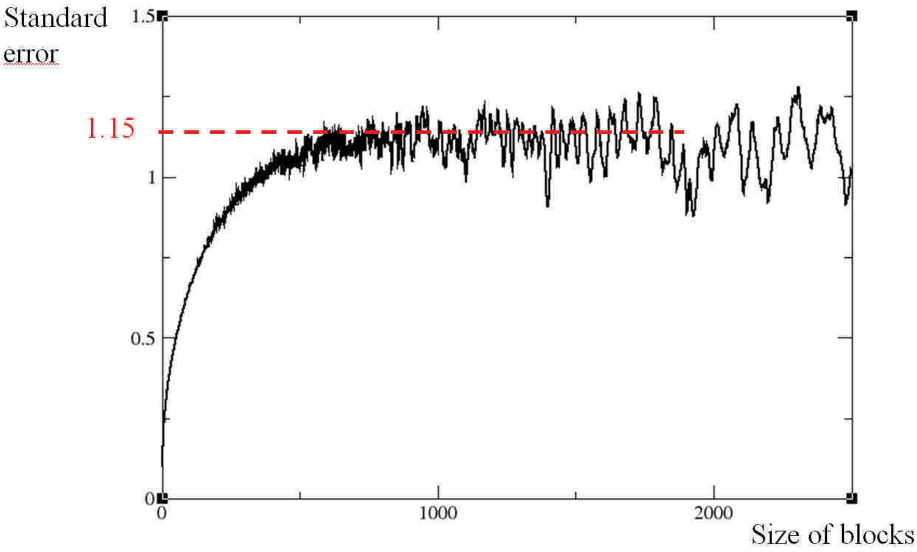

Figure A-II 2. Standard error of the mean temperature as a function of the size of the blocks.

Mann-Kendall tests

In order to calculate averages and confidence limits, we need to ensure that the system is at equilibrium: mean and variance must be independent of time over long period, without any monotonic increase or decrease. We can choose an equilibration time by visual analysis of a corresponding plot but a statistical analysis is preferable, e.g. by means of the Mann-Kendall tests.[62]

For instance, Figure A-II 3 shows the total energy (electronic and ionic, in eV) for an alkene in a protonic zeolite, in a constrained molecular dynamics run with a constant torsion angle (section II.5.2.3). On the plot, the start time for the production period can be chosen to be around 20 ps, which is consistent with the formation of the π-complex observed in the simulation (before 20 ps, the alkene is desorbed from the acid site). The average energy is – 688.96 eV on the 1st period (until 20 ps) and – 689.20 eV during the following 50 ps.

In the Mann-Kendall test, the test statistic S is evaluated:

$$S = 2I - \binom{n}{2}$$

where I is the number of times that $X_k > X_j$ for all k, j such as $k > j$. If the data were independent, for a size of the sample $n \geq 20$, the mean of S is 0, and its distribution is approximatively normal, with a standard deviation $\sigma_S = [n(n-1)(2n+5)/18]^{1/2}$.

The value of the standard normal deviation $u(S) = \frac{S}{\sigma_S}$ is tested to check if the hypothesis of independence of data can be accepted or rejected with a confidence of 95% for instance.[62]

For the example shown in Figure A-II 3, the test is successful when the equilibration time is 15 ps.

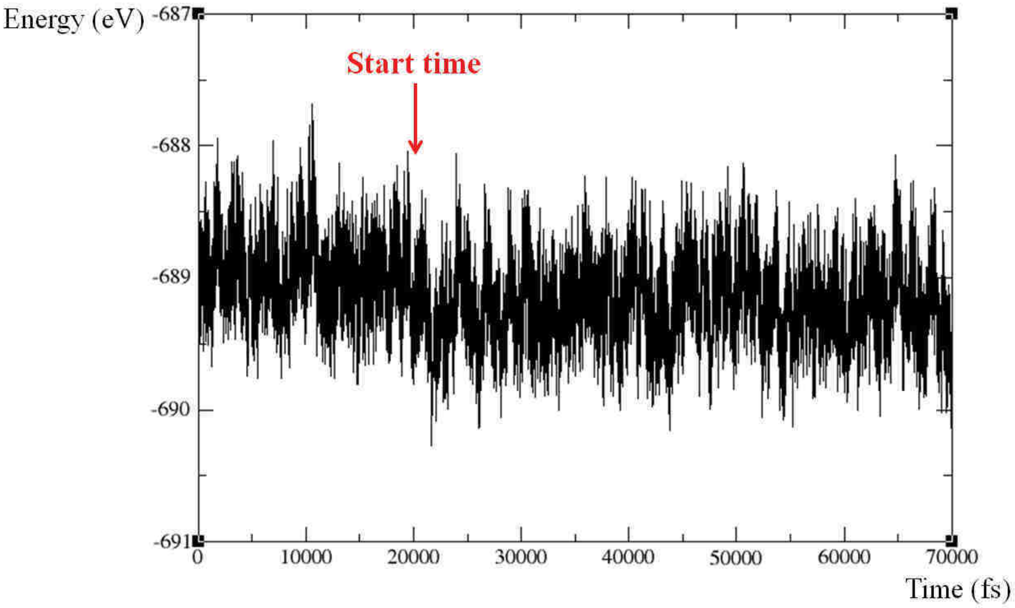

Figure A-II 3. Total energy (electronic and ionic) of) of 4-methyl-pent-2-ene adsorbed (with a constrained skeletal angle) in acid chabazite.

In practice, the Mann-Kendall test is performed on the mean and the variance of all quantities of interest.

A.II.3) Committor distribution

The committor $p_B(\boldsymbol{x})$, defined in each point $\boldsymbol{x}$ of the configurational space, is the fraction of trajectories starting at the point $\boldsymbol{x}$, with randomly Maxwell-Boltzmann distributed velocities, and reaching the basin of state **B** (the product for instance) before **A**. The committor has the formal properties of an ideal reaction coordinate (such as a monotonic evolution from reactant to product) but is not useable practically. It requires the simulations of many trajectories at each point $\boldsymbol{x}$, it does not allow to compute reaction rates easily and it does not provide mechanistic insight into the reaction.[64] The committor distribution test is used to check if the approximation to reaction coordinate is correct and if the supposed transition state $\boldsymbol{x}^{\ddagger}$ is really a transition state defined by $p_B(\boldsymbol{x}^{\ddagger})$ = ½. This test requires thousands of trajectories and is extremely time consuming (even with Peter's algorithmic improvements, the computational cost is at least similar to a full free energy calculation).[65] It is also not a definite proof of correctness of the approximation to reaction coordinate as it can be passed by a candidate collective variable that poorly describes bottlenecks in and out a stable intermediate.[64,65] As a consequence, this test is rarely used in *ab initio* MD calculations and we did not use it.

References

[1] A. Szabo, Ostlund, Neil, S., *Modern quantum chemistry:. Introduction to advanced electronic struture theory*, Macmillan Publishing Co., Inc., New York, **1982**.

[2] R. A. van Santen, M. Neurock, *Molecular Heterogeneous Catalysis. A Conceptual and Computational Approach*, Wiley-VCH, Weinheim, **2006**.

[3] C. Tuma, J. Sauer, *Angew. Chem. Int. Edit.* **2005**, *44*, 4769–4771.

[4] G. Piccini, M. Alessio, J. Sauer, *Angew. Chem. Int. Ed.* **2016**, *55*, 5235–5237.

[5] R. G. Parr, W. Yang, *Density-functional theory of atoms and molecules*, Oxford University Press, **1989**.

[6] G. Kresse, J. Furthmüller, *Comp. Mater. Sci.* **1996**, *6*, 15–50.

[7] S. Mohr, L. E. Ratcliff, P. Boulanger, L. Genovese, D. Caliste, T. Deutsch, S. Goedecker, *J. Chem. Phys.* **2014**, *140*, 204110.

[8] A. D. Becke, *J. Chem. Phys.* **2014**, *140*, 18A301.

[9] J. P. Perdew, K. Schmidt, *AIP Conference Porceedings* **2001**, *577*, 1–20.

[10] K. Burke, *J. Chem. Phys.* **2012**, *136*, 150901.

[11] J. P. Perdew, K. Burke, M. Ernzerhof, *Phys. Rev. Lett.* **1996**, *77*, 3865–3868.

[12] J. Klimes, A. Michaelides, *The Journal of chemical physics* **2012**, *137*, 120901.

[13] S. Grimme, *J. Comput. Chem.* **2006**, *27*, 1787–1799.

[14] S. Grimme, J. Antony, S. Ehrlich, H. Krieg, *J. Chem. Phys.* **2010**, *132*, 154104.

[15] M. Dion, H. Rydberg, E. Schroder, D. C. Langreth, B. I. Lundqvist, *Phys. Rev. Lett.* **2004**, *92*, 246401.

[16] K. Lee, E. D. Murray, L. Kong, B. I. Lundqvist, D. C. Langreth, *Phys. Rev. B* **2010**, *22*, 22201.

[17] F. Goltl, A. Gruneis, T. Bucko, J. Hafner, *J. Chem. Phys.* **2012**, *137*, 114111.

[18] J. Hafner, *J. Comput. Chem.* **2008**, *29*, 2044–2078.

[19] G. Kresse, J. Hafner, *Phys. Rev. B* **1993**, *47*, 558–561.

[20] G. Kresse, J. Hafner, *Phys. Rev. B* **1994**, *49*, 14251–14269.

[21] G. Kresse, J. Furthmüller, *Phys. Rev. B* **1996**, *54*, 11169–11186.

[22] G. Kresse, D. Joubert, *Phys. Rev. B* **1999**, *59*, 1758–1775.

[23] F. Neese, *WIREs Comput Mol Sci* **2012**, *2*, 73–78.

[24] F. Furche, R. Ahlrichs, C. Hättig, W. Klopper, M. Sierka, F. Weigend, *WIREs Comput Mol Sci* **2014**, *4*, 91–100.

[25] F. Bischoff, M. Alessio, M. John, M. Rybicki, J. Sauer, MonaLisa, Multi-Level Energy Landscapes: The MonaLisa Program, Humboldt-University: Berlin, **2017**.

[26] T. Bučko, L. Benco, J. Hafner, J. G. Ángyán, *J. Catal.* **2011**, *279*, 220–228.

[27] F. Jensen, *Introduction to computational chemistry. Second Edition,* 2nd ed. ed., John Wiley & Sons, Chichester England, Hoboken NJ, **2007**.

[28] a) B. J. Berne, G. Ciccotti, D. F. Coker (Eds.) *Classical and Quantum Dynamics in Condensed Phase Simulations*, World Scientific, Singapore, 1998; b) G. Henkelman, B. P. Uberuaga, H. Jónsson, *J. Chem. Phys.* **2000**, *113*, 9901–9904;

[29] G. Henkelman, H. Jónsson, *J. Chem. Phys.* **2000**, *113*, 9978–9985.

[30] D. Sheppard, R. Terrell, G. Henkelman, *J. Chem. Phys.* **2008**, *128*, 134106.

[31] P. Fleurat-Lessard, Opt'n Path, http://pfleurat.free.fr/ReactionPath.php.

[32] G. Henkelman, H. Jónsson, *J. Chem. Phys.* **1999**, *111*, 7010.

[33] A. Heyden, A. T. Bell, F. J. Keil, *J. Chem. Phys.* **2005**, *123*, 224101.

[34] a) K. Fukui, *J. Phys. Chem.* **1970**, *74*, 4161–4163; b) K. Fukui, *Accounts Chem. Res.* **1981**, *14*, 363–368;

[35] H. P. Hratchian, H. B. Schlegel, *J. Phys. Chem. A* **2002**, *106*, 165–169.

[36] D. Frenkel, B. Smit, *Understanding Molecular Simulation. From Algorithms to Applications*, Academic Press, **2002**.

[37] G. Piccini, M. Alessio, J. Sauer, Y. Zhi, Y. Liu, R. Kolvenbach, A. Jentys, J. A. Lercher, *J. Phys. Chem. C* **2015**, *119*, 6128–6137.

[38] J.J.W. McDouall, *Computational Quantum Chemistry. Molecular Structure and Properties in Silico*, Royal Society of Chemistry, Cambridge, **2013**.

[39] H. Eyring, *J. Chem. Phys.* **1935**, *3*, 107–115.

[40] M. E. Tuckerman, *Statistical Mechanics: Theory and Molecular Simulation*, Oxford University Press, **2010**.

[41] C. Chipot, A. Pohorille (Eds.) *Springer Series in Chemical Physics*, Springer Berlin Heidelberg, **2007**.

[42] G. Bussi, D. Branduardi, *Free-Energy Calculations with Metadynamics: Theory and Practice*, Wiley, Hoboken, **2015**, *Vol. 28*.

[43] E. A. Carter, G. Ciccotti, J. T. Hynes, R. Kapral, *Chem. Phys. Lett.* **1989**, *156*, 472–477.

[44] G. Ciccotti, M. Sprik, *J. Chem. Phys.* **1998**, *109*, 7737–7744.

[45] L. Grajciar, C. J. Heard, A. A. Bondarenko, M. V. Polynski, J. Meeprasert, E. A. Pidko, P. Nachtigall, *Chemical Society reviews* **2018**.

[46] J. P. Ryckaert, G. Ciccotti, H.J.C. Berendsen, *J. Comput. Phys.* **1977**, *23*, 327–341.

[47] P. Fleurat-Lessard, T. Ziegler, *J. Chem. Phys.* **2005**, *123*, 84101.

[48] H. Goldstein, *Classical Mechanics. Second Edition*, Addison-Wesley Publishing Company, **1980**.

[49] T. K. Woo, Magl, Peter M.,Blöchl, Peter E., T. Ziegler, *J. Phys. Chem. B* **1997**, *101*, 7877–7880.

[50] M. Iannuzzi, A. Laio, M. Parrinello, *Phys. Rev. Lett.* **2003**, *90*, 238302.

[51] D. Branduardi, F. L. Gervasio, M. Parrinello, *J. Chem. Phys.* **2007**, *126*, 54103.

[52] F. Pietrucci, A. M. Saitta, *Proceedings of the National Academy of Sciences of the United States of America* **2015**, *112*, 15030–15035.

[53] C. Dellago, P. G. Bolhuis, P. L. Geissler, *Advances in Chemical Physics* **2002**, *123*.

[54] P. G. Bolhuis, D. Chandler, C. Dellago, P. L. Geissler, *Annual review of physical chemistry* **2002**, *53*, 291–318.

[55] P. W. Atkins, J. de Paula, *Atkins' Physical chemistry,* 10th ed., Oxford University Press, New York, **2014**.

[56] T. Bučko, S. Chibani, J.-F. Paul, L. Cantrel, M. Badawi, *Phys. Chem. Chem. Phys.* **2017**, *19*, 27530–27543.

[57] D. A. Pearlman, B. G. Rao, *Free Energy Calculations. Methods and Applications*, **2002**, American Cancer Society, to be found under https://onlinelibrary.wiley.com/doi/full/10.1002/0470845015.cfa011.

[58] H. C. Andersen, *J. Chem. Phys.* **1980**, *72*, 2384–2393.

[59] V. van Speybroeck, K. de Wispelaere, J. van der Mynsbrugge, M. Vandichel, K. Hemelsoet, M. Waroquier, *Chem. Soc. Rev.* **2014**, *43*, 7326–7357.

[60] C. Jarzynski, *Phys. Rev. Lett.* **1997**, *78*, 2690–2693.

[61] S. Park, F. Khalili-Araghi, E. Tajkhorshid, K. Schulten, *J. Chem. Phys.* **2003**, *119*, 3559–3566.

[62] S. K. Schiferl, D. C. Wallace, *J. Chem. Phys.* **1985**, *83*, 5203–5209.

[63] H. Flyvbjerg, H. G. Petersen, *J. Chem. Phys.* **1989**, *91*, 461–466.

[64] B. Peters, *Annual review of physical chemistry* **2016**, *67*, 669–690.

[65] B. Peters, *J. Chem. Phys.* **2006**, *125*, 241101.

Section III. On the origin of the difference between type A and type B skeletal isomerization of alkenes catalyzed by zeolites: the crucial input of ab initio molecular dynamics

This section reproduces the text of a published paper (http://doi.org/10.1016/j.jcat.2019.04.014 from reference [1]). The corresponding Supporting Information is presented at the end of the section.

III.1. Introduction

Carbenium chemistry is at the core of a large set of chemical transformations in organic chemistry [2–7], with crucial current and prospective industrial repercussions. As a major example, the bi-functional isomerization of alkyl chains is a key reaction in refining [8,9], petrochemistry [9,10] and biomass conversion [11–13]. Hydrocracking and hydroisomerization are among the major industrial current processes based on carbenium chemistry. They are utilized for instance in production of diesel and jet fuels from conventional fossil resources [14], in technologies making use of the heaviest parts of hydrocarbons obtained via the Fischer-Tropsch process from different feedstock (coal, biomass or gas), or for very heavy unconventional crudes such as tar sands and shale oils [15,16]. Hydrocracking and hydroisomerization catalysts typically combine two functions: a hydrogenation/dehydrogenation function on a noble metal or a metallic sulfide and an acidic function of the Brønsted type provided by zeolites or amorphous silica-aluminas [16].

A sequence of reactions taking place in these processes begins by the dehydrogenation of alkanes into alkenes. The alkenes are protonated afterwards on the acidic function. Intermediate carbocations are formed and these species evolve by isomerization and β-scission reactions. The resulting shorter and isomerized alkenes are hydrogenated to form alkanes, which are eventually desorbed as products [16,17]. The isomerization reactions of alkenes are typically catalyzed by acid zeolites at temperatures around 250 °C and at a partial pressure of H_2 of around 1-10 bars [16,17].

The isomerization is classified as type A when it does not lead to any branching degree change (in practice, this corresponds to a direct hydride or 1,n alkyl transfer [18]), or type B when an increase in the branching degree of the chain occurs. These transformations involve non-classical carbonium ions such as protonated cyclopropane (PCP) [9,18–20]. The latter are often invoked for type B isomerization but are also likely to be relevant in the case of type A alkyl-shifts. Type B isomerization reactions are of interest when cracking is aimed at, as higher branching degree is expected to allow the preferential formation of tertiary or secondary carbenium ions (instead of primary ones) favoring easier cracking [9,21]. It is known that type A isomerization is several orders of magnitude faster than type B isomerization [9,16–18,22]. However, the molecular origin of such a ranking is still unknown. Moreover, the intermediate *versus* transition state nature of the PCP is debated for a long time [23]. Earlier static ab initio calculations dealing with zeolites suggest that it should be a transition state [24–29], but the determination of the energy profile was biased by the alkoxide nature of the reactants and products, whereas more recent *ab initio* molecular dynamics showed that, at finite temperature, tertiary carbenium ions exist in significant concentrations [30,31]. Finally, determining accurately the intrinsic free energy barrier for type A and type B isomerization reactions is rather challenging, as the isomerization reactions generally occur simultaneously, and together with hydrogenation-dehydrogenation reactions, plus cracking. Single-event kinetic schemes were successful in fitting experimental data in that respect, and also in reproducing the expected trend according to which type A is faster than type B [32–36]. However, considering the number of adjustable parameters in these models, quantifying the intrinsic free energy barriers for these elementary steps by an independent approach is called for.

Herein, we report a density functional theory (DFT) investigation addressing these issues. We analyze the free energetics of type B isomerization connecting a C_7 dibranched tertiary cation (2,4-dimethyl-pent-2-enium cation) to a tribranched tertiary cation (2,3,3-trimethyl-but-2-enium cation) and we compare the free energy barriers with those of type A isomerization involving the same tribranched tertiary cation (Figure 1). As a model for the catalyst, the acid chabazite zeolite is considered in this work. In the literature, the finite temperature effects are most often introduced via static approach to the transition state theory (TST) consisting of atomic relaxations followed by calculations of harmonic vibrational frequencies, which are subsequently employed in approximate formulae for free energy, enthalpy, and other thermodynamic quantities of interest. Previous theoretical work [37–39], however, demonstrated that such a simple approach can not provide satisfactory results for free energy analysis of hydrocarbon conversions in zeolites. Free energy methods based on molecular dynamics (MD) [30,31,37–47] or Monte Carlo (MC) simulations [48,49], which are designed to study chemical reactions, are free of limitations of the static approach. Due to their high computational cost and a non-trivial realization, the use of these methods in theoretical catalysis is still rather limited. To the best of our knowledge, they were never used for the type A versus type B isomerization of alkenes.

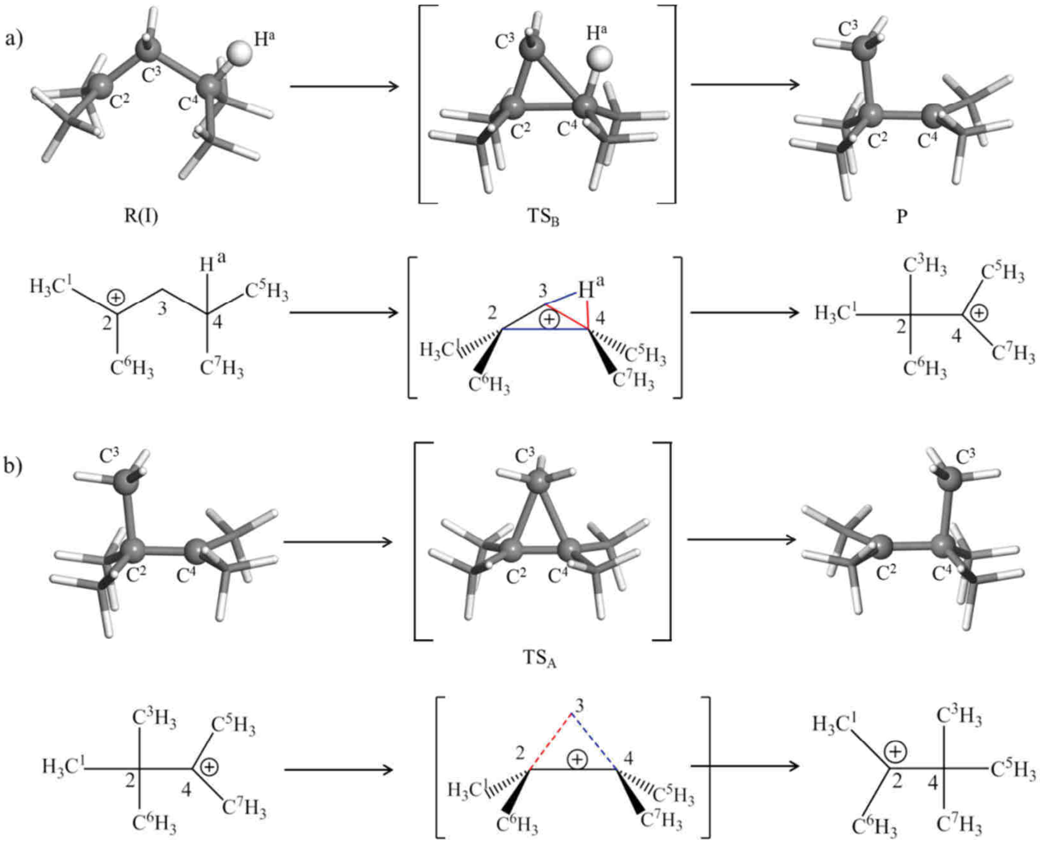

Figure 1. Isomerization reactions: a) type B between 2,4-dimethyl-pent-2-enium cation and 2,3,3-trimethyl-but-2-enium cation, b) type A between two symmetry equivalent 2,3,3-trimethyl-but-2-enium cations. Note that the reactant of reaction b) is identical with the product of reaction a). The ball and sticks structures are optimized in gas phase. The blue and red lines indicate the bonds that are, respectively, formed and broken during the reactions.

We investigate these mechanisms with advanced *ab initio* molecular dynamics methods (blue moon ensemble approach), that we compare with a more traditional static approach. The uncertainty of the latter is estimated by an ensemble of converged simulations describing a large set of stationary points. The treatment of interconversions between rotational isomers, that is largely overlooked in simulations in the literature, appeared to be key for the accurate determination of pathways and free energies: we propose here a rigorous treatment of this problem. We then reach, with aid of ab initio molecular dynamics, a quantification of the intrinsic free energy barriers and an atomistic explanation of the difference between type A and type B isomerization kinetics.

III.2. Methodology

III.2.1. Total energy calculations

Periodic DFT calculations were performed using the VASP code [50,51]. The Kohn-Sham equations have been solved variationally in a plane-wave basis set using the projector augmented-wave (PAW) method of Blöchl [52], as adapted by Kresse and Joubert [53]. The PBE exchange-correlation functional in the generalized gradient approximation proposed by Perdew et al. [54] was used. The D2 correction of Grimme [55] has been applied to account for long-range dispersion interactions that are not treated correctly by local and semilocal density-functional theory. Despite its simplicity, this approach has been shown [56] to improve predictions on structure, energetics, and elastic properties of wide range of materials where dispersion forces play an important role. The PBE+D2 method was also shown to predict reasonable adsorption energies for some of the zeolite-related applications [57]. As a relatively large supercell was employed in calculations (*vide infra*), the Brillouin zone sampling was restricted to the Γ-point. A plane-wave cutoff energy of 400 eV was used in all calculations and the convergence criterion for the electronic self-consistency cycle was set to 10^{-7} eV. In the simulations of cations in the gas phase, the charge neutrality of the simulation cell has been preserved by using a compensating uniform background charge.

III.2.2. Transition state search through the static approach

In order to ensure that the reactant, transition state, and product configurations obtained in atomic relaxations discussed in Sections 3.1 and 3.2 are linked by same reaction coordinate, the following strategy has been applied. In the first step, the first-order saddle point on the potential-energy surface corresponding to the transition state for the reaction of interest was identified using the improved dimer method [58,59]. Subsequently, the intrinsic reaction coordinate [60,61] (IRC) for the forward and backward reaction steps was identified using the damped velocity Verlet algorithm [62]. Next, the terminal points from the IRC calculations were relaxed using a conjugate-gradient algorithm [63]. In all atomic relaxations of minima and saddle points, the structures were considered as relaxed when all forces acting on the atoms were smaller than 0.005 eV/Å. Finally, the vibrational eigenspectrum of relaxed structures has been examined and additional line-minimization calculations along undesired unstable modes have been performed until the computed eigenspectrum contained a correct number of imaginary vibrational frequencies (i.e. zero for stable structures and one for transition states). All relaxations with fixed internal coordinates and a part of the TS optimizations have been performed using the optimization engine GADGET [64,65].

III.2.3. Molecular dynamics simulations

Born Oppenheimer molecular dynamics simulations (MD) have been performed in the (NVT) ensemble. The temperature was controlled with the Andersen thermostat [66] with a collision frequency per atom of 0.01 fs^{-1}. The classical equations of motion were integrated using the leapfrog algorithm with an integration step of 1 fs. The atomic mass of tritium has been chosen for all H atoms in order to avoid possible numerical instabilities due to the use of a relatively large integration step. Free energies have been computed using the simulation protocol described in Ref.

[44] In this approach based on the transition state theory [66,67], the free-energy of activation ($\varDelta A^{\ddagger}$) is defined as follows:

$$\varDelta A^{\ddagger} = \varDelta A_{\xi_{ref,R}\to\xi^{*}} - k_B T \ln\left(\frac{h}{k_B T}\frac{\langle|\dot{\xi}^{*}|\rangle}{2}P(\xi_{ref,R})g_R\right), \tag{1}$$

where $\varDelta A_{\xi_{ref,R}\to\xi^{*}}$ is the reversible work needed to shift the value of reaction coordinate (ξ) from some arbitrary reference value characteristic for reactant ($\xi_{ref,R}$) to the value ξ^{*} defining the free-energy transition state, $\langle|\dot{\xi}^{*}|\rangle$ is the average absolute value of velocity of reaction coordinate at the transition state, $P(\xi_{ref,R}) = \langle\delta(\xi - \xi_{ref})\rangle_R$ is the probability density of the state $\xi_{ref,R}$ in ensemble of all reactant (R) configurations, and g_R is the number of symmetry equivalent choices of $\xi_{ref,R}$ corresponding each to a different stable isomer of reactant. As in Ref. [44], the term $\varDelta A_{\xi_{ref,R}\to\xi^{*}}$ is obtained from the blue moon ensemble method (BM) [68,69] implemented in VASP [70], $P(\xi_{ref,R})$ is determined using the straightforward MD simulations, and $\langle|\dot{\xi}^{*}|\rangle$ is computed numerically using a constrained MD with $\xi(r) = \xi^{*}$. Free energies of reaction ($\varDelta A_{R\to P}$) are computed similarly:

$$\varDelta A_{R\to P} = \varDelta A_{\xi_{ref,R}\to\xi_{ref,P}} - k_B T \ln\left(\frac{g_R P(\xi_{ref,R})}{g_P P(\xi_{ref,P})}\right). \tag{2}$$

In Equation (2), $\varDelta A_{\xi_{ref,R}\to\xi_{ref,P}}$ is the reversible work needed to shift the value ξ from $\xi_{ref,R}$ to some arbitrary reference value $\xi_{ref,P}$ characteristic for product (P), $P(\xi_{ref,P})$ is the probability density of the state $\xi_{ref,P}$ which is, similarly to $P(\xi_{ref,R})$, determined using straightforward MD of the product state, and g_P is the number of symmetry equivalent choices of $\xi_{ref,P}$ corresponding each to a different stable isomer of product. We emphasize that the free energies computed using Equations (1) and (2) are independent of the particular choice of the approximation to the reaction coordinate, provided the approximation drives the transformation from reactant to product reversibly. This property is particularly important when comparing the free energetics of chemical reactions differing in reaction mechanisms and consequently also in definitions of ξ. Our method is very closely related to the Bennett-Chandler approach, which is by design invariant with the CV choice [44,66,67]. One can see from Equations (1) and (2) or related rate and equilibrium constants expressions [44,66] that all these quantities have correct dimensions independent of the CV choice.

Details of calculations of individual terms of Equations (1) and (2) as well as the corresponding numerical values are presented in Sections SI and SII. The length of straightforward MD simulations used to determine probability densities of reference states was at least 100 ps (see Table S.1) while the length of all constrained MD runs performed with the BM simulations was 50 ps. In each MD run, the initial period of 5 ps has been considered as equilibration and the corresponding data were not used in calculations of ensemble averages. Undesired by-reactions, such as the deprotonation of the reactant or product molecules, have been prevented by the use of restraining potentials described in Section SIII.

A slow growth simulation protocol [71] (MD in which a candidate CV is increased at a constant rate) has been employed in a qualitative way to make sure that the candidate CV can indeed drive smoothly the reaction of interest – from the reactant to the product state, as illustrated in Supporting Information SIV. Our choice of the approximation of reaction coordinate (CV) was validated in a number of internal tests (Supporting Information SIV).

III.2.4. Structural Model

A primitive rhombohedral cell of purely siliceous chabazite (CHA framework, symmetry group R$\overline{3}$m), with 12 symmetry equivalent tetrahedral sites, was obtained from International Zeolite Association (IZA) database [72]. The cell was optimized (with a cutoff energy of 800 eV) and the resulting lattice constants a =9.336 Å and α = 94.6° are found to be in a good agreement with the experimental reference values [72] (a = 9.304 Å and α = 94.6°). The relaxed structure was subsequently used to build a supercell defined by the lattice vectors $\mathbf{a}_1'$, $\mathbf{a}_2'$, and $\mathbf{a}_3'$ related to the primitive cell vectors of rhombohedral lattice $(\mathbf{a}_1, \mathbf{a}_2, \mathbf{a}_3)$ via the following transformations: $\mathbf{a}_1' = \mathbf{a}_2 + \mathbf{a}_3$, $\mathbf{a}_2' = \mathbf{a}_1 + \mathbf{a}_3$, and $\mathbf{a}_3' = \mathbf{a}_1 + \mathbf{a}_2$ (Figure 2). The shortest interatomic separation between the atoms in hydrocarbon and the atoms in its periodically repeated images was not shorter than 5.5 Å. We note that for the sake of consistency, the same supercell has been used also in the gas phase simulations. One of the Si atoms (which are all symmetry equivalent) has been substituted by an Al atom introducing thus a negative charge into the zeolite framework. This negative charge can be formally compensated by attaching a proton onto a framework oxygen atom creating thus a Brønsted acid site (BAS). In this work, however, we investigate reactions in which cationic molecular species occur at all stages whereby the positive charge of cations originates from the proton transferred from the BAS to a neutral molecule. For this reason, no particular Brønsted acid site needs to be considered.

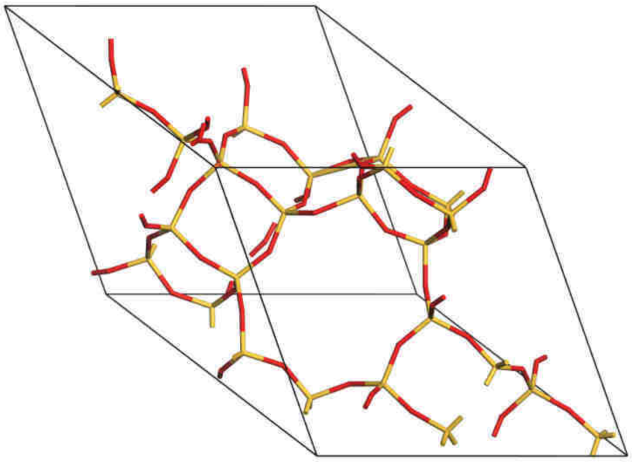

Figure 2. Supercell of chabazite used in simulations. (Si in yellow and O in red).

III.3. Results and discussion

III.3.1. Isomerization mechanisms and question of the reactant / product rotamers: static approach applied to gas phase reactions

We start by analyzing isomerization reactions of type B and A occurring in the gas phase, which represents the simplest realization of both reactions. The results presented here will be used as reference data for more complicated reactions occurring in zeolite (Sections 3.2, 3.3 and 3.4). Note that all stationary states have been obtained using unconstrained relaxations with very stringent relaxation criteria. A particular attention has been paid to ensure correctness of corresponding eigenvalue spectra. Thus all the stationary states representing reactants and products are all correct unconstrained potential energy minima.

The reactant molecule for type B isomerization (2,4-dimethyl-pent-2-enium cation) forms four stable rotational isomers (rotamers) that can be distinguished by measuring the torsional angle H^a-C^4-C^3-C^2 (τ): R(I) with $\tau = 180$ deg., R(III) with $\tau = 0$ deg., and two symmetry equivalent rotamers R(II) with $\tau = \pm 59.1$ deg. The structure of stable rotamers and the numbering of atoms are shown in Figure 3. Potential energy as a function of τ obtained in a series of constrained relaxations is shown in Figure 4. As evident, the most stable rotamer R(II) is 3.4 kJ/mol and 1.1 kJ/mol lower in potential energy compared to the cations R(I) and R(III), respectively. Importantly, however, only the conformation of rotamer R(I) is such that type B isomerization is sterically allowed (see below). Indeed, the hydrogen atom H^a is transferred from C^4 to C^3, while the C^2-C^4 bond is formed and the C^3-C^4 bond is broken in the course of this reaction (Figure 1 and Figure 3). Hence the first step of reaction is a transformation of a generic reactant molecule being in any of its stable rotational isomers into the rotamer R(I). As shown in Figure 4, the potential energy barriers for the transformations R(II) →R(I) and R(II) →R(III) (18.7 kJ/mol and 4.6 kJ/mol, respectively) are relatively small compared to the reaction barrier for type B isomerization (*vide infra*). It is therefore reasonable to expect that all rotamers are always at equilibrium with one another and the probability to find the state R(I) at the fixed temperature, volume, and number of particles (NVT ensemble) is given by the Boltzmann distribution law:

$$p\big(R(I)\big) = \frac{e^{-A(R(I))/k_BT}}{e^{-A(R(I))/k_BT} + 2e^{-A(R(II))/k_BT} + e^{-A(R(III))/k_BT}}, \qquad (3)$$

where $A(i)$ is the Helmhotz free energy of the state i and the factor 2 in the denominator reflects the two-fold degeneracy of the state $R(II)$. Using the usual harmonic oscillator and rigid rotor approximation (hereafter termed as static approach), we obtained the values of 4.6 % and 7.5 % for the term $p\big(R(I)\big)$ at T=300 K and 500 K, respectively. As discussed below, the term $p\big(R(I)\big)$ contributes to the free energy of activation.

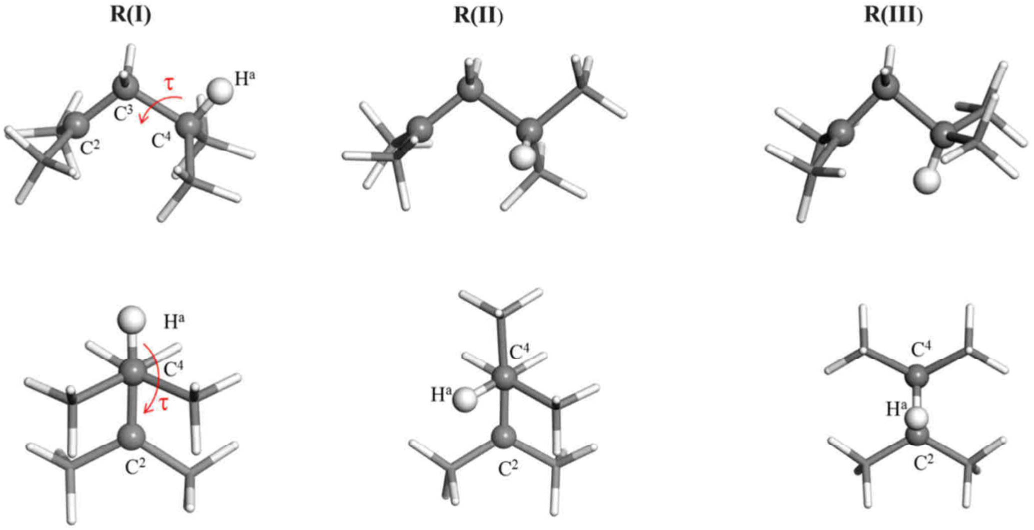

Figure 3. Rotational isomers R(I) (τ = 180 deg.), R(II) ($|\tau|$ = 59.1 deg) and R(III) (τ = 0 deg.) of the reactant 2,4-dimethyl-pent-2-enium cation. Top panel: side view; bottom panels: front view chosen so that the atom C^4 overlaps the atom C^3.

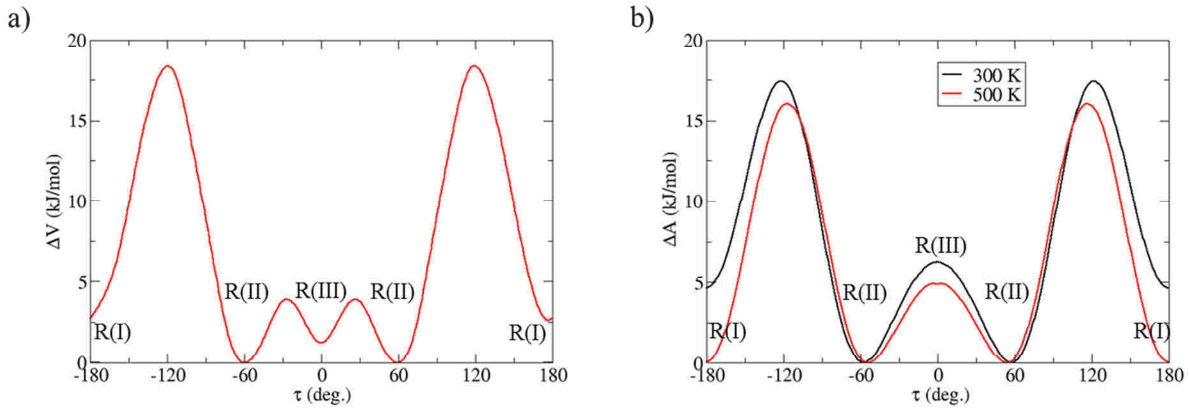

Figure 4. a) Potential energy profile along dihedral angle τ computed for the 2,4-dimethyl-pent-2-enium cation in the gas phase at T = 0 K, and b) free energy profile computed using MD for the same molecule in chabazite at 300 K and 500 K.

The transition state for type B isomerization (TS_B) in the gas phase was identified by the static approach and its structure is shown in Figure 1-a. TS_B is an edge-protonated PCP. In TS_B, the two pairs of methyl groups connected to C^2 and C^4 are face-to-face. By the IRC approach (see movie in supporting information), we show that TS_B is connected to the R(I) rotamer, in which these methyl groups are in the same conformation. Starting from another rotamer (Figure 3) necessary needs to rotate first to generate R(I) then TS_B that are connected. The computed electronic activation energy $\Delta A_{el,R(I)\to TS_B}$ equals 70.4 kJ/mol. The free-energy barrier for type B isomerization in the gas phase defined with respect to a generic reactant state R, consisting of all rotational isomers distributed according to the Boltzmann law, can be computed using the formula:

$$\Delta A_{R\to TS_B} = \Delta A_{R(I)\to TS_B} - k_B Tln\big(p(R(I))g_{R(I)}\big), \tag{4}$$

where the term $\Delta A_{R(I)\to TS_B} = A(TS_B) - A\big(R(I)\big)$, which we designate hereafter as the microprocess barrier, corresponds to the free energy of activation for the reaction starting from the active rotamer R(I), whereas the last term on the right hand side is the correction reflecting the fact that the state R(I) is only one of four possible reactant states. As the state R(I) is non-degenerate, the degeneracy factor $g_{R(I)}$ equals unity. The free energy barrier computed using the static approach $\Delta A_{R\to TS_B}$ increases with temperature as follows: 84.5 kJ/mol (300 K), and 93.4 kJ/mol (500 K). Similarly, the microprocess barriers ($\Delta A_{R(I)\to TS_B}$) computed for T=300 K, and 500 K are 76.8 kJ/mol, and 82.7 kJ/mol, respectively (see Figure 6). Clearly, the correction term $-k_B Tln(p(R(I)))$ is always positive leading to an increase of free-energy barrier. Furthermore, its contribution (of the order of 10 kJ/mol) increases with increasing temperature, which is obvious from the explicit presence of T in this term (the much weaker implicit dependence introduced via Equation (3) tends to decrease

$\Delta A_{R(I)\rightarrow TS_B}$ with increasing T). As shown by Tables S2 and S3, the rise of the microprocess barrier with T is mainly due to the entropic term $-T\Delta S_{R(I)\rightarrow TS_B}$ (in particular its vibrational component), which increases by 7.6 kJ/mol when T is changed from 300 K to 500 K, whereas the internal energy of activation changes only by -1.6 kJ/mol at the same temperature interval. The relatively large negative vibrational entropy of activation follows from the loose reactant and tight transition state picture: compared to the reactant, two new bonds (C^2-C^4 and C^3-H^a) are being formed while the bonds C^3-C^4 and C^4-H^a present also in the reactant are not yet completely broken in TS_B, and hence the PCP transition state structure is geometrically more constrained than the structure of reactant (Figure 1).

The reaction product, the 2,3,3-trimethyl-but-2-enium cation, forms six symmetry equivalent rotational isomers (see Figure S12) separated by a potential energy barrier of 3.0 kJ/mol. The free-energy of reaction R→P writes:

$$\Delta A_{R\rightarrow P} = \Delta A_{R(I)\rightarrow P(i)} - k_B T ln\left(\frac{p\big(R(I)\big)g_{R(I)}}{p\big(P(i)\big)g_{P(i)}}\right). \tag{5}$$

Similar to Equation (4), the term $\Delta A_{R(I)\rightarrow P(i)} = A\big(P(i)\big) - A\big(R(I)\big)$ is the free energy difference between the particular product and reactant configurations *P(i)* and *R(I)*, whereas the last term accounts for the fact that these states are formed with a certain likelihood among all possible product and reactant configurations. We note that the contributions of $p\big(P(i)\big)$ and $g_{P(i)}$ to Equation (5) cancel each other because all rotational isomers of the product states are symmetry equivalent and hence $p\big(P(i)\big) = \frac{1}{g_{P(i)}}$. The computed potential energy for the product cation is 4.4 kJ/mol lower than that of the configuration R(I) and the term $\Delta A_{R(I)\rightarrow P(i)}$ varies with T as follows: -4.9 kJ/mol (300 K), and -5.0 kJ/mol (500 K). The sign and magnitude of $\Delta A_{R(I)\rightarrow P(i)}$ are almost fully determined by the internal energy of reaction (Table S3), whereas the entropy of reaction is negligible (the computed values of $-T\Delta S_{R(I)\rightarrow P(i)}$ are 0.0 kJ/mol at 300 K and 0.6 kJ/mol at 500 K). Taking the configurational term $-k_B T ln(p(R(I)))$ into account, both the sign and the value of $\Delta A_{R\rightarrow P}$ change (2.8 kJ/mol (300 K) and 5.8 kJ/mol (500 K)).

The product of type B isomerization can further undergo type A isomerization reaction. The product of the latter reaction is, in the case considered in this work, chemically identical to the reactant (i.e. 2,3,3-trimethyl-but-2-enium cation), hence the free energy, internal energy, and entropy of reaction are zero by definition. Unlike type B isomerization, the free energy barrier $\Delta A_{P(i)\rightarrow TS_A}$ depends weakly on T (see Table S4), the computed values are 14.7 kJ/mol (300 K), and 16.2 kJ/mol (500 K) (see Figure 6). In this case, the effect of newly formed bond C^3-C^4 in transition state (TS_A) is compensated by a significant weakening of the C^2-C^3 bond, which is elongated to the same length as the newly formed C^3-C^4 (1.84 Å). TS_A is a corner-protonated PCP. Hence the structure of the PCP ring in TSA is not more strongly constrained than the reactant configuration and the tight reactant and loose transition state picture valid for type B isomerization does not apply to type A isomerization. This result explains why the computed entropy of activation takes a relatively small value (the computed values of $-T\Delta S_{P(i)\to TS_A}$ are 1.8 kJ/mol and 4.7 kJ/mol for T=300 K and 500 K, respectively). As all rotamers formed by the reactant (or product) molecule are equivalent by symmetry, the last term in the formula $\Delta A_{P\to TS_A} = \Delta A_{P(i)\to TS_A} - k_B T ln\big(p(P(i))g_{P(i)}\big)$ is zero due to cancellation of terms $p(P(i)$ and $g_{P(i)}$ and hence the free energy of activation is identical to the microprocess free energy barrier.

III.3.2. Static approach applied to reactions in zeolite

Within a zeolite framework, the mechanisms of both isomerization reactions remain the same as in the gas-phase because the atoms of the zeolite framework are not covalently bonded to the intermediates involved. Nevertheless, the electrostatic interaction and dispersion forces between the zeolite and the molecule increase tremendously the complexity of the potential energy surface (PES), which now contains many local stationary points corresponding to structures differing in the orientation and the relative position of the molecule with respect to the zeolite internal surface at each step of the reaction. In this section, we demonstrate that the increased complexity of PES introduces an unacceptably large and hard to control error into the calculations of reaction free-energetics determined via the static approach.

To this end, a set of seven TS configurations has been determined by means of geometric relaxations for both chemical reactions considered in this work, whereby the initial configurations (used for the relaxations) have been obtained from constrained molecular dynamics simulations described in Sections 3.3.3 and 3.4.3. In all cases, TS_A and TS_B remain corner and edge-protonated PCPs respectively (see also later, a detailed structural analysis in sections 3.3.4 and 3.4.4.). We emphasize that our sets of TS configurations are by no means exhaustive – they have been chosen only to highlight the strong limitation of the static approach applied to such complex systems. Upon determining the TS configurations, the reactant and product configurations have been obtained by means of the IRC analysis (see Section 2). The vibrational spectra of all relaxed configurations were carefully checked to ensure that all relaxed structures were correct stationary points of PES.

As shown in Table S5, the potential energies of optimized TS structures for type B isomerization are spread over a very broad range of values, the difference between the highest and the lowest TS energies being as large as 40.2 kJ/mol. This large variation in energy is due to significant differences in the TS orientation and position within the zeolite framework whereas the molecular structure of each TS is rather similar (Table S8). As shown in Figure S13, the potential energy of individual TS configurations correlates rather well with the parameter χ defined as

$$\chi = \sum_{i=1}^{N_C} \frac{1}{[d(Al - C^i)]^6} \tag{6}$$

where $d(Al - C^i)$ is the distance between aluminum atom and the carbon atom i, and the sum is over all carbon atoms in the system (N_C). Taking into account that the framework Al is surrounded by four oxygen atoms with increased negative charge and some of the C atoms bears a partial positive charge, we deduce that the variation of the potential energy of individual TS configurations is mainly attributed to the electrostatic and dispersion interactions between the PCP and the zeolitic framework. The distance C^4–Al in relaxed TS structures, for instance, varies from 3.88 Å to 5.96 Å (the two extreme cases are shown in Figure 5 while all TS structures are shown in Figure S14 and the corresponding data are given in Table S8) indicating that the PCP can be stabilized in many different places of the zeolite micropores.

The variation of vibrational contribution to free energy of TS_B resulting from differences in the low-frequency part of the vibrational spectra (Table S5) are as large as 13.6 kJ/mol (300 K) and 22.6 kJ/mol (500 K). The variation in the total free energy of TS_B configurations is ~40 kJ/mol for both temperatures considered in this work (Table S5), which is very similar to the variation in the potential energy reported above.

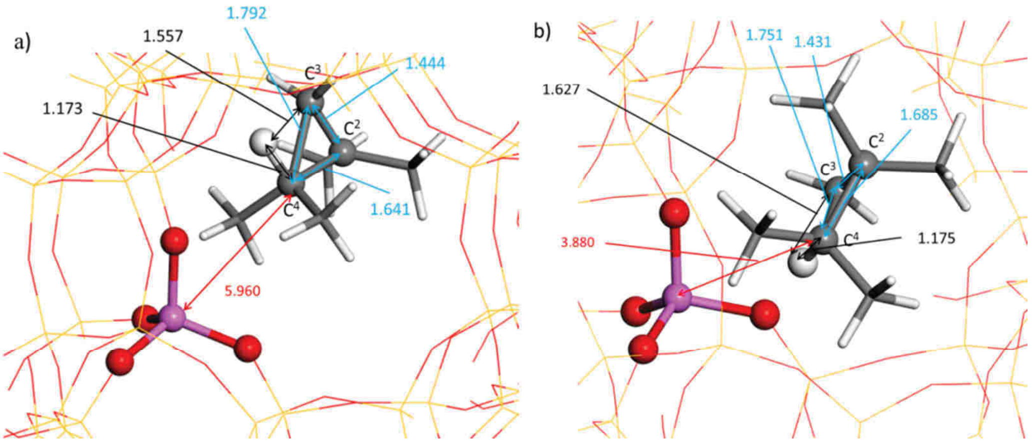

Figure 5. Selected transition state configurations for type B isomerization: relaxed structure with the longest (a) and the shortest (b) separation between atoms C^4 and Al. (Al in purple, H in white, Si in yellow and O in red). Selected interatomic distances are in Å.

Results obtained for type A isomerization (Table S11) show that the variation of potential energy for the relaxed TS_A structures spreads over a narrower interval of width of 11.1 kJ/mol (Table S9). As in the case of TS_B, the electronic energy of the TS_A structures identified in this work correlates rather well with the parameter χ defined above (see Figure S13), albeit the spread of the χ values is much narrower. The latter fact indicates that the variation of orientations and positions of TS_A sampled in our static calculations is much smaller than that for the TS_B configurations. The maximal and minimal vibrational free-energy determined for the TS structures at 300 K and 500 K differ by 13.3 kJ/mol and 20.7 kJ/mol, respectively. The resulting variation in the total free energy of TS_A is 11.8 kJ/mol and 17.4 kJ/mol for T=300 K and 500 K, respectively. Once again, the intramolecular structures of all relaxed reactant and product configurations are found to be rather similar to their gas-phase counterparts (see Figure S15 for the first two configurations and the Table S12 with geometric data of the PCPs) and the variation in the computed potential energy stems almost exclusively from the differences in the position and orientation of the molecule in the zeolite.

All these results have important practical consequence: if only a single static calculation is performed to explore a chemical reaction similar to those studied in this work, as it is often the case in the literature, the uncertainty in the computed free energy of TS_A is of order of 10 kJ/mol (40 kJ/mol for TS_B) and it increases with T.

In practice, however, one is usually interested in relative (e.g. free energies of reaction and activation) rather than in absolute free energies of a given state. Hence the important question is to which extent the above-mentioned uncertainty is reflected into the uncertainty in computed free-energy barriers. In order to address it, the reactant and product configurations linked with the different TS configurations have been determined by means of IRC analysis. The contributions to the total free energies are reported in Tables S7 and S11, and illustrated in Figure 6 for type B and type A isomerization reactions at T=300K. The uncertainty in computed free energy differences is enormous.

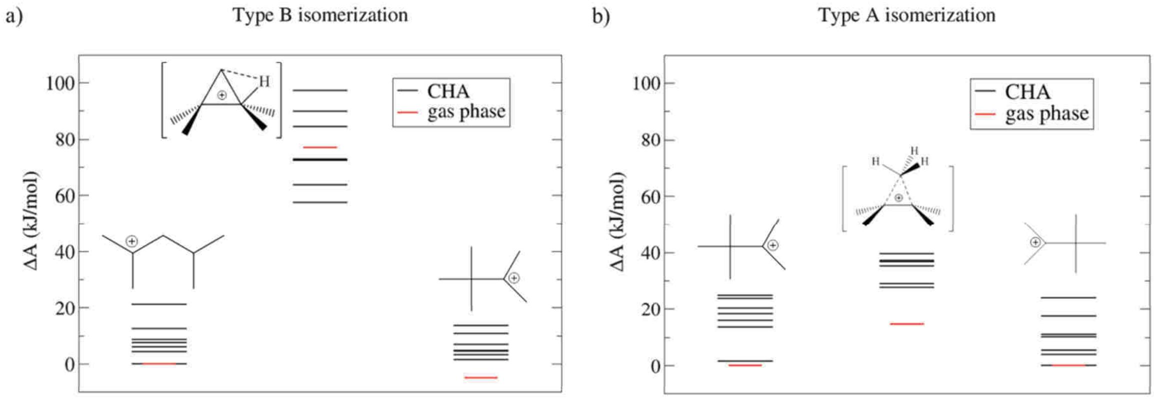

Figure 6. Distribution of free energy values computed in seven independent simulations based on static approach for the microprocess transformation of a) type B and b) type A isomerization reactions in chabazite at T = 300 K . For both reactions, the lowest energy of reactant states defines zero on the free energy scale. For the sake of comparison, the values computed for the reactions in gas phase are also shown.

Depending on the transition state, the microprocess barrier $\Delta A_{R(I)\rightarrow TS_B}$ for the forward mode of type B isomerization ranges between 50.1 kJ/mol to 84.5 kJ/mol at 300 K (76.8 kJ/mol in gas phase, Figure 6) and between 52.5 kJ/mol to 85.7 kJ/mol at 500 K (82.7 kJ/mol in gas phase), respectively (Table S7). The variation in the microprocess barrier for the reverse mode is similar: 46.8 kJ/mol to 92.6 kJ/mol at 300 K (81.7 kJ/mol in gas phase) and 49.5 kJ/mol to 94.0 kJ/mol at 500 K (87.7 kJ/mol in gas phase). The microprocess barrier for type A isomerization varies between 8.7 kJ/mol to 37.2 kJ/mol at 300 K and 5.1 kJ/mol to 42.6 kJ/mol at 500 K, respectively (Table S11). As mentioned in Section 3.1, the reactant and product states of type A isomerization studied in this work are chemically identical, and hence the forward and reverse reaction modes are indistinguishable.

Finally, we point out that the uncertainty in free energy of activation increases further if one does not ensure that all stationary states of reaction are linked by a common IRC, as it is unfortunately often the case in the literature. On basis of our results we estimate that in the most extreme case, the microprocess barrier for the forward reaction mode of type B isomerization at 300 K, for instance, can spread over the interval between 36.4 kJ/mol to 97.2 kJ/mol if the reactant and TS configurations are determined in two independent static calculations.

Altogether, we have shown that the use of the static approach to study isomerization reactions in zeolites is highly problematic. Clearly, in order to overcome the limitations of this approach, one has to efficiently sample the configuration space relevant for the reaction of interest. As we shall discuss in Sections 3.3 and 3.4, this task can be elegantly accomplished by means of molecular dynamics.

III.3.3. Molecular Dynamics of type B isomerization in zeolite

III.3.3.1. Choice of the approximation to the reaction coordinate

The MD method used in this study to determine the free energy of activation (Section 2.3) requires the use of a suitable approximation of the reaction coordinate (ξ), which must be able to reversibly drive the reaction from its initial to the final state. For this purpose, we used a path-based collective variable (ξ) introduced by Branduardi et al. [73], which is defined as follows:

$$\xi = \frac{1}{M-1}\frac{\sum_{i=1}^{M}(i-1)exp(-\lambda|\boldsymbol{q}-\tilde{\boldsymbol{q}}(i)|^2)}{\sum_{i=1}^{M}exp(-\lambda|\boldsymbol{q}-\tilde{\boldsymbol{q}}(i)|^2)}, \tag{7}$$

where $\boldsymbol{q}$ is a multidimensional vector whose components are primitive coordinates describing the changes in the structure of the system during the reaction, $\tilde{\boldsymbol{q}}(i)$ is the position vector (defined in the same primitive coordinate space as $\boldsymbol{q}$) of the i-th point of a discretized reaction path $\{\tilde{\boldsymbol{q}}(i); i = 1, \ldots, M\}, M$ is the total number of points in $\{\tilde{\boldsymbol{q}}(i)\}$, and λ is an adjustable parameter. The neighboring points of $\{\tilde{\boldsymbol{q}}(i)\}$ should be approximately equidistant and the parameter λ should be chosen so as to correspond to the inverse of the average value of $|\tilde{\boldsymbol{q}}(i) - \tilde{\boldsymbol{q}}(i+1)|^2$ [73,74]. By construction, the value of ξ ranges between 0 (reactant) and 1 (product).

As shown in Sections 3.1 and 3.2, the activation energy of type A isomerization is relatively small and hence this reaction can occur spontaneously during the MD simulations of the product configurations of type B isomerization. In order to prevent this undesired process, the coordinate ξ has been defined so as to cover both subsequent isomerization reactions. To this end, the following lengths of the carbon-carbon and carbon-hydrogen bonds involved in type B and A isomerization reactions have been chosen as the primitive coordinates defining $\tilde{\boldsymbol{q}}$ and $\boldsymbol{q}$: C^2-C^3, C^3-C^4, C^2-C^4, C^4-H^a, and C^3-H^a (Figure 3). We note that this choice has been made with type B isomerization in mind and it is not optimal for type A isomerization where the atom H^a plays no special role. The reaction coordinates for both reactions have been approximated by the corresponding IRC determined for the gas-phase reaction discussed in Section 3.1 and merged via the common point corresponding to the product of type B isomerization, which is identical to the reactant of type A isomerization (see Section 3.1). The discretized reaction path $\{\tilde{\boldsymbol{q}}(i)\}$ has been subsequently defined by choosing 20 approximately equidistant points. With this setting, the interval of ξ between 0 and ~0.77 corresponds to type B isomerization while the interval between ~0.77 and 1 covers type A isomerization.

III.3.3.2. Characterization of reactant and product states

As discussed in Section 3.1, out of four rotational isomers of the reactant molecule (2,4-dimethyl-pent-2-enium cation), only the rotamer designated as R(I) can be directly transformed into the transition state for type B isomerization. It is therefore natural to choose a high-likelihood state of the rotamer R(I) as a reference state $(\xi_{ref,R})$ for the use in the free energy calculations (Equation (1)). A direct calculation of the probability density $P(\xi_{ref,R})$ by the straightforward MD would be extremely inefficient due to the relatively high free energy barriers (as compared to k_BT) separating the stable rotational isomers of reactant (Figure 4). In order to circumvent this problem, we express the density of the reference reactant state as follows:

$$P(\xi_{ref,R}) = \tilde{P}(\xi_{ref,R}) \times p(R(I)), \qquad (8)$$

where $\tilde{P}(\xi_{ref,R}) = \langle \delta(\xi - \xi_{ref,R}) \rangle_{R(I)}$ is the probability density of the reference state in the ensemble of all realizations of the state R(I), and $p(R(I)) = \frac{\int_{q \in R(I)} dq dp\, e^{-\frac{H(q,p)}{k_B T}}}{\int_{q \in R} dq dp\, e^{-\frac{H(q,p)}{k_B T}}}$ is the probability of the state R(I) among all reactants states. The two terms of Equation (8) are computed in two different sets of simulations that we discuss below.

The term $p\big(R(I)\big)$ is obtained from the free energy profile $A(\tau)$ computed using the blue moon ensemble method [68,69] whereby the torsional angle τ is defined in Section 3.1. Altogether 10 integration points evenly distributed over the interval $0 \leq \tau < \pi$ have been used and the full profile A(τ) $(-\pi \leq \tau < \pi)$ has been built by employing the symmetry of the molecule dictating the relations $A(-\tau) = A(\tau) = A(\tau + 2\pi)$. As obvious from Figure 4, the finite temperature free energy profiles determined for reactant in chabazite are similar in shape to the zero temperature potential energy profile computed for the reactant in the gas phase. The only qualitative difference is the absence of the shallow minimum at τ=0. As we show in Section SV.1, this interesting variation is caused by the fact that, unlike the isomers R(I) and R(II), the rotamer R(III) (τ=0) is stable only if the skeletal angle C4-C3-C2 (α) is below 100 deg. At increased temperature, however, the thermal motion of atoms leads to an increase in average value of α making the isomer R(III) unstable. Apart from this detail, the calculations predicted the expected trends: an increase in temperature leads to a decrease in free energy differences between minima corresponding to the stable rotamers R(I) and R(II), and the barrier for the R(II)→R(I) transformation (transition states positioned at $\tau_{max,1} \approx -120°$ and $\tau_{max,2} \approx 120°$) decreases with increasing T. The probability of the state R(I) among all reactant configurations, computed using the formula $p\big(R(I)\big) = \frac{\int_{\tau_{max,1}}^{\tau_{max,2}} exp\left(-\frac{A(\tau)}{k_BT}\right)d\tau}{\int_{-\pi}^{\pi} exp\left(-\frac{A(\tau)}{k_BT}\right)d\tau}$, therefore increases from 6.4 % at T=300 K to 27.9 % at 500 K. We note that while the former value is similar to that determined using the static approach for the cation in gas phase (4.6 %), the latter is significantly greater than its static approach gas phase counterpart (7.5 %).

Probability density $\tilde{P}\big(\xi_{ref,R}\big)$ is determined using the straightforward MD of the state R(I). For both simulation temperatures considered in this work, the free energy barriers separating the rotamers R(I) and R(II) are relatively high compared to the k_BT term, which ensures that the transformation R(I)→ R(II) is a slow process occurring only very infrequently on the time scale of our MD simulations. The probability densities computed for T=300 K and 500 K are shown in Section SI. The values determined for the reference state $\xi_{ref,R} = 0.069$ are 23.5 (300 K) and 16.3 (500 K). Finally, we determine the following values of $P\big(\xi_{ref,R}\big)$ using Equation (8): 1.5 (300 K) and 4.5 (500 K).

A similar analysis has been performed also for the product state (2,3,3-trimethyl-but-2-enium cation formed in chabazite). In this case, the calculation was simplified by the fact that all six stable rotational isomers of the product state are equivalent by symmetry (see Section 3.1), and hence the following equality holds: $g_P P\big(\xi_{ref,P}\big) = \langle\delta(\xi - \xi_{ref,P})\rangle_{P(i)}$. Choosing the reference state $\xi_{ref,P} = 0.769$, the calculations based on the straightforward MD performed for the product state led to the following values of $g_P P\big(\xi_{ref,P}\big)$: 17.9 (300 K) and 14.9 (500 K).

III.3.3.3. Free energy calculations

In order to determine the terms $\Delta A_{\xi_{ref,R}\rightarrow\xi^*}$ and $\Delta A_{\xi_{ref,R}\rightarrow\xi_{ref,P}}$ used in calculations of free energies of activation and reaction (see Section 2.3), blue moon ensemble approach [68,69] has been employed. To this end a mesh of 16 integration points has been used corresponding to states distributed between the reference reactant ($\xi_{ref,R}$) and product ($\xi_{ref,P}$) states defined in Section 3.3.2. The free energy profiles $A(\xi)$ computed for T=300 K and 500 K are shown in Figure 7. The free energy transition state ($\xi^* \approx 0.338$) has been identified as the maximum on $A(\xi)$ and the values of the velocity term $|\dot{\xi}^*|$ ($1.75 \cdot 10^{12}$ s^{-1} and $2.29 \cdot 10^{12}$ s^{-1} for T=300 K and 500 K, respectively) have been determined as described in Section SII. The computed contributions of the term $\Delta A_{\xi_{ref,R}\rightarrow\xi^*} = A(\xi^*) - A(\xi_{ref,R})$ to the free energies of activation at 300 K and 500 K are 70.5 (± 3.4) kJ/mol and 80.5 (± 3.6) kJ/mol, respectively (taking into account the standard error on the mean values of the gradients of the free energy, for a confidence interval of 95%). Employing Equation (1) along with the data presented in Section 3.3.2, the free energies of activation of 74.4 (± 3.4) kJ/mol and 83.4 (± 3.6) kJ/mol have been obtained for T=300 K and 500 K, respectively. These values are ~10 kJ/mol lower than those computed using the simple static approach for the reaction in the gas phase discussed in Section 3.2. Such a difference is not unexpected as the latter simulations use a more approximate physical model and completely neglect the interactions between the molecule and zeolite. In this light it is remarkable that both sets of simulations predict almost the same change in the free energy of activation (~9 kJ/mol) due to the increase of T from 300 K to 500 K. This result suggests that the temperature trend in activation energy of this monomolecular reaction is entirely determined by entropy related to the intramolecular vibrations while the contribution of those degrees of freedom related to interactions with zeolite is negligible. This conclusion is even underlined by the similarity in average geometry of transition states identified in MD with the zero temperature TS geometry for the gas phase reaction (see Section 3.3.4), which is consistent with the tight TS and loose reactant picture.

The free energies of reaction computed using Equation (2) for T=300 K and 500 K are 1.9 (± 3.8) kJ/mol and 3.7 (± 4.2) kJ/mol, respectively. These results are, again, in qualitative agreement with predictions made on the basis of the simple static approach for the reaction in the gas phase predicting a negligible change in the free energy of reaction due to the temperature increase from 300 K to 500 K (see Section 3.1).

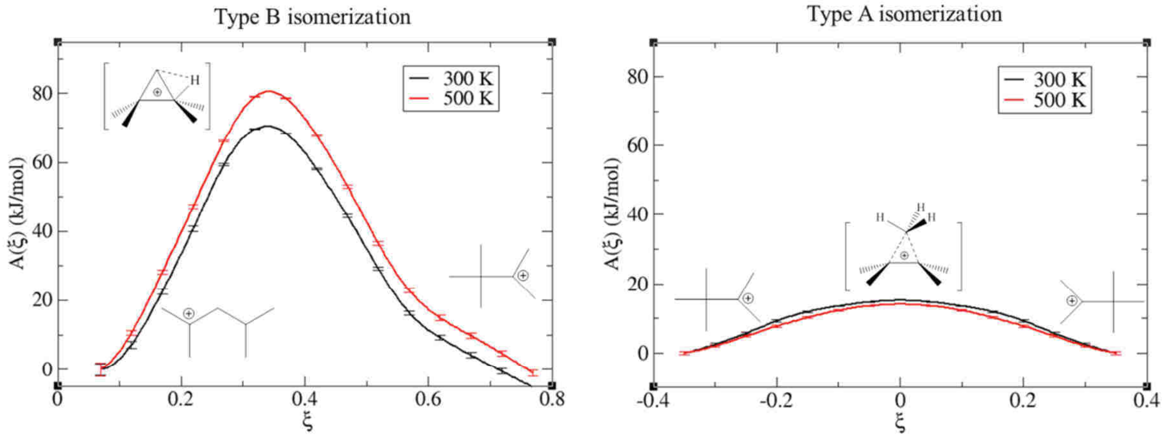

Figure 7. Free energy profiles ($A(\xi)$) computed using the bluemoon ensemble approach for type B (left) and type A (right) isomerization reactions in chabazite at T=300 K and 500 K. The error bars are determined from the standard errors on the free energy gradients [70].

III.3.3.4 Structural analysis of TS_B at finite temperature

a) C-C and C-H bonds

The distribution of the C-C and C-H bonds in the PCP obtained in the MD runs are reported in Figure 8. The C-C and C-H bonds in the TS_B are typical for the constrained edge protonated cyclopropane and their averages are very similar to the values found for TS_B in the gas phase reaction determined in the static approach (see Section SVII).

Furthermore, the relation between the standard deviation of the bond length distribution and its effective force constant [75] allows us to conclude that the bond C^2-C^4 formed during reaction is stronger in transition state than that in reactant, while the other two bonds involved in the PCP formation (C^3-C^4 and C^2-C^3) are comparably strong (see Section SVII.1 and Table S13) and this result is consistent with the tight TS loose reactant picture. The intramolecular geometry of structures optimized in the zeolite are rather similar to the average MD structures and this agreement indicates that the very large difference in energy and free energy between relaxed structures is not due to intramolecular geometric features.

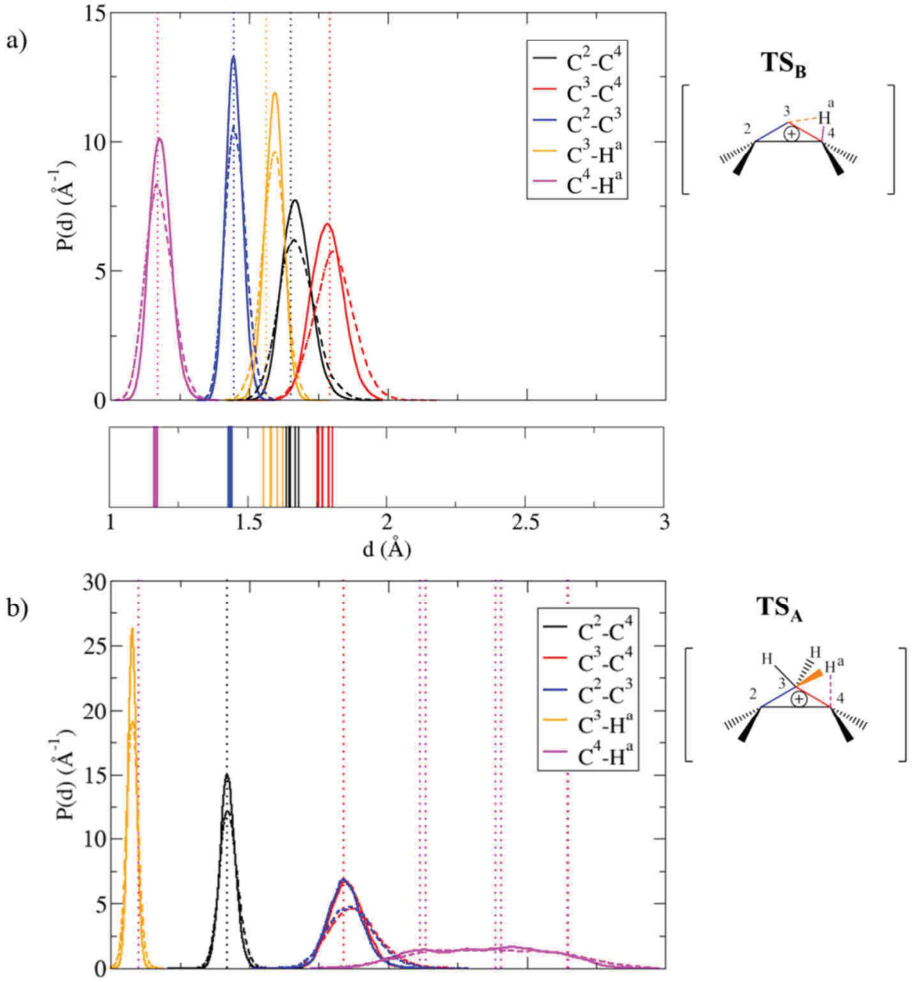

Figure 8. Probability distributions of selected C-C and C-H bond lengths in the transition states of (a) type B isomerization (TS$_B$), and (b) for type A isomerization (TS$_A$) determined using MD at 300 K (solid lines) and 500 K (dashed lines). For the sake of comparison, the static approach results for the gas phase reactions are also indicated by vertical dotted lines. Bottom panels show data determined for the series of static calculations for reactions in chabazite discussed in Section 3.2.

b) Location of TS$_B$ with respect to Al

In Section 3.2 we showed that the electronic energy of transition states correlates with the inverse distances between Al and C atoms (measured via parameter χ), which, in turn reflects the variation in distribution of the molecule within the cavity of zeolite. In the constrained molecular dynamics run of the transition state at 300 K (Figure 9-a), the parameter χ ranges between 0.0005 Å^{-6} and 0.0017 Å^{-6} and the distribution of χ is bimodal with maxima at $2.7\cdot10^{-4}$ Å^{-6} and $7.0\cdot10^{-4}$ Å^{-6}.

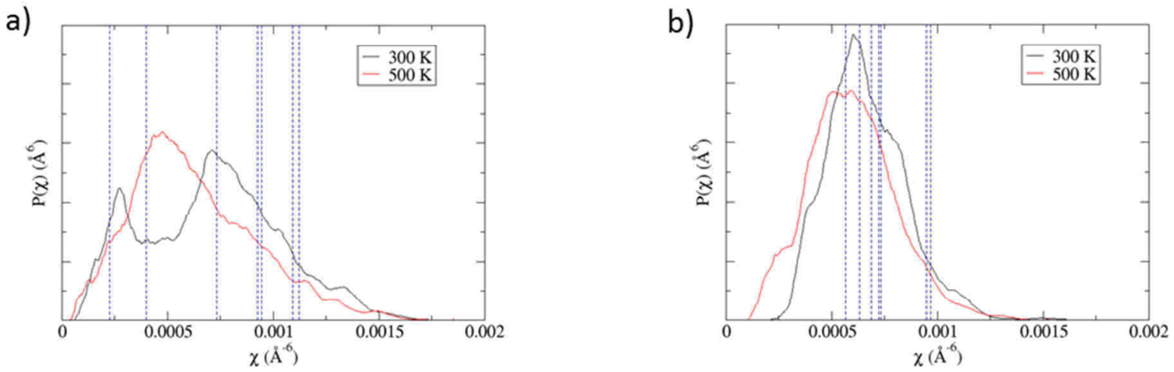

Figure 9. Probability distribution of the sum of inverse distances between the framework Al and all C atoms raised to the power of six (χ) determined for the transition state of type B (a) and type A (b) isomerization in chabazite determined using MD at T = 300 K and 500 K. For the sake of comparison, the static approach results for the reaction in chabazite are indicated by vertical dashed lines.

The various TS_B determined in the series of static calculations are located fall into different parts of this distribution. At 500 K, the shape of the distribution changes and the dominant peak is shifted towards longer distances (i.e. smaller χ). Obviously, such an effect cannot be taken into account using a simple static approach based on the harmonic approximation because the potential energy minimum structure is always the most likely configuration regardless of temperature.

III.3.4. Free energy calculations for type A isomerization reaction

III.3.4.1. Choice of the approximation to the reaction coordinate

As described in Section 3.3.1, the parameter ξ used in free energy calculations of type B isomerization has been constructed so as to cover also type A isomerization but the only purpose of such a choice was to prevent the uncontrolled transformation of the product configuration. Unfortunately, this approximation of reaction coordinate is not suitable for calculations related to type A isomerization because it involves two C-H distances defined for a specific hydrogen atom (H^a) which plays no particular role in this reaction. The undesired consequence is that any rotation of the CH_3 group containing H^a would be artificially hindered. In order to avoid such problems, we use for type A isomerization the following approximation of reaction coordinate which is defined only via positions of carbon atoms, and it is invariant with respect to the interchange of CH_3 groups attached to the same central carbon atom:

$$\xi = \eta(C^2) - \eta(C^4), \tag{9}$$

where $\eta(C^i)$ is the coordination number [76] of central carbon atom C^i with respect to the carbon atoms C^1, $C^3, C^5, C^6,$ and C^7 (the numbering of atoms is as in Figure 1-b), which we defined as follows:

$$\eta(C^i) = \sum_{j=1,3,5,6,7} \frac{1-\left(\frac{d(C^i-C^j)}{d_{ref}}\right)^9}{1-\left(\frac{d(C^i-C^j)}{d_{ref}}\right)^{14}} \tag{10}$$

with $d_{ref} = 1.7$ Å being the reference length for the C-C bond. During type A isomerization, the reaction coordinate varies in the interval between –0.4 to 0.4 and $\xi^* = 0$ by symmetry.

III.3.4.2. Characterization of reactant and product states

As explained in Section 3.1, the reactant and product of type A isomerization are symmetry equivalent. Because both states are equivalent to the product of type B isomerization, we employ in this section the labeling used in Section 3.3 and designate the reactant/product states of type A isomerization as P. The chosen reference state $\xi_{ref,P} = -0.35$ (see Equation (1)) corresponds to a high-likelihood state in the free MD runs at both temperatures considered in this study (see Figure S3). As the potential energy barrier for the transformation between the six symmetry equivalent rotational isomers is only 3.0 kJ/mol (see Section 3.1), straightforward MD simulations can be used to determine the probability density of the reference state. The values of $\tilde{P}(\xi_{ref,P}) = g_P P(\xi_{ref,P})$ computed for T=300 K and 500 K are 2.45 and 2.25, respectively.

III.3.4.3. Free energy calculations

As in Section 3.3.3, the blue moon ensemble approach [68,69] has been used to determine the term $\Delta A_{\xi_{ref,P}\rightarrow\xi_A^*}$. In our calculations, a mesh of eight integration points corresponding to states distributed between the reference reactant ($\xi_{ref,P} = -0.35$) and the transition states ($\xi_A^* = 0$) has been used. The full free energy profiles $A(\xi)$ computed for T=300 K and 500 K (Figure 7) have been subsequently obtained by making use of the symmetry of the problem ($A(-\xi) = A(\xi)$), which follows from the fact that the reactant and the product molecules are symmetry equivalent. The values of the velocity term $|\dot{\xi}^*|$ ($5.68\ 10^{12}$ s^{-1} and $7.34\ 10^{12}$ s^{-1} for T=300 K and 500 K, respectively) have been determined as described in Section SII. The computed contributions of the term $\Delta A_{\xi_{ref,P}\rightarrow\xi^*} = A(\xi^*) - A(\xi_{ref,P})$ to the free energies of activation of type A isomerization at 300 K and 500 K are 15.1 (± 0.8) kJ/mol and 14.0 (± 0.9) kJ/mol, respectively. Combined with the data presented in Section 3.4.2, the free energies of activation computed using Equation (1) are 14.9 (± 0.8) kJ/mol and 15.0 (± 0.9) kJ/mol for T=300 K and 500 K, respectively. Hence, the free energy of activation for type A isomerization is, according to our simulations, basically independent on temperature, which is in agreement with the conclusion made in Section 3.1, where a simple static approach for the reaction in the gas phase was discussed.

III.3.4.4 Structural analysis of TS_A at finite temperature

a) C-C and C-H bonds

The analysis of the distributions of the C^2-C^3 and C^3-C^4 bonds shows that they are both significantly looser than the chemical bond C^2-C^4, which is comparably strong as the C-C bonds in the reactant (see Figure 8-b and Section SVII.2 and Table S13). Moreover, visual inspection of the MD structures reveals that the methyl group shifted during the reaction freely rotates (unlike the CH_3 group formed during type B isomerization). This is clearly illustrated in Figure 8-b, where a narrow distribution of the C^3-H^a bond centered at a typical bonding distance (~1.1 Å) is found while the distribution for the non-bonding C^4-H^a distance is very broad because of rotations of the methyl group shifted during the reaction. This analysis confirms that the transition state for type A isomerization, of corner-protonated PCP nature, is much less constrained than that for type B isomerization, of edge-protonated nature. Altogether, despite the apparent similarity in TS structures of type A and B isomerization reactions (both TS are usually represented by very similar schemes in chemical textbooks), both structures differ in the strength of C-C bonds which are formed or broken, and in the specific role of the H transfer in TS_B, which in turn leads to significant differences in free energy of activation and in the thermal dependence of the latter.

b) Location of TS_A with respect to Al

As in the case of type B isomerization, we explore the distribution of the TS_A within the zeolite cavity by analyzing the parameter χ (see Section 3.2). As shown in Figure 9-b, χ varies between $1.4 \cdot 10^{-4}$ Å^{-6} and $1.4 \cdot 10^{-3}$ Å^{-6} and the distribution shows one dominant maximum which is shifted towards smaller χ with increased T ($6.1 \cdot 10^{-4}$ Å^{-6} (300 K) and $5.5 \cdot 10^{-4}$ Å^{-6} (500 K)). As evident from Figure 9-b, most of the first order saddle points on the PES determined in our static calculations (see Section 3.2) are located close to the maximum. While our static transition state search identified two configurations corresponding to TS_A with significantly larger than average χ (i.e. with shorter than average effective distances between Al and C atoms), no configuration from the region $\chi < 5 \cdot 10^{-4}$ Å^{-6} has been found (see Figure 9-b). The fact that the latter region is populated mainly at high T points once again at the systematic failure of the naïve static approach to account for non-trivial thermal effects.

III.3.5. On the atomic origin of the different kinetics of type A versus type B isomerization reactions in zeolites

Somewhat surprisingly at first sight, the results obtained using the sophisticated and time-consuming MD simulations are in qualitative and even semi-quantitative agreement with the calculations performed using the static approach for the gas phase reactions. Indeed, the latter set of calculations predicted the correct thermal trends for free energies of activation and of reaction for both temperatures, although the numerical values are overestimated by up to 16 %. Such a qualitative agreement is possible because of the following reasons: (i) the effect of interactions of molecule with CHA zeolite on reaction barriers is only modest, and (ii) the approximations used in the static approach are reasonable when applied to relatively small gas phase molecules. The point (i) can be understood because the CHA zeolite does not directly participate in chemical reactions analyzed in this work, and the nature of interaction between the CHA zeolite and the molecule does not change during the chemical reaction. Thus, confinement effect is roughly the same for the reactants, the transition states and the products in the case we are investigating. Note however that shifting from the CHA zeolite (used here) to another framework, or from one kind of channel/cage to another one contained within the same zeolite, the extent of the confinement effect is expected to change [77], likely altering the catalytic performance. In particular, in the case of smaller cages or channels (such as ZSM-22 for example, mono-dimensional 10 MR framework), one may expect a differentiation of the zeolite/cation interactions depending on subtle steric constraint changes, such as the one taking place in the course of the reactant → transition state → product transformation. Similar differentiation may occur in the case of bulkier reactants as compared to the C_7 molecules considered here. The point (ii) follows from the fact that the harmonic oscillator model used in the static approach performs rather well when describing vibrations of the intramolecular degrees of freedom [78,79]. Furthermore, the size and shape of the large CHA cavity where the reaction takes place restricts only very weakly the molecular rotations in our case, and this modest restriction is similar for all stages of reaction. Hence also the rotational contribution to free energy differences predicted by the gas phase model is reasonable. Finally, the translational contribution computed using the static approach for a gas phase molecule depends only on the molecular mass and the volume available for the motion [80]. As both of these quantities are constant in the case of the monomolecular reaction at the NVT conditions, the contribution of translational degrees of freedom to the relative free energetics of a monomolecular gas phase reaction must vanish. In the case of reaction in zeolite, the volume available for the translation motion of molecule remains approximately constant during the reaction. Because also the nature of interaction between the molecule and zeolite remains essentially unaltered, the contribution of translational degrees of freedom also largely vanishes in the MD based calculations of free energy differences for a monomolecular reaction in zeolite. In contrast, an attempt to describe hindered rotations and translations of a molecule in zeolite by harmonic oscillator model, as it is done when using the static approach in zeolite, necessarily fails because of large contribution of low frequency vibrational modes to free energy and because of complexity of underlying potential energy surface [30,31,37,47].

In our in-depth analysis of this problem, we considered for the first time all components contributing to free energy of activation. We have shown that the very large uncertainties in free energies of individual states, which are in the case of type B isomerization as large as 40 kJ/mol, do not cancel significantly even when the corresponding stationary points are carefully chosen so as to be linked by a common intrinsic reaction coordinate. The uncertainty in computed free energy of activation can increase further if the minima and TS configurations are obtained in independent relaxations, as it is often the case in literature. For instance, the computed free energy barrier for the forward mode of type B isomerization spreads over the interval between 36.4 kJ/mol to 97.3 kJ/mol. Counterintuitively, therefore, a gas phase model is indeed likely to provide more reliable results than a periodic model involving zeolite when the static approach is applied to a monomolecular reaction.

The qualitatively correct static gas phase model of type A and B isomerization reactions can be utilized in the interpretation of our MD results. Already from electronic activation energies in gas phase static calculations (ΔA_{el} in table S3 and S4, 70.4 and 13.7 kJ.mol^{-1} for type B and A isomerization reactions, respectively), the slower rate of type B isomerization with respect to type A isomerization can be deduced. The lower stability of TS_B can be intuitively understood because a larger number of chemical bonds is formed or broken in type B (C^2-C^4, C^3-C^4, H^a-C^3, and H^a-C^4) than in type A (C^3-C^2, C^3-C^4) isomerization and all those bonds are significantly stretched in TS_B structures compared to the corresponding bond lengths in reactant or product states, see Figure 1.

In the case of type B isomerization, the thermal dependence of free energy of activation is almost exclusively due to the difference in intramolecular contribution to vibrational entropy between reactant and transition state, which is an edge protonated cyclopropane. Such a result is again a consequence of the fact that the atomic motions in transition state are more constrained than those in reactant because a large number of strong chemical bonds are formed or broken in TS_B. In the case of type A isomerization, the entropy of activation nearly vanishes which results in a very small variation of the free energy of activation with temperature. In contrast to type B isomerization, the transition state for type A isomerization (a corner protonated cyclopropane) is not significantly more constrained than the reactant because the shifted CH_3 group is bound to the rest of molecule (similar to neutral 2,3-dimethyl but-2-ene) by only very loose bonds, which is evident also from the analysis of the MD data (see Sections 3.3.4 and 3.4.4).

In the end, the edge position of the H^a in TS_B (edge-protonated PCP) has both energetic and entropic consequences, causing its lower stability (despite independent stronger bonds, as probed by the vibrational analysis) compared to less constrained TS_A. This is the atomic origin of the much higher rate constants found in single-event kinetic models fitted for type A isomerization with respect to type B isomerization [9,16,17].

III.4. Conclusion

In this work, a comprehensive ab initio investigation of isomerization reactions of 2,4-dimethyl-pent-2-enium and 2,3,3-trimethyl-but-2-enium cations in chabazite is reported, which provides atomic scale interpretation of the kinetic differences between type A and type B isomerization of alkenes. A proper quantification of the respective free energy barriers of type A and type B isomerization elementary steps is given for the first time by ab initio calculations, and the differences in terms of rate constants is related to structure of the transition states.

Accurate free energy calculations have been performed by means of molecular dynamics in combination with blue moon ensemble approach [68,69]. The problem with non-ergodic sampling of reactant state due to slow transformation between individual rotational isomers, often overlooked in literature, has been addressed. In the case of type B isomerization, this problem is particularly serious since only one of three symmetrically non-equivalent rotamers can directly undergo the atomic rearrangement associated with this chemical reaction. In this work we proposed and applied a simple solution consisting in explicit sampling of the slow skeletal rotation by the blue moon ensemble approach (other techniques designed to study rare events, such as metadynamics or umbrella sampling, could be used as well [44,81]). The resulting free energy profile is then used to determine the likelihood of the active rotamer among all reactant configurations, which, in combination with the probability density of an arbitrarily chosen reference state of the active rotamer, allows for the determination of the corresponding contribution to free energy changes defined with respect to a generic reactant state.

The free energies of activation and reaction computed using MD for type B isomerization at T=300 K are 74.4 kJ/mol and 1.9 kJ/mol, respectively. Increasing temperature to 500 K, which is closer to the conditions relevant for hydrocarbon transformations in zeolite [9,17], the free energy barrier increases to 83.4 kJ/mol, while the free energy of reaction changes only negligibly (3.7 kJ/mol). For type A isomerization, the free energy of activation determined for T=300 K is significantly lower than that for type B isomerization and its numerical value changes only negligibly with T (15.1 kJ/mol (300 K) and 14.0 kJ/mol (500 K)). The corresponding kinetic constants determined via the Eyring equation [82] are reported in Scheme 1. Such rate constants, which are compatible in order of magnitude with the rate constants of similar compounds in superacid media[17], are likely to be representative of C_7 type A and B isomerization of alkenes between two tertiary carbenium ions.

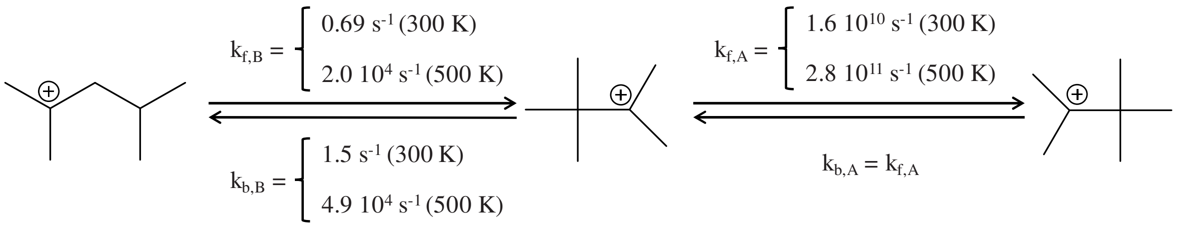

Scheme 1. Kinetic constants at 300 K and 500 K for type B and A isomerization reactions.

The former result is consistent with the experimental observation that the measured reaction rate for type A isomerization is several orders of magnitude higher than that for type B isomerization [9,16,17]. As type A isomerization considered in this work leads to formation of product that is symmetry equivalent to reactant, the free energy of reaction is, by definition, zero at all temperatures.

A static calculation analysis appeared to be irrelevant when performed in the zeolite, due to the many stable configurations of different energies that can be found, but insightful when performed for gas phase reactions. Confinement effects indeed appeared to be comparable for the reactants, the transition states and products in our case. The origin of the difference in rate for type A versus type B isomerization reactions was identified on the basis of our calculations: the transition state TS_A (a corner protonated PCP) has a loose structure, with two large C-C bounds at the PCP, and free rotation of the moving methyl group, whereas TS_B (an edge-protonated PCP) is much tighter due to the bridging hydrogen atom, and to the many bonds that are formed or broken at this elementary step.

The simulation protocol developed within this work represents a powerful tool for the investigation of isomerization reactions of alkenes in acidic zeolites and it is currently used to elucidate the more complex mechanisms involving short-lived secondary carbenium ions obtained from proton transfer from zeolite to alkenes. Moreover, the comparison of the transformations of linear to mono-branched, then to di-branched carbenium ions, in comparison with the present di-branched to tri-branched conversion, would be useful to get a more complete view of the full isomerization reaction network. Notably, going beyond DFT may be needed to reach chemical accuracy when describing non-classical species such as the PCP transition states. This was shown for several reactions involving carbenium and carbonium, up to the coupled-cluster level [83–86]. Transposing these approaches to alkene isomerization is a clear perspective to the present work. However, combining this level of calculation with the MD approach is currently prohibitive, so that the problem of the identification by static calculations of ensemble of configurations in the zeolite and ensemble of rotamers for each state in the zeolite needs to be addressed.

References

[1] J. Rey, A. Gomez, P. Raybaud, C. Chizallet, T. Bučko, J. Catal. 373 (2019) 361–373.
[2] T. Li, K.D. Janda, R.A. Lerner, Nature 379 (1996) 326–327.
[3] W.O. Haag, R.M. Lago, P.B. Weisz, Nature 309 (1984) 589–591.
[4] G.A. Olah, Science 168 (1970) 1298–1311.
[5] J.-I. Yoshida, A. Shimizu, R. Hayashi, Chem. Rev. 118 (2018) 4702–4730.
[6] G.A. Olah, Angew. Chem. Int. Ed. Engl. 34 (1995) 1393–1405.
[7] G.A. Olah, J. Am. Chem. Soc. 94 (1972) 808–820.
[8] J. Zečević, G. Vanbutsele, K.P. de Jong, J.A. Martens, Nature 528 (2015) 245–248.
[9] C. Marcilly, Acido-Basic Catalysis: Application to Refining and Petrochemistry, Technip, 2005.
[10] E. Gutierrez-Acebo, C. Leroux, C. Chizallet, Y. Schuurman, C. Bouchy, ACS Catal. 8 (2018) 6035–6046.
[11] J.A. Martens, D. Verboekend, K. Thomas, G. Vanbutsele, J.-P. Gilson, J. Pérez-Ramírez, ChemSusChem 6 (2013) 421–425.
[12] P.A. Jacobs, M. Dusselier, B.F. Sels, Angew. Chem. Int. Ed. 53 (2014) 8621–8626.
[13] D.-P. Phan, E. Lee, Catalysts 8 (2018) 131.
[14] C. Marcilly, J. Catal. 216 (2003) 47–62.
[15] W. Vermeiren, J.-P. Gilson, Top. Catal. 52 (2009) 1131–1161.
[16] C. Bouchy, G. Hastoy, E. Guillon, J.A. Martens, Oil Gas Sci. Technol. – Rev. IFP Energies nouvelles 64 (2009) 91–112.
[17] J. Weitkamp, ChemCatChem 4 (2012) 292–306.
[18] D.M. Brouwer, Hogeven H., Prog. Phys. Org. Chem. 9 (1972) 179–240.
[19] J. Weitkamp, Ind. Eng. Chem. Prod. Res. Dev. 21 (1982) 550–558.
[20] D.M. Brouwer, J.M. Oelderik, Recl. Trav. Chim. Pays-Bas 87 (1968) 721–736.
[21] P. Raybaud, A. Patrigeon, H. Toulhoat, J. Catal. 197 (2001) 98–112.
[22] Ester Gutierrez-Acebo, J. Rey, C. Bouchy, Y. Schuurman, C. Chizallet, ACS Catal. 9 (2019) 1692–1704.
[23] J.D. Petke, J.L. Whitten, J. Am. Chem. Soc. 90 (1968) 3338–3343.
[24] C. Wattanakit, S. Nokbin, B. Boekfa, P. Pantu, J. Limtrakul, J. Phys. Chem. C 116 (2012) 5654–5663.
[25] M.V. Frash, V.B. Kazansky, A.M. Rigby, R.A. van Santen, J. Phys. Chem. B 101 (1997) 5346–5351.
[26] T. Demuth, X. Rozanska, Benco, L.: Hafner, J., R.A. van Santen, H. Toulhoat, J. Catal. 214 (2003) 68–77.
[27] B. Huang, P. Bai, M. Neurock, R.J. Davis, Appl. Catal. A-Gen. 546 (2017) 149–158.
[28] M.A. Natal-Santiago, R. Alcalá, J.A. Dumesic, J. Catal. 181 (1999) 124–144.
[29] V.B. Kazansky, I.N. Senchenya, J. Catal. 119 (1989) 108–120.
[30] J. Hajek, J. van der Mynsbrugge, K. de Wispelaere, P. Cnudde, L. Vanduyfhuys, M. Waroquier, V. van Speybroeck, J. Catal. 340 (2016) 227–235.
[31] P. Cnudde, K. de Wispelaere, J. van der Mynsbrugge, M. Waroquier, V. van Speybroeck, J. Catal. 345 (2017) 53–69.
[32] J.W. Thybaut, L.C.S. Narasimhan, G.B. Marin, J.F.M. Denayer, G.V. Baron, P.A. Jacobs, J.A. Martens, Catal. Lett. 94 (2004) 81–88.
[33] G.G. Martens, G.B. Marin, J.A. Martens, P.A. Jacobs, G.V. Baron, J. Catal. 195 (2000) 253–267.
[34] L.P. de Oliveira, D. Hudebine, D. Guillaume, J.J. Verstraete, J.F. Joly, Oil Gas Sci. Technol. – Rev. IFP Energies nouvelles 71 (2016) 45.
[35] B.D. Vandegehuchte, J.W. Thybaut, G.B. Marin, Ind. Eng. Chem. Res. 53 (2014) 15333–15347.
[36] B.D. Vandegehuchte, J.W. Thybaut, A. Martínez, M.A. Arribas, G.B. Marin, Appl. Catal. A-Gen. 441-442 (2012) 10–20.

[37] T. Bučko, L. Benco, J. Hafner, J.G. Ángyán, J. Catal. 279 (2011) 220–228.
[38] V. van Speybroeck, K. de Wispelaere, J. van der Mynsbrugge, M. Vandichel, K. Hemelsoet, M. Waroquier, Chem. Soc. Rev. 43 (2014) 7326–7357.
[39] P. Cnudde, K. de Wispelaere, L. Vanduyfhuys, R. Demuynck, J. van der Mynsbrugge, M. Waroquier, V. van Speybroeck, ACS Catal. 8 (2018) 9579–9595.
[40] T. Bučko, L. Benco, J. Hafner, J.G. Ángyán, J. Catal. 250 (2007) 171–183.
[41] T. Bučko, L. Benco, O. Dubay, C. Dellago, J. Hafner, J. Chem. Phys. 131 (2009) 214508.
[42] T. Bučko, J. Hafner, J. Phys-Condens. Matter 22 (2010) 384201.
[43] T. Bučko, J. Hafner, J. Catal. 329 (2015) 32–48.
[44] T. Bučko, S. Chibani, J.-F. Paul, L. Cantrel, M. Badawi, Phys. Chem. Chem. Phys. 19 (2017) 27530–27543.
[45] S.L.C. Moors, K. de Wispelaere, J. van der Mynsbrugge, M. Waroquier, V. van Speybroeck, ACS Catal. 3 (2013) 2556–2567.
[46] J. van der Mynsbrugge, A. Janda, S. Mallikarjun Sharada, L.-C. Lin, V. van Speybroeck, M. Head-Gordon, A.T. Bell, ACS Catal. 7 (2017) 2685–2697.
[47] V. van Speybroeck, K. Hemelsoet, L. Joos, M. Waroquier, R.G. Bell, C.R.A. Catlow, Chem. Soc. Rev. 44 (2015) 7044–7111.
[48] A. Janda, B. Vlaisavljevich, L.-C. Lin, S. Mallikarjun Sharada, B. Smit, M. Head-Gordon, A.T. Bell, J. Phys. Chem. C 119 (2015) 10427–10438.
[49] A. Janda, B. Vlaisavljevich, B. Smit, L.-C. Lin, A.T. Bell, J. Phys. Chem. C 121 (2017) 1618–1638.
[50] G. Kresse, J. Hafner, Phys. Rev. B 47 (1993) 558–561.
[51] G. Kresse, J. Hafner, Phys. Rev. B 49 (1994) 14251–14269.
[52] P.E. Blöchl, Phys. Rev. B 50 (1994) 17953–17979.
[53] G. Kresse, D. Joubert, Phys. Rev. B 59 (1999) 1758–1775.
[54] J.P. Perdew, K. Burke, M. Ernzerhof, Phys. Rev. Lett. 77 (1996) 3865–3868.
[55] S. Grimme, J. Comput. Chem. 27 (2006) 1787–1799.
[56] T. Bučko, J. Hafner, S. Lebègue, J.G. Ángyán, J. Phys. Chem. A 114 (2010) 11814–11824.
[57] F. Göltl, A. Grüneis, T. Bučko, J. Hafner, J. Chem. Phys. 137 (2012) 114111.
[58] G. Henkelman, H. Jónsson, J. Chem. Phys. 111 (1999) 7010.
[59] A. Heyden, A.T. Bell, F.J. Keil, J. Chem. Phys. 123 (2005) 224101.
[60] K. Fukui, J. Phys. Chem. 74 (1970) 4161–4163.
[61] K. Fukui, Accounts Chem. Res. 14 (1981) 363–368.
[62] H.P. Hratchian, H.B. Schlegel, J. Phys. Chem. A 106 (2002) 165–169.
[63] W.H. Press, S.A. Teukolsky, W.T. Vetterling, B.P. Flannery, Numerical Recipes in FORTRAN (2Nd Ed.): The Art of Scientific Computing, Cambridge University Press, New York, NY, USA, 1992.
[64] T. Bučko, J. Hafner, J.G. Angyán, J. Chem. Phys. 122 (2005) 124508.
[65] T. Bučko, Theor. Chem. Acc. 137 (2018) 164.
[66] D. Frenkel, B. Smit, Understanding Molecular Simulation: From Algorithms to Applications, Academic Press, 2002.
[67] N.E. Henriksen, F.Y. Hansen, Theories of Molecular Reaction Dynamics: The Microscopic Foundation of Chemical Kinetics, Oxford University Press, 2008.
[68] E.A. Carter, G. Ciccotti, J.T. Hynes, R. Kapral, Chem. Phys. Lett. 156 (1989) 472–477.
[69] G. Ciccotti, M. Sprik, J. Chem. Phys. 109 (1998) 7737–7744.
[70] T. Bučko, J. Phys. Condens. Matter. 20 (2008) 64211.
[71] T.K. Woo, Magl, Peter M.,Blöchl, Peter E., T. Ziegler, J. Phys. Chem. B 101 (1997) 7877–7880.
[72] C. Baerlocher, J.K. McCusker, International Zeolite Association, http://www.iza-structure.org/databases/, 2017.
[73] D. Branduardi, F.L. Gervasio, M. Parrinello, J. Chem. Phys. 126 (2007) 54103.

[74] G. Bussi, D. Branduardi, Free-Energy Calculations with Metadynamics: Theory and Practice, Wiley, Hoboken, 2015.

[75] R. Baron, W.F. van Gunsteren, P.H. Hünenberger, Trends Phys. Chem. 11 (2006) 87–122.

[76] M. Iannuzzi, A. Laio, M. Parrinello, Phys. Rev. Lett. 90 (2003) 238302.

[77] H. Toulhoat, P. Raybaud, E. Benazzi, J. Catal. 221 (2004) 500–509.

[78] A.D. Boese, J.M.L. Martin, The Journal of chemical physics 121 (2004) 3405–3416.

[79] S. Parthiban, J.M.L. Martin, J. Chem. Phys. 114 (2001) 6014–6029.

[80] F. Jensen, Introduction to computational chemistry: Second Edition, 2nd ed., John Wiley & Sons, Chichester England, Hoboken NJ, 2007.

[81] L. Grajciar, C.J. Heard, A.A. Bondarenko, M.V. Polynski, J. Meeprasert, E.A. Pidko, P. Nachtigall, Chemical Society reviews (2018).

[82] W.F.K. Wynne-Jones, H. Eyring, The Journal of chemical physics 3 (1935) 492–502.

[83] C. Tuma, J. Sauer, Phys. Chem. Chem. Phys. 8 (2006) 3955–3965.

[84] C. Tuma, T. Kerber, J. Sauer, Angew. Chem. Int. Edit. 49 (2010) 4678–4680.

[85] G. Piccini, M. Alessio, J. Sauer, Angew. Chem. Int. Ed. 55 (2016) 5235–5237.

[86] M. Rybicki, J. Sauer, J. Am. Chem. Soc. 140 (2018) 18151–18161.

On the origin of the difference between type A and type B skeletal isomerization of alkenes catalyzed by zeolites: the crucial input of ab initio molecular dynamics. Supporting information.

Contents

SI. Probability distribution functions P(ξ) for reactant and product states of type A and B isomerizations 108

SII. Determination of the velocity term $\langle|\dot{\xi}^{*}|\rangle$ 110

SIII. Avoiding the by-reactions 110

SIV. Validation of the approximation to reaction coordinate 112

SV. Static calculations of the gas phase reactions 114

- SV.1. Type B isomerization 114
- SV.2. Type A isomerization 117

SVI. Static calculations of isomerization reactions in chabazite 119

- SVI.1. Type B isomerization 120
- S.VI.2. Type A isomerization 124

SVII. Additional structural MD data 127

- SVII.1. Analysis of the C-C bonds involved in the PCPs 127
- SVII.2. Fluctuation of potential energy 129

References 130

SI. Probability distribution functions $\tilde{P}(\xi)$ for reactant and product states of type A and B isomerizations

In this section we provide probability densities $\tilde{P}(\xi)$ for the reaction coordinate ξ computed using straightforward molecular dynamics (Figures S1, S2, S3) for the reactant and product configurations of isomerization B and A. The values of $\tilde{P}(\xi_{ref})$ employed in the free-energy calculations (see Equations (1) and (2) in the main text), discussed in Sections 3.3.2 and 3.4.2 in the main text, are listed in Table S1. In each case, the reference state ξ_{ref} was chosen such that the corresponding value of probability density was sufficiently high so that it could be determined with a good accuracy. We emphasize that the particular choice of value of ξ_{ref} does not affect the numerical results of the free energy calculations (provided the value of $\tilde{P}(\xi_{ref})$ is sufficiently accurate). Note that Figures S2 and S3 show distributions for the same chemical species but for different approximation to reaction coordinate (see Sections 3.3.1 and 3.4.1 in the main text).

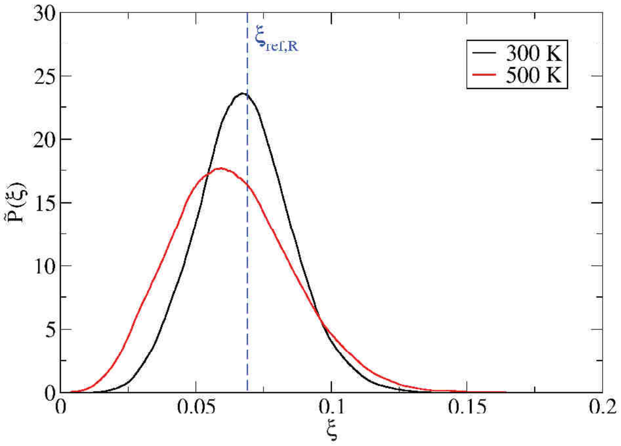

Figure S1. Probability distribution function $\tilde{P}(\xi)$ computed for the reactant state R(I) of type B isomerization at 300 K and 500 K.

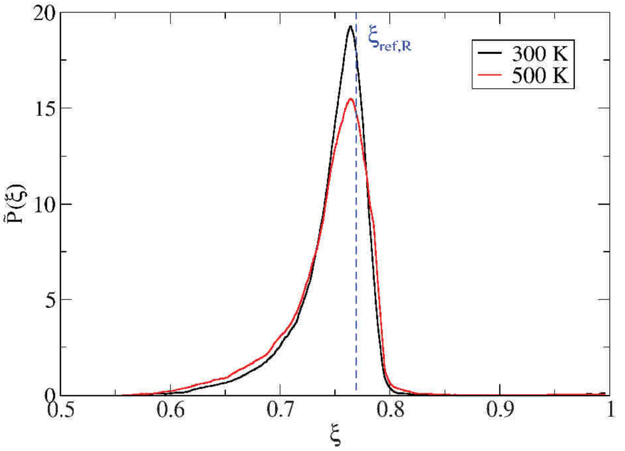

Figure S2. Probability distribution function $\tilde{P}(\xi)$ computed for the product state P of type B isomerization at 300 K and 500 K. The approximation to reaction coordinate (ξ) has been chosen as described in Section 3.3.1 in the main text.

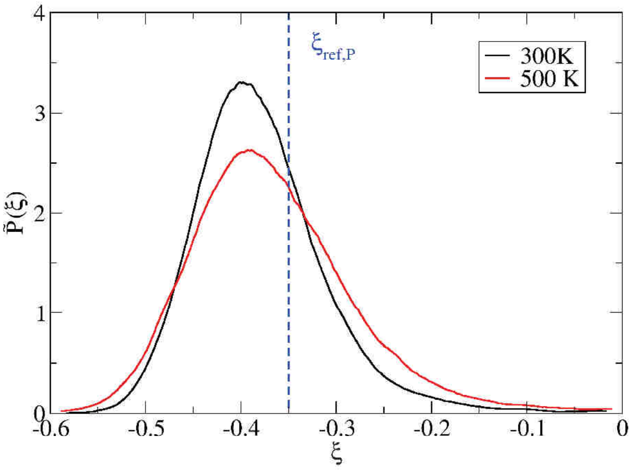

Figure S3. Probability distribution function $\tilde{P}(\xi)$ computed for the reactant/product state P of type A isomerization at 300 K and 500 K. The approximation to reaction coordinate (ξ) has been chosen as described in Section 3.4.1 in the main text.

Table S1. Values of ξ_{ref} for the reactant and product states of type A and B isomerizations, and the corresponding values of probability density ($\tilde{P}(\xi_{ref})$. The lengths of production runs of MD simulations (τ) used to compute $\tilde{P}(\xi_{ref})$ are also listed. As different approximations to reaction coordinate were used in calculations of free energies of both reactions, the values of ξ_{ref} and $\tilde{P}(\xi_{ref})$ listed fort the product of type B isomerization and reactant/product of type A isomerization are different although all these states are chemically identical.

	Type B isomerization			
	T (K)	τ (ps)	ξ_{ref}	$\tilde{P}(\xi_{ref})$
Reactant R(I)	300	195	0.069	23.5
	500	195	0.069	16.3
Product P	300	109	0.769	17.9
	500	161	0.769	14.9
	Type A isomerization			
Reactant/product P	300	109	–0.35	2.45
	500	161	–0.35	2.25

SII. Determination of the velocity term $|\dot{\xi}^*|$

The determination of free energies of activation according to the Equation (1) presented in the main text require the knowledge of average generalized velocity of reaction coordinate at the transition state ($\langle|\dot{\xi}^*|\rangle$). In our calculations, this term is determined using the constrained MD simulations via the formula [1]:

$$\langle|\dot{\xi}^*|\rangle = \frac{\left\langle Z^{-1/2}|\dot{\xi}|\right\rangle_{\xi^*}}{\left\langle Z^{-1/2}\right\rangle_{\xi^*}}, \qquad \text{(Eq. S1)}$$

where the term enclosed in $\langle \ldots \rangle_{\xi^*}$ is computed as a statistical average for a constrained ensemble with $\xi(\boldsymbol{r}) = \xi^*$, the mass metric tensor is:

$$Z = \sum_{i=1}^{N} \frac{1}{m_i} \sum_{\mu=x,y,z} \left(\frac{\partial \xi}{\partial r_{i,\mu}}\right)^2, \qquad \text{(Eq. S2)}$$

and $\dot{\xi}$ is defined as follows:

$$\dot{\xi} = \sum_{i=1}^{N} \sum_{\mu=x,y,z} \frac{\partial \xi}{\partial r_{i,\mu}} \dot{r}_{i,\mu}, \qquad \text{(Eq. S3)}$$

with $r_{i,\mu}$ being the Cartesian component μ of position vector of an atom i and the sums are over all atoms and Cartesian components. In our calculations, the value of $|\dot{\xi}^*|$ is computed for 1000 configurations generated by constrained MD with $\xi(\boldsymbol{r}) = \xi^*$ and 500 sets of vectors $\dot{r}$ generated randomly according to the Maxwell-Boltzmann distribution law.

SIII. Avoiding the by-reactions

In our MD simulations, several undesired by-reactions could possibly occur, which would cause severe problems in the free energy calculations. First of all, both reactions considered in this work can be described as transformations of molecular cations created through the protonation of alkenes by Brønsted acid sites of zeolite. Although the cations representing reactants and products indeed correspond to true minima on potential energy surface (as thoroughly verified in Section 3.2. of the main text), the thermal atomic motion might occasionally lead to deprotonation of cations because this undesired process is fast (i.e. linked with a relatively small free energy barrier) compared to the reactions studied in this work. In order to avoid this problem, which is most likely to occur in constrained MD simulations of unstable reaction intermediate states, a restraining potential of the following form:

$$V(R) = \frac{1}{2}K(R - R_0)^2 \qquad \text{(Eq. S4)}$$

has been added to reinforce all C-H bonds involving hydrogen atoms which are not directly involved in the reaction of interest (all 15 C-H bonds in the case of type A isomerization and 14 C-H bonds (all C-H bonds except of that involving the atom H^a, see Figure 1 in the main text) in type B isomerization). In Eq. S4, R stands for the interatomic bonding distance C-H, R_0 =1.1 Å corresponds approximately to the equilibrium length of the C-H bond, and the force constant K is set to 100 eV.Å^{-2}.

Another undesired process that could occur in the case of type B isomerization is a transformation of rotational isomer R(I) into R(II) (Figure 3). As only R(I) can directly undergo the atomic rearrangement linked with type B isomerization, it was necessary to avoid such an uncontrolled transformation between stable rotamers in our blue moon sampling simulations (as explained in Section 3.3.2 in the main text, the contribution of state R(II) to free energy of activation is accounted for via $P(\xi_{ref})$). To this end, a smeared step potential (shown in Figure S4) acting on torsional angle H^a–C^4–C^3-C^2 (τ) (see Figure 1 in the main text for labeling of atoms) was added in the constrained simulations where R(I) was present. The form of potential was as follows:

$$V(\tau) = \sum_{i=1}^{2} \frac{A_i}{1 + exp\left(-D_i\left(\frac{\tau}{\tau_{0,i}} - 1\right)\right)}, \qquad \text{(Eq. S5)}$$

where the parameters were set to the following values: $A_1 = A_2 = -2$ eV, $D_1 = D_2 = 20$, $\tau_{0,1}$ =120 deg., and $\tau_{0,2} = -120$ deg. (cf. Figure 4 in the main text). As obvious from Figure S4 (plotted between 0 and 360 deg. using the 360 deg. periodicity), the restraining potential is nearly perfectly flat in the region characteristic for R(I) ($\tau \approx 180$ deg.). The extra forces acting on atoms of R(I) due to the presence of $V(\tau)$ are therefore negligible unless a fluctuation attempting the R(I) →R(II) transformation occurs.

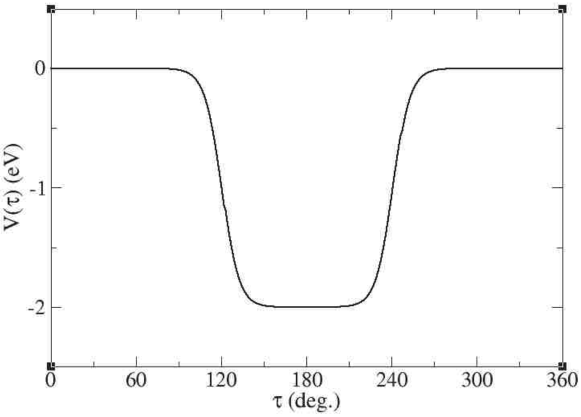

Figure S4. Restraining potential acting on the torsional angle H^a–C^4–C^3-C^2 (τ).

A similar potential (shown in Figure S5) has also been used to act on dihedral angle C^3-C^2-C^4-C^5 (θ) of the states on the product side of type B isomerization in constrained MD simulations which effectively prevented rotations of the three CH_3 groups attached to C^2 around the C^2-C^4 bond. In this case, such a restrain was needed because of the choice of the approximation of the reaction coordinate, which is not invariant with respect to the interchange of methyl groups (see Section 3.3.2 in the main text). The restraining potential has the same form as Eq. S5 and its parameters are set as follows: A_1 =2 eV, $A_2 = -2$ eV, $D_1 = D_2 = 100$, $\tau_{0,1} = -113$ deg., and $\tau_{0,2} = -67$ deg. In this way, the dihedral angle θ were restricted to the values of about –90 deg. characteristic for this particular rotational isomer of the product molecule. Once again, the restraining potential is nearly perfectly flat in the region characteristic for the rotamer of interest and hence the forces due to the restraining potential are negligible unless transition to other rotamer is attempted.

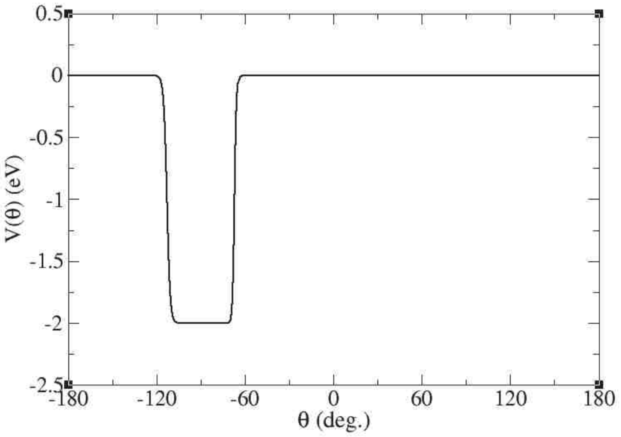

Figure S5. Restraining potential acting on the dihedral angle C^3-C^2-C^4-C^5 (θ).

SIV. Validation of the approximation to reaction coordinate

In this section, we describe the tests performed to validate our choice of the approximation to reaction coordinates.

First, a slow growth simulation protocol (MD in which a candidate CV is increased at a constant rate) has been employed to make sure that the candidate CV can indeed drive smoothly the reaction of interest – from the reactant to the product state and back. The fact that, despite a finite transformation rate, a negligible hysteresis was observed (see Figure S6) is already a good indication of reversibility of the process driven by the given CV. These simulations, that we use solely for the purpose of a qualitative analysis, are performed with a run of length of about 20 ps.

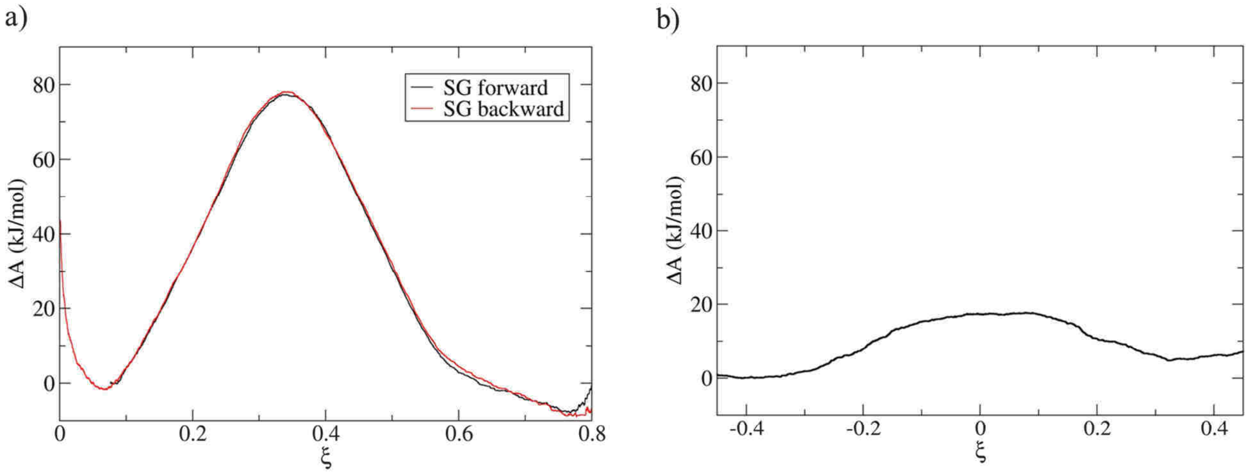

Figure S6. Slow growths simulations for a) the type B isomerization (in gas phase) and b) the type A isomerization (in chabazite) at T = 300 K.

Second, the distribution of free energy gradients has been monitored for all points along the CV used in the blue moon simulation. As it follows from Figure 1.18 of reference [2] or Figure 1 of reference [3], an incorrect CV would lead to a two-modal distribution of contributions to free energy gradients computed for a point near the separatrix (which follows from the fact that, in such a case, the free energy computed for the subspace of the configurational space orthogonal to CV would have two (or more) minima. In contrast, a correct CV must yield a unimodal distribution at the same point (because there is only one free energy minimum in the subspace spanned by all coordinates orthogonal to CV). As shown in Figure S7, the free energy gradients evaluated for the free energy transition states (and also for all other points) of both reactions studied in our work exhibit a correct behavior.

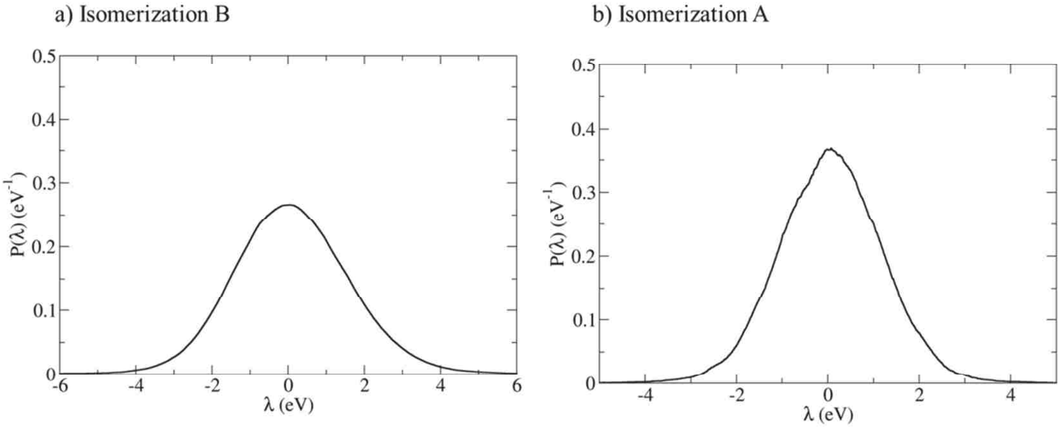

Figure S7. Probability distribution function of the Lagrange multiplier λ associated with the reaction coordinate for the transition states of a) type B isomerization and b) type A isomerization, at 300 K. The Lagrange multiplier λ is the main component of the free-energy gradient [1,4,5]. We note that the approximation to reaction coordinates used in our simulations are dimensionless. The unimodal shape of distributions indicates that our CV corresponds to the case where the reaction is correctly described by the CV [2,3].

Third, an uncontrolled process would be identified by a presence of discontinuity in computed free energy gradients where a small variation in CV would cause a large change in gradient (usually accompanied by a change of its sign). We carefully monitored the free energy gradients computed in our blue moon simulations and, as shown in Figure S8, they do not show any trace of such a discontinuity (besides a small numerical noise due to the statistical uncertainty given by the finite simulation time). Finally, the correctness of our choice is evident also from the semi-quantitative agreement with the static gas phase reactions for which, arguably, the "static" approach represents a more reasonable choice than for the reaction in zeolite.

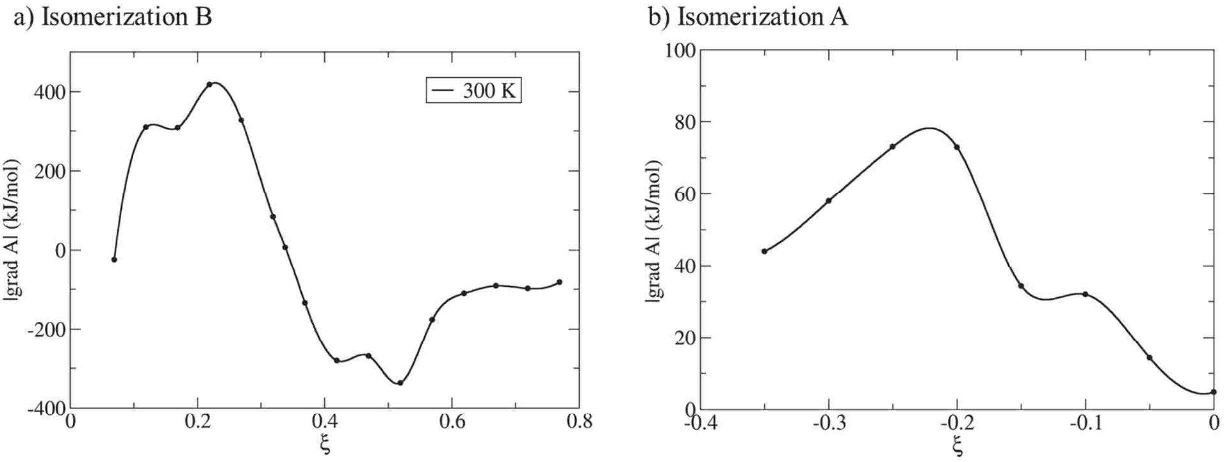

Figure S8. Free energy gradients computed in our blue moon simulations, for a) isomerization B and b) isomerization A. For the type A isomerization, the gradient is plotted for $\xi < 0$, the free energy A being an even function by symmetry of reactant and product. We note that the approximation to reaction coordinates used in our simulations are being dimensionless, hence the units of gradients.

SV. Static calculations of the gas phase reactions

SV.1. Type B isomerization

Figure S9 shows potential energy of reactant R as a function of torsional and bonding angles $\tau = H^a–C^4–C^3-C^2$ and $\alpha = C^4-C^3-C^2$ (see Figure 1 for the numbering of atoms) with minima representing two equivalent rotational isomers R(II) ($\tau = \pm 59$ deg.) and the rotamer R(III) ($\tau = 0$ deg.). As evident, the angle α in the isomer R(III) takes much smaller value (~93 deg.) than in R(II) (~106 deg.) or R(I) (~109 deg.). The thermal motion of atoms at the finite temperature MD simulation of R(III) with τ fixed at 0 deg. has a tendency to increase the average value of α to 102-106 deg. depending on the temperature (see Figure S10). According to Figure S6, the system is in a state which is higher in energy compared to R(II) where α assumes a similar value. Consequently, the system naturally relaxes to R(II) if the constraint on τ is removed. This effect explains why R(III) is found to be unstable in our MD simulations (see Section 3.3.2 in the main text).

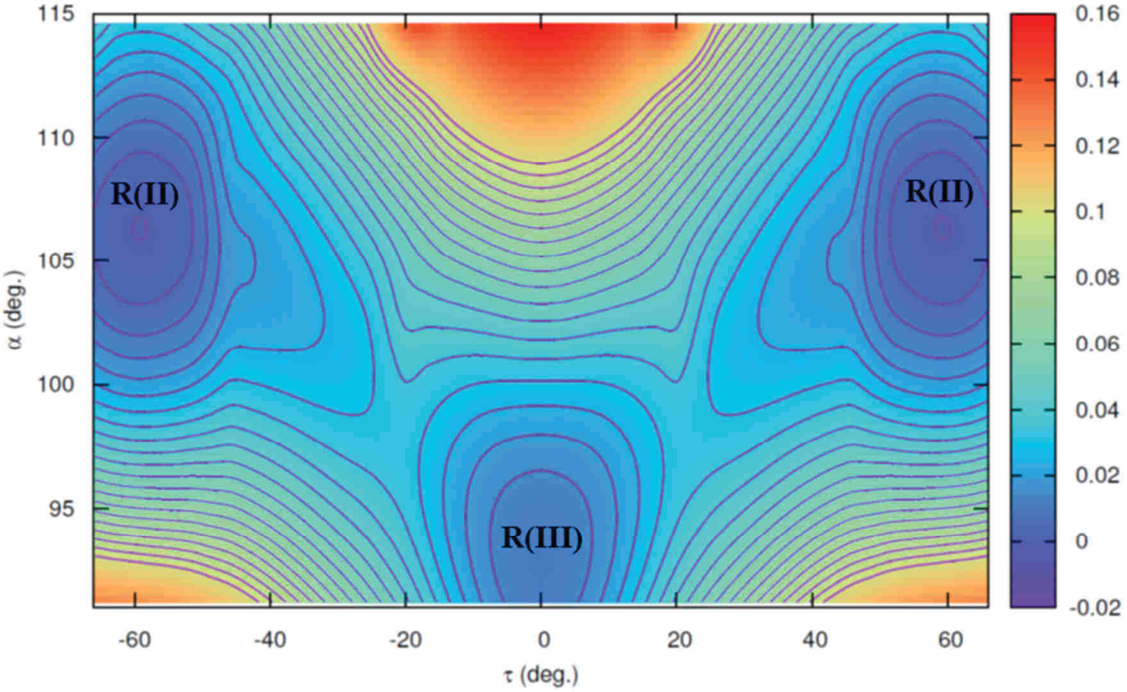

Figure S9. Potential energy of reactant of isomerization B as a function of torsional and bonding angles $\tau = \mathrm{H^a{-}C^4{-}C^3{-}C^2}$ and $\alpha = \mathrm{C^4{-}C^3{-}C^2}$. The isoenergetic levels are in eV.

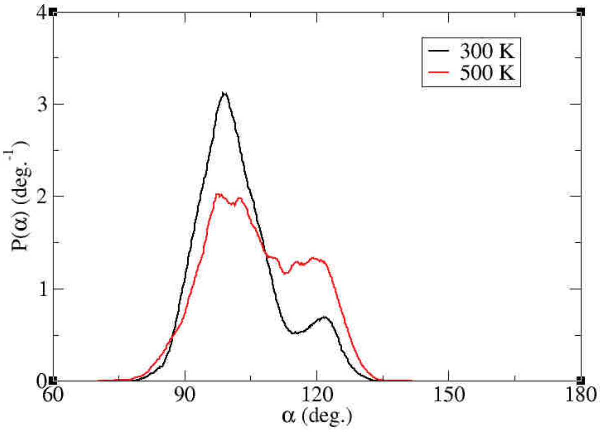

Figure S10. Probability distribution function $P(\alpha)$ for the rotamer R(III) in zeolite at 300 K and 500 K.

Table S2. Helmholtz free energies computed using the static approach for three different rotamers of reactant molecule (R(I), R(II), and R(III)), transition state (TS), and product of type B isomerization reaction of 2,4-dimethyl-pent-2-enium cation in the gas phase. Contributions of the electronic (A_{el}), vibrational (A_{vib}), rotational (A_{rot}), and translational (A_{trans}) degrees of freedom to the total free energy (A_{tot}) of each state at 300 K and 500 K are indicated. All values are in kJ/mol.

	A_{el}	300 K				500 K			
		A_{vib}	A_{rot}	A_{trans}	A_{tot}	A_{vib}	A_{rot}	A_{trans}	A_{tot}
R(I)	-11000.6	499.9	-31.2	-43.6	-10575.6	467.6	-55.2	-78.0	-10666.2
R(II)	-11004.0	497.8	-31.4	-43.6	-10581.2	464.3	-55. 5	-78.0	-10673.2
R(III)	-11002.9	500.6	-31.3	-43.6	-10577.3	468.3	-55.4	-78.0	-10668.0
TS	-10930.2	505.9	-30.9	-43.6	-10498.8	479.3	-54.6	-78.0	-10583.6
P(i)	-11005.0	499.1	-31.0	-43.6	-10580.5	466.6	-54.8	-78.0	-10671.2

Table S3. Individual contributions to the $\Delta A_{R(I)\to TS_B}$ and $\Delta A_{R(I)\to P(i)}$ terms (cf. Equation (4) in the main text) computed for type B isomerization of 2,4-dimethyl-pent-2-enium cation in the gas phase. All values are in kJ/mol.

	T=300 K		T=500 K	
	$R(I) \to TS_B$	$R(I) \to P(i)$	$R(I) \to TS_B$	$R(I) \to P(i)$
ΔA_{el}	70.4	-4.4	70.4	-4.4
ΔA_{vib}	6.0	-0.8	11.7	-1.1
ΔA_{rot}	0.3	0.3	0.6	0.6
ΔA_{trans}	0.0	0.0	0.0	0.0
$\boldsymbol{\Delta A_{total}}$	**76.8**	**-4.9**	**82.7**	**-5.0**
ΔU_{el}	70.4	-4.4	70.4	-4.4
ΔU_{vib}	-1.8	-0.6	-3.4	0.1
ΔU_{rot}	0.0	0.0	0.0	0.0
ΔU_{trans}	0.0	0.0	0.0	0.0
$\boldsymbol{\Delta U_{total}}$	**68.6**	**-5.0**	**67.0**	**-4.3**
$T\Delta S_{el}$	0.0	0.0	0.0	0.0
$T\Delta S_{vib}$	-7.8	0.2	-15.1	1.1
$T\Delta S_{rot}$	-0.3	0.2	-0.6	-0.5
$T\Delta S_{trans}$	0.0	0.0	0.0	0.0
$\boldsymbol{T\Delta S_{total}}$	**-8.1**	**0.0**	**-15.7**	**0.6**

SV.2. Type A isomerization

The reactant (and product) of type A isomerization has 6 equivalent stable rotamers. The dihedral angle θ between C^3-C^2-C^4-C^5 is -90 deg. for the first stable rotamer, and the five remaining rotational isomers are created by increasing θ by an integral multiple of increment $\Delta\theta$ =60 deg.

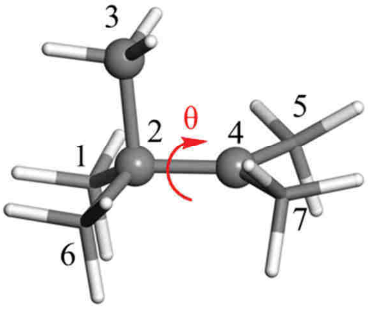

Figure S11. Numbering of the atoms of the first rotamer of P and dihedral angle θ (C^3-C^2-C^4-C^5).

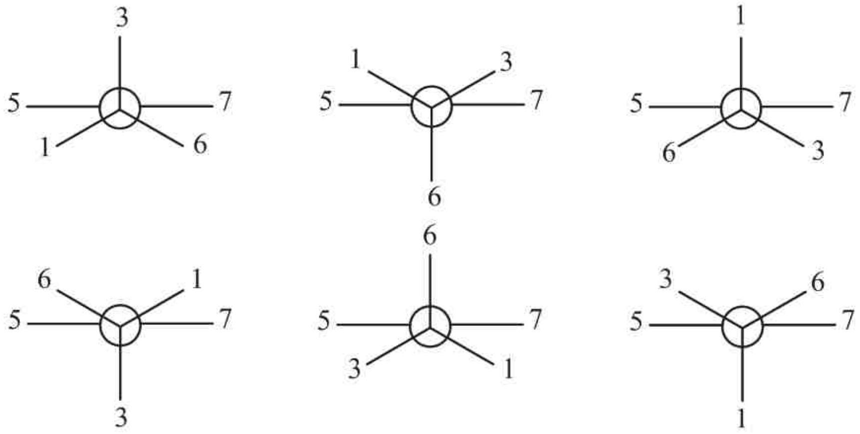

Figure S12. Schematic drawing showing six equivalent rotamers of the product P viewed along the direction parallel with the bond C^2-C^4 (cf. Figure S8).

Table S4. Individual contributions to the term $\Delta A_{P(i)\rightarrow TS_A}$ computed for type A isomerization of 2,2,4-trimethyl-butenium cation in the gas phase. All values are in kJ/mol.

	$P(i) \rightarrow TS_A$	
	300 K	500 K
ΔA_{el}	13.7	13.7
ΔA_{vib}	1.0	2.5
ΔA_{rot}	0.0	0.1
ΔA_{trans}	0.0	0.0
$\boldsymbol{\Delta A_{total}}$	**14.7**	**16.2**
ΔU_{el}	13.7	13.7
ΔU_{vib}	-0.8	-2.1
ΔU_{rot}	0.0	0.0
ΔU_{trans}	0.0	0.0
$\boldsymbol{\Delta U_{total}}$	**12.9**	**11.6**
$T\Delta S_{el}$	0.0	0.0
$T\Delta S_{vib}$	-1.8	-4.6
$T\Delta S_{rot}$	0.0	-0.1
$T\Delta S_{trans}$	0.0	0.0
$\boldsymbol{T\Delta S_{total}}$	**-1.8**	**-4.7**

SVI. Static calculations of isomerization reactions in chabazite

In this section we provide numerical values of all contributions to the free energies of stable and transition states (Tables S5-S7, and S9-S11) and of selected structural parameters (Tables S8 and S12) for types B and A isomerizations in zeolite investigated using the static approach. Furthermore, structures of selected states are shown in Figures S14 and S15. Figure S13 shows the correlation between the electronic contribution to free energy of transition states TS_A and TS_B with the parameter χ defined in the main text ($\chi = \sum_{i=1}^{N_C} \frac{1}{[d(Al-C^i)]^6}$, see Equation (6)). For easier orientation the data for type B isomerization are presented in Section SVI.1 while those for type A isomerization in Section SVI.2.

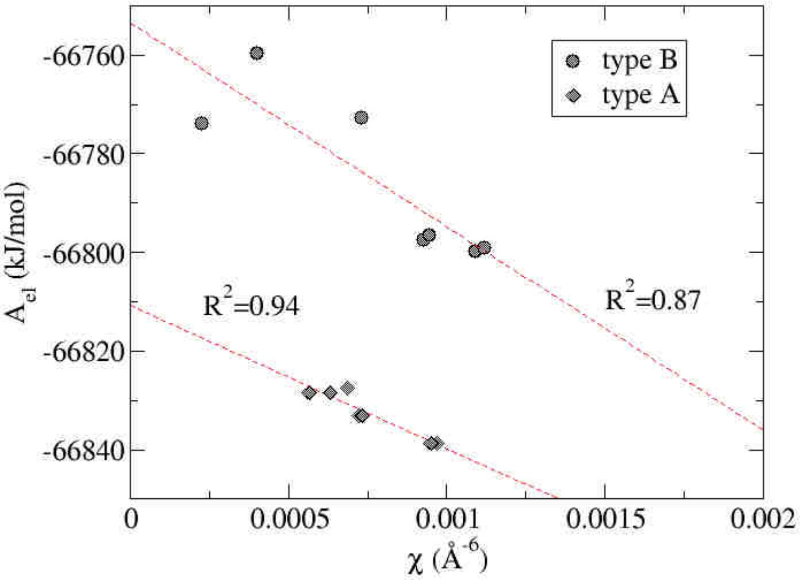

Figure S13. Correlation between the electronic contribution to free energy of TS_A and TS_B with sum of inverse distances between the framework Al and all C atoms raised to the power of six (χ). Dashed lines indicate the fitted linear functions and the corresponding correlation coefficients (R2) are indicated.

SVI.1. Type B isomerization

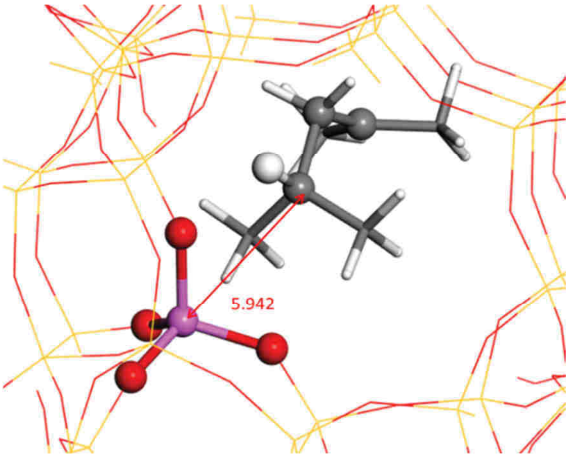	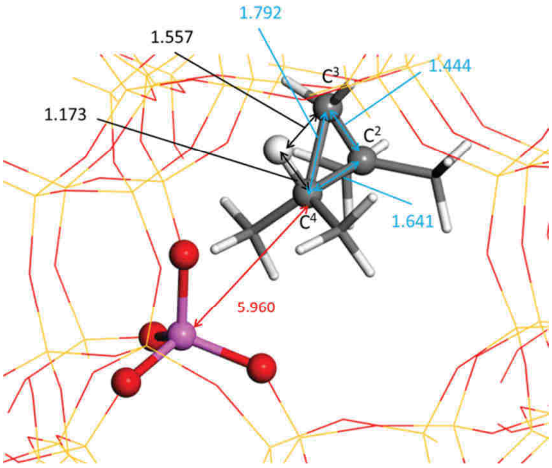
Reactant 1st configuration	TS 1st configuration
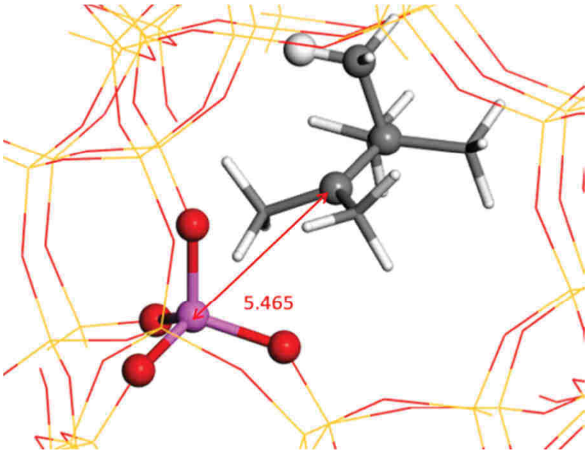	
Product 1st configuration	
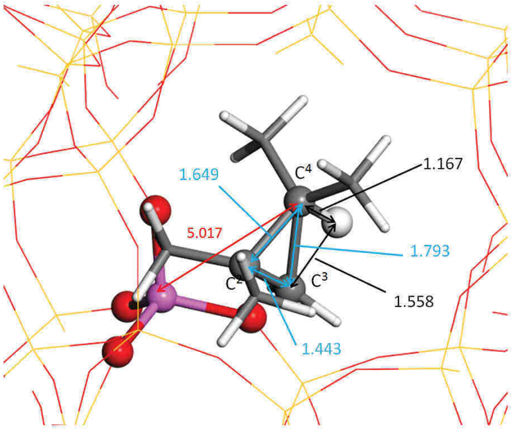	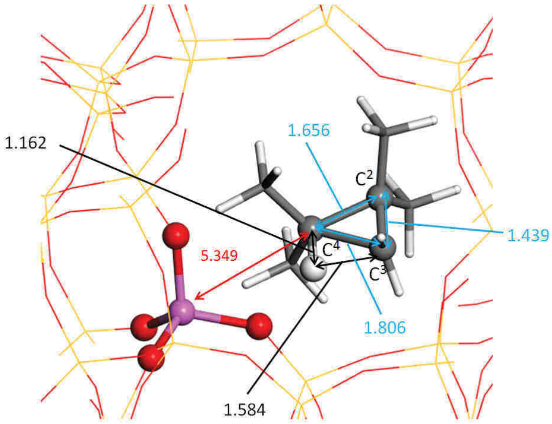
TS 2nd configuration	TS 3rd configuration

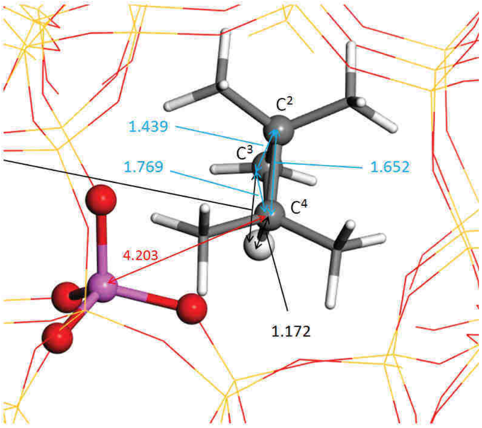

TS 4th configuration

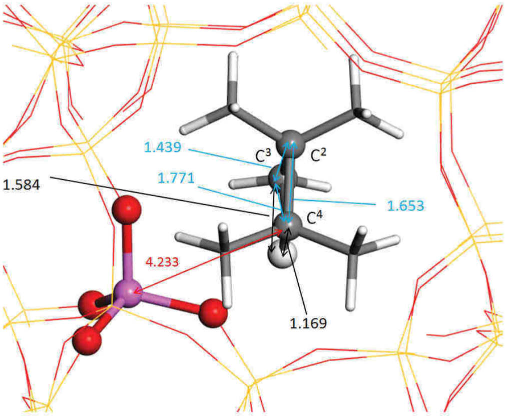

TS 5th configuration

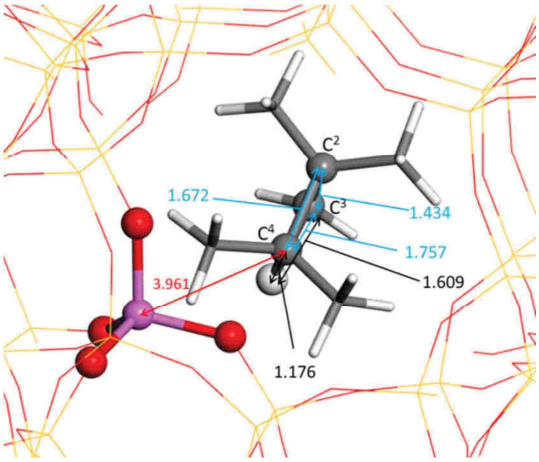

TS 6th configuration

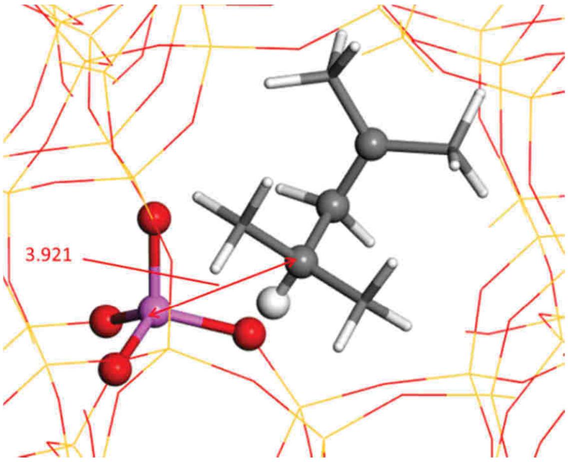

Reactant 7th configuration

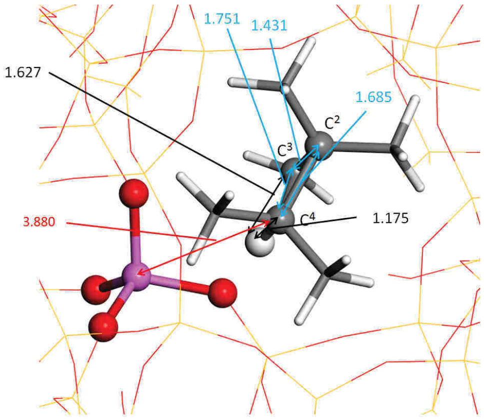

TS 7th configuration

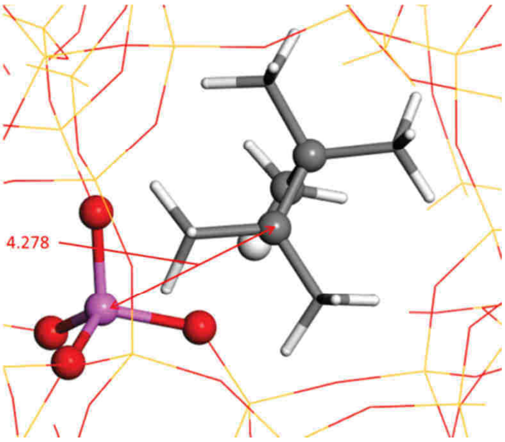

Product 7th configuration

Figure S14. TS configurations, for type B isomerization. Reactant and product for the 1st and 7th configurations are also shown. Al in purple, H in white, Si in yellow and O in red. Selected interatomic distances are in Å.

Table S5. Helmholtz free energies computed using the static approach for seven transition state structures of type B isomerization reaction of 2,4-dimethyl-pent-2-enium cation in zeolite. Contributions of the electronic (A_{el}) and vibrational (A_{vib}) degrees of freedom to the total free energy (A_{tot}) of each state at 300 K and 500 K are indicated. All values are in kJ/mol.

Configuration	A_{el}	300 K		500 K	
		A_{vib}	A_{tot}	A_{vib}	A_{tot}
1	-66773.9	1034.6	-65739.6	701.8	-66072.3
2	-66772.6	1027.9	-65744.9	690.9	-66081.9
3	-66759.6	1027.6	-65732.2	690.0	-66069.8
4	-66797.4	1040.9	-65756.7	712.0	-66085.7
5	-66796.6	1039.5	-65757.3	709.6	-66087.2
6	-66799.8	1034.3	-65765.6	701.2	-66098.8
7	-66799.0	1027.3	-65771.9	689.4	-66109.8

Table S6. Helmholtz free energies computed using the static approach for the seven reactant (R(I)) and product (P) structures of type B isomerization reaction of 2,4-dimethyl-pent-2-enium cation in zeolite. Contributions of the electronic (A_{el}) and vibrational (A_{vib}) degrees of freedom to the total free energy (A_{tot}) of each state at 300 K and 500 K are indicated. All values are in kJ/mol.

Configuration	A_{el}	300 K		500 K	
		A_{vib}	A_{tot}	A_{vib}	A_{tot}
1 R(I)	-66842.2	1025.5	-65817.0	686.2	-66156.3
1 P	-66840.5	1018.3	-65822.4	674.4	-66166.3
2 R(I)	-66856.1	1026.9	-65829.4	688.8	-66167.6
2 P	-66845.6	1021.1	-65824.8	679.2	-66166.7
3 R(I)	-66832.9	1024.8	-65808.3	684.9	-66148.2
3 P	-66853.6	1029.0	-65824.9	692.5	-66161.3
4 R(I)	-66850.1	1029.6	-65820.7	692.3	-66158.0
4 P	-66858.8	1031.1	-65828.0	696.2	-66162.8
5 R(I)	-66850.1	1026.9	-65823.4	688.0	-66162.3
5 P	-66858.8	1032.8	-65826.2	699.1	-66159.9
6 R(I)	-66847.5	1022.7	-65825.0	681.3	-66166. 5
6 P	-66842.2	1026.5	-65815.9	686.3	-66156.0
7 R(I)	-66847.4	1025.7	-65821.9	685.3	-66162.3
7 P	-66842.4	1024.0	-65818.7	683.4	-66159.3

Table S7. Electronic (ΔA_{el}) and vibrational (ΔA_{vib}) contributions to the barriers $\Delta A_{R(I)\rightarrow TS_B}$ and $\Delta A_{P(i)\rightarrow TS_B}$ computed for type B isomerization of 2,4-dimethyl-pent-2-enium cation in zeolite. All values are in kJ/mol.

Configuration	ΔA_{el}	300 K		500 K	
		A_{vib}	ΔA_{tot}	ΔA_{vib}	ΔA_{tot}
1 R(I)→TS	68.3	9.1	77.4	15.6	84.0
1 P(i)→TS	66.6	16.3	82.8	27.5	94.0
2 R(I)→TS	83.5	1.0	84.5	2.2	85.7
2 P(i)→TS	73.0	6.8	79.8	11.7	84.8
3 R(I)→TS	73.2	2.8	76.0	5.2	78.4
3 P(i)→TS	94.0	-1.3	92.6	-2.5	91.5
4 R(I)→TS	52.7	11.3	64.0	19.7	72.4
4 P(i)→TS	61.4	9.9	71.2	15.8	77.1
5 R(I)→TS	53.5	12.6	66.1	21.7	75.2
5 P(i)→TS	62.3	6.7	69.0	10.5	72.8
6 R(I)→TS	47.7	11.6	59.3	19.9	67.7
6 P(i)→TS	42.4	7.9	50.3	14.9	57.3
7 R(I)→TS	48.4	1.6	50.1	4.1	52.5
7 P(i)→TS	43.5	3.3	46.8	6.0	49.5

Table S8. Lengths of the C-C and C-H bonds involved in the formation and the opening of the protonated cyclopropane, which is transition state of type B isomerization. All distances are in Å.

Configuration	d(Al-C^4)	d(C^4-C^3)	d(C^4-C^2)	d(C^2-C^3)	d(H^a-C^4)	d(H^a-C^3)
1	5.960	1.792	1.641	1.444	1.173	1.557
2	5.017	1.793	1.649	1.443	1.167	1.558
3	5.349	1.806	1.656	1.439	1.162	1.584
4	4.203	1.769	1.652	1.439	1.172	1.584
5	4.233	1.771	1.653	1.439	1.169	1.584
6	3.961	1.757	1.672	1.434	1.176	1.609
7	3.880	1.751	1.685	1.431	1.175	1.627

S.VI.2. Type A isomerization

Table S9. Helmholtz free energies computed using the static approach for seven transition state structures of type A isomerization reaction of 2,2,4-trimethyl-butenium cation in zeolite. Contributions of the electronic (A_{el}) and vibrational (A_{vib}) degrees of freedom to the total free energy (A_{tot}) of each state at 300 K and 500 K are indicated. All values are in kJ/mol.

Configuration	A_{el}	300 K		500 K	
		A_{vib}	A_{tot}	A_{vib}	A_{tot}
1	-66833.1	1033.7	-65799.4	699.1	-66134.0
2	-66828.4	1031.9	-65796.5	696.7	-66131.7
3	-66828.4	1029.5	-65798.9	693.2	-66135.2
4	-66827.5	1020.4	-65807.1	678.4	-66149.1
5	-66838.6	1030.3	-65808.3	693.8	-66144.8
6	-66833.1	1032.2	-65800.9	696.7	-66136.4
7	-66838.6	1031.4	-65807.2	695.6	-66143.0

Table S10. Helmholtz free energies computed using the static approach for indistinguishable reactant/product structures of type A isomerization reaction of 2,2,4-trimethyl-butenium cation in zeolite. Contributions of the electronic (A_{el}) and vibrational (A_{vib}) degrees of freedom to the total free energy (A_{tot}) of each state at 300 K and 500 K are indicated. All values are in kJ/mol.

Configuration	A_{el}	300 K		500 K	
		A_{vib}	A_{tot}	A_{vib}	A_{tot}
1	-66860.9	1026.4	-65834.5	688.2	-66172.7
	-66842.0	1029.9	-65812.1	692.8	-66149.2
2	-66846.4	1026.3	-65820.1	687.1	-66159.3
	-66857.3	1031.4	-65825.9	695.7	-66161.6
3	-66839.8	1028.6	-65811.2	690.7	-66149.1
	-66858.2	1022.1	-65836.1	680.4	-66177.8
4	-66843.9	1028.0	-65815.9	689.7	-66154.2
	-66854.9	1024.2	-65830.7	684.1	-66170.8
5	-66848.3	1030.5	-65817.8	694.2	-66154.1
	-66854.0	1029.0	-65825.0	691.5	-66162.5
6	-66842.0	1029.8	-65812.2	692.6	-66149.4
	-66860.9	1028.7	-65832.2	692.0	-66168.9
7	-66854.1	1031.5	-65822.6	695.6	-66158.5
	-66848.3	1029.6	-65818.7	692.5	-66155.8

Table S11. Electronic (ΔA_{el}) and vibrational (ΔA_{vib}) contributions to the barrier $\Delta A_{P(i)\rightarrow TS_A} \equiv \Delta A_{tot}$ computed for type A isomerization of 2,2,4-trimethyl-butenium cation in zeolite. All values are in kJ/mol. Reactant and product being indistinguishable, two values are given for each configuration of the transition state (for reactant to transition state and for product to transition state).

Configuration	ΔA_{el}	300 K		500 K	
		ΔA_{vib}	ΔA_{tot}	ΔA_{vib}	ΔA_{tot}
1	27.8	7.3	35.0	10.9	38.6
	8.9	3.8	12.7	6.3	15.2
2	18.0	5.6	23.6	9.7	27.7
	28.9	0.5	29.4	1.0	29.9
3	11.4	0.9	12.3	2.4	13.8
	29.8	7.4	37.2	12.8	42.6
4	16.4	-7.7	8.7	-11.3	5.1
	27.4	-3.8	23.6	-5.6	21.8
5	9.7	-0.2	9.5	-0.3	9.3
	15.4	1.3	16.8	2.4	17.8
6	8.9	2.4	11.3	4.0	12.9
	27.8	3.4	31.3	4.6	32.5
7	15.5	-0.1	15.3	0.0	15.5
	9.7	1.8	11.5	3.0	12.7

Table S12. The interatomic distances Al-C^4 and Al-C^2, and the lengths of the C-C bonds involved in the formation and the opening of the protonated cyclopropane in the transition state of the type A isomerization. All distances are in Å.

Configuration	d(Al-C^4)	d(Al-C^2)	d(C^4-C^2)	d(C^4-C^3)	d(C^2-C^3)
1	5.912	4.560	1.421	1.886	1.768
2	4.510	4.968	1.419	1.830	1.870
3	5.470	4.526	1.420	1.895	1.805
4	4.617	5.994	1.422	1.818	1.874
5	5.386	4.213	1.419	1.848	1.795
6	5.905	4.550	1.421	1.885	1.769
7	5.412	4.225	1.419	1.846	1.801

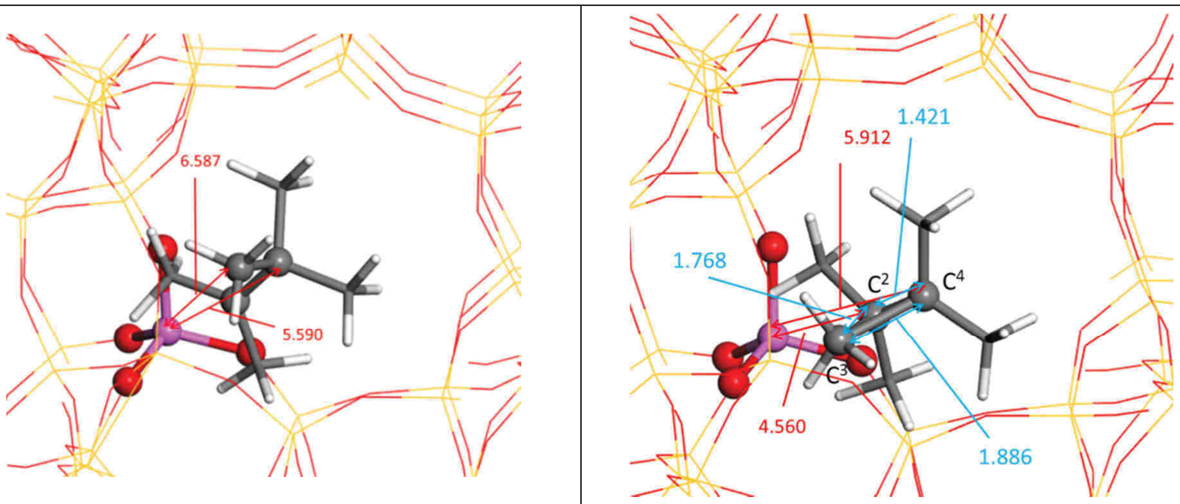

Reactant 1st configuration

TS 1st configuration

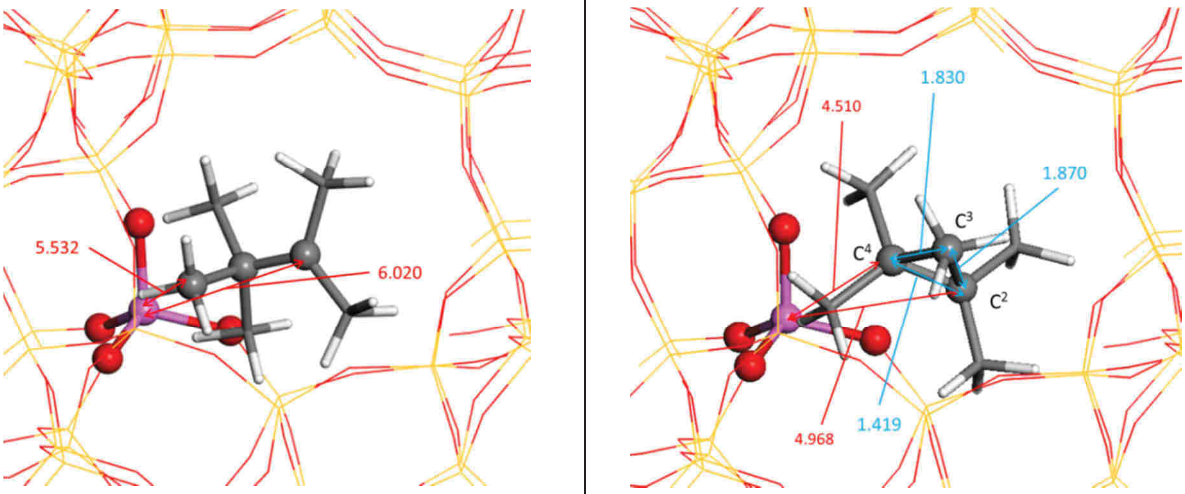

Product 1st configuration

TS 2nd configuration

Figure S15. Selected reactant, product, and TS configurations, for type A isomerization. Al in purple, H in white, Si in yellow and O in red. Selected interatomic distances are in Å.

SVII. Additional structural MD data

SVII.1. Analysis of the C-C bonds involved in the PCPs

The probability distribution functions for the three C-C bonds (C^2-C^3, C^3-C^4 and C^2-C^4) involved in the reactions determined using the data generated by MD of reactant, transition state, and product states are shown in Figures S13-S16. These distributions were fitted by the Gaussian function:

$$f(d) = \frac{1}{\sqrt{2\pi\sigma^2}} exp\left(-\frac{(d-\mu)^2}{2\sigma^2}\right). \qquad \text{(Eq. S6)}$$

Assuming that each bond (d) can be represented by a harmonic oscillator with the force constant κ, the standard deviation (σ) of the corresponding distribution can be identified [6] with the term $\sqrt{\frac{k_B T}{\kappa}}$. Hence the relative strength of the bond can be estimated from the width of the corresponding probability distribution. The parameter μ stands for the average value of the bond. The values of fitting parameters μ and σ are presented in Table S13.

Table S13. The parameters μ and σ (in Å) obtained by fitting the MD data for the reactant (R(I)), transition state (TS_B), and product (P) configurations of type B isomerization, and transition state (TS_A) for type A isomerization by the normal distribution. Note that P is also the reactant/product of type A isomerization.

		T = 300 K		T = 500 K	
bond	species	μ	σ	μ	σ
C^2-C^3	R(I)	1.45168	0.0328534	1.45361	0.0415915
C^2-C^4	R(I)	2.53987	0.0807952	2.56763	0.106345
C^3-C^4	R(I)	1.62466	0.0529897	1.62719	0.0722078
C^2-C^3	TS_B	1.44327	0.0296228	1.44745	0.037927
C^2-C^4	TS_B	1.66545	0.0496497	1.66697	0.0643271
C^3-C^4	TS_B	1.77854	0.0567455	1.80294	0.0710366
C^2-C^3	P	1.60597	0.0481422	1.62574	0.067394
C^2-C^4	P	1.47203	0.0339286	1.46641	0.0451147
C^3-C^4	P	2.31329	0.0927257	2.28838	0.133306
C^2-C^4	TS_A	1.42161	0.0268869	1.42394	0.0329199
C^3-C^4	TS_A	1.85121	0.0601533	1.87182	0.0868662
C^2-C^3	TS_A	1.84396	0.0591849	1.86382	0.083486

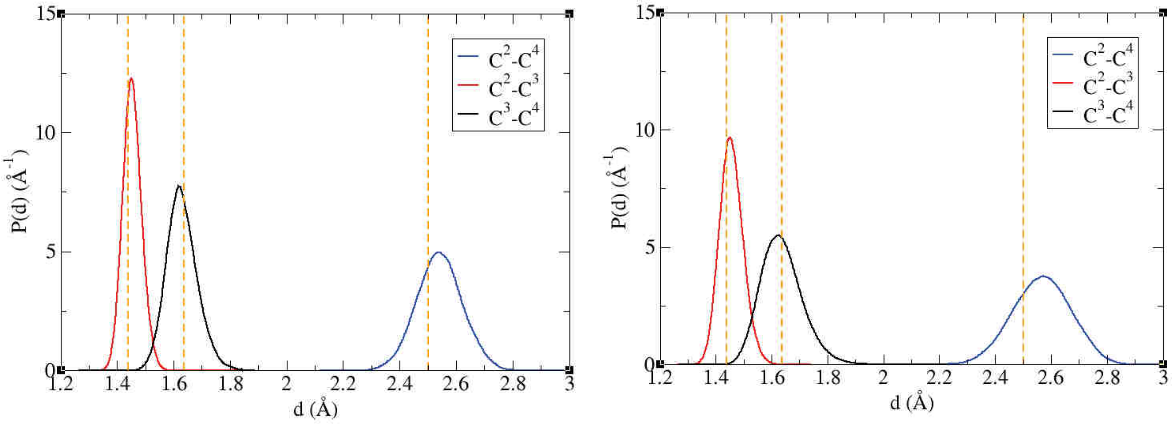

Figure S16. Probability distribution functions (solid lines) for the C-C bonds (d) in reactant R(I) of type B isomerization at T = 300 K (left) and T = 500 K (right). Dashed lines indicate results from the static approach applied to the reaction in the gas phase.

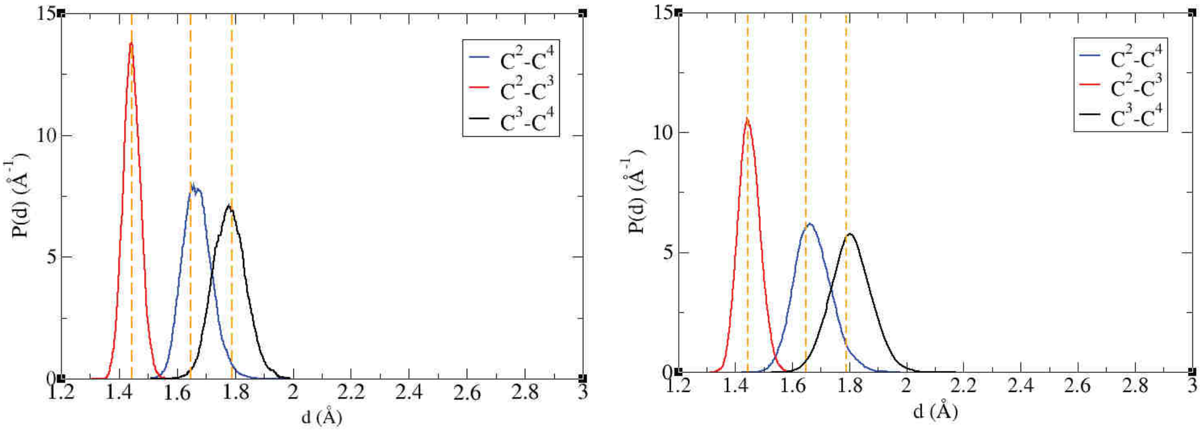

Figure S17. Probability distribution functions (solid lines) for the C-C bonds (d) in the transition state TSB of type B isomerization at T = 300 K (left) and T = 500 K (right). Dashed lines indicate results from the static approach applied to the reaction in the gas phase.

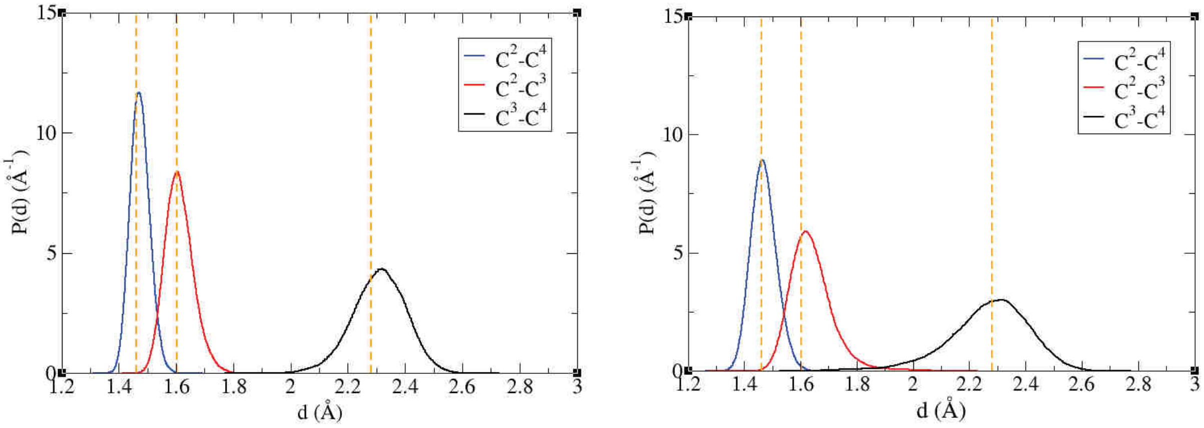

Figure S18. Probability distribution functions (solid lines) for the C-C bonds (d) in the product P of type B isomerization at T = 300 K (left) and T = 500 K (right). Dashed lines indicate results from the static approach applied to the reaction in the gas phase. Note that P is also the reactant/product for type A isomerization.

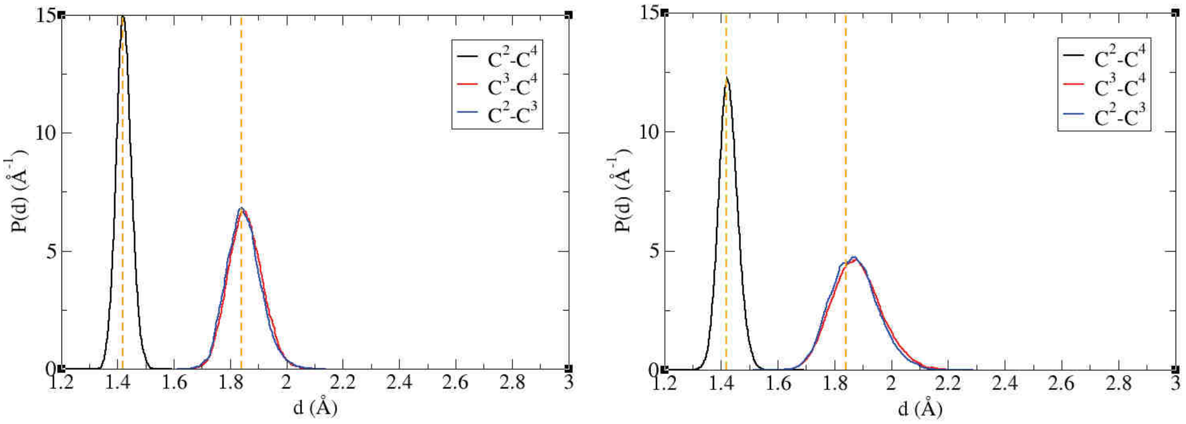

Figure S19. Probability distribution functions (solid lines) for the C-C bonds (d) in the transition state TSA of type A isomerization at T = 300 K (left) and T = 500 K (right). Dashed lines indicate results from the static approach applied to the reaction in the gas phase.

SVII.2. Fluctuation of potential energy

An example of the potential energy distribution $\delta E = E_p - \langle E_p \rangle$ computed for the free energy transition state of type B isomerization is shown Figure S20. As expected, the distribution is much broader than the potential energy differences between individual TS configurations identified in our static calculations (within around 40 kJ/mol, see Sec. 3.2. in the main text). This behavior is a natural consequence of thermal fluctuations of a many-body system.

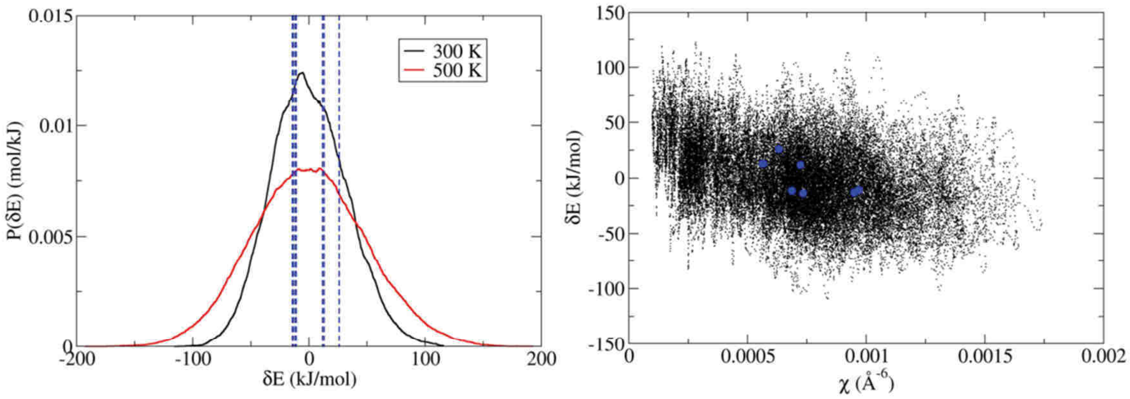

Figure S20. Left: probability distribution function for the fluctuation of potential energy $\delta E = E_p - \langle E_p \rangle$ for the TS of type B isomerization at 300 and 500 K. The values of δE determined in the static approach are indicated by vertical dot lines. Right: same fluctuation δE at 300K as a function of χ (Equation (6) in the main text). The values determined in the static approach are indicated by blue dots.

References

[1] E.A. Carter, G. Ciccotti, J.T. Hynes, R. Kapral, Chem. Phys. Lett. 156 (1989) 472–477.
[2] C. Dellago, P.G. Bolhuis, P.L. Geissler, Advances in Chemical Physics 123 (2002).
[3] B. Peters, Annual review of physical chemistry 67 (2016) 669–690.
[4] T. Bučko, J. Phys-Condens. Matter 20 (2008) 64211.
[5] G. Ciccotti, M. Sprik, J. Chem. Phys. 109 (1998) 7737–7744.
[6] R. Baron, W.F. van Gunsteren, P.H. Hünenberger, Trends Phys. Chem. 11 (2006) 87–122.
[7] B. Peters, J. Chem. Phys. 125 (2006) 241101.

Section IV. Competition of Secondary versus Tertiary Carbenium Routes for the Type B Isomerization of Alkenes over Acid Zeolites Quantified by AIMD Simulations

This section reproduces the text of a paper submitted for publication. The corresponding Supporting Information is presented at the end of the section.

IV.1. Introduction

Zeolite-catalyzed isomerization and cracking reactions of alkenes are core transformations in hydrocarbon chemistry. Many reactions in refining,[1,2] petrochemistry[2,3] and biomass conversion[4–6] involve alkene skeletal isomerization steps. In hydrocracking of alkanes, for example, bifunctional catalysts are required, with a (de)hydrogenation function on a noble metal or a metallic sulfide and an acidic function (of the Brønsted type) provided by zeolites or amorphous silica-aluminas.[7] Alkenes are protonated on the acid sites of the catalyst before the isomerization and cracking take place. By analogy with conventional organic chemistry, general mechanisms are written with carbenium ions (or classical trivalent carbocations) and carbonium ions (or tetra- or pentacoordinated non-classical carbocations) playing the role of reactive intermediates or of transition states.[2,7–10] In super-acidic media, it is well-known that secondary carbenium ions are less stable than tertiary carbenium ions.[11] The only carbenium ions detected experimentally in zeolites are highly resonant tertiary cations.[12,13] The first direct evidence of the existence of the shorter tert-butyl cation was reported very recently.[14,15] In pioneering calculations, carbenium ions were considered as transition states whereas alkoxides were identified as stable species.[16,17] Denayer et al. experimentally observed that the relative intrinsic reaction rates of skeletal branching and cracking reaction steps for various alkanes are catalyst independent (within a series of Pt/USY catalysts), supporting the idea of a carbenium-like reactivity, rather than an alkoxide-mediated one.[18] With periodic calculations[19–22] and more sophisticated static calculations,[23–25] tertiary cations were found to be local energy minima. Using advanced *ab initio* molecular dynamics methods, van Speybroeck and coworkers concluded that the stability of alkoxides relative to the cationic forms had been overestimated in previous studies.[26,27] Importantly, the tertiary carbenium ions were found to be stable at 773 K in the zeolite, whereas secondary cations were shown to be metastable only.

Secondary carbenium ions thus appear as transient species. Their stability increases with the number of carbons and highly branched carbenium ions undergo fast transformations into more stable cationic species.[28]

The isomerization is classified as type A when it does not involve any branching degree change (in practice, this corresponds to a direct 1,n hydride or alkyl transfer), or type B when it increases the branching degree of the chain.[2] In the present work, we aim at quantifying the respective reactivity of secondary and tertiary carbenium ions in the skeletal isomerization into a dibranched carbenium ion. It has been demonstrated that finite temperature effects for isomerization and cracking reactions of hydrocarbons in zeolites cannot be described with a sufficient accuracy within the static approach to the transition state theory.[26–31] Free energy methods based on ab initio molecular dynamics represent the current state-of-art approach to this problem and we adapt this technique (based on the blue moon ensemble approach[32,33]) to study the mechanism of isomerization reaction occurring after the protonation of a reactant C_7 alkene. C_7 alkanes, dehydrogenated into C_7 alkenes on the metallic function of bi-functional catalysts, are good model molecules for hydrocraking, representative of the behavior of a large range of molecule sizes,[18,34] with a large network of isomerization and cracking reactions and a significant effect of confinement on selectivity.[35]

The type B isomerization reaction described in this work increases the branching degree of the reactant (hereafter labelled as R), transforming a monobranched secondary carbocation (the 4-methyl-hexen-2-ium cation) into a dibranched tertiary carbocation, the 2,3-dimethyl-penten-3-ium cation (latter called I_3, Figure 1.a). In this reaction, a single protonated cyclopropane (PCP), non-classical carbocation, is expected as a transition state connecting two classical carbocations. The acid chabazite zeolite is used as a model for the catalyst. In our previous work,[31] we investigated the mechanism of an isomerization reaction between tertiary carbenium ions, transforming a dibranched into a tri-branched carbenium ion. To the best of our knowledge, the isomerization reaction type studied here has never been investigated by any method beyond a simple static approach.[36,37,38]

In this study, we also present an alternative (mechanism II) to the conventional mechanism (mechanism I) of isomerization involving a 1,3 hydride shift between secondary and tertiary carbenium ions (Figure 1.b), that appears to take place spontaneously in the course of certain MD simulations. In experimental and kinetic modeling[39] practice, it is impossible to conclude about the preferred route. Thus, a detailed investigation of the individual rates is required to determine the intrinsic free energy barriers for the conventional as well as for the alternative reaction mechanisms at relevant temperatures (300 K and 500 K) which allows us to compare kinetics of these two pathways.

For that purpose, the crucial question of the correct sampling of the different rotational isomers dictating the mechanisms, which has been overlooked in previous simulations of reactions of hydrocarbons in zeolites, is rigorously addressed here, following the method developed in our previous work.[31] This question is challenging because a direct sampling of all the conformations is inefficient in a straightforward *ab initio* molecular dynamics.

The detailed study of these reactions also provides the opportunity to compare the thermal stabilization of secondary carbenium ions in zeolites with respect to that of tertiary carbenium ions. In-depth structural analysis is also performed to identify similarities and differences between type A (methyl shift, 1,3-hydride shift) and type B transition states, considering the results of the present study and our previous work.[31] Finally, a general ranking between various type A and type B isomerization kinetics at the atomic scale has been obtained, and discussed with the empirically proposed ranking.[2,9,11,34,39–42]

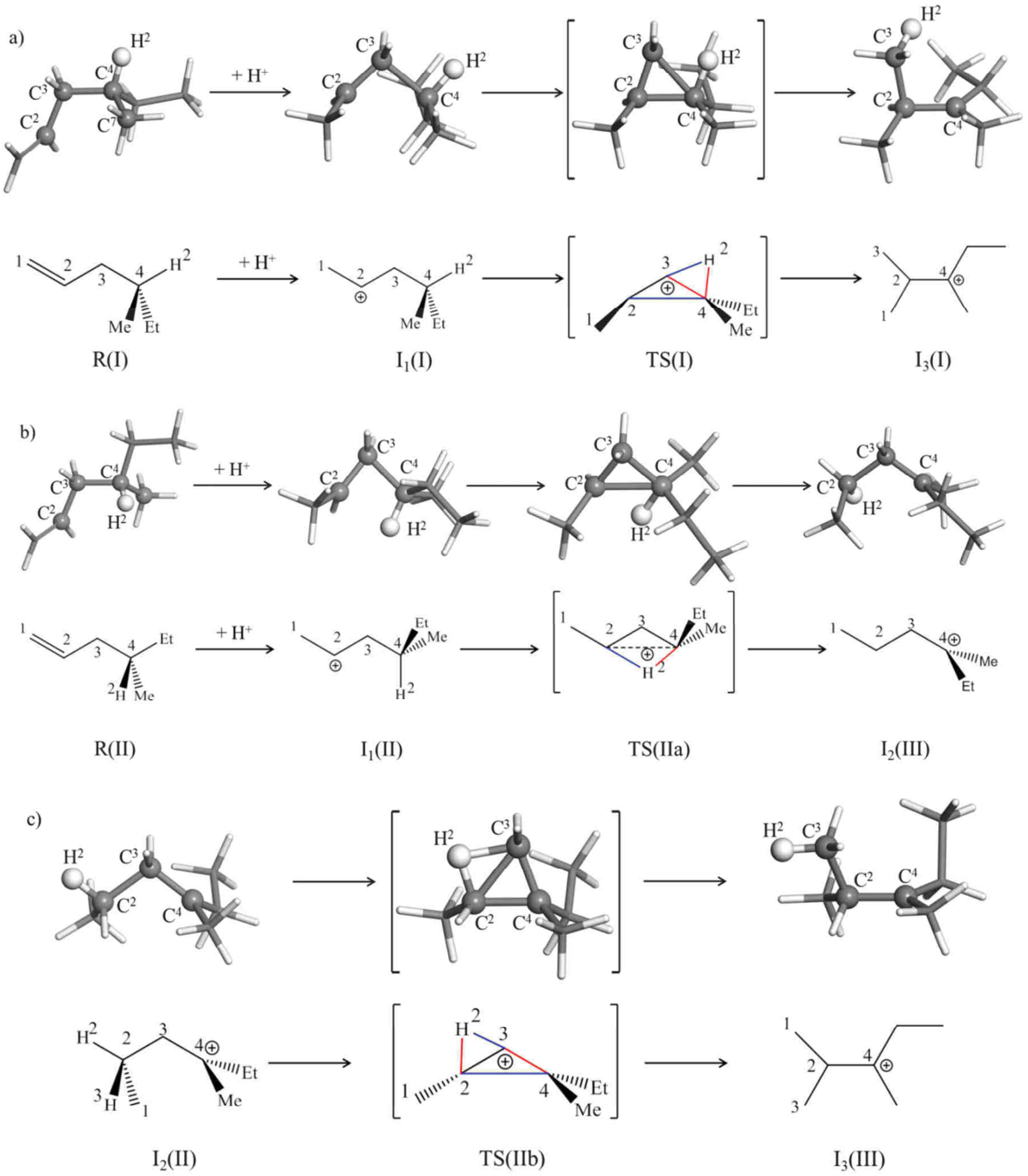

Figure 1. Conventional (mechanisms I) and alternative (mechanism II) mechanisms for the transformation of 4-methyl-hex-1-ene into 2,3-dimethyl-penten-3-ium cation: a) mechanism I - type B isomerization between a secondary and a tertiary carbenium; b) mechanism II, step 1 – 1,3 hydride shift and c) mechanism II, step 2 - type B isomerization between two tertiary carbenium ions. The displayed structures have been optimized with static calculations in the gas phase (see Section 2). The blue and red lines indicate the bonds that are, respectively, formed and broken during the reactions. For reactants, intermediates and products, the symbols I, II, and III displayed in brackets refer to different rotational isomers (see Section 3.1 for R and SIII for I_2 and I_3).

IV.2. Methodology

Periodic DFT calculations were performed using the VASP code.[43–45] The Kohn-Sham equations have been solved variationally in a plane-wave basis set using the projector augmented-wave (PAW) method of Blöchl[46], as adapted by Kresse and Joubert[47]. The PBE exchange-correlation functional in the generalized gradient approximation proposed by Perdew et al.[48] was used. The D2 correction of Grimme[49] was applied to account for long-range dispersion interactions taking place upon the adsorption of hydrocarbon molecules in zeolites[50–52]. As a relatively large supercell (see Figure 2 and Section SI) was used for describing the chabazite zeolite, the Brillouin zone sampling was restricted to the Γ-point. A plane-wave cutoff energy of 400 eV was used in all calculations and the convergence criterion for the electronic self-consistency cycle was set to 10^{-6} eV.

All relaxations related to the gas phase reactions were performed using the optimization engine GADGET[53,54] requiring that the forces acting on all atoms be smaller than 0.005 eV/Å. The intrinsic reaction coordinate [55,56] (IRC) analysis has been employed using the damped velocity Verlet algorithm[57] in order to ensure that identified potential energy minima representing reactant and product states are linked by a common path on a potential energy landscape crossing a single first-order saddle point (transition state). The vibrational eigenspectra of resulting potential energy minima and saddle points have been examined in order to ensure that the number of imaginary frequencies was correct (i.e zero for reactants and products and one for transition states).

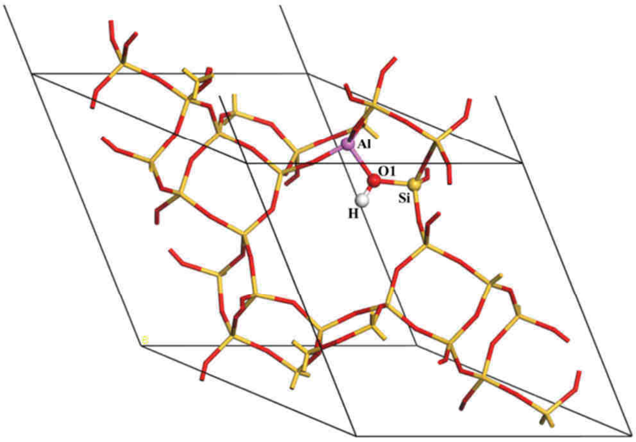

Figure 2. Unit cell of protonated chabazite.

Born Oppenheimer Molecular dynamics simulations (MD) have been performed in the NVT ensemble. The simulation temperatures of 300 K and 500 K have been considered, their average values have been maintained by the Andersen thermostat[58] with a collision frequency per atom of 0.01 fs^{-1}. The classical equations of motion were integrated using the leap-frog algorithm with an integration step of 1 fs. The atomic mass of tritium has been chosen for all H atoms in order to avoid numerical instabilities possibly caused by the use of a relatively large integration step. Free energies have been computed using the simulation protocol described in Ref.[59], which is based on the blue moon ensemble method,[32,33] as implemented in VASP.[60] In this approach, derived from the transition state theory,[58] the free-energy of activation ($\Delta A^{\ddagger}$) for the process $X \rightarrow Y$ is defined as follows:

$$\Delta A^{\ddagger} = \Delta A_{\xi_{ref,X} \rightarrow \xi^*} - k_B T \ln\left(\frac{h}{k_B T}\frac{\langle|\dot{\xi}^*|\rangle}{2} P(\xi_{ref,X})\right), \tag{1}$$

where $\Delta A_{\xi_{ref,X} \rightarrow \xi^*}$ is a reversible work needed to shift the value of reaction coordinate (ξ) from some arbitrary reference value characteristic for reactant ($\xi_{ref,X}$) to the value ξ^* defining the free-energy transition state, $\langle|\dot{\xi}^*|\rangle$ is the average velocity of the reaction coordinate at the transition state, and $P(\xi_{ref,X})$ is the probability density of the state $\xi_{ref,X}$ in ensemble of all reactant (X) configurations. As described in Ref.[59], the term $\Delta A_{\xi_{ref,X} \rightarrow \xi^*}$ is obtained from the bluemoon ensemble method,[32,33] $P(\xi_{ref,X})$ can be determined using the straightforward MD simulations, and $\langle|\dot{\xi}^*|\rangle$ is computed numerically using a constrained MD with $\xi(r) = \xi^*$ (see Supporting Information SIII). Free energies of reaction ($\Delta A_{X \rightarrow Y}$) are computed similarly:

$$\Delta A_{X \rightarrow Y} = \Delta A_{\xi_{ref,X} \rightarrow \xi_{ref,Y}} - k_B T \ln\left(\frac{P(\xi_{ref,X})}{P(\xi_{ref,Y})}\right). \tag{2}$$

In Equation (2), $\Delta A_{\xi_{ref,X} \rightarrow \xi_{ref,Y}}$ is the reversible work needed to shift the value $\xi(\boldsymbol{r})$ from $\xi_{ref,X}$ to some arbitrary reference value $\xi_{ref,Y}$ characteristic for product (P), and $P(\xi_{ref,Y})$ is the probability density of the state $\xi_{ref,Y}$. It is an important property of Equations (1) and (2) that the computed free energies are independent of the particular choice of the approximation to the reaction coordinate (provided the approximation drives the transformation from reactant to product reversibly) which is particularly important when comparing the free energetics of chemical reactions differing in reaction mechanisms and consequently also in definitions of ξ. The calculation of statistical uncertainties of $\Delta A^{\ddagger}$ and $\Delta A_{X \rightarrow Y}$ is discussed in Section SX.

The length of straightforward MD simulations used to determine probability densities of reference states was at least 100 ps (see Section SIV in Supporting Information) while the length of all constrained MD runs performed within the BM simulations was 50 ps. In each MD run, the initial period of 5 ps has been considered as equilibration and the corresponding data were discarded from the calculations of ensemble averages. Undesired by-reactions, such as the deprotonation of the reactant or product molecules, have been prevented by the use of appropriate restraining potentials described in Section SV.

IV.3. Results

The scheme describing the conventional mechanism (designated hereafter as the mechanism I) of the 4-methyl-1-hexene isomerization is shown in Figure 1.a. In the first step, the alkene reactant R(I) is protonated to form a secondary carbenium cation I_1(I) (4-methyl-hexen-2-ium cation, the Roman numeral (I) is used to label the specific rotamer involved (*vide infra*)). Next, the C^2–C^4 bond is formed, the C^3–C^4 bond is broken, while the hydrogen atom H^2 is shifted from C^4 to C^3. The 2,3-dimethyl-penten-3-ium tertiary cation I_3 is obtained. All the events of the latter reaction step are assumed to proceed via a single transition state (TS(I)) corresponding to a protonated cyclopropane (PCP).[2,7,8,35,36]. Hence, due to steric reasons, this reaction step requires a specific orientation of the shifted hydride with respect to the C^3–C^4 bond in the reaction intermediate I_1(I). As a product of this reaction step, tertiary carbenium cation I_3 is formed.

In order to learn about the finite-temperature behavior of the system at different stages of reaction, exploratory metadynamics[60,61] calculations in the NVT ensemble have been performed with T = 300 K. In these simulations, the cation I_1(I), when created, was almost always transformed into another rotamer (hereafter labelled as I_1(II), Figure 1.b before the expected second reaction step described above started. Hence, instead of observing the $I_1(I) \rightarrow I_3$ reaction, an alternative process (1,3 hydride shift) has been identified leading to formation of monobranched tertiary cation (3-methyl-hexen-3-ium cation) I_2(III). Such 1,3 hydride shift reactions have been reported in the literature, as a way to avoid the formation of intermediate secondary carbenium ions, and as an alternative to two consecutive 1,2 hydride shifts.[40] As the state I_2(II) can be transformed into the I_3 formed in the conventional reaction mechanism, we consider the $I_1(II) \rightarrow I_2 \rightarrow I_3$ sequence as an alternative reaction route (mechanism II).

IV.3.1. Characterization of the reactant state

a) Gas phase simulations

As discussed in the previous section, the different variants of isomerization mechanism of 4-methyl-1-hexene require different internal geometry of the reactant molecule. The relevant geometry changes can be controlled via variation of the dihedral angle (τ) between atoms C^2-C^3-C^4-C^7 (Figure 3) in a gas phase simulation. It is therefore instructive to explore the dependence of potential energy of the reactant molecule in the gas phase on this parameter. The corresponding potential energy profile (ΔV vs. dihedral angle τ) obtained in a series of constrained relaxations with a fixed value of τ is shown in Figure 4.a. Three stable rotamers (corresponding to potential energy minima) have been identified (Figure 3). The corresponding structures, hereafter labelled as R(I), R(II), and R(III), are nearly degenerate in energy, the difference between the lowest (R(III)) and the highest (R(I)) energy states being only ~3 kJ/mol. The rotamers R(II) and R(III) are separated by a relatively low barrier of ~13 kJ/mol, while the two barriers separating the state R(I) from the other two rotamers are ~5 kJ/mol higher. When the molecule is protonated to create cation I_1, the corresponding potential energy profile changes significantly (Figure 4.a) whereby only two stable rotational isomers, I_1(I) and I_1(II), are identified. The protonation of the rotamer R(I) leads to formation of a secondary cation I_1(I) in which the value of τ remains basically unchanged. Interestingly, the protonation of R(II) and R(III) at fixed τ would create unstable structures that both relax to the same minimum I_1(II) when the constraint is removed. The cation I_1(II) is significantly (15 kJ/mol) lower in energy compared to the I_1(I) state. The barrier for the $I_1(II) \rightarrow I_1(I)$ transformation (31 kJ/mol) increases dramatically compared to the barriers determined for the neutral molecule, while that for the reverse process remains modest (15 kJ/mol). All these results explain the behavior observed in our exploratory metadynamics run (*vide supra*), as I_1(II) is the rotamer giving rise to the 1,3 hydride shift instead of the direct isomerization (via TS(I)). In particular, it is obvious that, due its significantly lower energy, the I_1(II) state is formed with a greater likelihood than the rotamer I_1(I). Moreover, even if the state I_1(I) is formed, it is likely to transform into I_1(II) before the reaction $I_1(I) \rightarrow I_3$ is completed, which follows from the fact that the barrier for the transformation is at least a factor four lower compared to that for the reaction (*vide infra*).

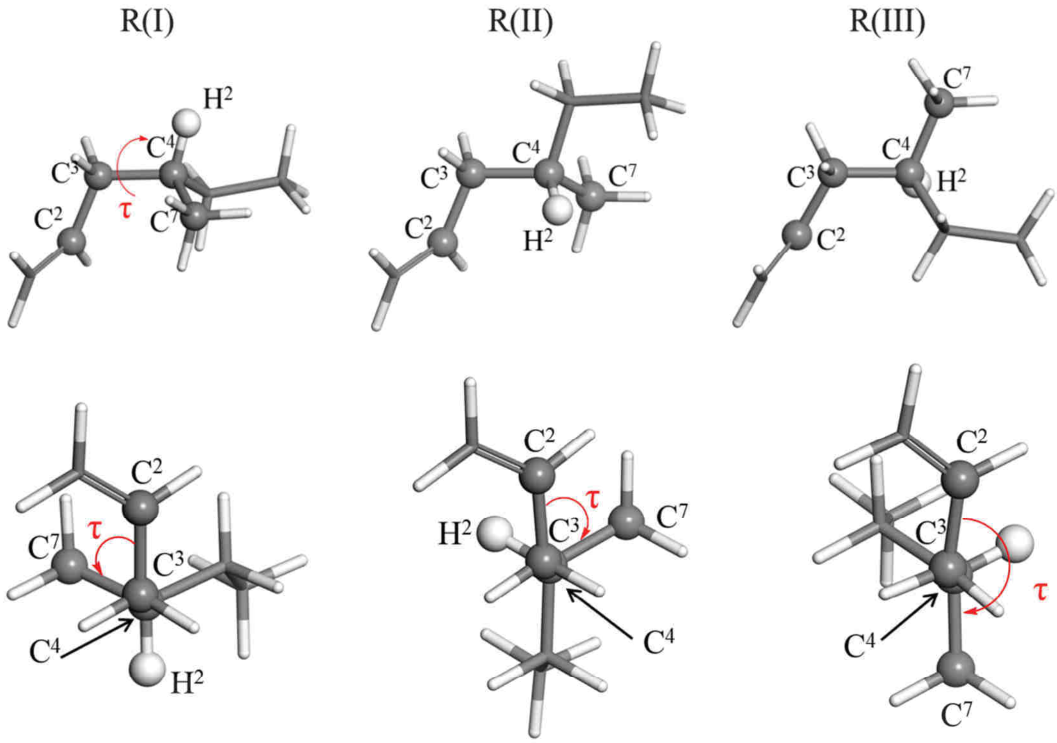

Figure 3. Rotational isomers R(I) ($\tau \approx$ -60 deg.), R(II) ($\tau \approx$ 60 deg) and R(III) ($\tau \approx$ 180 deg.) of the reactant 4-methyl-hexene, obtained for the gas phase reaction. Top panels: side view; bottom panels: front view chosen so that the atom C^4 overlaps the atom C^3.

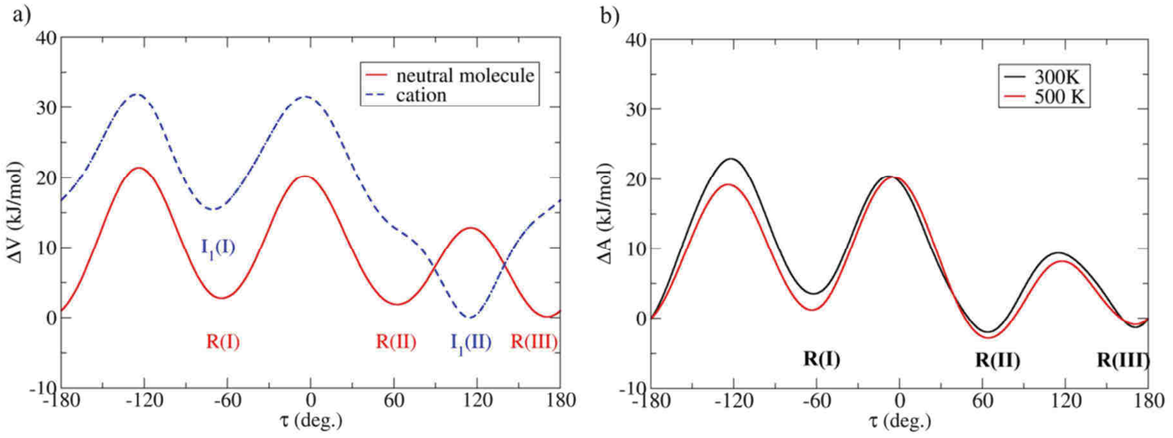

Figure 4. a) Potential energy as a function of dihedral angle (τ) defined by the atoms C^2, C^3, C^4, and C^7 (cf. Figure 3) computed using constrained relaxations of neutral molecule (R) and cation (I1) in the gas phase. Zero on the energy axis is defined by the lowest energy found for each profile. b) Free energy profile as a function of the torsion angle τ for the neutral molecule (R) in chabazite at T = 300 K and 500 K. Note that periodic boundary conditions apply, i.e. the point $\tau = -180$ deg. is identical to the point $\tau = 180$ deg.

b) Reactant adsorbed in chabazite

Next, we shall examine whether the results from our analysis of the molecular systems remain valid for the reaction taking place in zeolite at finite temperature. To this end, a blue moon simulation has been carried out for the reactant molecule in CHA to study the free energy as a function of τ for T = 300 K and 500 K. This constrained blue moon simulation has been performed using a grid of 20 integration points evenly distributed over the interval $-180\ \text{deg.} \leq \tau < 180\ \text{deg.}$ The computed free energy profiles are presented in Figure 4.b. The shapes of the free energy profiles at both temperatures are qualitatively similar to the potential energy determined for the neutral molecule (Figure 4.a) indicating that the energetics of the internal rotation of molecule is determined mainly by mutual interactions of atoms constituting it, while the confining environment provided by zeolite can be considered as a small perturbation to the relative stability of rotamers. The observed modest thermal effect is not unexpected for a monomolecular reaction. We note that a free energy profile cannot be determined for the secondary cation I_1 in chabazite, because of its too short lifetime given by the fact that this state is not a deep free energy minimum and easily transform into π-complexes or alkoxides (see Sections 3.2 and 3.3).

For the purpose of further analysis (see later, Sections 3.2 and 3.3), we determine the likelihoods of occurrence of individual rotamers among all reactant states. Using the free energy profile $A(\tau)$, the likelihood of the state R(I) is computed as follows:

$$p\big(R(I)\big) = \frac{\int_{\tau_{max,1}}^{\tau_{max,2}} exp\left(-\frac{A(\tau)}{k_B T}\right) d\tau}{\int_{-180°}^{180°} exp\left(-\frac{A(\tau)}{k_B T}\right) d\tau}, \tag{3}$$

where $\tau_{max,1}$ and $\tau_{max,2}$ are the positions of the first and the second maxima on the free energy profile shown in Figure 4.b, respectively. Probabilities for states R(II) and R(III) are defined analogically. The values of $p\big(R(I)\big)$, $p\big(R(II)\big)$, and $p\big(R(III)\big)$ computed for T=300 K are 5.8 %, 55.7 % and 38.5 %, respectively. At T = 500K, these values change to 16.7 %, 49.8 % and 33.5 % respectively.

IV.3.2. Mechanism I

All terms needed to determine the free energies of activation and of reaction via Equations (1) and (2) are summarized in Table 1. The free energy profiles $(\Delta A(\xi))$, corresponding to the reversible work needed to shift the value of reaction coordinate from the reference value characteristic for reactant to the given value of ξ, have been computed using the blue moon ensemble approach[32,33]. The following approximation to the reaction coordinate has been chosen:

$$\xi = \frac{d(C^1 - H^1)}{d(O^1 - H^1)} + \frac{d(C^3 - H^2)}{d(C^4 - H^2)}, \tag{4}$$

where $d(X - Y)$ stands for distance between atoms X and Y and the labelling of atoms is as explained in Figure 5. This approximation to reaction coordinate involves only the moving hydrogen atoms and the atoms (oxygen and/or carbon) to which they are bound at various stages of the reaction. The skeletal rearrangement of carbon atoms turns out to be a consequence of the proton transfer driven by ξ.

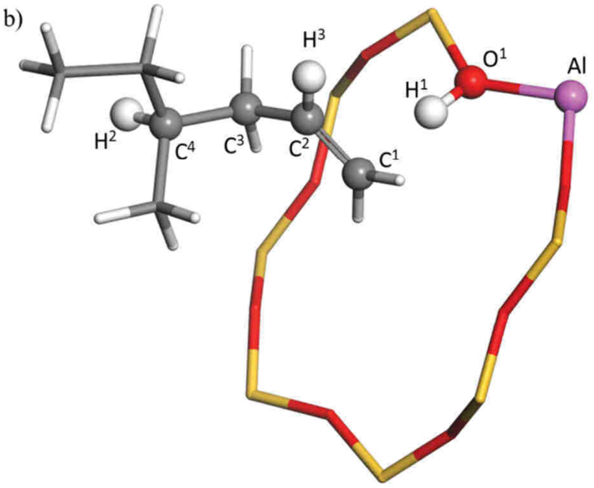

Figure 5. π-complex of 4-methyl-hex-1-ene adsorbed in chabazite with numbering of the atoms used in Equation (4).

For the integration of free energy gradients, a mesh of 22 points has been used covering the intermediate states distributed between the alkene molecule (R(I)) and the tertiary carbenium ion I_3. The reference state ($\xi_{ref,R} = 3.76$) has been chosen as a high likelihood state identified on probability distribution function determined for R(I) using straightforward MD (Section SIV.1). The resulting free energy profiles are shown in Figure 6. The transition state TS(I) ($\xi^* = 1.56$ for both temperatures) has been identified as the maximum on $\Delta A(\xi)$.

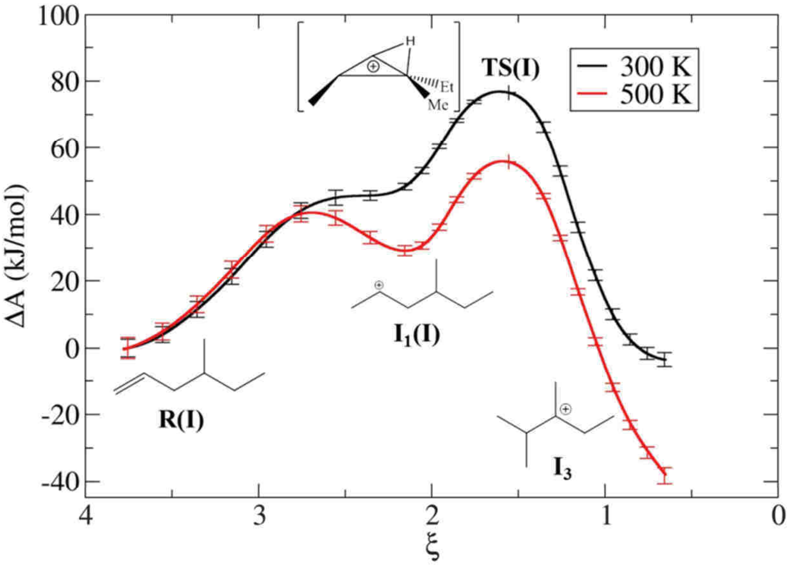

Figure 6. Free energy profiles, ΔA(ξ), computed using the blue moon ensemble approach for the isomerization reaction via mechanism (I) in chabazite at T = 300 K and 500 K. The error bars are determined from the standard errors of the free energy gradients.[60]

The initial parts of profiles, ranging between the reference value for the alkene ($\xi = 3.76$) and the transition state of protonation ($\xi^* = 2.76$) and corresponding to the protonation of the alkene, are very similar for both temperatures. The transition state of protonation becomes apparent at 500 K as a consequence of the stabilization of the secondary cation (*vide infra*) and its structure can be characterized by measuring the two distances changing during the protonation, O^1-H^1 (1.47 Å) and C^1-H^1 (1.26 Å) (Figure S15 in Section SVII.3).

The second part of the profile, ranging from $\xi = 2.76$ to $\xi = 2.16$ (the secondary carbenium ion), exhibits significant variations with T, which can be explained by the relative entropic stabilization of free forms (carbenium ions) with respect to the bound forms (π-complexes). A similar conclusion was reported by Cnudde and coworkers when comparing the π–complexes, alkoxides and carbenium ions formed by pentene in H-ZSM-5.[26–28] The stabilization of the cationic form has a significant impact on the value of the term $\Delta A_{\xi_{ref,R} \rightarrow \xi^*}$ constituting a major contribution to the free energy of activation (see Equation (1)): its value decreases from 76.6 ± 5.4 kJ/mol to 55.7 ± 6.4 kJ/mol as T is raised from 300 K to 500 K. We note that the secondary cation has a classical structure (Figure 1 and Section SVIII.2) in agreement with the fact that non-classical hydrido-bridged structures[62,63] are only found at very low temperatures.[64]

The third part of the profile corresponds to the monomolecular transformation between the secondary ($\xi = 2.16$) and tertiary ($\xi = 0.66$) cations by the type B isomerization. TS(I) is an edge-protonated cyclopropane (Figure 1), the structure of which will further be discussed in Section 4.2. As expected for a monomolecular transformation, the thermal effect is weak and, as evident from the almost identical shapes of profiles computed for different T (the segments with $1 < \xi <2.16$ can be brought into an almost perfect coincidence via a simple rigid shift by 18 kJ/mol), a large part of this profile is virtually independent of temperature. This result is also in line with our static gas phase simulations predicting only a small increases in free energy of activation for the forward (by 5.9 kJ/mol) and reverse (by 5.2 kJ/mol) modes of the $I_1 \rightarrow I_3$ transformation when T is increased from 300 K to 500 K. As evident from the data presented in Table S6, these small variations in free energy of activation originate mainly in vibrational entropy which decreases (due to looser bonding) when transition state is formed in either direction of transformation. The difference between the final and the initial state ($\Delta A_{\xi_{ref,R} \rightarrow \xi_{ref,I_3}}$) contributing to the free energy of reaction (Equation (2)) increases significantly with T (-3.4 ± 6.8 kJ/mol (300 K) and -37.5 ± 8.0 kJ/mol (500 K)), which is given by the relative stabilization of the cationic form with respect to the π–complex. Once again, the origin of the major part of the difference in $\Delta A_{\xi_{ref,R} \rightarrow \xi_{ref,I_3}}$ computed for different T can be traced back to the region between $\xi = 2.76$ and 2.16 where the protonation of reactant is completed and the newly formed secondary cation is fully detached from the zeolite framework, gaining thus in entropy due to newly acquired hindered translations.

Following the idea developed in our previous study,[31] the term $P(\xi_{ref,R})$ is defined as follows:

$$P(\xi_{ref,R}) = \tilde{P}(\xi_{ref,R})\, p(R(I)), \qquad (5)$$

where $\tilde{P}(\xi_{ref,R})$ is the probability density of the configuration $\xi_{ref,R}$ among the configurations of rotational isomer R(I) (0.94 (300 K) and 0.34 (500 K), see Section SIV.1), and $p(R(I))$ is the probability to find rotamer R(I) among all reactant configurations. The formulation via Equation (5) allows us to compute $P(\xi_{ref,R})$ efficiently despite the relatively high free energy barriers separating the individual rotamers. In particular, the term $\tilde{P}(\xi_{ref,R})$ is determined using a straightforward MD run performed for the rotational isomer R(I) and the probability $p\big(R(I)\big)$ is obtained from the free energy profiles $A(\tau)$ as discussed in Section 3.1.

Finally, the term $P\big(\xi_{ref,I_3}\big)$ needed in the calculations of $\Delta A_{R\rightarrow I_3}$ has been determined for $\xi_{ref,I_3} = 0.66$. Because of the presence of two different rotational isomers separated by small but significant barriers (Section SII.2), the determination of $\tilde{P}\big(\xi_{ref,I_3}\big)$ has been performed with dedicated blue moon simulations (Section SIV.3).

The computed free energies of activation are 84.1 ± 5.4 kJ/mol (300 K) and 69.2 ± 6.4 kJ/mol (500 K). As evident, the decrease of $\Delta A^{\ddagger}$ with T is slightly less significant than that for $\Delta A_{\xi_{ref,R}\rightarrow\xi^{*}}$ obtained from the free energy profiles.

The free energies of reaction computed for 300 K and 500 K are 6.0 ± 6.8 kJ/mol and -25.3 ± 8.0 kJ/mol, respectively. This trend, once again, reflects the stabilization of the cationic form with respect to the π–complex. Although the difference in $\Delta A_{R\rightarrow I_3}$ is very similar to that computed for $\Delta A_{\xi_{ref,R}\rightarrow\xi_{ref,I_3}}$, the numerical values computed for the fixed T differ significantly (see Table I) which is primarily caused by the additional positive work needed to create the initial reactant configuration and which is accounted for only in the former term. This result, together with the significant differences in the $\Delta A^{\ddagger}$ values underline the importance of correct treatment of all terms in the free energy calculations.

Table 1. The values of computed terms used in the calculation of free energies of activation ($\Delta A^{\ddagger}$) and of reaction ($\Delta A_{X\rightarrow Y}$) via Equation (1) and (2), respectively.

Mechanism I							
T (K)	$\langle\lvert\dot{\xi}^{*}\rvert\rangle$ (s^{-1})	$P(\xi_{ref,R})$	$P(\xi_{ref,I_3})$	$\Delta A_{\xi_{ref,R}\rightarrow\xi^{*}}$ (kJ/mol)	$\Delta A^{\ddagger}$ (kJ/mol)	$\Delta A_{\xi_{ref,R}\rightarrow\xi_{ref,I_3}}$ (kJ/mol)	$\Delta A_{R\rightarrow I_3}$ (kJ/mol)
300	$1.10 \cdot 10^{13}$	0.055	2.39	76.6 ± 5.4	84.1 ± 5.4	-3.4 ± 6.8	6.0 ± 6.8
500	$1.40 \cdot 10^{13}$	0.057	1.08	55.7 ± 6.4	69.2 ± 6.4	-37.5 ± 8.0	-25.3 ± 8.0

Mechanism II, step 1							
T (K)	$\langle\lvert\dot{\xi}^{*}\rvert\rangle$ (s^{-1})	$P(\xi_{ref,R})$	$P(\xi_{ref,I_2})$	$\Delta A_{\xi_{ref,R}\rightarrow\xi^{*}}$ (kJ/mol)	$\Delta A^{\ddagger}$ (kJ/mol)	$\Delta A_{\xi_{ref,R}\rightarrow\xi_{ref,I_2}}$ (kJ/mol)	$\Delta A_{R\rightarrow I_2}$ (kJ/mol)
300	$1.08 \cdot 10^{13}$	0.84	2.38	58.7 ± 4.6	59.5 ± 4.6	-0.1 ± 7.8	2.6 ± 7.8
500	$1.45 \cdot 10^{13}$	0.37	4.87	51.5 ± 5.6	57.1 ± 5.6	-21.0 ± 7.5	-10.3 ± 7.5

Mechanism II, step 2							
T (K)	$\langle\lvert\dot{\xi}^{*}\rvert\rangle$ (s^{-1})	$P(\xi_{ref,I_2})$	$P(\xi_{ref,I_3})$	$\Delta A_{\xi_{ref,I_2}\rightarrow\xi^{*}}$ (kJ/mol)	$\Delta A^{\ddagger}$ (kJ/mol)	$\Delta A_{\xi_{ref,I_2}\rightarrow\xi_{ref,I_3}}$ (kJ/mol)	$\Delta A_{I_2\rightarrow I_3}$ (kJ/mol)
300	$9.90 \cdot 10^{12}$	1.54	0.44	77.8 ± 2.6	77.3 ± 2.6	0.3 ± 3.0	-2.8 ± 3.0
500	$1.26 \cdot 10^{13}$	0.93	1.46	83.8 ± 4.1	86.2 ± 4.1	2.4 ± 4.8	4.2 ± 4.8

IV.3.3. Mechanism II

Mechanism II consists of two elementary reaction steps, namely the transformation from the π-complex R to the intermediate tertiary cation I$_2$, and the type B isomerization reaction from I$_2$ to I$_3$ (Figure 1). These two activated processes are explored in two independent sets of simulations with the following approximations to the reaction coordinates (see Figure 5 for the numbering): the transformation between the π-complex and the tertiary cation I$_2$ is described by the following parameter

$$\xi_a = \frac{d(C^1 - H^1)}{d(O^1 - H^1)} + \frac{d(C^2 - H^2)}{d(C^4 - H^2)}, \tag{6}$$

while the transformation between two tertiary cations I$_2$ and I$_3$ is studied using the parameter

$$\xi_b = \frac{d(C^3 - H^2)}{d(C^2 - H^2)}. \tag{7}$$

The blue moon simulations have been performed using 20 integration points distributed along ξ_a and 22 integration points along ξ_b and the resulting free energy profiles are displayed in Figure 7.

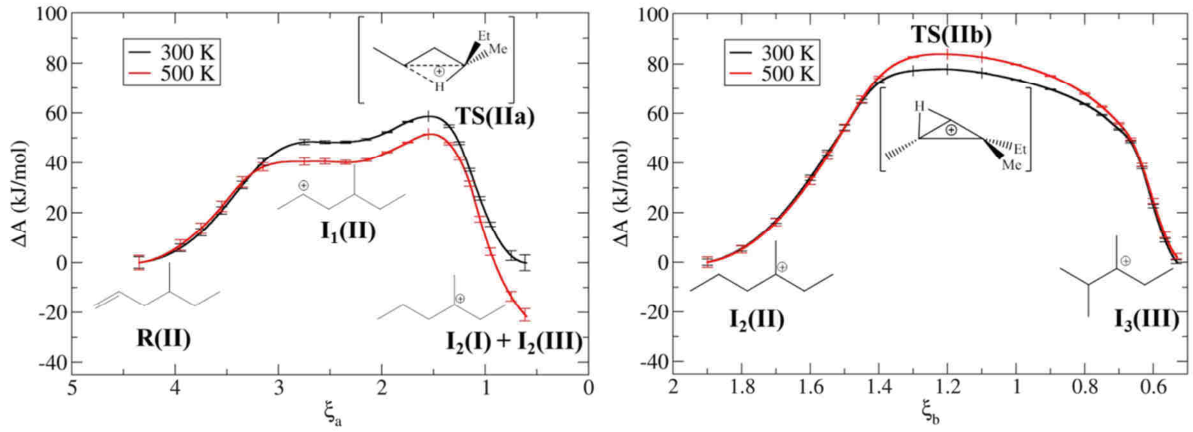

Figure 7. Free energy profiles, ΔA(ξ), for the transformations between the π-complex R and the intermediate tertiary cation I_2 (left), and between the tertiary cations I_2 and I_3 (right) taking place within the mechanism (II) of isomerization of 4-methyl-hex-1-ene into 2,3-dimethyl pent-2-ene.

The free energy profile for the first step starting from the π–complex of rotamer R(II) ($\xi_{ref,R} = 4.35$) exhibits some of the features observed in the case of the mechanism I. First, the part of the profile corresponding to the protonation of R ($\xi < 3.30$) is nearly identical at both temperatures. Second, the difference between profiles computed for different temperatures develops in a narrow region ($3.30 \leq \xi < 2.80$) where a metastable secondary cation is formed. As before, this difference is related to the thermal stabilization of the cationic forms with respect to the π–complex. Third, the region where the monomolecular 1,3 hydride shift between secondary and tertiary cation occurs ($2.80 \leq \xi$) is nearly temperature independent (i.e. the two profiles can be brought into coincidence via a shift by a constant). This latter finding is consistent with the gas phase results reported in Table S7 predicting a very modest increase in the free activation barrier for the $I_1 \rightarrow I_2$ transformation due to increased T (2.1 kJ/mol (300 K) and 5.4 kJ/mol (500 K)). The computed values of $\Delta A_{\xi_{ref,R} \rightarrow \xi^*}$ and $\Delta A_{\xi_{ref,R} \rightarrow \xi_{ref,I_2}}$ for T=300 K are 58.7 ± 4.6 kJ/mol and -0.1 ± 7.8 kJ/mol, respectively. As a consequence of the thermal stabilization of the cation, $\Delta A_{\xi_{ref,R} \rightarrow \xi^*}$ and $\Delta A_{\xi_{ref,R} \rightarrow \xi_{ref,I_2}}$ decrease to 51.5 ± 5.6 kJ/mol and -21.0 ± 7.5 kJ/mol, respectively, when T is increased to 500 K. The free energy transition state for the 1,3 hydride shift occurs at $\xi^* \approx 1.56$ and its structure is similar to that of the reaction in the gas phase (see Figure 1), i.e. it can be considered as an edge-protonated cyclopropane (see Section 4.2). The values of $P\left(\xi_{ref,R}\right)$ were computed as described in Sec. 3.2. As two different rotamer states (I_2(I) + I_2(III)) separated by relatively large free energy barriers are present, dedicated blue moon sampling simulations have been performed (Section SII.1) to determine $P\left(\xi_{ref,I_2}\right)$. All terms needed to compute free energies of activation and of reaction via Equations (1) and (2) are compiled in Table 1.

Unlike the term $A_{\xi_{ref,R}\rightarrow\xi^*}$, the free energy of activation $\Delta A^{\ddagger}$ is nearly independent of temperature, with the numerical values being 59.5 ± 4.6 kJ/mol (300 K) and 57.1 ± 5.6 kJ/mol (500 K).

The values $\Delta A_{R\rightarrow I_2}$ computed for the first step of mechanism II are 2.6 ± 7.8 kJ/mol (300 K) and -10.3 ± 7.5 (500 K) and these values are, again, much lower than $A_{\xi_{ref,R}\rightarrow\xi_{ref,I_2}}$. Up to this point, the first step of mechanism II has been discussed as proceeding via the rotamer R(II). Note, however, that the states R(II) and R(III) are similar in structure (they differ only by the exchange of methyl and ethyl group on C^4 atom, see Figure 3) and they are nearly energy degenerate (Figure 4.b). Furthermore, as discussed in Section 3.1, they form the same intermediate secondary cation I_2 upon their protonation. The reaction involving R(III) should differ from the one proceeding via R(II) only in the initial part. Hence it is reasonable to consider R(III) as another microstate of reactant that is active in mechanism II, and this fact can be taken into account by modifying the term $P\left(\xi_{ref,R}\right) = \tilde{P}\left(\xi_{ref,R}\right)\left(p\left(R(II)\right) + p\left(R(III)\right)\right)$ used in Equation (1) making use of the fact that the probability distribution functions $\tilde{P}\left(\xi_{ref,R}\right)$ for R(II) and R(III) are very similar. Such a modification leads to a very small decrease of the free energy of activation $\Delta A^{\ddagger}$, which is now 58.0 ± 4.6 (300 K) and 54.6 ± 5.6 kJ/mol (500 K) and of the free energy of reaction $\Delta A_{R\rightarrow I_2}$ that changes to 1.1 ± 7.8 (300 K) and -12.8 ± 7.5 kJ/mol (500 K).

In the second reaction step, one form of tertiary cation I_2(II) (3-methyl-hexen-3-ium cation) is transformed into another one I_3(III) (2,3-dimethyl-penten-3-ium cation) via a type B isomerization reaction. The transition state is again an edge-protonated cyclopropane (see Section 4.2). As shown in Figure 7, the free energy profiles computed for two different temperatures differ mainly in the transition region ($0.7 \leq \xi < 1.5$), while the regions close to the states I_2 ($\xi \approx 1.90$) and I_3 ($\xi \approx 0.53$) are nearly temperature independent. In particular, restricted molecular vibrations in the transition state ($\xi^* \approx 1.56$) are responsible for negative activation entropy[31] (see Table S8 for the relevant static gas phase data) causing an increase in $\Delta A_{\xi_{ref,I2}\rightarrow\xi^*}$ with T (77.8 ± 2.6 kJ/mol (300 K) vs. 83.8 ± 4.1 kJ/mol (500 K)). Taking into account the contributions from $P\left(\xi_{ref,I_2}\right) = \tilde{P}\left(\xi_{ref,I_2}\right) \cdot p\left(I_2(II)\right)$ and $\langle|\dot{\xi}^*|\rangle$ (see Table 1) determined as described in Section SIII, the free energy of activation ${\Delta A^{\ddagger}}_{I_2 \rightarrow TS}$ computed for 300 K and 500 K is 77.3 ± 2.6 kJ/mol and 86.2 ± 4.1 kJ/mol, respectively. These results are in excellent agreement with the values of 74.4 ± 3.4 kJ/mol (300 K) and 83.4 ± 3.6 kJ/mol (500 K) reported in our previous work for a similar reaction involving related but different reactant (2,4-dimethyl-penten-2-ium cation).[31]

Due to the similarity between the initial and the final state of this reaction, the term $\Delta A_{\xi_{ref,I_2} \rightarrow \xi_{ref,I_3}}$ is very small (0.3 ± 3.0 kJ/mol (300 K) and 2.4 ± 4.8 kJ/mol (500 K)). Also the values of $P\left(\xi_{ref,I_2}\right)$ and $P\left(\xi_{ref,I_3}\right)$ differ only modestly within the given temperature (see Table 1) and hence the computed free energies of reaction $\Delta A_{I_2 \rightarrow I_3}$ are only -2.8 ± 3.0 kJ/mol and 4.2 ± 4.8 kJ/mol. The latter results compare very well with the values of 1.9 ± 3.8 kJ/mol and 3.7 ± 4.2 kJ/mol, obtained for the type B isomerization of 2,4-dimethyl-penten-2-ium cation reported in our previous work.[31]

IV.4. Discussion

IV.4.1. Thermal variation of the overall free energy profiles

The overall free energy profiles computed according to Equations (1) and (2) for both mechanisms at 300 K and 500 K are compared in Figure 8.

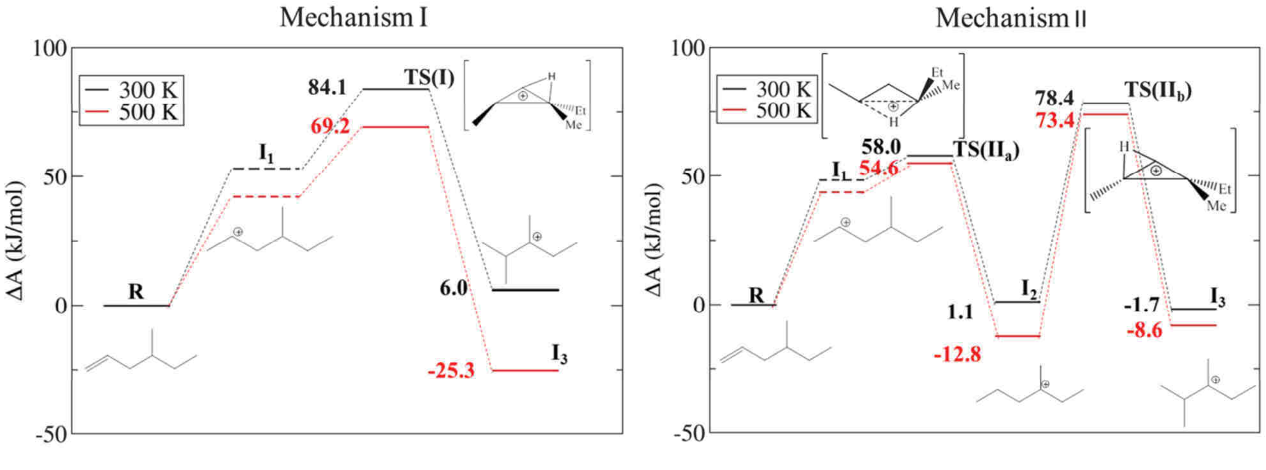

Figure 8. Overall free energy profiles for mechanisms I and II at 300 K and 500 K. A qualitative estimate of the free energy of secondary cation I_1 is indicated by a dash line and cumulated error bars along the profiles are displayed.

The dominant trend governing the thermal variation of the free energy profiles is the thermal stabilization of all free cationic species with respect to the neutral π-complex considered as reactant, by 6-33 kJ/mol. This is mainly entropic effect that favors unbonded forms over the structures in which the molecular motion is restricted due to interactions with zeolite and it has been reported also in the previous theoretical work by Cnudde et al. comparing the relative stabilities of π-complexes, alkoxides and carbenium ions formed by pentene in H-ZSM-5.[10,11,13] Another factor contributing to the shape of the overall free energy profile is the shift of transition states towards higher free energies with respect to the carbenium intermediate which is caused by vibrational entropy changes during the transformation. As we discussed in our previous work,[31] this effect can be estimated reasonably well by using a simple gas phase model and we utilized the same approach also in this work. As typical for monomolecular reactions, all transition states found for mechanisms I and II are more constrained than the corresponding stable states linked via common reaction coordinate leading to negative vibrational entropy of activation. As shown in Tables S6-S8, this entropy term always dominates over the internal energy contribution of relevant gas phase reactions and consequently the free energy of activation increases when T is raised from 300 K to 500 K (by 5.9 kJ/mol, 3.3 kJ/mol, and 5.5 kJ/mol for mechanism I, and first and second steps of mechanism II, respectively).

The relative free energies of the state I_3 created in both mechanisms should be identical. However, the statistical error, mainly due to the accumulation of uncertainties in free energy gradients integrated over the all reaction paths, and the systematic error, e.g. due to the noise in forces computed at the DFT level, numerical integration errors, or the use of approximations to reaction coordinate, imply that the values of $\Delta A_{R\to I_3}$computed for both mechanisms differ. For the lower temperature, this difference (7.7 kJ/mol) is well below the theoretical limit $1.96\sqrt{\sigma_I^2 + \sigma_{II,1}^2 + \sigma_{II,2}^2} =$ 10.8 kJ/mol, with σ_I and $\sigma_{II,1}$ and $\sigma_{II,2}$ being the standard errors determined for the free energies of reaction for mechanisms I, and steps 1 and 2 of the mechanism II (Table 1), respectively, and the factor 1.96 corresponds to 95 % confidence interval assumed throughout this work. Hence the difference in $\Delta A_{R\to I_3}$computed for the two reaction routes at 300 K is not statistically significant. For the higher T, the values of $\Delta A_{R\to I_3}$differ by 16.7 kJ/mol, which is slightly more than the theoretical value computed from the individual statistical uncertainties ($1.96\sqrt{\sigma_I^2 + \sigma_{II,1}^2 + \sigma_{II,2}^2} =$ 12.0 kJ/mol) indicating that our high T results are, to some extent, affected by the errors, statistical or systematic, which are hard to control. In any case, it is clear from our results that the relative free energy of the final state I_3 decreases when T is increased, and it is also evident that the temperature tends to stabilize the state I_3 relative to R.

IV.4.2. Comparison of structure and stability of the transition states for the 1,3 hydride shift and type B isomerization

Although the TS(I), TS(IIa) and TS(IIb) transition states show some structural similarities (they apparently all belong to the edge-protonated PCP family), they are very different in terms of stability. A deeper structural analysis may help in the identification of relevant differences between these states.

First, we showed that different rotamers of the reactant are involved in the 1,3 hydride shift or type B isomerization reaction, which explains the difference between seemingly similar transition states. This conclusion confirms the intuition of Brouwer and Hogeven who suggested, in an early work, that the existence of a high rotational energy barrier between conformations of the reactant could be responsible for the difference between the rates of these two reactions.[11] Concerning the 1,3 hydride shift, which is considered as a type A isomerization because it induces no change in the branching degree,[2] we find that the transition state is an edge-protonated PCP (TS(IIa)). However, its free energy is significantly lower as compared to the transition states of the type B isomerization reactions (TS(I) and TS(IIb)). According to our static gas phase simulations, the free energy difference between transition states with seemingly similar structures considered here stems mainly from the electronic contribution to free energy A_{el}. In fact, A_{el} for the TS(IIa) formed in the gas phase is 26.3 kJ/mol lower than that of TS(I) and 35.1 kJ/mol lower than that computed for TS(IIb) (Table S7 in Section SVII). Our calculations are in qualitative agreement with known experimental facts. In measurements performed in superacid solutions at -80°C, for instance, it was demonstrated that the 1,3 hydride shift between tertiary cations (starting from 2,4-dimethyl-penten-3-ium) is much easier than type B isomerization reactions. The experimentally deduced Gibbs free energy barriers are 36 kJ/mol and 71 kJ/mol for the 1,3 hydride shift and type B isomerization, respectively.[11,40] A qualitatively similar conclusion was obtained with DFT (B3LYP) calculations on C_6 species in the gas phase (with potential energy barriers of 72 kJ/mol for the 1,3 H-shift (tertiary to secondary cation) and 94 kJ/mol for the type B isomerization starting from the same tertiary cation).[38]

The analysis of the distributions of the bonds involved in the transition states (Figure 9 and Table S11 in Section SVIII.1) can provide some insight into the structural differences between the three protonated cyclopropanes (TS(I), TS(IIA) and TS(IIb)). In our blue moon simulations, the C-C distance between the two C atoms holding the extra hydrogen atom in TS(IIa) (C^2–C^4) is longer than in TS(I) (C^3–C^4) and TS(IIb) (C^2–C^3). The strength of this C–C bond is also much weaker, mainly at 500 K (see Section SVIII.1). This difference may be at the origin of the electronic energy difference between the 1,3 hydride shift transition state and other PCPs for type B isomerization reactions. As compared to other PCPs, the C^2-C^4 bond in TS(IIa) is elongated to 1.89 Å (for T=300 K) and 1.92 Å (for T=500 K) but since the average distance does not exceed 2 Å it is still possible to classify TS(IIa) as a PCP. The structure of the transition state for the 1,3 hydride shift reactions has been the subject of an intense debate in the literature[11,40,65–67,63] devoted to super-acidic media, discussing its PCP nature versus a four center TS. The PCP-type structure of TS(IIa) obtained in our MD simulations is consistent with structures proposed at the MP2 level.[63]

The type B isomerization reactions transition states (TS(IIb) and TS(I)) only differ in the location of the edge proton, see Figure 1. Their free energies (Figure 8) and local structures described by length of C-C bonds constituting PCP are similar (Figure 9 and Table S11 in Section SVIII.1). As compared to TS(IIa), the lengths of bonds C^3-C^4 in TS(I) and C^2-C^3 in TS(IIb) where the H^2 atom is located, are smaller (1.808 Å and 1.757 Å for T=300 K). Moreover, all interatomic distances within the C^2-C^3-C^4 cycle in TS(I) and TS(IIb) are rather insensitive to change in temperature, whereas the corresponding interatomic distances in TS(IIa) vary significantly with T. This result reflects the constrained nature of the TS(I) and TS(IIb) PCP, whereas TS(IIa) is intrinsically more flexible. The transition state TS(IIb), between monobranched to dibranched tertiary carbenium ions (mechanism II), is also comparable to that for the related transformation between dibranched to tribranched tertiary carbenium ions investigated in our previous paper.[31] These results suggest a certain degree of universality among the kinetic parameters of similar chemical reactions, even if the branching degree of the carbenium ion is different. The stability of the PCP for such reactions is not strongly affected by the number of alkyl groups attached to the cyclopropane ring, in agreement with previous findings made in super-acidic media.[11]

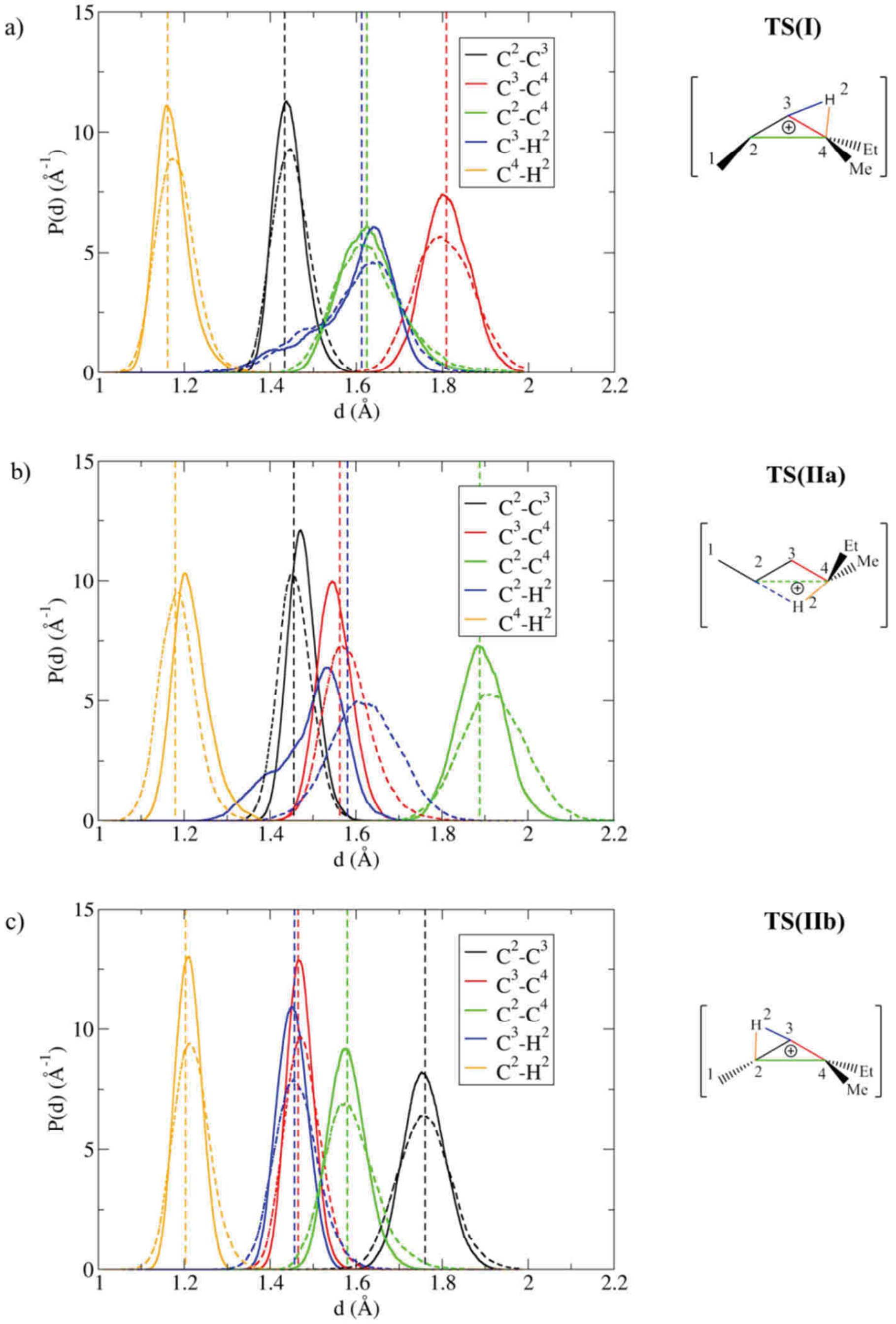

Figure 9. Probability distribution functions of selected C-C and C-H bonds in the transition states of (a) mechanism (I), (b) mechanism II, step 1, and (c) mechanism II, step 2 determined using MD at 300 K (solid lines) and 500 K (dash lines). The static approach results in gas phase are reported by vertical dashed lines.

IV.4.3. Implication for the kinetic modeling of isomerization reaction networks

IV.4.3.1. Comparison with kinetic modeling reported in the literature

Reaction networks for alkene isomerization (embedded in hydroisomerization-hydrocracking models) have been the object of numerous kinetic modeling approaches,[68] from simple global kinetics[3,18,69] up to single-event models.[9,34,39,41,42,70–72] In the latter case, the whole network of elementary steps is defined, and species are gathered in lumps, defined by the carbon number and the degree of substitution of the carbenium (mono, di and tribranched). Each rate constant for the transformation of a lump into another one is written as a combination of parameters which depend on the type of reactant and product carbenium (secondary: s, tertiary: t, primary carbenium are discarded). A set of assumptions is generally made, and mechanistic conclusions are drawn from the fitting of experimental data, that we can now discuss in the light of our ab initio molecular dynamics results.

In kinetic modeling, the entropy of the physisorbed state (that we consider to be the π-complex) is often considered to be higher than that of the carbenium ions,[34,39] considering that the adsorbed olefin still has the same rotational entropy as in the gas phase, while at least a part of translational entropy is expected to be lost upon adsorption. According to our simulations, this last assumption is confirmed as the physisorbed state is confined to the neighborhood of the Brønsted acid site of the zeolite. Indeed, in free MD runs corresponding to the π-complex (see Section SIX), the distance between the center of the C=C bond and the proton on the zeolite exhibits a sharp maximum close to 2.1 Å, meaning that a big part of the translational entropy of the molecule in the gas phase is lost upon adsorption.

In microkinetic models, however, the enthalpy of the π-complex is supposed to be higher than that of the carbenium by about 110 (secondary) to 150 (tertiary) kJ/mol.[39] More recent estimations predicted protonation enthalpies of the secondary and tertiary olefins of -65 kJ/mol and -95 kJ/mol, respectively.[9] Even if in our static simulations in gas phase we cannot easily connect the enthalpic behavior of the π-complex with respect to that of carbenium ions, such a difference should lead to a better stability of carbenium ions with respect to π-complexes.[34] Our MD results (in terms of free energies, Figure 8) do not confirm this scheme (that they established in terms of enthalpy). In particular, the I_1 secondary carbenium ion is about 40 kJ/mol less stable than the corresponding π-complex. For tertiary carbenium ion, the free energy levels are more or less comparable to that of the π-complex. In practice however, the kinetic modeling is not performed by fitting the protonation versus intrinsic isomerization activation free energies, but their sum (see below), so that the quality of the fitting is not affected by this erroneous representation of the relative energy levels. Also, in their estimate of the relative protonation enthalpy yielding secondary versus tertiary carbenium ions, Martens et al.[39] and Thybaut et al.[9] find that the enthalpy of tertiary carbenium ions is 40 kJ/mol lower than that of secondary carbenium, in a very good agreement with our current estimation.

Within the lumping approach, the (monobranched, dibranched or tribranched) species are connected by type A isomerization reactions (hydride or alkyl transfers), observed to be much quicker than type B isomerization reactions.[39] As discussed in the previous section, this is in qualitative agreement with our findings involving the 1,3-hydride shift studied here and the methyl shift reported in our previous work.[31] Note, however, that the free energy of the 1,3-hydride shift transition state (TS(IIa)) is not significantly lower than that of the type B isomerization transition states (about 20 kJ/mol of difference with TS(IIb)), due to its connection with a secondary carbenium ion (with high free energy). This means that caution must be taken when equilibrating all type A isomerization steps, when secondary carbenium ions are concerned.

In kinetic modeling, the intrinsic rotational entropy of the transition state for type B isomerization reactions is expected to be close to that of the carbenium ions.[39] Considering the values reported in table S6 to S8 for gas phase simulations ($T\Delta S_{rot}$ close to zero, which is a consequence of small changes in structures and in moments of inertia), these assumptions seem to be reasonable. The vibrational entropy of the transition state for type B isomerization reactions is also supposed to be roughly equal to that of the carbenium ions.[39] This is found ($T\Delta S_{vib}$ in table S6-S8 for gas phase simulations) to be more debatable: as also found in our previous work, the type B isomerization transition states are more constrained than the corresponding reactant and products, mainly due to entropic vibrational contributions (of the order of 10 to 15 kJ/mol at 500 K). Thus, in the end, considering that the carbenium species have lost all translational degrees of freedom, the activation entropy is set to zero (same entropy for the carbenium and edge-protonated PCPs) in the kinetic models.[39] We claim that this leads to an overestimation of the pre-factor, likely compensated by an overestimation of the activation energy in the course of the fitting.

Concerning the enthalpy components, the composite isomerization activation energies are defined in some single-event models as the sum of the intrinsic isomerization activation energy (from the carbenium playing the role of the reactant) and the protonation enthalpy of the corresponding physisorbed olefin.[39] They are determined by fitting the experimental kinetic data. The composite rate constants for type B isomerization reactions connecting a secondary to a tertiary carbenium ion (s,t), and that of the reverse reaction (t,s), are supposed to be equal.[39,42] Assuming that the energy levels of all physisorbed olefins are almost the same, this assumption is true, as by definition the transition state TS(I) connects secondary and tertiary carbenium ions in both directions (forward and backward). However, it would be incorrect to conclude that the intrinsic barriers are the same, if one considers the carbenium ions as the reactants. The I_1 secondary carbenium is indeed far less stable (by 45 to 65 kJ/mol at 500 K from tables S6 and S7) than all tertiary carbenium ions modeled (I_2 and I_3). This implies that the kinetic constant of the (s,t) reaction is higher than that for the (t,s) reaction. However, the secondary carbenium ion is not a stable intermediate, and is very easily converted into the corresponding π-complex (Figure 8), with a very moderate free energy barrier (close to 10 kJ/mol at 500 K, see Figure 6) and a non-negligible reaction free energy gain (close to 40 kJ/mol at 500 K). Thus, the kinetically relevant species is actually not the secondary carbenium ion, but the corresponding π–complex. If one considers the later as the reactant or product instead of the secondary carbenium, it indeed appears that the free energy barrier is similar for the (s,t) and the (t,s) processes, even if the higher the temperature, the more stable the tertiary carbenium will be with respect to the π–complex, making the (t,s) reaction somewhat slower as compared to the (s,t) one. Thus, our work provides a strong message for mechanistic interpretation of kinetic data: in the case of reactions involving secondary carbenium ions (poorly stable species), the kinetically relevant species is not the carbenium itself, but the corresponding π–complex, exhibiting comparable stability with tertiary carbenium ions.

The extraction of intrinsic isomerization enthalpies was proposed in some kinetic works,[39,9] by subtracting to the composite enthalpies a protonation enthalpy determined by ab initio calculations (static, in gas phase). These values can be in principle compared to ours. They are, however, much too high (between 128 and 191 kJ/mol from a tertiary carbenium, and between 98 and 147 kJ/mol from a secondary carbenium) compared to our gas phase data (ΔU_{total} of activation: 12 and 75 kJ/mol at 500 K from a secondary and tertiary ion respectively) and the uncertainty is very large, with a strong dependence on the model used for the estimation of the protonation enthalpies (with differences from 30 to 70 kJ/mol). Note that our (t,t) activation enthalpy of 75 kJ/mol is in excellent agreement with the extrapolation at 453 K[41] of the data obtained in super-acidic media at lower temperature.[11] The deviation between our results and the kinetic modeling estimates can tentatively be assigned to the difficult estimation of the protonation enthalpy, and the issue with the overestimated prefactor (entropy component), likely leading to an overestimation of the activation energies in kinetic fitting by compensation. Thus, in the end, the zeolite catalyst seems to behave more closely to a super-acid than previously thought.[39]

Finally, single event modeling also made the comparison between (t,t) and (s,t) =(t,s) type B isomerization rates possible. In our simulations, no clear trend emerges, the free energy levels of TS(I) and TS(IIb) being comparable, in agreement with the weak difference indicated in kinetic modeling.[39,34]

In the end, mechanisms I and II are coupled as they represent two alternatives to reach the same products. Despite the very low stability of the secondary carbenium, we find that the corresponding π-complex is a relevant connected stable intermediate. The global free energy barriers of both mechanisms appear to be very close, and in a slight favor of mechanism I (through direct isomerization of the secondary carbenium) when the temperature is increased from 300 K to 500 K. Thus, it remains important to include such options in the kinetic modeling, as done in the previous single-event investigations, although at that time the secondary carbenium were believed to be stable intermediates.

IV.4.3.2. Calculated kinetic constants involved in mechanisms I and II and in type B isomerization between dibranched and tribranched isomers from ref.[31]

The global kinetic picture that we get from these simulations is summarized in Scheme 1, together with data obtained in our previous work.[31]

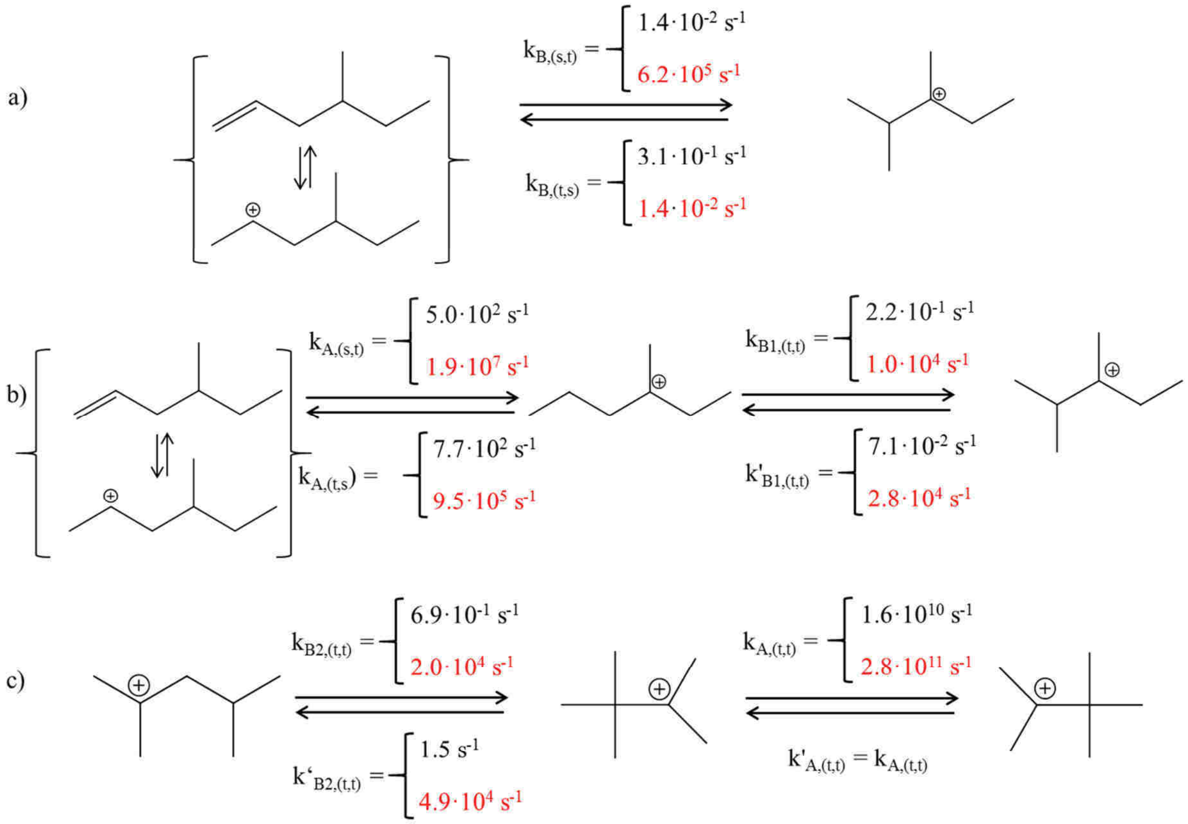

Scheme 1. Kinetic constants estimated by ab initio molecular dynamics at 300 K (black) and 500 K (red) for type A and B isomerization reactions starting from 4-methyl-hex-1-ene (a) mechanism I and b) mechanism II) and from 2,4-dimethyl-penten-2-ium cation (c).[31] k_B and k_A stand for rate constants determined for type B and A isomerization reaction, respectively, and the nature of the carbenium ion is symbolized by s (secondary) or t (tertiary). When available, and when more stable

than the corresponding carbenium ion, the π-complex was used as the reference state for the calculation of the rate constant instead of the carbenium ion.

IV.4.3.3. Relative contributions of mechanisms I and II

As shown in Figure 8, the free energies of the least stable transition states are rather similar for both mechanism. It is therefore not immediately clear which reaction mechanism is favorable at different conditions. We plugged the rate constants, determined via the Eyring equation[73] from the free energies reported in this work into a kinetic model treating the reactions $R \rightarrow I_3$ and $R \rightleftharpoons I_2 \rightarrow I_3$ as parallel competing processes (see Section SVI). We terminated our simulations when 10% of reactant was converted into the final state I_3, which allowed us to neglect the reverse reactions from the final state that are most significantly affected by the statistical errors of free energies of activation (see Section 4.1.) We find that the mechanism II is slightly more favorable at T=300 K: a higher fraction of the product (I_3) molecules is formed via this reaction route (74.5 ± 0.2 %) as compared to mechanism I (25.5 ± 0.2 %). When the temperature is raised to 500 K, the least stable transition state of mechanism II lies 73.4 kJ/mol above the reactant on the free energy scale. Remarkably, this value is close to that determined for 300 K (78.4 kJ/mol), suggesting that the effective barrier for this mechanism is only weakly temperature dependent. In contrast, the barrier for mechanism I decreases to 69.2 k/mol. This significant change causes that the mechanism I becomes dominant at 500 K (according to our kinetic model, 72.5 ± 0.2 % of product molecules are formed via this mechanism). Even considering the statistical uncertainty in the results of our kinetic model which are given by the uncertainty in the computed free energies (see Table 1), our results clearly show that both reaction mechanisms occur with significant frequencies (although with varying relative contributions) at conditions considered in this work.

IV.5. Conclusion

In this work, a detailed ab initio molecular dynamics study of isomerization transformation of 4-methyl-hex-1-ene into 2,4-dimethyl-penten-2-ium cation has been presented. In addition to the conventional one-step mechanism (mechanism I), consisting in a proton transfer from the zeolite followed by a type B isomerization transforming a secondary carbenium into a tertiary carbenium, an alternative reaction route, (mechanism II) has been described. This mechanism consists of two steps involving (i) proton transfer from the zeolite and an intramolecular 1,3 hydride-shift producing a tertiary carbenium, and (ii) a type B isomerization between two tertiary carbenium ions. The global kinetic picture that we get from these simulations is summarized in Scheme 1, together with data obtained in our previous work.[31] The main conclusions that we obtain are the following:

- The secondary carbenium ion is a poorly stable species, even not defined as a free energy minimum in some conditions. In this case, the kinetically relevant species is the corresponding π-complex (linked to the secondary carbenium ion by a protonation-deprotonation reaction).
- All transition states calculated for type B isomerization reactions exhibit comparable stability and structure (edge-protonated cyclopropane), suggesting a certain level of universality of the present findings.
- Consistently with empirical knowledge, transition states for type A isomerization reactions are more stable than those of type B isomerization reactions. The transition state structure can, however, differ from one type of reaction to another. Whereas for methyl shifts a corner-PCP plays the role of the transition state, in the case of the 1,3 hydride shift, an edge-PCP is found, which is more stable than the one found for type B isomerization reactions. One of the C-C bonds of the triangle is longer than for type B edge-PCPs.
- Increasing the temperature from 300 to 500 K leads to a systematic stabilization of carbenium ions with respect to the neutral π-complex. Such stabilization is generally stronger for intermediates than for PCPs.

In the end, both mechanisms (I and II) significantly contribute to the global reaction rate, with a predominance of mechanism I (type B isomerization connecting a tertiary and a secondary carbenium ion) at 500 K. A priori, mechanism II should have been preferred over mechanism I, as it is expected to quickly convert a secondary carbenium into a tertiary carbenium by a type A isomerization. We however see that this is an oversimplified picture, that eventually depends on thermal effects.

This work brings new quantified data and mechanistic information that may help the building of more relevant kinetic models in the future. The species investigated herein being also susceptible of cracking at high conversion,[35] additional data are also required for these reactions as well.

References

(1) Zečević, J.; Vanbutsele, G.; Jong, K. P. de; Martens, J. A. Nanoscale Intimacy in Bifunctional Catalysts for Selective Conversion of Hydrocarbons. *Nature* **2015**, *528*, 245–248.
(2) Marcilly, C. *Acido-Basic Catalysis. Application to Refining and Petrochemistry;* Technip, 2005.
(3) Gutierrez-Acebo, E.; Leroux, C.; Chizallet, C.; Schuurman, Y.; Bouchy, C. Metal/Acid Bifunctional Catalysis and Intimacy Criterion for Ethylcyclohexane Hydroconversion. *ACS Catal.* **2018**, *8*, 6035–6046.
(4) Martens, J. A.; Verboekend, D.; Thomas, K.; Vanbutsele, G.; Gilson, J.-P.; Pérez-Ramírez, J. Hydroisomerization of Emerging Renewable Hydrocarbons Using Hierarchical Pt/H-ZSM-22 Catalyst. *ChemSusChem* **2013**, *6*, 421–425.
(5) Jacobs, P. A.; Dusselier, M.; Sels, B. F. Will Zeolite-Based Catalysis Be as Relevant in Future Biorefineries as in Crude Oil Refineries? *Angew. Chem. Int. Ed.* **2014**, *53*, 8621–8626.
(6) Phan, D.-P.; Lee, E. Catalytic Hydroisomerization Upgrading of Vegetable Oil-Based Insulating Oil. *Catalysts* **2018**, *8*, 131.
(7) Bouchy, C.; Hastoy, G.; Guillon, E.; Martens, J. A. Fischer-Tropsch Waxes Upgrading via Hydrocracking and Selective Hydroisomerization. *Oil Gas Sci. Technol. – Rev. IFP Energies nouvelles* **2009**, *64*, 91–112.
(8) Weitkamp, J. Catalytic Hydrocracking-Mechanisms and Versatility of the Process. *ChemCatChem* **2012**, *4*, 292–306.
(9) Thybaut, J. W.; Narasimhan, L. C. S.; Marin, G. B.; Denayer, J. F.M.; Baron, G. V.; Jacobs, P. A.; Martens, J. A. Alkylcarbenium Ion Concentrations in Zeolite Pores During Octane Hydrocracking on Pt/H-USY Zeolite. *Catal. Lett.* **2004**, *94*, 81–88.
(10) Olah, G. A. General Concept and Structure of Carbocations Based on Differentiation of Trivalent (Classical) Carbenium Ions from Three-Center Bound Penta- or Tetracoordinated (Nonclassical) Carbonium Ions. The Role of Carbocations in Electrophilic Reactions. *J. Am. Chem. Soc.* **1972**, *94*, 808–820.
(11) Brouwer, D. M.; Hogeven H. Electrophilic Substitutions at Alkanes and in Alkylcarbonium Ions. *Prog. Phys. Org. Chem.* **1972**, *9*, 179–240.
(12) Nicholas, J. B.; Haw, J. F. The Prediction of Persistent Carbenium Ions in Zeolites. *J. Am. Chem. Soc.* **1998**, *120*, 11804–11805.
(13) Ivanova, I. I.; Kolyagin, Y. G. Impact of in Situ MAS NMR Techniques to the Understanding of the Mechanisms of Zeolite Catalyzed Reactions. *Chem. Soc. Rev.* **2010**, *39*, 5018–5050.
(14) Dai, W.; Wang, C.; Yi, X.; Zheng, A.; Li, L.; Wu, G.; Guan, N.; Xie, Z.; Dyballa, M.; Hunger, M. Identification of tert-Butyl Cations in Zeolite H-ZSM-5: Evidence from NMR Spectroscopy and DFT Calculations. *Angew. Chem. Int. Edit.* **2015**, *54*, 8783–8786.
(15) Huang, M.; Wang, Q.; Yi, X.; Chu, Y.; Dai, W.; Li, L.; Zheng, A.; Deng, F. Insight into the Formation of the tert-butyl Cation Confined inside H-ZSM-5 Zeolite from NMR Spectroscopy and DFT Calculations. *Chem. Commun.* **2016**, *52*, 10606–10608.
(16) Kazansky, V. B.; Senchenya, I. N. Quantum Chemical Study of the Electronic Structure and Geometry of Surface Alkoxy Groups as Probable Active Intermediates of Heterogeneous Acidic Catalysts. What Are The Adsorbed Carbenium Ions? *J. Catal.* **1989**, *119*, 108–120.
(17) Frash, M. V.; Kazansky, V. B.; Rigby, R. A.; van Santen, R. A. Cracking of Hydrocarbons on Zeolite Catalysts: Density Functional and Hartree−Fock Calculations on the Mechanism of the β-Scission Reaction. *J. Phys. Chem. B* **1998**, *102*, 2232–2238.

(18) Denayer, J. F.; Baron, G. V.; Vanbutsele, G.; Jacobs, P. A.; Martens, J. A. Evidence for Alkylcarbenium Ion Reaction Intermediates from Intrinsic Reaction Kinetics of C6–C9 n-Alkane Hydroisomerization and Hydrocracking on Pt/H–Y and Pt/USY Zeolites. *J. Catal.* **2000**, *190*.
(19) Boronat, M.; Viruela, P. M.; Corma, A. Reaction Intermediates in Acid Catalysis by Zeolites: Prediction of the Relative Tendency to form Alkoxides or Carbocations as a Function of Hydrocarbon Nature and Active Site Structure. *J. Am. Chem. Soc.* **2004**, *126*, 3300–3309.
(20) Leydier, F.; Chizallet, C.; Costa, D.; Raybaud, P. Revisiting Carbenium Chemistry on Amorphous Silica-Alumina: Unraveling their Milder Acidity as Compared to Zeolites. *J. Catal.* **2015**, *325*, 35–47.
(21) Rey, J.; Raybaud, P.; Chizallet, C. Ab Initio Simulation of the Acid Sites at the External Surface of Zeolite Beta. *ChemCatChem* **2017**, *9*, 2176–2185.
(22) Ester Gutierrez-Acebo; Rey, J.; Bouchy, C.; Schuurman, Y.; Chizallet, C. Location of the Active Sites for Ethylcyclohexane Hydroisomerization by Ring Contraction and Expansion in the EUO Zeolitic Framework. *ACS Catal.* **2019**, *9*, 1692–1704.
(23) Tuma, C.; Sauer, J. Protonated Isobutene in Zeolites: tert-butyl Cation or Alkoxide? *Angew. Chem. Int. Edit.* **2005**, *44*, 4769–4771.
(24) Tuma, C.; Sauer, J. Treating Dispersion Effects in Extended Systems by Hybrid MP2:DFT Calculations-Protonation of Isobutene in Zeolite Ferrierite. *Phys. Chem. Chem. Phys.* **2006**, *8*, 3955–3965.
(25) Tuma, C.; Kerber, T.; Sauer, J. The tert-butyl Cation in H-Zeolites: Deprotonation to Isobutene and Conversion into Surface Alkoxides. *Angew. Chem. Int. Edit.* **2010**, *49*, 4678–4680.
(26) Cnudde, P.; Wispelaere, K. de; van der Mynsbrugge, J.; Waroquier, M.; van Speybroeck, V. Effect of Temperature and Branching on the Nature and Stability of Alkene Cracking Intermediates in H-ZSM-5. *J. Catal.* **2017**, *345*, 53–69.
(27) Hajek, J.; van der Mynsbrugge, J.; Wispelaere, K. de; Cnudde, P.; Vanduyfhuys, L.; Waroquier, M.; van Speybroeck, V. On the Stability and Nature of Adsorbed Pentene in Brønsted Acid Zeolite H-ZSM-5 at 323K. *J. Catal.* **2016**, *340*, 227–235.
(28) Cnudde, P.; Wispelaere, K. de; Vanduyfhuys, L.; Demuynck, R.; van der Mynsbrugge, J.; Waroquier, M.; van Speybroeck, V. How Chain Length and Branching Influence the Alkene Cracking Reactivity on H-ZSM-5. *ACS Catal.* **2018**, *8*, 9579–9595.
(29) van Speybroeck, V.; Hemelsoet, K.; Joos, L.; Waroquier, M.; Bell, R. G.; Catlow, C. R. A. Advances in Theory and their Application within the Field of Zeolite Chemistry. *Chem. Soc. Rev.* **2015**, *44*, 7044–7111.
(30) Bučko, T.; Benco, L.; Hafner, J.; Ángyán, J. G. Monomolecular Cracking of Propane over Acidic Chabazite. *J. Catal.* **2011**, *279*, 220–228.
(31) Rey, J.; Gomez, A.; Raybaud, P.; Chizallet, C.; Bučko, T. On the Origin of the Difference Between Type A and Type B Skeletal Isomerization of Alkenes Catalyzed by Zeolites: The Crucial Input of ab initio Molecular Dynamics. *J. Catal.* **2019**, *373*, 361–373.
(32) Carter, E. A.; Ciccotti, G.; Hynes, J. T.; Kapral, R. Constrained Reaction Coordinate Dynamics for the Simulation of Rare Events. *Chem. Phys. Lett.* **1989**, *156*, 472–477.
(33) Ciccotti, G.; Sprik, M. Free Energy from Constrained Molecular Dynamics. *J. Chem. Phys.* **1998**, *109*, 7737–7744.
(34) Thybaut, J.W.; Marin, G.B.; Baron, G.V.; Jacobs, P.A.; Martens, J.A. Alkene Protonation Enthalpy Determination from Fundamental Kinetic Modeling of Alkane Hydroconversion on Pt/H–(US)Y-Zeolite. *J. Catal.* **2001**, *202*, 324–339.

(35) Raybaud, P.; Patrigeon, A.; Toulhoat, H. The Origin of the C7-Hydroconversion Selectivities on Y, β, ZSM-22, ZSM-23, and EU-1 Zeolites. *J. Catal.* **2001**, *197*, 98–112.
(36) Demuth, T.; Rozanska, X.; Benco, L.: Hafner, J.; van Santen, R. A.; Toulhoat, H. Catalytic Isomerization of 2-pentene in H-ZSM-22—A DFT Investigation. *J. Catal.* **2003**, *214*, 68–77.
(37) Huang, B.; Bai, P.; Neurock, M.; Davis, R. J. Conversion of n-Hexane and n-Dodecane over H-ZSM-5, H-Y and Al-MCM-41 at Supercritical Conditions. *Appl. Catal. A-Gen.* **2017**, *546*, 149–158.
(38) Natal-Santiago, M. A.; Alcalá, R.; Dumesic, J. A. DFT Study of the Isomerization of Hexyl Species Involved in the Acid-Catalyzed Conversion of 2-Methyl-Pentene-2. *J. Catal.* **1999**, *181*, 124–144.
(39) Martens, G. G.; Marin, G. B.; Martens, J. A.; Jacobs, P. A.; Baron, G. V. A Fundamental Kinetic Model for Hydrocracking of C8 to C12 Alkanes on Pt/US–Y Zeolites. *J. Catal.* **2000**, *195*, 253–267.
(40) Brouwer, D. M.; van Doorn, J. A. Spectroscopic Observation of a 1,3-Hydrogen Shift in 2,4-Dimethylpentyl Cation. *Recl. Trav. Chim. Pays-Bas* **1969**, *88*, 573–576.
(41) Baltanas, M. A.; van Raemdonck, K. K.; Froment, G. F.; Mohedas, S. R. Fundamental Kinetic Modeling of Hydroisomerization and Hydrocracking on Noble Metal-Loaded Faujasites. 1. Rate Parameters for Hydroisomerization. *Ind. Eng. Chem. Res.* **1989**, *28*, 899–910.
(42) Schweitzer, J.-M.; Galtier, P.; Schweich, D. A Single Events Kinetic Model for the hydrocracking of Paraffins in a Three-Phase Reactor. *Chem. Eng. Sci.* **1999**, *54*, 2441–2452.
(43) Kresse, G.; Hafner, J. Ab Initio Molecular Dynamics for Liquid Metals. *Phys. Rev. B* **1993**, *47*, 558–561.
(44) Kresse, G.; Hafner, J. Ab Initio Molecular-Dynamics Simulation of the Liquid-Metal–Amorphous-Semiconductor Transition in Germanium. *Phys. Rev. B* **1994**, *49*, 14251–14269.
(45) Kresse, G.; Furthmüller, J. Efficient iterative schemes for ab initio total-energy calculations using a plane-wave basis set. *Phys. Rev. B* **1996**, *54*, 11169–11186.
(46) Blöchl, P. E. Projector Augmented-Wave Method. *Phys. Rev. B* **1994**, *50*, 17953–17979.
(47) Kresse, G.; Joubert, D. From Ultrasoft Pseudopotentials to the Projector Augmented-Wave Method. *Phys. Rev. B* **1999**, *59*, 1758–1775.
(48) Perdew, J. P.; Burke, K.; Ernzerhof, M. Generalized Gradient Approximation Made Simple. *Phys. Rev. Lett.* **1996**, *77*, 3865–3868.
(49) Grimme, S. Semiempirical GGA-Type Density Functional Constructed with a Long-Range Dispersion Correction. *J. Comput. Chem.* **2006**, *27*, 1787–1799.
(50) Göltl, F.; Grüneis, A.; Bučko, T.; Hafner, J. Van der Waals Interactions between Hydrocarbon Molecules and Zeolites: Periodic Calculations at Different Levels of Theory, from Density Functional Theory to the Random Phase Approximation and Møller-Plesset Perturbation Theory. *J. Chem. Phys.* **2012**, *137*, 114111.
(51) Silaghi, M.-C.; Chizallet, C.; Petracovschi, E.; Kerber, T.; Sauer, J.; Raybaud, P. Regioselectivity of Al–O Bond Hydrolysis during Zeolites Dealumination Unified by Brønsted–Evans–Polanyi Relationship. *ACS Catal.* **2015**, *5*, 11–15.
(52) Bučko, T.; Hafner, J.; Lebègue, S.; Ángyán, J. G. Improved Description of the Structure of Molecular and Layered Crystals. *J. Phys. Chem. A* **2010**, *114*, 11814–11824.
(53) Bučko, T.; Hafner, J.; Angyán, J. G. Geometry Optimization of Periodic Systems Using Internal Coordinates. *J. Chem. Phys.* **2005**, *122*, 124508.
(54) Bučko, T. Transition state optimization of periodic systems using delocalized internal coordinates. *Theor. Chem. Acc.* **2018**, *137*, 164.

(55) Fukui, K. Formulation of the Reaction Coordinate. *J. Phys. Chem.* **1970**, *74*, 4161–4163.
(56) Fukui, K. The Path of Chemical Reactions - the IRC Approach. *Accounts Chem. Res.* **1981**, *14*, 363–368.
(57) Hratchian, H. P.; Schlegel, H. B. Following Reaction Pathways Using a Damped Classical Trajectory Algorithm. *J. Phys. Chem. A* **2002**, *106*, 165–169.
(58) Frenkel, D.; Smit, B. *Understanding Molecular Simulation. From Algorithms to Applications*; Computational science series; Academic Press, 2002.
(59) Bučko, T.; Chibani, S.; Paul, J.-F.; Cantrel, L.; Badawi, M. Dissociative Iodomethane Adsorption on Ag-MOR and the Formation of AgI clusters: An Ab Initio Molecular Dynamics Study. *Phys. Chem. Chem. Phys.* **2017**, *19*, 27530–27543.
(60) Bučko, T. Ab Initio Calculations of Free-Energy Reaction Barriers. *J. Phys. Condens. Matter.* **2008**, *20*, 64211.
(61) Laio, A.; Parrinello, M. Escaping Free-Energy Minima. *Proc. Natl. Acad. Sci. U.S.A.* **2002**, *99*, 12562–12566.
(62) Rasul, G.; Prakash, G. K. S.; Olah, G. A. MP2, CCSD(T), and Density Functional Theory Study of the 2-Butyl Cation: New Insight into the Methyl- and Hydrogen-Bridged Structures. *J.Phys.Chem. A* **2015**, *119*, 5762–5769.
(63) Vrček, I. V.; Vrček, V.; Siehl, H.-U. Quantum Chemical Study of Degenerate Hydride Shifts in Acyclic Tertiary Carbocations. *J. Phys. Chem. A* **2002**, *106*, 1604–1611.
(64) Olah, G. A.; Prakash, G. K. S.; Rasul, G. Ab Initio/GIAO-CCSD(T) 13C NMR Study of the Rearrangement and Dynamic Aspects of Rapidly Equilibrating Tertiary Carbocations, C6H13(+) and C7H15(+). *J. Comput. Chem* **2016**, *37*, 70–77.
(65) Collins, C. J. Protonated Cyclopropanes. *Chem. Rev.* **1969**, *69*, 543–550.
(66) Karabatsos, G. J.; Orzech, C. E. Carbonium Ion Rearrangements. V.11,3-Hydride Shifts in the 1-Propyl Cation. *J. Am. Chem. Soc.* **1962**, *84*, 2838–2839.
(67) Lee, C. C.; Gruber, L. Protonated Cyclopropanes. II. The Solvolysis of Cyclopropane in Tritiated Sulfuric Acid. *J. Am. Chem. Soc.* **1968**, *90*, 3775–3778.
(68) Oliveira, L. P. de; Hudebine, D.; Guillaume, D.; Verstraete, J. J.; Joly, J. F. A Review of Kinetic Modeling Methodologies for Complex Processes. *Oil Gas Sci. Technol. – Rev. IFP Energies nouvelles* **2016**, *71*, 45.
(69) Mendes, P. S. F.; Silva, J. M.; Ribeiro, M. F.; Duchêne, P.; Daudin, A.; Bouchy, C. Quantification of metal-acid balance in hydroisomerization catalysts: A step further toward catalyst design. *AIChE J.* **2017**, *63*, 2864–2875.
(70) Surla, K.; Guillaume, D.; Verstraete, J. J.; Galtier, P. Kinetic Modeling using the Single-Event Methodology. *Oil Gas Sci. Technol. – Rev. IFP Energies nouvelles* **2011**, *66*, 343–365.
(71) Vandegehuchte, B. D.; Thybaut, J. W.; Marin, G. B. Unraveling Diffusion and Other Shape Selectivity Effects in ZSM5 Using n -Hexane Hydroconversion Single-Event Microkinetics. *Ind. Eng. Chem. Res.* **2014**, *53*, 15333–15347.
(72) Valéry, E.; Guillaume, D.; Surla, K.; Galtier, P.; Verstraete, J.; Schweich, D. Kinetic Modeling of Acid Catalyzed Hydrocracking of Heavy Molecules. *Ind. Eng. Chem. Res.* **2007**, *46*, 4755–4763.
(73) Wynne-Jones, W. F. K.; Eyring, H. The Absolute Rate of Reactions in Condensed Phases. *The Journal of chemical physics* **1935**, *3*, 492–502.

SI. Supercell of chabazite

A primitive rhombohedral cell of purely siliceous chabazite (CHA framework, symmetry group R $\overline{3}$ m), with 12 symmetry equivalent tetrahedral sites, was obtained from International Zeolite Association (IZA) database.[1] The cell was reoptimized yielding the lattice constants a = 9.336 Å and α = 94.6°, which are in good agreement with the reference values[1] (a = 9.304 Å and α = 94.6°). The relaxed structure was subsequently used to build a supercell defined by lattice vectors $\mathbf{a}_1'$, $\mathbf{a}_2'$, and $\mathbf{a}_3'$ related to the primitive cell vectors of rhombohedral lattice ($\mathbf{a}_1, \mathbf{a}_2, \mathbf{a}_3$) via the following transformations: $\mathbf{a}_1' = \mathbf{a}_2 + \mathbf{a}_3$, $\mathbf{a}_2' = \mathbf{a}_1 + \mathbf{a}_3$, and $\mathbf{a}_3' = \mathbf{a}_1 + \mathbf{a}_2$. The shortest interatomic separation between the atoms in hydrocarbon and atoms in its periodically repeated images in the supercell was at least 5.5 Å. The Brønsted acid site was created by replacing one Si atom by an Al atom and inserting the H atom onto the framework oxygen atom O1 (Figure 2 in the main text), which is, according to experiment,[2] one of the two most populated proton sittings in CHA. In the gas phase simulations, the same unit cell as in the periodic calculations has been used.

SII. Rotational isomers of the intermediate I_2 and of the product I_3

In this section we provide the free energy profiles along the torsion coordinate τ defined below for the intermediate cation I_2 and the product I_3 in the gas phase and in chabazite. The relevant rotational isomers are identified, and their likelihoods of occurrence are computed.

SII.1. Intermediate I_2

The changes in geometry of the intermediate I_2 related to steps 1 and 2 of mechanism II can be controlled via the dihedral angle (τ) between the atoms C^1, C^2, C^3 and C^4 (Figure S1). The potential energy as a function of τ (Figure S2(a)) has been determined for the cation in the gas phase in a series of constrained relaxations. The corresponding free energy profiles and likelihoods of occurrence of individual rotamers among all I_2 states in chabazite (Figure S2(b)) have been determined by blue moon sampling in the same procedure as described in Section 3.1 for the R state.

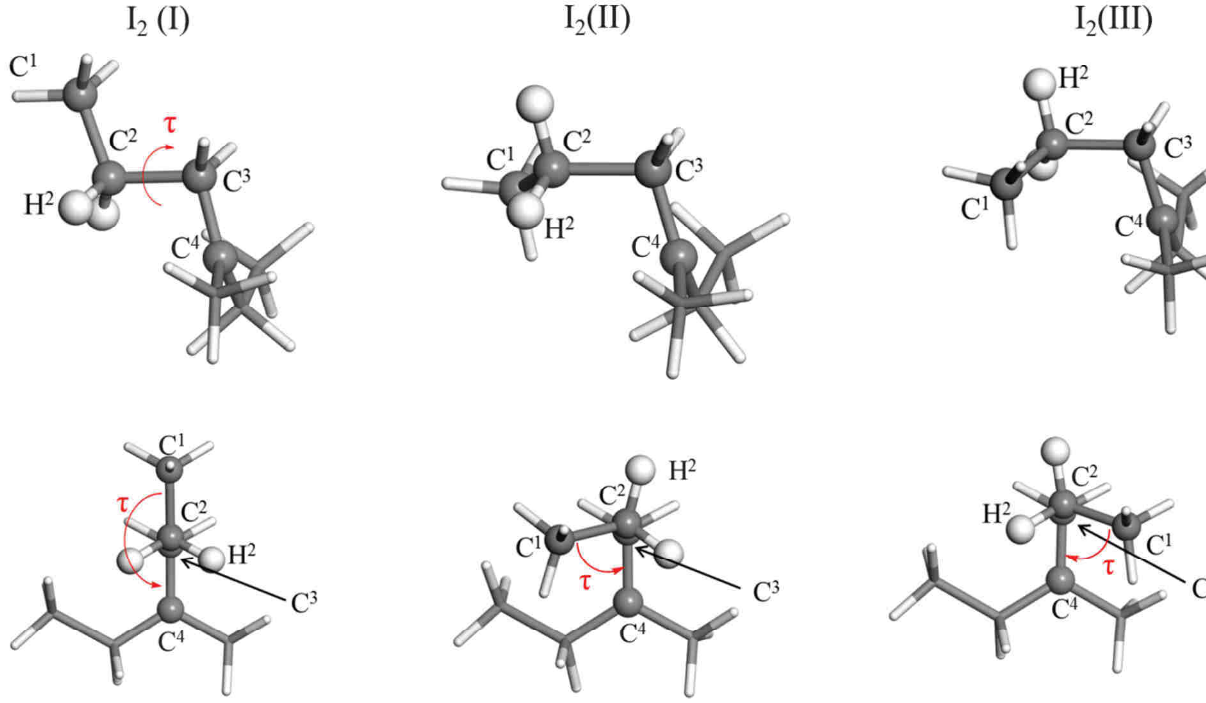

Figure S1. Rotational isomers I2(I) (τ ≈ –180 deg.), I2(II) (τ ≈ –69 deg.), and I2(III) (τ≈ 69 deg.) of the product 2,3-dimethyl-penten-3-ium. Top panels: side view; bottom panels: front view chosen so that the atom C2 overlaps the atom C3.

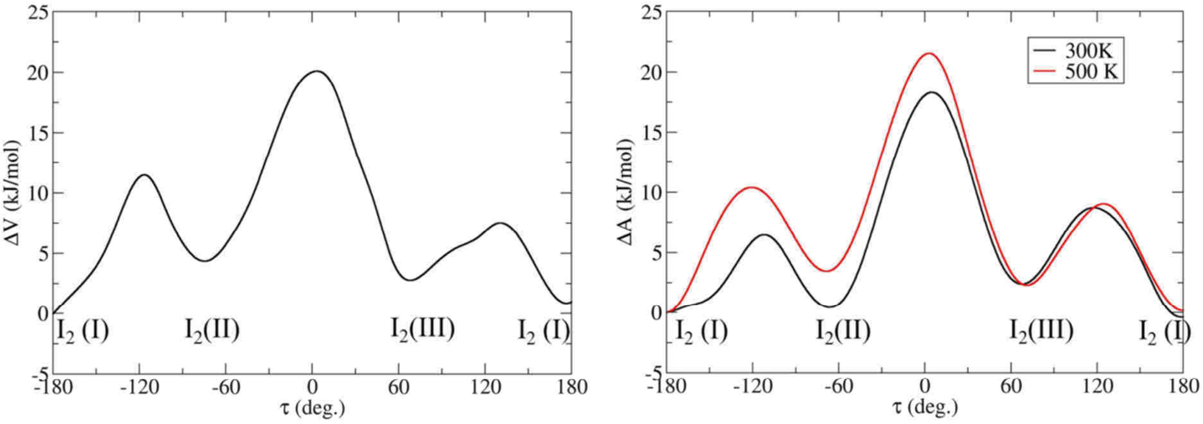

Figure S2. a) Potential energy as a function of dihedral angle (τ) defined by the atoms C^1, C^2, C^3 and C^4 (see Figure S1) computed using constrained relaxations of the cation (I_2) in the gas phase. Zero on the energy axis is defined by the energy of the lowest energy state. b) Free energy profile as a function of τ for the same cation I_2 located in chabazite at T = 300 K and 500 K. Note that periodic boundary conditions apply, i.e. the point $\tau = -180$ deg. is identical to the point $\tau = 180$ deg.

The numerical likelihoods of occurrence are compiled in Table S1.

Table S1. Likelihoods (%) of occurrence of individual rotamers of I_2 at 300 and 500 K.

	300 K	500 K
$p(I_2(I))$	56.5	49.7
$p(I_2(II))$	30.1	21.8
$p(I_2(III))$	13.4	28.5

SII.2. Product I_3

For the I_3 product, the changes in geometry related to mechanisms I and II can be controlled via the dihedral angle (τ) between the atoms C^3, C^2, C^4, and C^7 (Figure S3). The free energy profiles and likelihoods of occurrence of individual rotamers of I_2 among all states in chabazite (Figure S4) have been obtained in the same way as for the state R described in Section 3.1.

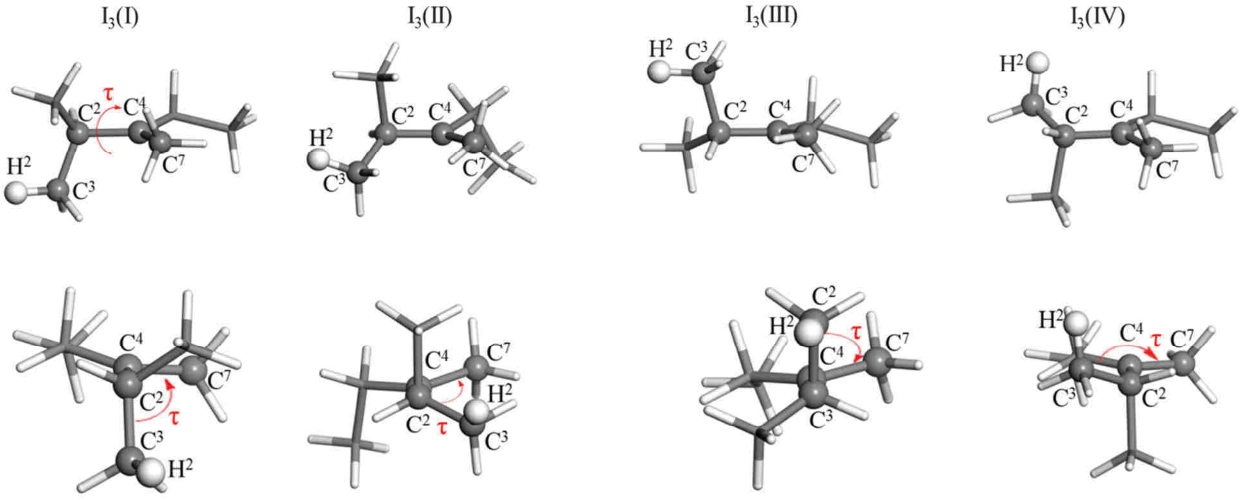

Figure S3. Rotational isomers $I_3(I)$ ($\tau \approx -90$ deg.), $I_3(II)$ ($\tau \approx -30$ deg.), $I_3(III)$ ($\tau \approx 90$ deg.) and $I_3(IV)$ ($\tau \approx 150$ deg.) of the 2,3-dimethyl-penten-3-ium cation I_3. Top panels: side view; bottom panels: front view chosen so that the atom C^2 overlaps the atom C^3.

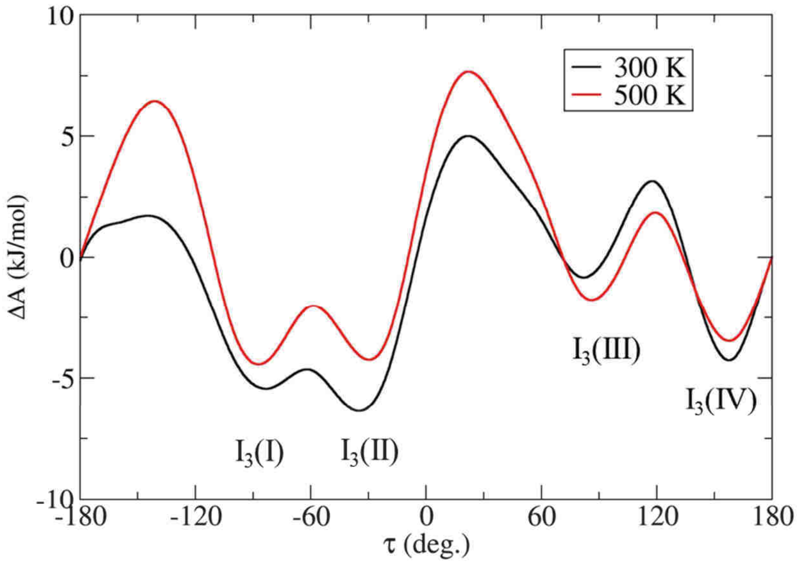

Figure S4. Free energy profiles as functions of the dihedral angle (τ) defined by the atoms C^3, C^2, C^4, and C^7 (Figure S3) for the product I_3 in chabazite at T = 300 K and 500 K. Note that periodic boundary conditions apply, i.e. the point $\tau = -180$ deg. is identical to the point $\tau = 180$ deg.

The likelihoods of occurrence are given in Table S2.

Table S2. Likelihoods (%) of occurrence of individual rotamers of I_3 at 300 and 500 K.

	300 K	500 K
p(I_3(I))	35.0	29.1
p(I_3(II))	44.5	27.8
p(I_3(III))	5.6	17.3
p(I_3(IV))	14.9	25.8

SIII. Determination of the velocity term $|\dot{\xi}^*|$

The term $\langle|\dot{\xi}^*|\rangle$ required in the calculations of free energy of activation (see Equation (1) in the main text) is determined using the constrained MD simulations via the formula:[3,4]

$$\langle|\dot{\xi}^*|\rangle = \sqrt{\frac{k_B T}{2\pi}} \frac{1}{\langle Z^{-1/2}\rangle_{\xi^*}}, \qquad \text{(Eq. S1)}$$

where the term enclosed in $\langle\ldots\rangle_{\xi^*}$ is computed as a statistical average for a constrained ensemble with $\xi(\boldsymbol{r}) = \xi^*$, and Z is the inverse of the mass metric tensor:

$$Z = \sum_{i=1}^{N} \frac{1}{m_i} \sum_{\mu=x,y,z} \left(\frac{\partial \xi}{\partial r_{i,\mu}}\right)^2, \qquad \text{(Eq. S2)}$$

with $r_{i,\mu}$ being the Cartesian component μ of the position vector of an atom i and the sums are over all atoms and Cartesian components. We note that the term $\left\langle Z^{-1/2} \right\rangle_{\xi^*}$ is readily available from the constrained MD performed for the state ξ^* within the $\Delta A_{\xi_{ref,X} \to \xi^*}$ calculation. The values of $\langle |\dot{\xi}^*| \rangle$ are compiled in Table S3.

Table S3. Average velocity $\langle |\dot{\xi}^*| \rangle$ (in s^{-1}) of reaction coordinate at the different transition states.

	Mechanism I	
	T (K)	$\langle \lvert\dot{\xi}^*\rvert \rangle$ (s^{-1})
TS(I)	300	$1.10 \cdot 10^{13}$
	500	$1.40 \cdot 10^{13}$

	Mechanism II	
	T (K)	$\langle \lvert\dot{\xi}^*\rvert \rangle$ (s^{-1})
TS(IIa)	300	$1.08 \cdot 10^{13}$
	500	$1.45 \cdot 10^{13}$
TS(IIb)	300	$9.90 \cdot 10^{12}$
	500	$1.26 \cdot 10^{13}$

SIV. Probability distribution functions $\tilde{P}(\xi)$ for reactant, intermediate and product states of isomerization reactions

In order to avoid problems with non-ergodic sampling due to the presence of significant barriers separating individual stable rotamers in a given intermediate state of interest (X = R, I_2, I_3), probability density of a reference state ($\xi_{ref,X}$) has been determined as a product of two terms ($P(\xi_{ref,X}) = \tilde{P}(\xi_{ref,X})\, p(X(I))$), each been computed separately as discussed in Section 3.2. In this section we provide the probability densities $\tilde{P}(\xi_{ref,X})$. The reference state $\xi_{ref,X}$ was chosen so as to achieve a sufficiently high probability density, so that $\tilde{P}(\xi_{ref,X})$ could be determined with a good accuracy in a MD run. According to Equations (1) and (2) presented in the main text, the results of free energy calculation are independent of the choice of the reference state, provided the value of $\tilde{P}(\xi_{ref,X})$ is determined accurately. In Section SIV.1, we provide probability densities $\tilde{P}(\xi_{ref,R})$ for the reactant of mechanisms I and II. Straightforward molecular dynamics has been used for these calculations. In Sections SIV.2 and SIV.3, $\tilde{P}(\xi_{ref,X})$ are computed for the relevant mixture of rotational isomers of I_2 and I_3 by determination of a weighted histogram using the configurations sampled in the blue moon sampling of the torsion coordinate performed for the states I_2 and I_3 (see Section SII). The values of $P(\xi_{ref,X})$ computed with $p(X(I))$ are also reported (Equation (5) in the main text).

SIV.1. Reactant R

Figure S5 and Figure S6Figure S6 show the distributions $\tilde{P}(\xi_{ref,R})$ for different rotamers of the species R, determined for different approximations to reaction coordinate used to study mechanisms I and II. The numerical values of the corresponding reference states are collected in Table S4. As the barriers separating different rotamers of R are large enough to effectively prevent mutual interconversions within our relatively short MD runs, we were able to sample the R(I) and R(II) rotational isomers separately in straightforward molecular dynamics.

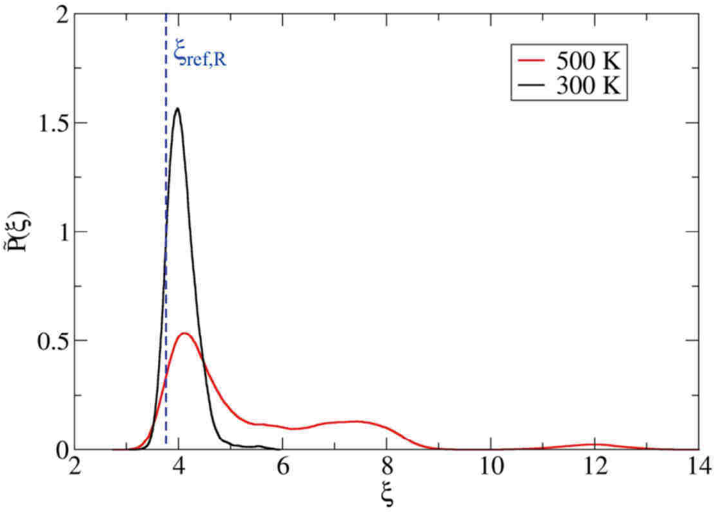

Figure S5. Probability distribution functions $\tilde{P}(\xi)$ computed for the reactant state R(I) at 300 K and 500 K.

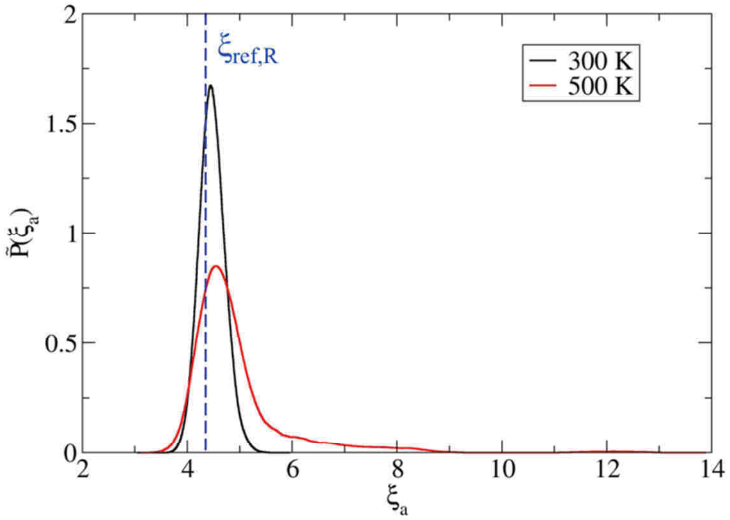

Figure S6. Probability distribution functions $\tilde{P}(\xi)$ computed for the reactant state R(II) at 300 K and 500 K.

Table S4. Values of ξ_{ref} for the reactant states R(I) and R(II), and the corresponding values of the probability density ($\tilde{P}(\xi_{ref,R})$. The lengths of production runs of MD simulations (τ) used to compute $\tilde{P}(\xi_{ref,R})$ are also listed. Note that the values of ξ_{ref} and $\tilde{P}(\xi_{ref,R})$ listed for the reactant of mechanisms I and II differ because of the use of different approximations to reaction coordinate.

	Mechanism I				
	T (K)	τ (ps)	$\xi_{ref,R}$	$\tilde{P}(\xi_{ref,R})$	$P(\xi_{ref,R})$
Reactant R(I)	300	100	3.76	0.94	0.055
	500	200	3.76	0.34	0.057

	Mechanism II				
	T (K)	τ (ps)	$\xi_{ref,R}$	$\tilde{P}(\xi_{ref,R})$	$P(\xi_{ref,R})$
Reactant R(II)	300	180	4.35	1.51	0.84
	500	180	4.35	0.74	0.37

SIV.2. Intermediate I$_2$

The first reaction step of mechanism II does not require formation of a specific rotamer for I$_2$ and consequently, the rotational isomers (I) and (III) (see Section SI.1) have been formed in the constrained MD simulations of I$_2$. Importantly, swapping between these two states has no significant effect on the value of free energy gradient indicating that the corresponding transformation between the rotamers is decoupled from the approximation to the reaction coordinate used in our calculations. In these constrained MD simulations, the states I$_2$(I) and I$_2$(III) are present at similar proportions as those deduced from the free energy profile shown in Figure S1.

In order to determine the value of $\tilde{P}(\xi_{ref,I_2})$, we used the data from the constrained MD simulations employed in calculations of the free energy profiles described in Section SII.1, taking into account the symmetry equivalent atoms in the analysis of the approximation to reaction coordinate:

$$\tilde{P}(\xi_{ref,I_2}) = \frac{\int_{I_2(I),I_2(III)} d\tau\, \delta(\xi - \xi_{ref,I_2}) \exp\left\{-\frac{A(\tau)}{k_B T}\right\}}{\int_{I_2(I),I_2(III)} d\tau\, \exp\left\{-\frac{A(\tau)}{k_B T}\right\}}, \qquad \text{(Eq. S3)}$$

the probability density of the reference being defined by:

$$P(\xi_{ref,I_2}) = \tilde{P}(\xi_{ref,I_2})\, p(I_2(I), I_2(III)), \qquad \text{(Eq. S4)}$$

with:

$$p(I_2(I), I_2(III)) = \frac{\int_{I_2(I),I_2(III)} d\tau\, \exp\left\{-\frac{A(\tau)}{k_B T}\right\}}{\int_{I_2} d\tau\, \exp\left\{-\frac{A(\tau)}{k_B T}\right\}}. \qquad \text{(Eq. S5)}$$

The resulting probability distribution functions $\tilde{P}(\xi)$ are displayed in Figure S7 and the relevant numerical values are compiled in Table S5 along with $P(\xi_{ref,I_2})$.

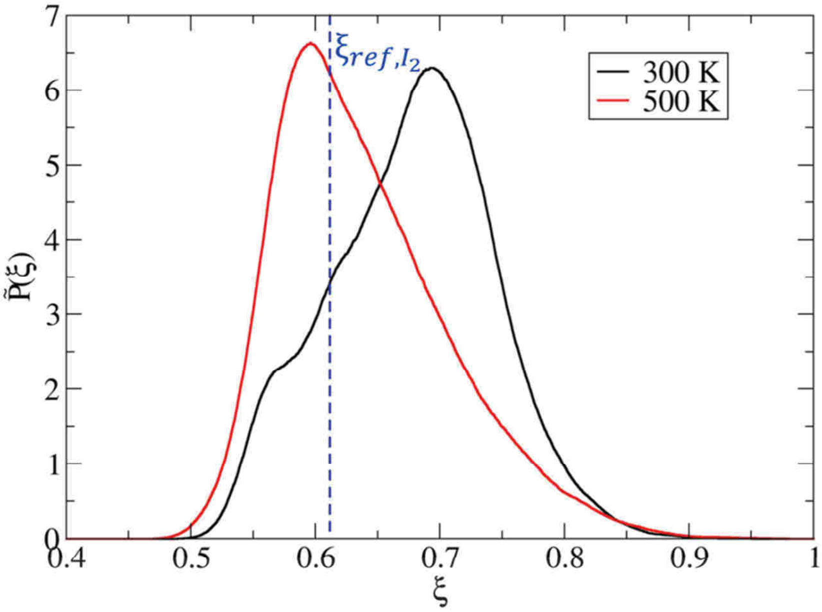

Figure S7. Probability distribution functions $\tilde{P}(\xi)$ computed for the intermediate state I_2 formed in the first step of mechanism II at 300 K and 500 K.

The second reaction step of mechanism II is a type B isomerization and it requires a specific arrangement of the state I_2 that corresponds to the rotational isomer I_2(II). The values of $\tilde{P}\left(\xi_{ref,I_2}\right)$ were obtained in a similar procedure as described above for the first reaction step whereby the data from our constrained MD runs with controlled value of τ have been employed. The resulting probability distribution functions $\tilde{P}(\xi)$ are given in Figure S8 and the numerical results are compiled in Table S5 along with $P\left(\xi_{ref,I_2}\right)$.

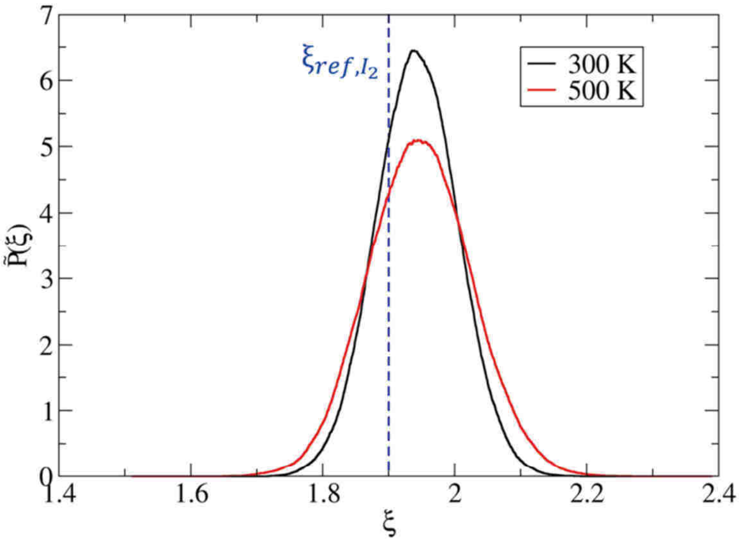

Figure S8. Probability distribution function $\tilde{P}(\xi\quad)$ computed for the intermediate state I_2 formed as reactant in the second step of mechanism II at 300 K and 500 K.

Table S5. Values of ξ_{ref} for the intermediate I_2 playing role of the product state for mechanism II, step 1, and reactant state of mechanism II, step 1, and the corresponding values of probability densities $\tilde{P}(\xi_{ref,I_2})$ and $P(\xi_{ref,I_2})$. Note that the values of ξ_{ref,I_2} and $\tilde{P}(\xi_{ref,I_2})$ listed for the two reaction steps differ because of the use of different approximation to reaction coordinate.

	Mechanism II, step 1			
	T (K)	ξ_{ref,I_2}	$\tilde{P}(\xi_{ref,I_2})$	$P(\xi_{ref,I_2})$
Intermediate I_2	300	0.61	3.41	2.38
	500	0.61	6.23	4.87

	Mechanism II, step 2			
	T (K)	ξ_{ref,I_2}	$\tilde{P}(\xi_{ref,I_2})$	$P(\xi_{ref,I_2})$
Intermediate I_2	300	1.90	5.12	1.54
	500	1.90	4.28	0.93

SIV.3. Product I_3

Mechanism I

At 300 K, both the rotamers I_3(I) and I_3(II), separated by a small barrier (see Section S1.2), are formed in our blue moon simulations. Similarly, I_3(III) and I_3(IV) are present at 500 K. The resulting probability distribution functions $\tilde{P}(\xi)$ are computed using our constrained MD data (see Section SII.2) for these particular blends of rotamers as in Section SIV.2 and they are given in Figure S9 and the corresponding numerical results are compiled in Table S6.

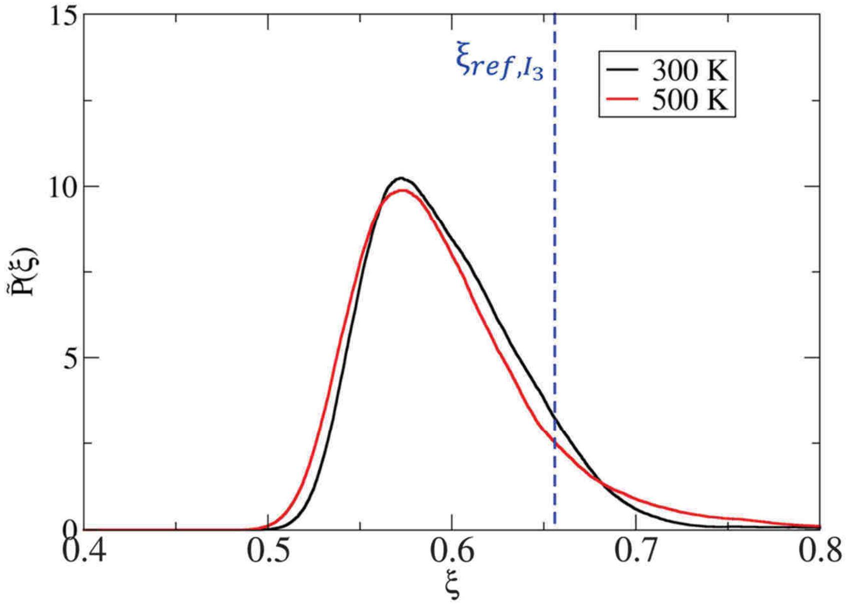

Figure S9. Probability distribution function $\tilde{P}(\xi)$ computed for the product I_3 formed via mechanism I at 300 K and 500 K.

Mechanism II

As a product of type B isomerization reaction (second step of Mechanism II), the specific rotational isomer I$_3$(III) is formed, hence we determined the value of $\tilde{P}\left(\xi_{ref,I_3}\right)$ for this specific rotamer. Once again, our constrained MD data from the free energy calculations presented in Section SII.2 were employed for this purpose and the resulting probability distribution functions $\tilde{P}(\xi)$ are given in Figure S10 while the corresponding numerical results are compiled in Table S6.

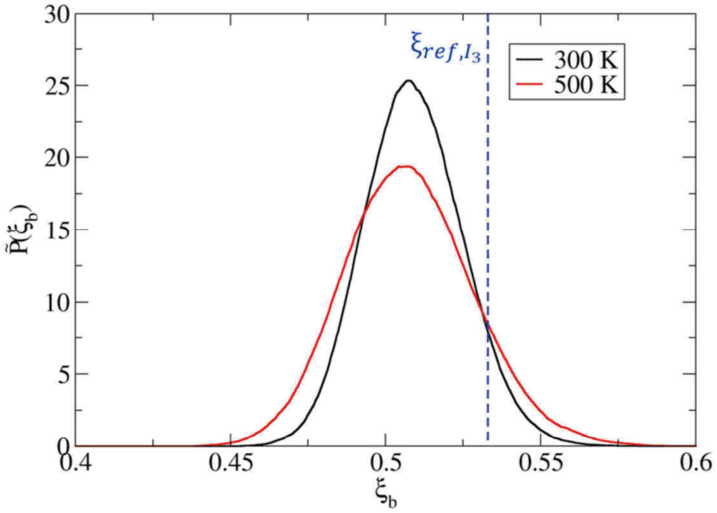

Figure S10. Probability distribution function $\tilde{P}(\xi)$ computed for the product I$_3$(III) of mechanism II at 300 K and 500 K.

Table S6. Values of ξ_{ref} for the product I$_3$ of mechanisms I and II, and the corresponding values of probability density ($\tilde{P}\left(\xi_{ref,I_3}\right)$). The values of ξ_{ref} and $\tilde{P}\left(\xi_{ref,I_3}\right)$ listed for the mechanisms I and II are different because of the use of different approximation to reaction coordinate.

	Mechanism I			
	T (K)	ξ_{ref,I_3}	$\tilde{P}\left(\xi_{ref,I_3}\right)$	$P\left(\xi_{ref,I_3}\right)$
Product I$_3$	300	0.66	3.0	2.39
	500	0.66	2.5	1.08

	Mechanism II			
	T (K)	ξ_{ref,I_3}	$\tilde{P}\left(\xi_{ref,I_3}\right)$	$P\left(\xi_{ref,I_3}\right)$
Product I$_3$	300	0.53	7.85	0.44
	500	0.53	8.42	1.46

SV. Avoiding the by-reactions

In our free energy calculations, several undesired by-reactions could occur. For instance, the cations (and mainly the secondary ones) can undergo occasional deprotonations or alkoxide formations. In order to restrict the sampling to the part of configurational space of interest, we followed the same strategy as in our previous work.[5] A restraining potential of the following form

$$V(R) = \frac{1}{2}K(R - R_0)^2 \qquad \text{(Eq. S6)}$$

has been added to reinforce the 13 C-H bonds involving hydrogen atoms which are not directly involved in the reactions of interest (*i.e.* all CH bonds except those involving H^1 and H^2, see Figure 5 in the main text). In Eq. S4, R stands for the interatomic bonding distance C-H, R_0 =1.1 Å corresponds to an approximate equilibrium length of the C-H bond, and the force constant K is set to 100 eV.Å^{-2}.

We had to prevent also other by-reactions such as the formation of an alkoxide formation between the C^2 atom of the secondary cation I_1 and the oxygen atom O^1 of the zeolitic framework, and the formation of a pi-complex by deprotonation of the newly formed I_1 (when H^1 returns to the framework oxygen atom next to the aluminium atom in Figure 5). A smeared step potential (shown in Figure S11) acting on the distance R between the corresponding atoms was used to prevent these processes:

$$V(R) = \frac{A_i}{1 + exp\left(-D\left(\frac{\mathrm{R}}{\mathrm{R}_{0,i}} - 1\right)\right)}, \qquad \text{(Eq. S7)}$$

where the parameters were set to the following values: $A = -2$ eV, $D = 20$, $\mathrm{R}_{0,1} = 2.5$ Å for CO and $\mathrm{R}_{0,2} = 1.5$ Å for OH. The restraining potential shown in Figure S11 generates extra forces acting on atoms only if a fluctuation attempts to create the C-O or O-H bonds involved.

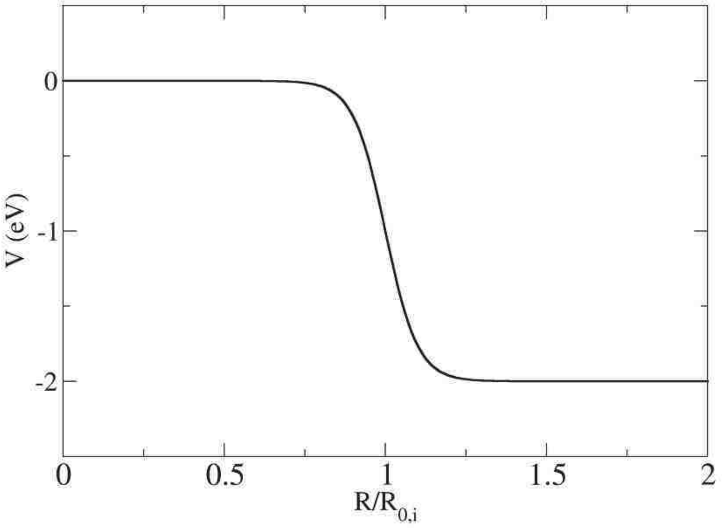

Figure S11. Restraining smeared step potential acting on a distance R between two atoms.

Yet another undesired processes that could occur in the case of the isomerization reactions are the transformations of rotational isomers into one another. As explained in Section 3.1, it is crucial to control the presence of appropriate rotamer in the blue moon sampling simulation of the reactant R because the mechanism under consideration depends on the arrangement of reactant. For the reactant R, the free energy barriers between rotamers are large enough (see Figure 3 in the main text) to prevent frequent transformations. We checked the value of the dihedral angle (τ) between the atoms C^2, C^3, C^4, and C^7 characterizing the rotamers and we restarted the simulations in rare cases where an undesired transformation between rotamers occurred.

The second step of mechanism II also requires formation of a specific rotational isomer of the cations I_2 and I_3. In particular, the hydrogen atom H^2 must be in position sterically allowing its shift from C^2 to C^3.

In the constrained simulations of I_2 at 300 K, only the rotamer I_2(II) was observed (see Section SII.1). At 500 K, the rearrangements between different rotamers were frequent for the two points of the blue moon simulation near I_2 and we used a smeared step restraining potential acting on the dihedral angle (τ) defined by the atoms C^1, C^2, C^3 and C^4. This restraining potential is shown in Figure S12 and its form is as follows:

$$V(\tau) = \sum_{i=1}^{2} \frac{A_i}{1 + exp\left(-D_i\left(\frac{\tau}{\tau_{0,i}} - 1\right)\right)}, \qquad \text{(Eq. S8)}$$

where the parameters were set to the following values: $A_1 = 2$ eV, $D_1 = 100$, $\tau_{0,1} = -115$ deg., and $A_2 = -2$ eV, $D_2 = 20$, $\tau_{0,2} = -11$ deg.

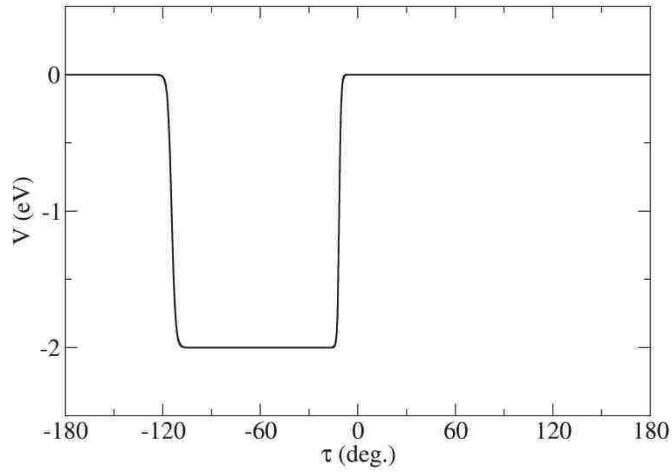

Figure S12. Restraining potential acting on the dihedral angle C^3-C^2-C^4-C^5 (θ).

Once again, the restraining potential is flat in the region defining the rotamer I_2(II) (–115 deg. < τ < –11 deg.) and hence the forces due to $V(\tau)$ are negligible unless a transition to some other rotamer is attempted. This assumption was demonstrated by reproducing the constrained simulation on the third point of the simulation, where only I_2(II) was present. The same value for the gradient of the free energy was obtained with and without the restraining potential acting on τ, confirming the correct convergence of the gradient and a negligible effect of the restraining potential.

SVI. Kinetic analysis

In order to compare relative importance of two competing reaction mechanisms I and II of transformation of reactant state R into product I_3, a simple kinetic model has been used in which two processes involving common initial and final states have been considered:

$$R \to I_3,$$

$$R \rightleftharpoons I_2 \to I_3.$$

The corresponding kinetic equations

$$\frac{dc_R(t)}{dt} = -\left(k_{R\to I_3} + k_{R\to I_2}\right)c_R(t) + k_{I_2\to R}c_{I_2}(t),$$

$$\frac{dc_{I_2}(t)}{dt} = k_{R\to I_2}c_R(t) - \left(k_{I_2\to R} + k_{I_2\to I_3}\right)c_{I_2}(t),$$

$$c_R(t) + c_{I_2}(t) + c_{I_3}(t) = c_R(0)$$

have been solved using a simple Euler method with time steps of 10^{-5} s and 10^{-12} s for T=300 K and 500 K, respectively. The following initial concentrations have been considered: $c_R(0) = 1$ mol/m^3, $c_{I_2}(0) = c_{I_3}(0) = 0$ mol/m^3. The rate constants k_X for the process X have been computed using the Eyring equation. The integration was stopped after the period T when the condition $c_{I_3}(t = T) = 0.10 \cdot c_R(0)$ was fulfilled. Such a low conversion regime corresponds to reaction conditions at which the reverse reactions from the final state I_3 can be neglected. The percentage of the product molecules formed via mechanism I was determined as

$$x_I = \frac{\int_0^T dt\, k_{R\to I_3}\, c_R(t)}{\int_0^T dt\, k_{R\to I_3}\, c_R(t) + \int_0^T dt\, k_{I_2\to I_3}\, c_{I_2}(t)} \times 100\%$$

and the same quantity for the mechanism II is defined as $x_{II} = 100\% - x_I$. In order to explore the effect of the statistical uncertainty on the values of x_I and x_{II}, 2000 independent evaluations of the kinetic model have been performed, whereby the free energy barriers have been modified by adding a noise uniformly distributed within the corresponding confidence intervals (see Table 1). The standard deviation of mean values computed in such a way provide us with an estimate of error (i.e. standard error) for the quantities x_I and x_{II}. The values for x_I (x_{II}) determined for T=300 K and 500 K are 25.5 ± 0.2 % and 72.5 ± 0.2 % (74.5 ± 0.2 % and 27.5 ± 0.2 %).

SVII. Static calculations for the gas phase reactions

In this section we provide thermodynamic data for the two mechanisms in gas phase computed using the harmonic transition state theory[6] within the static approach, along with the rigid rotor and ideal gas approximations: individual contributions of different types of degrees of freedom to free energies of activation $\Delta A_{X_i(j)\rightarrow TS_i}$ and to free energies of reaction $\Delta A_{X_i(j)\rightarrow Y_i(k)}$ for the microprocess transformation starting from the active rotamer $X_i(j)$ of the reactant X_i and yielding the rotamer $Y_i(k)$ of the product Y_i.

Table S7. Electronic free energies A_{el} for the molecules in the gas phase. All values are in kJ/mol.

	Mechanism I		
	I_1(I)	TS(I)	I_3(I)
A_{el}	-10942.14	-10926.98	-11004.68

	Mechanism II, step 1		
	I_1(II)	TS(IIa)	I_2(III)
A_{el}	-10955.62	-10953.33	-11000.93

	Mechanism II, step 2		
	I_2(II)	TS(IIb)	I_3(III)
A_{el}	-10998.25	-10918.24	-10998.54

Table S8**.** Individual contributions to the $\Delta A_{I_1(I)\rightarrow TS(I)}$ and $\Delta A_{I_1(I)\rightarrow I_3(I)}$ terms computed for mechanism I of the reaction in the gas phase. All values are in kJ/mol.

	T=300 K		T=500 K	
	$I_1(I) \rightarrow TS(I)$	$I_1(I) \rightarrow I_3(I)$	$I_1(I) \rightarrow TS(I)$	$I_1(I) \rightarrow I_3(I)$
ΔA_{el}	15.2	-62.5	15.2	-62.5
ΔA_{vib}	6.7	0.5	12.4	1.1
ΔA_{rot}	0.2	0.1	0.4	0.1
ΔA_{trans}	0.0	0.0	0.0	0.0
$\boldsymbol{\Delta A_{total}}$	**22.0**	**-62.0**	**27.9**	**-61.3**
ΔU_{el}	15.2	-62.5	15.2	-62.5
ΔU_{vib}	-1.0	-0.6	-3.2	-0.4
ΔU_{rot}	0.0	0.0	0.0	0.0
ΔU_{trans}	0.0	0.0	0.0	0.0
$\boldsymbol{\Delta U_{total}}$	**14.1**	**-63.1**	**12.0**	**-63.0**
$T\Delta S_{el}$	0.0	0.0	0.0	0.0
$T\Delta S_{vib}$	-7.7	-1.0	-15.6	-1.6
$T\Delta S_{rot}$	-0.2	-0.1	-0.4	-0.1
$T\Delta S_{trans}$	0.0	0.0	0.0	0.0
$\boldsymbol{T\Delta S_{total}}$	**-7.9**	**-1.1**	**-16.0**	**-1.7**

Table S9. Individual contributions to the $\Delta A_{I_1(II)\rightarrow TS(IIa)}$ and $\Delta A_{I_1(II)\rightarrow I_2(I)}$ terms computed for the first step of mechanism II of the reaction in the gas phase. All values are in kJ/mol.

	T=300 K		T=500 K	
	$I_1(II) \rightarrow TS(IIa)$	$I_1(II) \rightarrow I_2(I)$	$I_1(II) \rightarrow TS(IIa)$	$I_1(II) \rightarrow I_2(I)$
ΔA_{el}	2.3	-45.3	2.3	-45.3
ΔA_{vib}	-0.3	-7.3	2.9	-10.4
ΔA_{rot}	0.1	0.0	0.2	0.0
ΔA_{trans}	0.0	0.0	0.0	0.0
$\boldsymbol{\Delta A_{total}}$	**2.1**	**-52.6**	**5.4**	**-55.7**
ΔU_{el}	2.3	-45.3	2.3	-45.3
ΔU_{vib}	-4.5	-2.7	-6.2	-2.5
ΔU_{rot}	0.0	0.0	0.0	0.0
ΔU_{trans}	0.0	0.0	0.0	0.0
$\boldsymbol{\Delta U_{total}}$	**-2.2**	**-48.0**	**-3.9**	**-47.8**
$T\Delta S_{el}$	0.0	0.0	0.0	0.0
$T\Delta S_{vib}$	-4.2	4.6	-9.1	8.0
$T\Delta S_{rot}$	-0.1	0.0	-0.2	0.0
$T\Delta S_{trans}$	0.0	0.0	0.0	0.0
$\boldsymbol{T\Delta S_{total}}$	**-4.3**	**4.6**	**-9.2**	**8.0**

Table S10. Individual contributions to the $\Delta A_{I_2(II)\rightarrow TS(IIb)}$ and $\Delta A_{I_2(II)\rightarrow I_3(III)}$ terms computed for the second step of mechanism II of the reaction in the gas phase. All values are in kJ/mol.

	T=300 K		T=500 K	
	$I_2(II) \rightarrow TS(IIb)$	$I_2(II) \rightarrow I_3(III)$	$I_2(II) \rightarrow TS(IIb)$	$I_2(II) \rightarrow I_3(III)$
ΔA_{el}	80.0	-0.3	80.0	-0.3
ΔA_{vib}	4.0	0.7	9.3	0.3
ΔA_{rot}	0.4	0.2	0.6	0.4
ΔA_{trans}	0.0	0.0	0.0	0.0
$\boldsymbol{\Delta A_{total}}$	**84.4**	**0.6**	**89.9**	**0.4**
ΔU_{el}	80.0	-0.3	80.0	-0.3
ΔU_{vib}	-3.1	1.1	-4.8	1.3
ΔU_{rot}	0.0	0.0	0.0	0.0
ΔU_{trans}	0.0	0.0	0.0	0.0
$\boldsymbol{\Delta U_{total}}$	**76.9**	**0.8**	**75.2**	**1.1**
$T\Delta S_{el}$	0.0	0.0	0.0	0.0
$T\Delta S_{vib}$	-7.1	0.4	-14.1	1.0
$T\Delta S_{rot}$	-0.4	-0.2	-0.6	-0.4
$T\Delta S_{trans}$	0.0	0.0	0.0	0.0
$\boldsymbol{T\Delta S_{total}}$	**-7.5**	**0.2**	**-14.7**	**0.6**

SVIII. Structural data

SVIII.1. Analysis of the C-C bonds involved in the PCPs

The probability distribution functions for the three C-C bonds (C^2-C^3, C^3-C^4 and C^2-C^4) involved in the PCP of the transition states determined using the data generated by MD are shown in Figure 9 in the main text. These distributions were fitted by the Gaussian function:

$$f(d) = \frac{1}{\sqrt{2\pi\sigma^2}} exp\left(-\frac{(d-\mu)^2}{2\sigma^2}\right). \qquad \text{(Eq. S9)}$$

Assuming that each bond (d) can be represented by a harmonic oscillator with the force constant κ, the standard deviation (σ) of the corresponding distribution can be identified with the term $\sqrt{\frac{k_B T}{\kappa}}$.[7] Hence the relative strength of the bond can be estimated from the width of the corresponding probability distribution. The parameter μ stands for the average length of the bond. The values of fitting parameters μ and σ are presented in Table S11.

Table S11. Parameters μ and σ (in Å) obtained by fitting of the MD data for the three edge protonated cyclopropanes obtained as transition states of mechanism (I) (TS(I)), mechanism II, step 1 (TS(IIa)) and mechanism II, step 2 (TS(IIb)).

TS(I)

T = 300K	μ	σ
C^2-C^3	1.434	0.035
C^3-C^4	1.808	0.054
C^2-C^4	1.623	0.067

T = 500K	μ	σ
C^2-C^3	1.445	0.043
C^3-C^4	1.802	0.069
C^2-C^4	1.620	0.076

TS(IIa)

T = 300K	μ	σ
C^2-C^3	1.472	0.041
C^3-C^4	1.548	0.040
C^2-C^4	1.890	0.055

T = 500K	μ	σ
C^2-C^3	1.456	0.039
C^3-C^4	1.576	0.054
C^2-C^4	1.918	0.076

TS(IIb)

T = 300K	μ	σ
C^2-C^3	1.757	0.049
C^3-C^4	1.468	0.031
C^2-C^4	1.576	0.044

T = 500K	μ	σ
C^2-C^3	1.757	0.062
C^3-C^4	1.473	0.042
C^2-C^4	1.580	0.058

SVIII.2. Secondary cation

In mechanism I, the structures for the rotamer I_1(I) of the secondary cation have been identified with the point $\xi = 2.15$ of the simulation, corresponding to the local free energy minimum occurring at 500 K (Figure 6). Similarly, in mechanism II, for the rotamer I_1(II), we identified the secondary cation with the point $\xi = 2.15$ of the blue moon simulation which is a very shallow minimum at 500 K (Figure 7). The probability distribution functions for the C-C bonds (C^2-C^3, C^3-C^4 and C^2-C^4) of the rotamer I_1(I) and I_1(II) of the secondary cation determined using the data generated by MD are shown Figure S13.

We note that the probability distribution functions of C^2-C^4 and C^2-H^2 distances are sensitive to temperature and openings of the $C^2C^3C^4$ triangle occur when the temperature increases. This effect is more important for I_1(II).

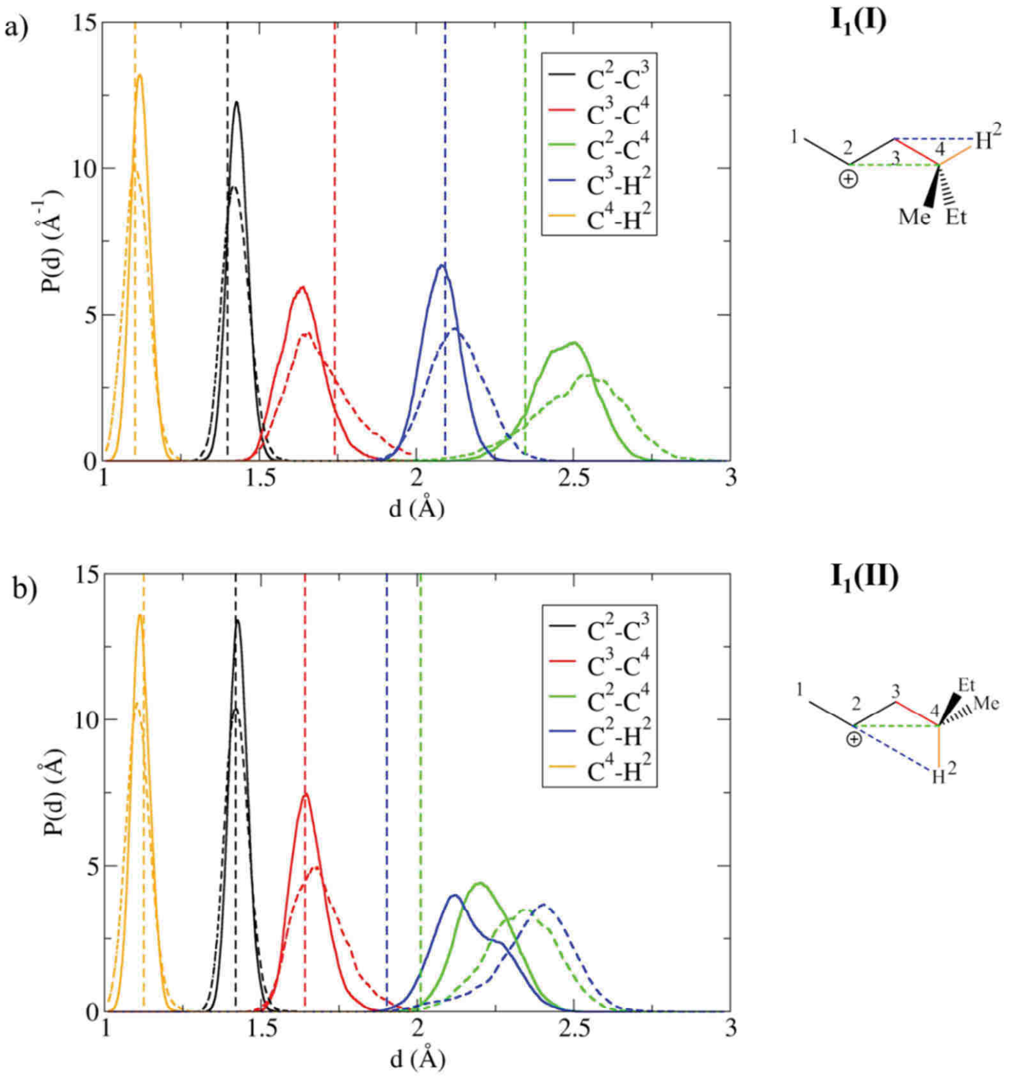

Figure S13. Probability distribution functions of selected C-C and C-H bonds in the two reactive rotamers of the secondary carbenium ion I_1 in (a) I_1(I), and (b) I_1(II) determined using MD at 300K (solid lines) and 500K (dash lines). The static approach results for the gas phase reaction are reported by vertical dashed lines.

SVIII.3. Transition state of protonation

The probability distribution functions for the O^1-H^1 distance and C^1-H^1 distance in the transition state of protonation of the initial alkene R(I) are shown in Figure S14. In the case of mechanism I at T=500 K, this transition state is located at $\xi^* = 2.76$(Figure 6 in the main text).

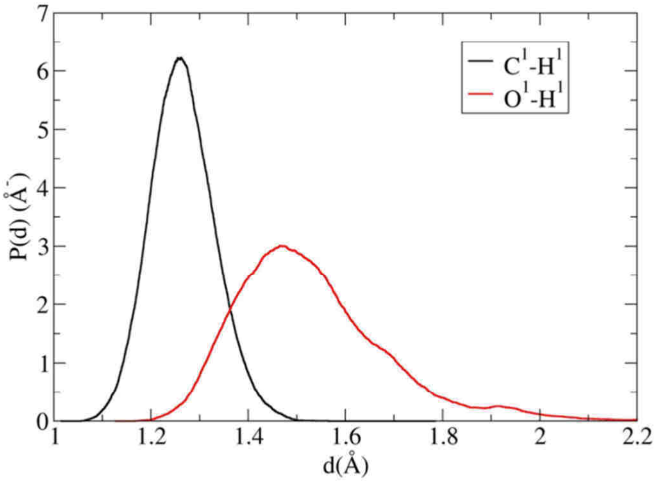

Figure S14. Probability distributions of C^1-H^1 and O^1-H^1 distances in the transition state of protonation occurring in mechanism I at 500 K.

SIX. Interaction of alkene in the reactant state with the acid site of the zeolite

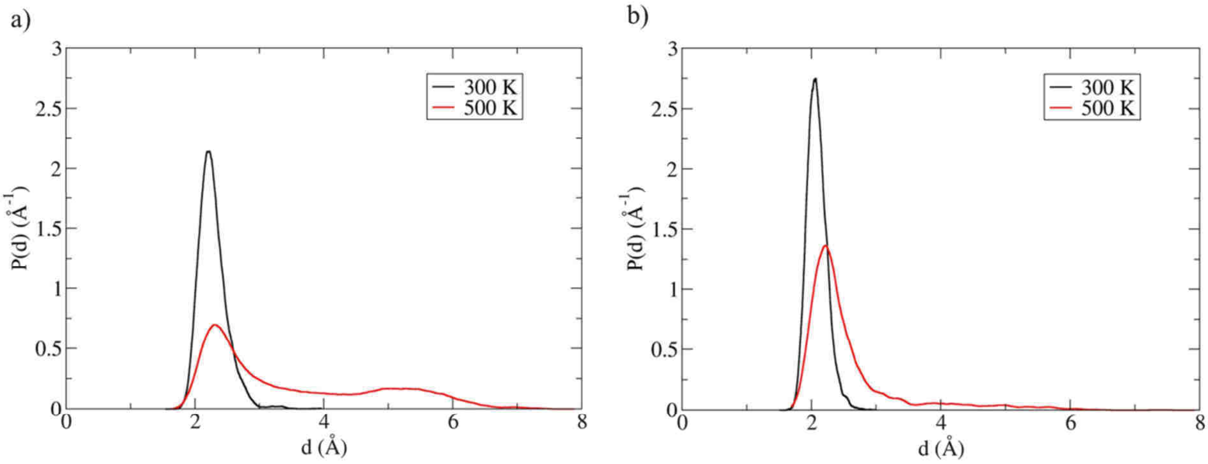

Figure S15. Distance d between the hydrogen atom of the zeolite and the center of the C=C bond in the free MD runs of reactant a) R(I) and b) R(II).

As shown in Figure S15, the adsorption complex formed by the alkene in the reactant configuration and the acid site of zeolite is fairly stable at both temperatures considered in this work: the distributions $P(d)$ are peaked at ~2.1 Å and the molecule spends spends the majority of simulation time (99% at 300 K and 51 % at 500 K) in the vicinity of the acid site with d<3.0 Å.

SX. Statistical Error Estimations

Using standard formulae for error propagation[8], the standard error for the free energy of activation ($\sigma(\Delta A^{\ddagger})$) computed using Equation (1) writes:

$$\sigma(\Delta A^{\ddagger}) = \sqrt{\sigma^2(\Delta A_{\xi_{ref,X}\to\xi^*}) + (k_B T)^2 \sigma^2\left(\ln\left(\frac{h}{k_B T}\frac{\langle|\dot{\xi}^*|\rangle}{2}P(\xi_{ref,X})\right)\right)}. \qquad \text{(Eq. S10)}$$

According to our tests, the most significant contributions to $\sigma(\Delta A^{\ddagger})$ are from the terms $\sigma(\Delta A_{\xi_{ref,X}\to\xi^*})$ while the uncertainties from the terms $\langle|\dot{\xi}^*|\rangle$ and $\sigma\left(\ln\left(P(\xi_{ref,X})\right)\right)$ turned out to be small compared to dominant sources of statistical error and were neglected in this work, simplifying thus the expression for $\sigma(\Delta A^{\ddagger})$ to

$$\sigma(\Delta A^{\ddagger}) = \sqrt{\sigma^2(\Delta A_{\xi_{ref,X}\to\xi^*})}. \qquad \text{(Eq. S11)}$$

An analogous formula:

$$\sigma(\Delta A_{X\to Y}) = \sqrt{\sigma^2\left(\Delta A_{\xi_{ref,X}\to\xi_{ref,Y}}\right)}. \qquad \text{(Eq. S12)}$$

was used to estimate the statistical uncertainty for the free energies of reaction.

As the term $\Delta A_{\xi_{ref,X}\to\xi^*}$ is computed via numerical integration using the expression

$$\Delta A_{\xi_{ref,X}\to\xi^*} = \sum_{i=1}^{M} w_i A'_i,$$

where the sum is over all integration points, w_i is the weight whose value depends on the choice of the integration algorithm (here $w_i = \frac{\xi_{i+1}-\xi_i}{2}$ for $i = 1$ and $i = M$, and $w_i = \frac{\xi_{i+1}-\xi_{i-1}}{2}$ for $1 < i < M$) and A'_i is the free energy gradient evaluated at the point ξ_i. The corresponding standard error $\sigma(\Delta A_{\xi_{ref,X}\to\xi^*})$ therefore writes

$$\sigma\left(\Delta A_{\xi_{ref,X}\to\xi^*}\right) = \sqrt{\sum_{i=1}^{M} w_i^2 \sigma^2(A'_i)}, \qquad \text{(Eq. S13)}$$

where the terms $\sigma(A'_i)$ are determined using the block method of Flyvbjerg and Petersen.[9,10] The error bars reported in this work correspond to confidence interval of 95 %, i.e. the uncertainty in the computed free energies of activation and of reaction are expressed as $\pm 1.96 \cdot \sigma(\Delta A^{\ddagger})$ and $\pm 1.96 \cdot \sigma(\Delta A_{X\to Y})$, respectively.

References

(1) Baerlocher, C., McCusker, J. K. International Zeolite Association. http://www.iza-structure.org/databases/.

(2) Smith, L. J.; Davidson, A.; Cheetham, A. K. A Neutron Diffraction and Infrared Spectroscopy Study of the Acid Form of the Aluminosilicate Zeolite, Chabazite (H- SSZ-13). *Catal. Lett.* **1997**, *49*, 143–146.

(3) Henriksen, N. E.; Hansen, F. Y. *Theories of Molecular Reaction Dynamics: The Microscopic Foundation of Chemical Kinetics;* Oxford University Press, 2008.

(4) Carter, E. A.; Ciccotti, G.; Hynes, J. T.; Kapral, R. Constrained Reaction Coordinate Dynamics for the Simulation of Rare Events. *Chem. Phys. Lett.* **1989**, *156*, 472–477.

(5) Rey, J.; Gomez, A.; Raybaud, P.; Chizallet, C.; Bučko, T. On the Origin of the Difference Between Type A and Type B Skeletal Isomerization of Alkenes Catalyzed by Zeolites: The Crucial Input of ab initio Molecular Dynamics. *J. Catal.* **2019**, *373*, 361–373.

(6) Eyring, H. The Activated Complex in Chemical Reactions. *J. Chem. Phys.* **1935**, *3*, 107–115.

(7) Baron, R.; van Gunsteren, W. F.; Hünenberger, P. H. Estimating the Configurational Entropy from Molecular Dynamics Simulations: Anharmonicity and Correlation Corrections to the Quasi-Harmonic Approximation. *Trends Phys. Chem.* **2006**, *11*, 87–122.

(8) Ku, H. H. Notes on the Use of Propagation of Error Formulas. *J. Res. Nat. Bur. Stand., Sec. C* **1966**, *70C*, 263–273.

(9) Flyvbjerg, H.; Petersen, H. G. Error estimates on averages of correlated data. *J. Chem. Phys.* **1989**, *91*, 461–466.

(10) Frenkel, D.; Smit, B. *Understanding Molecular Simulation. From Algorithms to Applications*; Computational science series; Academic Press, 2002.

Section V. Relevant cracking intermediates and transition states for β-scission reactions of alkenes over acid zeolites revealed by AIMD simulations

The corresponding Supporting Information is presented at the end of the section.

V.1. Introduction

The cracking of alkenes is a key reaction to optimize the size of hydrocarbon molecules and / or to open cyclic molecules. It can be achieved catalytically thanks to acid catalysts, in the framework of bifunctional catalysis mechanisms.[1–3] The latter consist in the transformation of alkanes, and involve a dehydrogenation function to generate alkenes that are then protonated, isomerized and cracked on the acidic phase, such as a protonic zeolite. In practice, such reactions take place in the hydrocracking process where they are aimed at, but are undesired in other contexts, such as the isomerization of short alkanes (C_7 and C_8),[4] aromatics[5] or MTO processes.[6] Knowing the rate of cracking reactions with respect to isomerization reactions is thus key for selectivity control of such reactions. Experimental results showed that in superacid liquids[7] and in USY zeolite[8] the rates of cracking reactions (β-scissions) and isomerization reactions of alkenes decrease in the following order: type A β-scission (from tertiary to tertiary cation), type B isomerization reactions (with increase of branching degree), type B_1 and B_2 β-scission reactions (Figure 1), following the terminology introduced by Weitkamp et al.[9] Notably, the easiest type A β-scissions (between tertiary cations) require alkanes with at least 8 carbon atoms and they cannot occur on the C_7 species investigated in the present work.

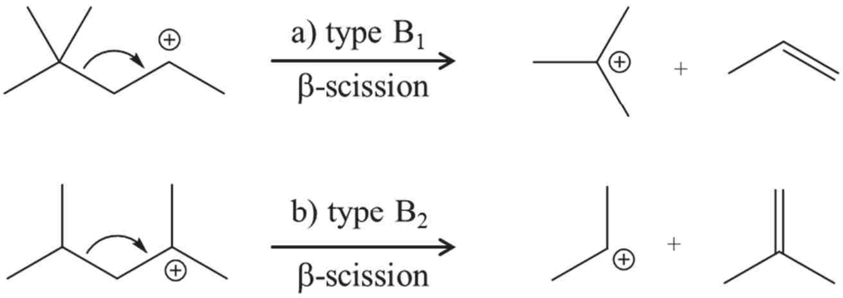

Figure 1. a) Type B_1 β-scission (secondary to tertiary cations) of 4,5-dimethyl-penten-2-ium in isobutenium cation and propene. b) Type B_2 β-scission (tertiary to secondary cations) of 2,4-dimethyl-penten-2-ium in propenium cation and isobutene.

Until very recently, the theoretical determination of mechanisms of cracking of olefins and of the corresponding barriers was done within the framework of static DFT calculations, most often with alkoxides as reactant and products, and without consideration of thermal and dynamic effects.[10–13] Large potential energy barriers were computed with static DFT calculations. Mazar and coworkers[10] obtained potential energy barriers of 92 and 115 kJ/mol for type A cracking of C_8 alkenes in H-ZSM-5, depending on the initial conformation. They computed potential energy barriers for a type B_1 β-scission starting from a secondary alkoxyde that are as large as 150 kJ/mol. For type B_2 reactions starting from different rotamers of the same tertiary cation, they predicted barriers of 89 kJ/mol or 171 kJ/mol. The activation energies determined for type C cracking (secondary to secondary cation) starting from a secondary alkoxide are around 160-170 kJ/mol. For type D cracking (secondary to primary cations) of hex-1-ene in H-ZSM-5, Guo et al[11] found, in a static calculation on a large cluster of zeolite starting from a π-complex, a potential energy barrier of around 180 kJ/mol whereby an intermediate secondary cation was predicted to be 115 kJ/mol higher in energy than the initial π-complex. In H-SAPO34 catalyst, Wang et al[12] determined potential energy barriers between 120 and 178 kJ/mol for the cracking of C_7 species, depending on the mode of the reaction, starting from alkoxides. Potential energy barriers of around 170 kJ/mol were also computed for type C and D cracking reactions (starting from alkoxides) of C_6 alkene in H-ZSM-5, much higher than the barrier for a type B isomerization reaction (92 kJ/mol).[13] All these static investigations show that depending on the configuration chosen as a starting point, large variation in predicted barriers is observed.

In these static DFT calculations, the limitations of the methods are apparent. Significant uncertainties come from the initial configuration chosen,[10] which was also demonstrated on the case of a B_2 β-scission of a C_8 tertiary carbenium ion: van Speybroeck and coworkers found enthalpy barriers ranging from 94 to 151 kJ/mol (and free energy barriers varying between 90 to 167 kJ/mol at 773 K) for four different conformations of the same initial cation.[14] Similar limitations of the static approach were previously highlighted for propane cracking in chabazite,[15] for alkene cracking in H-ZSM-5,[14] and for isomerization reactions in chabazite.[16] All these studies clearly showed that the static approach is highly problematic for such reactions, relying on a single configuration to describe reactant, transition state and products, and underestimating the entropic effects at finite temperature.

Kinetic modeling, based on fitting of experimental data, is another source of information.[8,17–20] As discussed below, the range of barriers computed with these methods is extremely large which raises questions about their relevance.

For type A cracking of C_8 to C_{12} alkenes in zeolite Y, Martens et al. found intrinsic enthalpy barriers ranging between 110 and 184 kJ/mol depending on the choice of the model to estimate the protonation enthalpy of the alkene reactant.[17] These barriers are higher than or similar in magnitude to their barriers for type B isomerization reactions. In single-event kinetic models, enthalpy barriers of 143 kJ/mol for type C cracking of C_6 on H-ZSM-5,[18] 170 kJ/mol for type B_1 cracking of 1-pentene in HZSM-5,[20] and 118 kJ/mol (type B_2) to 152 kJ/mol (type B_1) were proposed for C_{12} cracking in H-BEA.[19] Similarly, barriers from 125 to 149 kJ/mol were estimated for type A to type C β-scission of octane in Pt/H-USY zeolite.[21]

In kinetic modeling, large uncertainties are due to the fitting of numerous parameters, to the approximations in the protonation enthalpy of the initial alkene, and to the difficulty to properly estimate the kinetic prefactor related to the entropy of activation.

Ab initio molecular dynamics is thus expected to provide a more reliable description of these effects. For pentane and hexane cracking in H-ZSM-5, dynamics and entropic effects were shown to be necessary to describe the diversity of the products and to study the selectivity.[22,23] In a very recent study, with biased MD (umbrella sampling), activation barriers were computed for the cracking of C_8 alkenes in H-ZSM-5, starting from tertiary cations: 53 kJ/mol (type A), around 70 kJ/mol (type B_2) and 112 kJ/mol (type E_2, from tertiary to primary cations). These values are much lower than the corresponding static barriers (90 to 197 kJ/mol for the type B_2 cracking).[14]

However, in molecular dynamics, the exploration of such mechanisms is also challenging, with many factors that must be taken into account: different possible sites for the reactions in the zeolite, mobility of the two fragments (cationic and alkene) after cracking, and large number of by-reactions mainly with secondary cations (hydrogen and methyl shifts, proton exchange between the cationic fragment and the alkene, formation of alkoxides and π-complexes). Under such circumstances, identifying a reliable approximation to reaction coordinate driving the process of interest reversibly is a difficult task.[14] A particular site and a particular reactive channel have to be chosen to describe correctly the reaction in MD.

The role of secondary cations in these reactions is also an open question. In textbooks[1] or reviews[24,25] on hydrocracking, the mechanisms of the step of cracking, by β-scission, are written with carbenium ions as reactants. However, as shown in previous theoretical studies,[14,26–28] secondary cations are highly reactive and short-lived species, making it difficult to investigate mechanisms starting from a secondary cation. This problem will be addressed in this work.

Following our previous investigation of the isomerization reactions of C_7 alkenes,[16,28] our objective in the present work is to provide an accurate determination of mechanisms and rate constants for the cracking of C_7 alkenes which are unwished reactions degrading the targeted selectivity of the hydroisomerization process. At about 500 K, the predominant bifunctional cracking products of C_7 alkanes formed in zeolites Y, ZSM-23 and EU-1 are propane and isobutane. As described in Figure 1, two mechanisms account for the formation of propane and isobutane from a dibranched species: a type B_1 β-scission from secondary to tertiary cations and a type B_2 β-scission from tertiary to secondary cations.[4]

In Section 3.1.1, we investigate the type B_1 mechanism of cracking of the 4,5-dimethyl-penten-2-ium secondary cation and its relation with a more stable dibranched reactant, the 2,3-dimethyl-penten-2-ium tertiary cation. Variants of this cracking mechanism, involving an alkoxide and a π-complex are investigated in Section 3.1.2. In Section 3.2, a second route producing propane and isobutane from a dibranched C_7 cation through a type B_2 β-scission (from tertiary to secondary cations as illustrated in Figure 1.b) is explored and compared with the previous type B_1 β-scission. For the two types of β-scission mechanisms, we will provide a detailed analysis of the structure and electronic features of the transition states, revealing unexpected nature of transitions states, in particular for the B_2 type cracking, with strong impact for catalysis.

V.2. Methodology

The methodology used in this chapter is the same as in our previous work.[16,28] The supercell of chabazite is shown in Figure 2 (see also Section SI), where O^1 and O^4 oxygen atoms (following the labeling introduced in ref.[29]) involved in the transformations considered in this study have been highlighted. The main formulas for free energy calculations are reproduced below. The free-energy of activation ($\Delta A^{\ddagger}$) for the process $X \rightarrow Y$ is defined as follows:

$$\Delta A^{\ddagger} = \Delta A_{\xi_{ref,X}\to\xi^*} - k_B T\ln\left(\frac{h}{k_B T}\frac{\langle|\dot{\xi}^*|\rangle}{2}P(\xi_{ref,X})\right), \tag{1}$$

where $\Delta A_{\xi_{ref,X}\to\xi^*}$ is a reversible work needed to shift the value of reaction coordinate (ξ) from some arbitrary reference value characteristic for reactant ($\xi_{ref,X}$) to the value ξ^* defining the free-energy transition state, $\langle|\dot{\xi}^*|\rangle$ is the average velocity of reaction coordinate at the transition state, and $P(\xi_{ref,X})$ is the probability density of the state $\xi_{ref,X}$ in ensemble of all reactant (X) configurations. The term $\Delta A_{\xi_{ref,X}\to\xi^*}$ is obtained from the bluemoon ensemble method,[30,31] $P(\xi_{ref,X})$ can be determined using the straightforward MD simulations, and $\langle|\dot{\xi}^*|\rangle$ is computed numerically using a constrained MD with $\xi(r) = \xi^*$ (see Supporting Information SII). Free energies of reaction ($\Delta A_{X\to Y}$) are computed similarly:

$$\Delta A_{X\to Y} = \Delta A_{\xi_{ref,X}\to\xi_{ref,Y}} - k_B T\ln\left(\frac{P(\xi_{ref,X})}{P(\xi_{ref,Y})}\right). \tag{2}$$

In Equation (2), $\Delta A_{\xi_{ref,X}\to\xi_{ref,Y}}$ is the reversible work needed to shift the value $\xi(\boldsymbol{r})$ from $\xi_{ref,X}$ to some arbitrary reference value characteristic for product (Y), $\xi_{ref,Y}$, and $P(\xi_{ref,Y})$ is the probability density of the state $\xi_{ref,Y}$.

Undesired by-reactions, such as the deprotonation of the reactant or product molecules, have been prevented by the use of appropriate restraining potentials described in Section SIII.1. Transition path sampling (TPS) simulations have been used as described in the methodology Section II.5.2.4.

All simulations are performed at the temperature T = 500 K which is close to the relevant experimental conditions.[4,17]

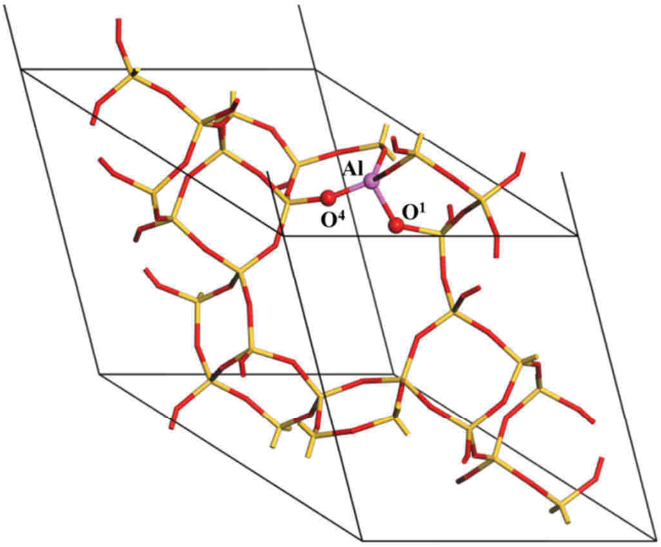

Figure 2. Unit cell of chabazite (Si in yellow, O in red, Al in purple). The proton is omitted in this representation as we started our investigations from a cation which has captured the proton of the acid site of the zeolite.

V.3. Results and discussion

V.3.1. Type B_1 β-scission

In this section the type B_1 β-scission of the 4,5-dimethyl-penten-2-ium dibranched secondary cation (I) is investigated (Figure 1.a). In free MD runs in zeolites at 500 K, secondary cations spontaneously evolve within a few hundreds of femtoseconds (less than 2 picoseconds in general) into π-complexes, alkoxides or cracking products (see below).[14,16,28] Thus it is not possible to investigate this type B_1 β-scission starting directly from the secondary cation. However, all dibranched C_7 cations are expected to be connected one to another by fast type A isomerization reactions (including hydride and methyl shifts).[1,2] In a preliminary free run in gas phase (see below), type A isomerization of the secondary cation I into a more stable tertiary dibranched reactant, the 2,3-dimethyl-penten-2-ium tertiary cation (R) was observed (Figure 3). In Section 3.1.1, we started to investigate the type A isomerization of the dibranched tertiary cation R into the secondary one I, and the subsequent transformations of I including also cracking. Variants of the cracking mechanism, involving an alkoxide and a π-complex are investigated in Section 3.1.2 and the transition states are analyzed in Section 3.1.3.

V.3.1.1 Formation and cracking of the 4,5-dimethyl-penten-2-ium secondary cation

Characterization of reactant state

a) Gas phase analysis

Starting from a stable tertiary cation, the 2,3-dimethyl-penten-2-ium cation (R), the isomerization of R into the reactive secondary cation, the 4,4-dimethyl-penten-2-ium (I), proceeds via two type A isomerization steps (methyl and hydride shifts). The mechanism of isomerization (Figure 3) has been investigated by the static approach on the molecular system in gas phase (see the potential energy profile along the intrinsic reaction coordinate in Figure S3).

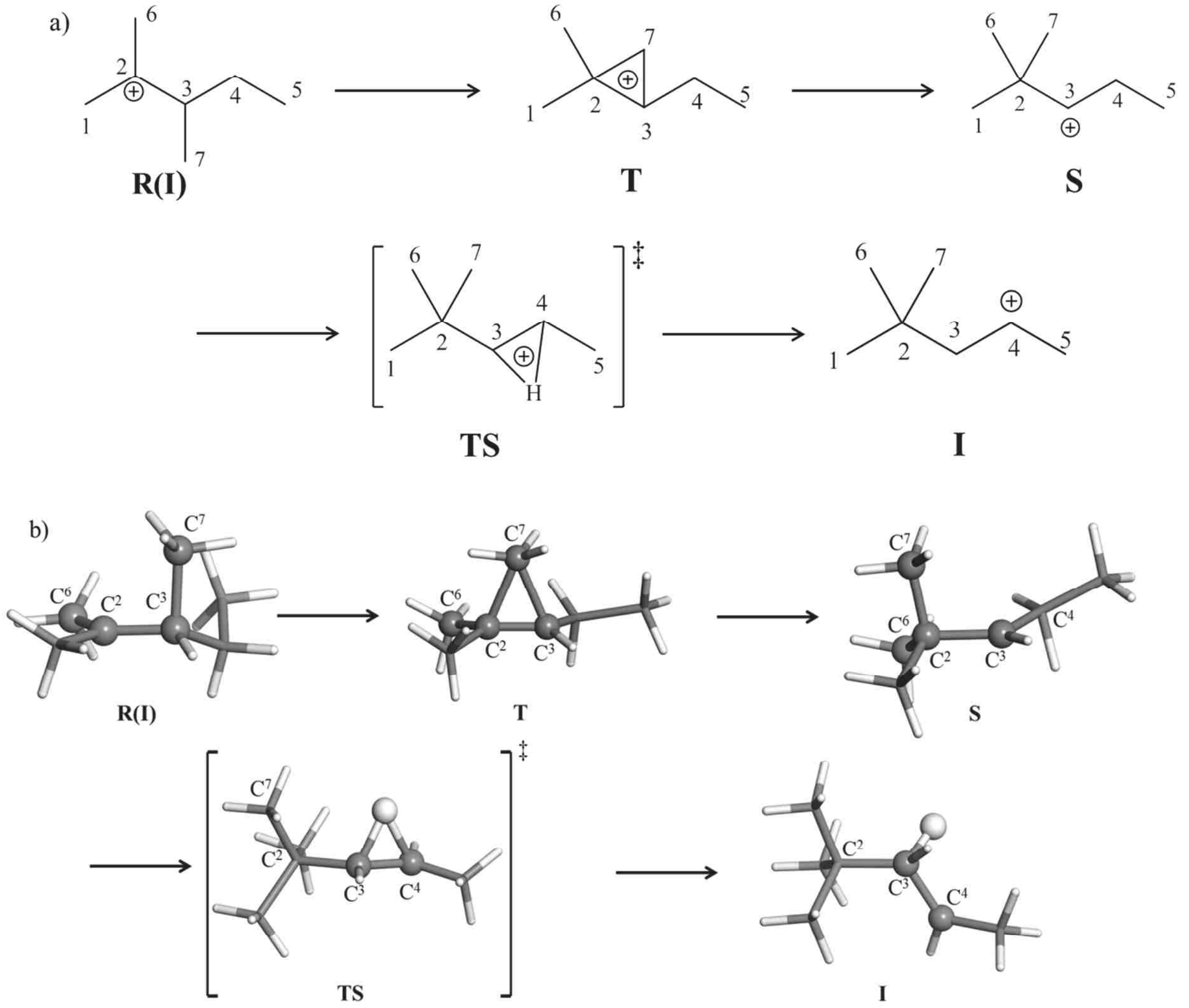

Figure 3. a) Mechanism of formation of the intermediate secondary cation I, starting from the rotational isomer R(I) of the reactant. Note that the corner protonated cyclopropane T and secondary cation S formed during the transformation between the reactant R(I) and the TS are not stationary points on the potential energy surface for the reaction in gas phase (Figure S3.b) The ball and sticks structures have been extracted from the constrained MD runs in chabazite.

The transformation of the rotational isomer R(I) of the reactant begins with a methyl shift giving a highly unstable secondary cation (S) via a corner protonated cyclopropane (T) (Figure 3). S undergoes a subsequent hydride shift to give the secondary cation I. We emphasize that the structures T and S are not stationary points on the potential energy surface for the gas phase reaction (Figure S3). As already discussed in the literature, secondary cations such as S, with the positive charge on the carbon atom next to a quaternary carbon atom, are highly elusive species.[14] As a consequence, the unique transition state on the path connecting potential energy minima R(I) and I is located between the secondary cations S and I where a hydride shift takes place.

Consistent with our previous work on isomerization reactions,[16,28] the IRC analysis for the gas phase reaction (Figure S3) showed that a specific rotational isomer R(I) is required for the initial methyl shift between the configurations R and S formed in the course of reaction (Figure 3). The dihedral angle (τ) defined by the sequence of atoms C^6-C^2-C^3-C^7 (Figure 3) is the relevant parameter to control the geometry of the reactant. In the specific conformations involved in the C^7H_3 methyl shift, the value of (τ) must be around ± 90 deg.

b) In chabazite

The free energy of the reactant R in CHA as a function of τ at T = 500 K has been determined by a blue moon simulation. The constrained simulations have been performed with 10 points evenly distributed in the range -90 deg. $\leq \tau <$ 90 deg. The computed free energy profile is shown in Figure 4. Note that the periodicity $A(\tau+180\ deg.) = A(\tau)$ follows from the symmetry of the reactant molecule. We identified two stable rotamers, hereafter labeled as R(I) and R(II) (Figure 5), corresponding to the minima on the free energy profile. The rotational isomer R(II) is 4.9 kJ/mol more stable than the state R(I) and the smallest barrier separating these two states is only 6.7 kJ/mol. The free energy profile $A(\tau)$ has been used to compute the probability of occurrence of the rotamer R(I) defined by the formula:

$$p\big(R(I)\big) = \frac{\int_{\tau_{max,1}}^{\tau_{max,2}} exp\left(-\frac{A(\tau)}{k_B T}\right) d\tau}{\int_{-180}^{0} exp\left(-\frac{A(\tau)}{k_B T}\right) d\tau}, \tag{3}$$

where $\tau_{max,1}$ and $\tau_{max,2}$ are the maxima on the free energy profile separating R(I) and R(II). The computed value for $p\big(R(I)\big)$ is 20.9 %.

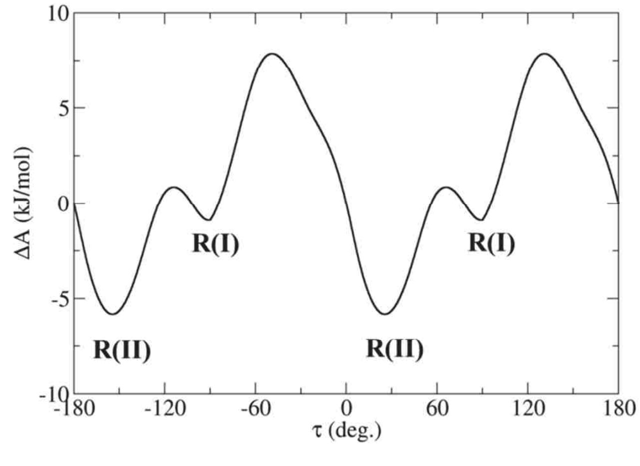

Figure 4. Free energy profile as a function of the torsion angle τ defined by the carbon atoms C^6, C^2, C^3, and C^7 in the reactant (R) adsorbed in chabazite. Note that periodic boundary conditions apply, i.e. the point $\tau = -180$ deg. is identical to the point $\tau = 180$ deg.

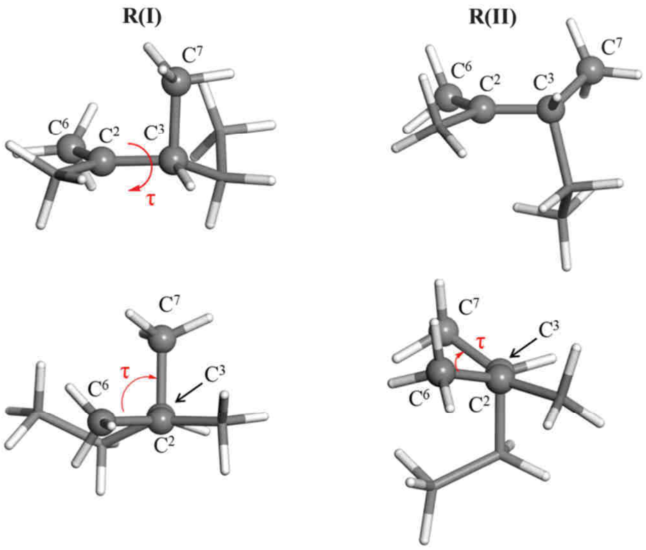

Figure 5. Rotational isomers R(I) ($\tau \approx 90$ deg.) and R(II) ($\tau \approx 30$ deg) of the reactant 2,3-dimethyl-penten-2-ium cation. Top panels: side view; bottom panels: front view was chosen so that the atom C^2 overlaps the atom C^3.

Free energy profile for the isomerization step from R to I

We used for this reaction the following approximation to reaction coordinate, ξ (Equation (4)) which drives the methyl shift of C^{7}H$_3$ from C^3 to C^2 and the hydride shift of one hydrogen atom of C^4 to C$^{3.}$ ξ is invariant with respect to the interchange of the three methyl groups C^{1}H$_3$, C^{6}H$_3$, C^{7}H$_3$ and of the three hydrogen atoms H^a, H^b and H^c of C^3 and C^4 (the numbering of atoms is given in Figure 3).

$$\xi = \sum_{j=1,6,7} \eta\left(C^2 - C^j\right) - \sum_{j=1,6,7} \eta\left(C^3 - C^j\right) + \sum_{j=a,b,c} \eta\left(C^3 - H^j\right) - \sum_{j=a,b,c} \eta\left(C^4 - H^j\right) \tag{4}$$

where $\eta(A - B)$ is the coordination number of the A–B bond:[32]

$$\eta(A - B) = \frac{1 - \left(\dfrac{d(A - B)}{d_{A-B,ref}}\right)^9}{1 - \left(\dfrac{d(A - B)}{d_{A-B,ref}}\right)^{14}}, \tag{5}$$

with $d_{CC,ref} = 1.7$ Å being the reference length for the C-C bonds and $d_{CH,ref} = 1.3$ Å the reference length for the C-H bonds.

Upon integration of free energy gradients computed for a grid of 16 points, we obtained the free energy profile shown in Figure 6.

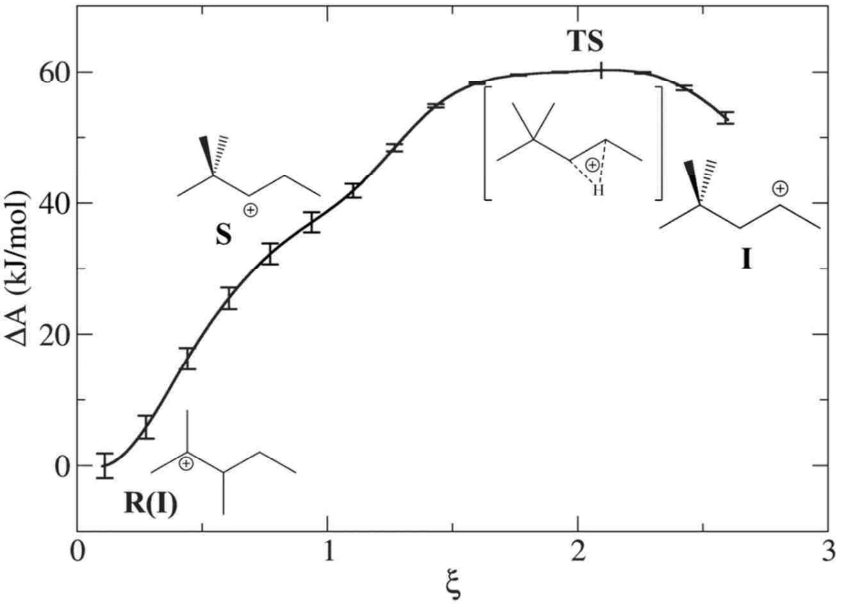

Figure 6. Free energy profile (A(ξ)) computed at 500 K using the blue moon ensemble approach for the isomerization reaction via mechanism (I) in chabazite.

The initial part of the profile, from the reference state R(I) ($\xi_{ref,R} = 0.11$) to S ($\xi \approx 0.9$) corresponds to the methyl shift. An hydride shift transforms S into the secondary cation 4,4-dimethyl-penten-2-ium (I). The transition state is located at $\xi^* = 2.1$. Its structure is discussed in Section 3.1.3. The value of the term $\Delta A_{\xi_{ref,R} \to \xi^*}$ is 60.3 ± 3.8 kJ/mol.

The free energy of activation $\Delta A^{\ddagger}$ is determined via Equation (1). The computed value of the velocity term $\langle |\dot{\xi}^*| \rangle$ is $1.9 \cdot 10^{13}$ s^{-1}. The term $P(\xi_{ref,R})$ cannot be computed efficiently in a straightforward MD run because of the free energy barrier separating R(I) and R(II). Following the computational strategy suggested in our previous work,[16,28] we express $P(\xi_{ref,R})$ as a product of two terms computed separately:

$$P(\xi_{ref,R}) = \tilde{P}(\xi_{ref,R})\, p(R(I)), \qquad (6)$$

where $\tilde{P}(\xi_{ref,R})$ is the probability density of the configuration $\xi_{ref,R}$ among the configurations of rotational isomer R(I), and $p(R(I))$ is the probability to find the rotamer R(I) among all reactant configurations. The value of the former term determined in a long MD run (Section SIII.3) is 4.58, while that of the latter, $p(R(I))$ obtained in blue moon simulations (*vide supra*), is 0.209. The resulting free energy of activation $\Delta A^{\ddagger}$ is 60.9 ± 3.8 kJ/mol.

Thus, it appears that the two type A isomerizations needed to connect R with I are consecutive and not synchronous, and moreover, S (obtained after methyl shift) is not defined as an intermediate on the free energy surface, contrary to the general belief. The TS is the one that connects the two secondary carbenium ions S and I. In the end, the barrier for these two consecutive type A isomerization reactions (60.9 kJ/mol) is slightly lower than that of a 1,3 hydride shift from a tertiary to a secondary carbenium ion as calculated in our previous work (67.4 kJ/mol at 500 K).[28] Thus, these type A isomerization reactions have comparable kinetics and are faster than type B isomerization reaction, as expected empirically.[1]

The calculation of the free energy of reaction is complicated by the fact that the secondary cation 4,4-dimethyl-penten-2-ium (I) formed after crossing the free energy barrier is not stable in a MD run that is long enough to collect a sufficient statistics, which is caused by the fact that this metastable cation can readily undergo many different transformations. The investigation of the fate of the secondary cation I therefore requires a special attention and we provide a more detailed discussion of this problem in the next section.

β-scission of the secondary cation (I) investigated by transition path sampling

A preliminary long free MD run in the gas phase has shown that the secondary cation 4,4-dimethyl-penten-2-ium (I) undergoes spontaneous cracking, with a very small free energy barrier of ~7 kJ/mol (see Section SIII.5). In chabazite, our exploratory free runs starting from the secondary cation revealed that many different spontaneous processes (including cracking) can occur. In order to identify the most important of these processes, and draw the landscape of possible processes, we employed the transition path sampling method[33,15] that is best suited for this purpose.

The initial reactive trajectory was obtained by joining two segments starting from a potential energy saddle point of the hydride shift between the secondary cations I and S and generated by integrating equations of motion initiated with random generated (and Maxwell-Boltzmann distributed) atomic momenta forward and backward in time. 200 trial moves were generated by the shooting trial moves,[33] with an acceptance rate of 73 %. The length of trajectories was fixed to 500 ps, which was enough to describe the formation of the reactant (R) on the one side, and the intermediate secondary cation (I) or one of its by-products on the other side. The approximation to reaction coordinate defined in Equation (4) was used as an order parameter to distinguish reactant state ($\xi < 1.2$) and product states ($\xi > 1.7$), in whatever forms (secondary cation, π-complexes or alkoxides). The reactive trajectories harvested in the TPS simulations were subsequently prolonged up to 2 ps to identify the final stable products. The different products identified in this way as well as their respective likelihoods of occurrence are given in Figure 7. A large number of different reactions was identified: 4.5% of the trajectories led to direct cracking while in most of the simulations (81%), the secondary cation evolved into alkoxide or π-complex. In 3% of the cases, the secondary cation survived to the extended run of 2 ps and in 11.5% it transformed back to the reactant state. Only one kind of alkoxide (4,4-dimethyl-pent-2-oxide) was observed, located on the oxygen atom O^4 (Figure 2), whereas three different π-complexes (among which 4,4-dimethyl-pent-1-ene (45.9%), (Z) (1,5%) and (E)-4,4-dimethyl-pent-2-ene (52.6%)) were formed with proton located on two oxygen atoms O^1 and O^4 (in 41% and 59% of the cases giving a total of six different reactions for the formation of π-complexes.

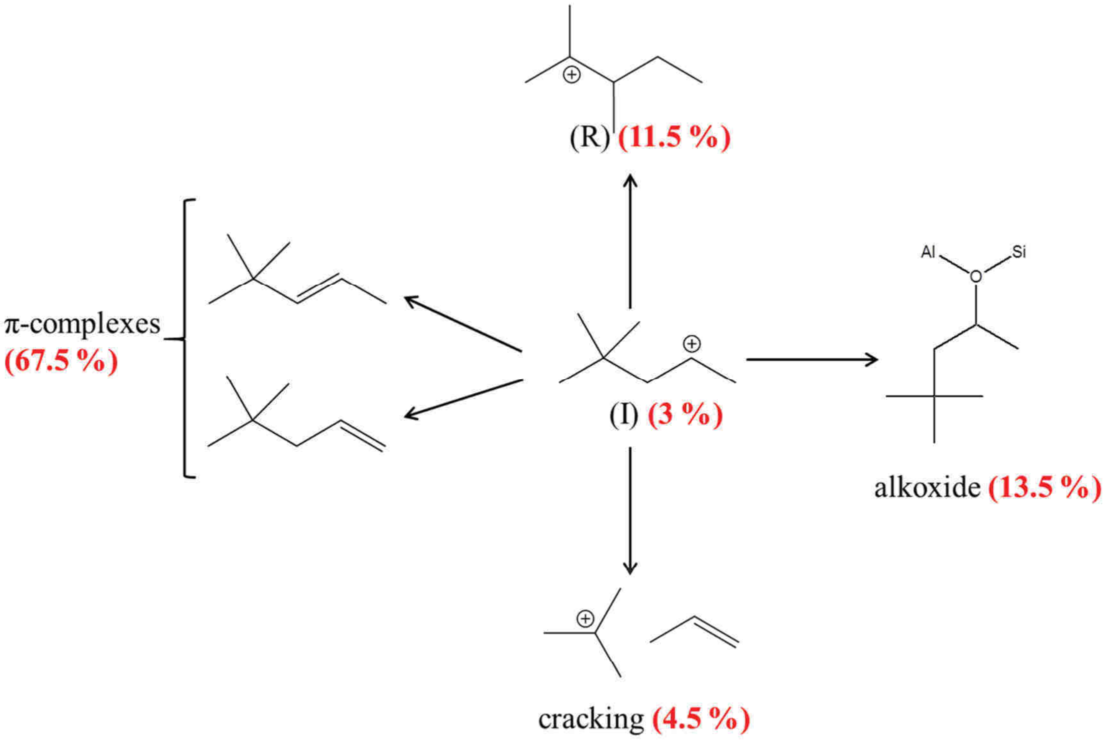

Figure 7. Percentages of trajectories generated by transition path sampling leading to different products.

This investigation of the transformations of the secondary 4,5-dimethyl-penten-2-ium cation (I), precursor of a cracking reaction, revealed a complex ensemble of reactions linked to the same free energy transition state. Once this secondary cation is formed in an activated process (with a free energy barrier of 60.9 kJ/mol from the stable tertiary cation 2,3-dimethyl-penten-2-ium (R), Section 3.1.2), small barriers can be spontaneously overcome to give different products. The direct cracking reaction appears to be a relatively infrequent transformation scenario. On the other hand, the alkoxide and π-complexes are occurring with high likelihood: the possibility for these two kinds of species to undergo subsequent cracking needs to be therefore considered. In Section 3.1.2., we show that such a scenario is indeed feasible.

V.3.1.2. Type B$_1$ β-scission from alkoxide or π-complex

In the previous section, we demonstrated that the transformation of the secondary cation 4,4-dimethyl-penten-2-ium (I) into alkoxide or π-complex is more likely than the direct cracking. In this section, the free energetics of type B$_1$ β-scission starting from alkoxide and π-complex is thus investigated. The mechanisms and the numbering of atoms are described in Figure 8. The reactants (4,4-dimethyl-pent-2-oxide and (E)-4,4-dimethyl-pent-2-ene adsorbed on the oxygen atom O^4) were considered in our analysis as they were formed as predominant products in our TPS simulations.

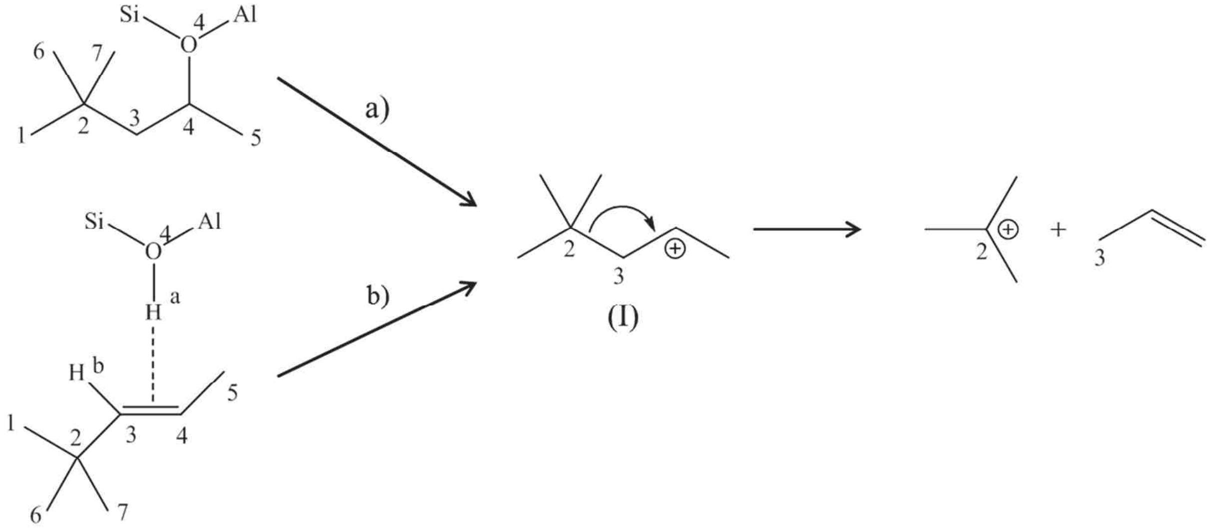

Figure 8. Mechanisms of the type B$_1$ β-scission starting from an alkoxide (a) or a π-complex (b), with the numbering of atoms used in the definition of the approximation to reaction coordinate.

Reaction starting from a π-complex.

For this reaction, the following approximation to reaction coordinate was used to drive the protonation of the π-complex and the breaking of the C^2-C^3 bond:

$$\xi = \eta(C^3 - H^a) + \eta(C^3 - H^b) - \eta(C^2 - C^3), \qquad (7)$$

where the coordination number $\eta(A - B)$ is defined as in Equation (5), with $d_{C-H,ref} = 1.3$ Å and $d_{C-C,ref} = 1.7$ Å..

The blue moon simulations have been performed using 20 integration points along ξ and the resulting free energy profile is displayed in Figure 9.a. In the first part of the profile, from $\xi_{ref,R} = 0.16$ to $\xi = 0.95$, the proton transfer between the zeolite and the chemisorbed alkene takes place, giving the secondary cation (I) which appears as a very shallow local minimum. Then, from

$\xi \approx 0.95$ to $\xi_{ref,P} = 1.70$, the cracking occurs: the C^2–C^3 bond is broken and tert-butylium cation and propene are formed. The transition state for cracking is located at $\xi^* \approx 1.45$.

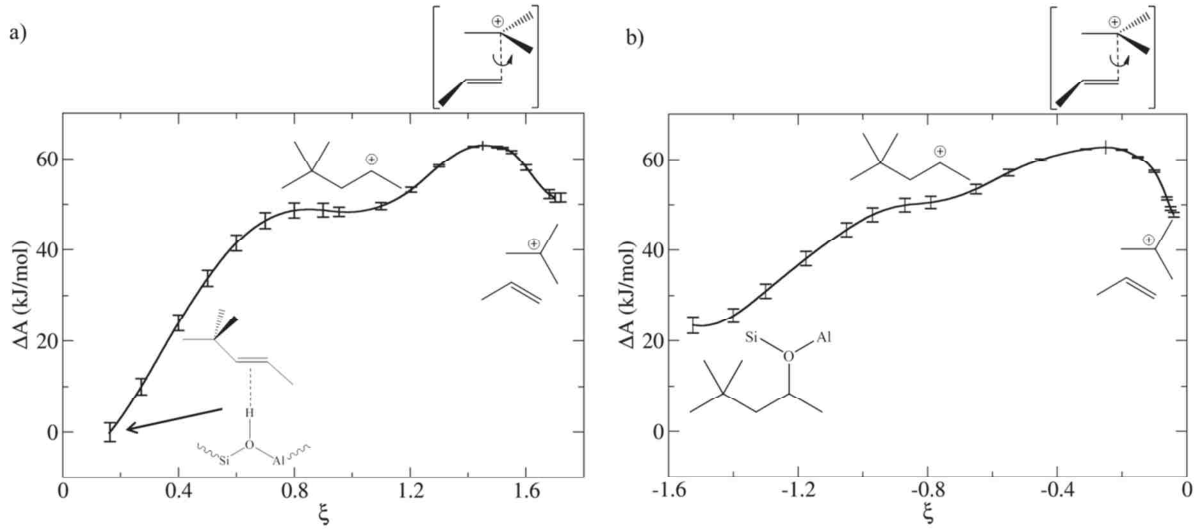

Figure 9. Free energy profiles (A(ξ)) computed using the blue moon ensemble approach for a) the type B_1 β-scission starting from a π-complex, and b) the type B_1 β-scission starting from an alkoxide, in chabazite at T = 500 K. The profile b) has been shifted to make the common transition states coincide.

The values of the terms $\Delta A_{\xi_{ref,R}\rightarrow\xi^*}$, $P(\xi_{ref,R})$ (with $\xi_{ref,R} = 0.16$, see Section SIV.1), and $\langle|\dot{\xi}^*|\rangle$ needed to determine $\Delta A^{\ddagger}$ are 63.0 ± 4.2 kJ/mol, 3.27 and $1.27 \cdot 10^{13}$ s^{-1}, respectively. The resulting value of free energy of activation computed using Equation (1) is 60.1 ± 4.2 kJ/mol. Finally the free energy of reaction, computed using Equation (2) is 52.5 ± 4.6 kJ/mol, whereby the terms $\Delta A_{\xi_{ref,R}\rightarrow\xi_{ref,P}} = 51.5 \pm 4.6$ kJ/mol and $P(\xi_{ref,P}) = 4.19$ (determined for $\xi_{ref,P} = 1.70$, see Section SIV.1) have been employed.

Reaction starting from an alkoxide

For this reaction, the following approximation to reaction coordinate was used to describe the desorption of the alkoxide and the breaking of the C^2-C^3 bond:

$$\xi = -\eta(O^4 - C^4) - \eta(C^2 - C^3), \qquad (8)$$

where $\eta(A - B)$ is the coordination number of the A–B bond (Equation (5)) with $d_{ref} = 1.7$ Å for C–C and C–O bonds. The numbering of atoms is defined in Figure 8.

The blue moon simulations have been performed using 19 integration points along ξ. The computed free energy profile is displayed in Figure 9.b. In the first part of the profile, from

$\xi_{ref,R} = -1.52$. to $\xi \approx -0.79$, the O^a–C^4 bond is broken and the secondary cation 4,4-dimethyl-penten-2-ium (I) is formed. It is localized in a flat zone of the free energy profile. In the next stage of reaction occurring in the interval between $\xi \approx -0.79$ and $\xi_{ref,P} = -0.04$, the C^2–C^3 bond is broken, forming tert-butylium cation and propene. The transition state is located at $\xi^* \approx -0.25$. The value of the term $\Delta A_{\xi_{ref,R} \to \xi^*}$ is 39.3 ± 3.7 kJ/mol.

The free energy of activation $\Delta A^\ddagger$ is determined via Equation (1), employing the terms $\langle|\dot{\xi}^*|\rangle = 3.2 \cdot 10^{12}$ s^{-1} and $P(\xi_{ref,R}) = 4.44$ (Section SIV.2). The computed value of $\Delta A^\ddagger$ is 40.9 ± 3.7 kJ/mol. Finally, the free energy of reaction, computed using Equation (2) combined with the terms $\Delta A_{\xi_{ref,R} \to \xi_{ref,P}} = 24.4 \pm 3.8$ kJ/mol and $P(\xi_{ref,P}) = 7.13$ (Section SIV.2) is 26.4 ± 3.8 kJ/mol.

Complete free energy diagram

The isomerization of the stable tertiary cation 2,3-dimethyl-penten-2-ium (R) into the active secondary cation 4,4-dimethyl-penten-2-ium (I) acting as the precursor of cracking by two successive type A isomerization reactions (a methyl and an hydride shifts) is an activated process with a free energy barrier of 60.9 kJ/mol (Section 3.1.1). The secondary cation (I), being extremely reactive, can undergo spontaneous cracking or, with even higher likelihood, it can be transformed into an alkoxide or into several π-complexes which can be subsequently cracked. In order to build a full free energy profile for this pool of reactions (Figure 10), a blue moon simulation connecting the initial reactant (R) to the π-complex (E)-4,4 dimethyl-pent-2-ene has been performed. This reaction is equivalent to a methyl shift plus proton shift from the carbenium to the zeolite network. The transition state corresponds to that of the proton transfer to the zeolite. Details of this simulations are given in Section SV. We found a value of the free energy of reaction of 7.0 ± 3.4 kJ/mol. Thus, at least at the temperature considered in this study (500 K), tertiary cations and π-complexes are intermediates of similar stability in acid chabazite, the alkoxide being less stable than the π-complex by 23.9 kJ/mol.

Once the secondary cation (I) is formed, it can undergo an easy spontaneous direct cracking or it can be transformed without any significant barrier into π-complex or alkoxide. In turn, these two former species can crack, with a free energy barrier of the same order of magnitude as the initial isomerization for the initial tertiary cation into (I). With similar free energy barriers, and similar stability of the reactant, the cracking mechanism from the 2,3-dimethyl-penten-2-ium (R) (via I) and from the π-complex (E)-4,4-dimethyl-pent-2-ene are competitive (Figure 10).

As previously discussed, in most of the static DFT studies, the reactant was considered as an alkoxide.[10,12] We find here that tertiary cations and π-complexes are more relevant intermediates, being more stable than the alkoxide (with a free energy difference of 26 and 19 kJ/mol respectively). The free energy barriers obtained for the type B_1 β-scission (60.1 kJ/mol starting from a π-complex, 67.1 kJ/mol starting from a tertiary cation) are much lower than the barriers determined previously in the static approach (potential energy barriers of 153 kJ/mol for B_1 cracking of C_8 alkene,[10] and 120 kJ/mol for the B_1 cracking of C_7 alkene in H-SAPO34,[12] starting from alkoxides) and in kinetic modeling (170 kJ/mol for type B_1 cracking of C_5 alkene in H-ZSM-5[20] and 152 kJ/mol for C_{12} in H-BEA[19]). On the other hand, our free energy barriers are consistent with the ones obtained by biased MD for type A (53 kJ/mol) and B_2 (around 70 kJ/mol) β-scissions in by Van Speybroeck and coworkers.[14] and with experimental evidence giving the following decreasing order of reactivity : type A cracking, type B isomerization, type B_1 and B_2 cracking.[1]

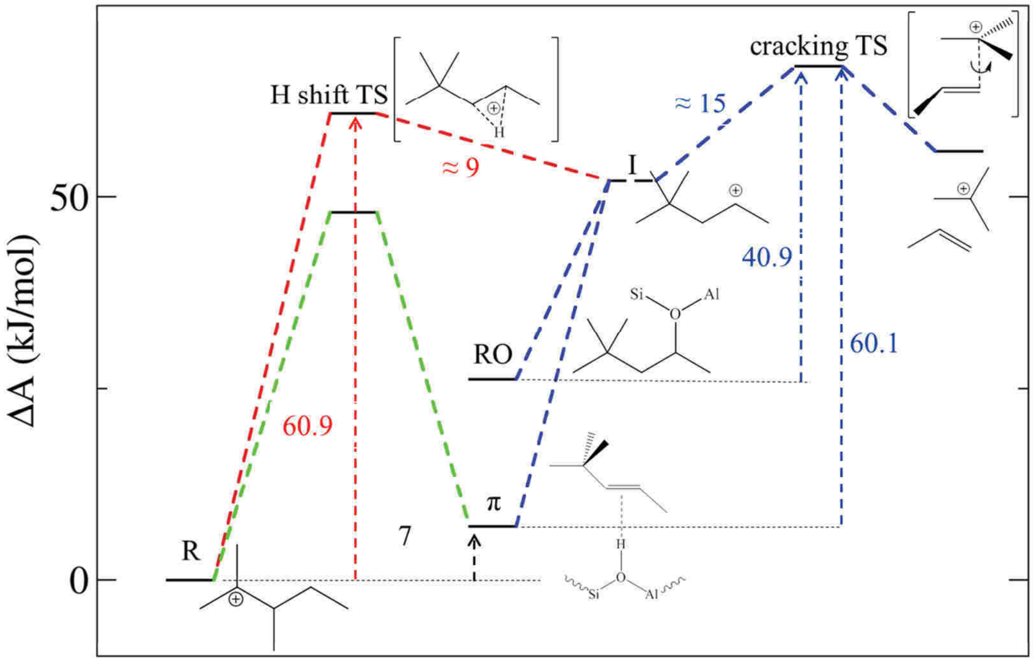

Figure 10. Overall free energy profile of the different routes involved in the type B_1 β-scission and investigated by MD simulations. A qualitative estimate of the free energy of the secondary cation 4,4-dimethyl-penten-2-ium (I) is indicated by a horizontal dash line. The free energy profile from the reactant 2,3-dimethyl-penten-2-ium (R) to (I) is depicted by red dash lines. The cracking reaction starting from alkoxide (RO) or a π-complex (π) are displayed with blue dash lines and the transformation from (R) to the π-complex (π) with green dash lines.

V.3.1.3. Structural analysis of transition states

Transition state of the tertiary to secondary cation transformation

The probability distributions of the C–C and C–H bond involved in the transition state of the isomerization of the stable tertiary cation (the 2,3-dimethyl-penten-2-ium cation R) into the reactive secondary cation (the 4,5-dimethyl-penten-2-ium I) are shown in Figure S5. As already mentioned, this TS is in fact related to the 1,2 H shift process. The C^3–H^a bond is much shorter than C^4-H^a bond, signifying that the structure of the transition state is closer to the secondary cation (I) than to the highly unstable secondary cation (S) (Figure 3). The structure of the transition state optimized in the static approach in gas phase is even more dissymmetric, the C^3–H^a bond being much shorter and C^4–H^a much longer than in MD. Such a difference between MD results in zeolite and static results in gas phase was already observed for secondary cations in our previous work:[28] the structure of secondary cations is very constrained at 0 K and more flexible on the free energy surface at finite temperature.

Transition state of B_1 β-scission

The cracking reaction requires a specific conformation of TS to occur, where the planes of the two hydrocarbon fragments are approximately parallel (Figure 11). The average of the distance C^2–C^3 between the two carbon atoms of the breaking bond is very similar in both MD simulations of Section 3.1.2: 2.19 Å starting from the π-complex and 2.23 Å starting from the alkoxide (Figure 11). The analysis of the distribution of the C^2-C^4 distance (average of 2.64 Å), which is longer than C^2-C^3 (Figure 11), shows that in the transition state, the carbon atom C^2 of the tert-butylium cation to be formed interacts preferentially with the carbon atom C^3 of the double bond C^3-C^4 of the propene in formation. This interaction makes a free virtually rotation of the two fragments with respect to each other possible, as shown by the large distribution of the dihedral angle defined by the sequence C^1-C^2-C^3-C^4 (Figure S9).

A global rotation of the C_7 species is observed during the cracking reaction, with exchange of the fragment close to the aluminum atom of the framework (the conjugated basic site of the acid zeolite), initially the propene fragment, and at the end, the tert-butylium fragment.

The average positions of these two products of cracking are measured via a parameter χ (χ_1 for propene, χ_2 for tert-butylium) which is the time average of the sum of inverse distance between the carbon atoms of the species raised to the power of six (Equation (9)).

$$\chi = \left\langle \sum_i \frac{1}{{R_{Al-C_i}}^6} \right\rangle \tag{9}$$

For the type B_1 β-scission starting from an alkoxide (Section 3.1.2), the evolution of the χ_1 and χ_2 parameters as a function of ξ is described in Figure 12.a., from the secondary cation I ($\xi \approx -0.8$) to the cracked products ($\xi \rightarrow 0$). When the secondary cation I is formed, the propene part of the C_7 skeleton is located near the aluminium atom and $\chi_1 > \chi_2$. During the cracking reaction, this propene in formation moves away from the aluminium atom and the tert-butylium cation gets closer to it, χ_1 becomes inferior to χ_2.

This evolution of the χ_1 and χ_2 parameters can be related to the change of the charge distribution of the atoms involved in the cracking reaction. Hirsheld –I charges[34,35] have been computed for different states occuring in the cracking reaction, from I to the cracked products. Results are given in Figure 12.b. For each carbon atom, the charge displayed is an average determined on 45 structures distributed evenly along the 45 ps long production period of the constrained MD run (after the 5 ps equilibration).

When I is formed ($\xi \approx -0.8$), after breaking of the C^4-O^4 bond of the initial alkoxide on the O^4 oxygen atom of the framework, the positive charge is shared between C^2 and C^4 atoms and the future propene fragment is still close to the aluminum atom. At the end of the reaction ($\xi \rightarrow 0$), the two fragments are free to move in the microporosity of chabazite and the tert-butylium cation, with a large positive charge on the C^2 atom being closer to the aluminium atom. In the large cavity of chabazite, this global rotation of the C_7 species is not hindered.

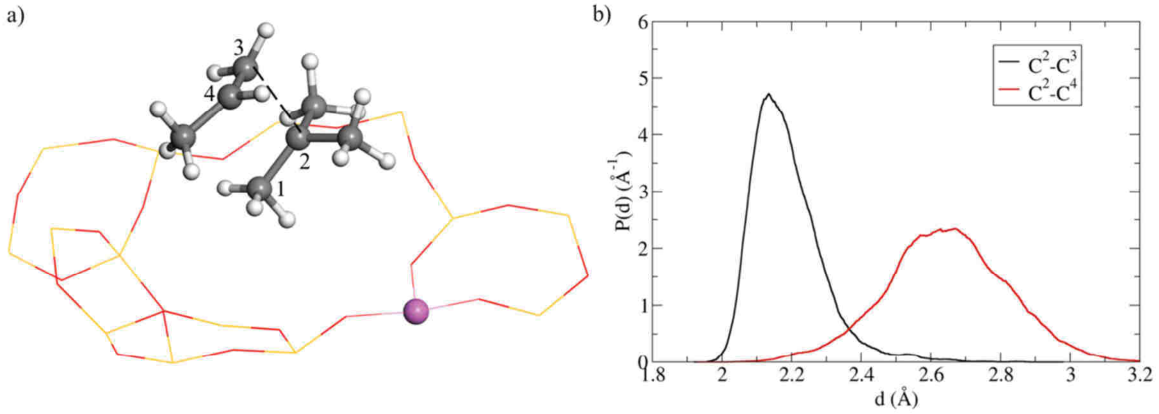

Figure 11. a) A selected structure from the constrained MD simulation of the transition state of the type B_1 cracking reaction starting from the π-complex (E)-4,4-dimethyl-pent-2-ene. The average C^2–C^3 distance is around 2.2 Å, and the average C^2-C^4 distance is around 2.6 Å. b) Probability distributions of the C^2–C^3 and C^3–C^4 distances involved in the transition state of the type B_1 cracking reaction starting from the π-complex (E)-4,4-dimethyl-pent-2-ene determined using MD at 500 K.

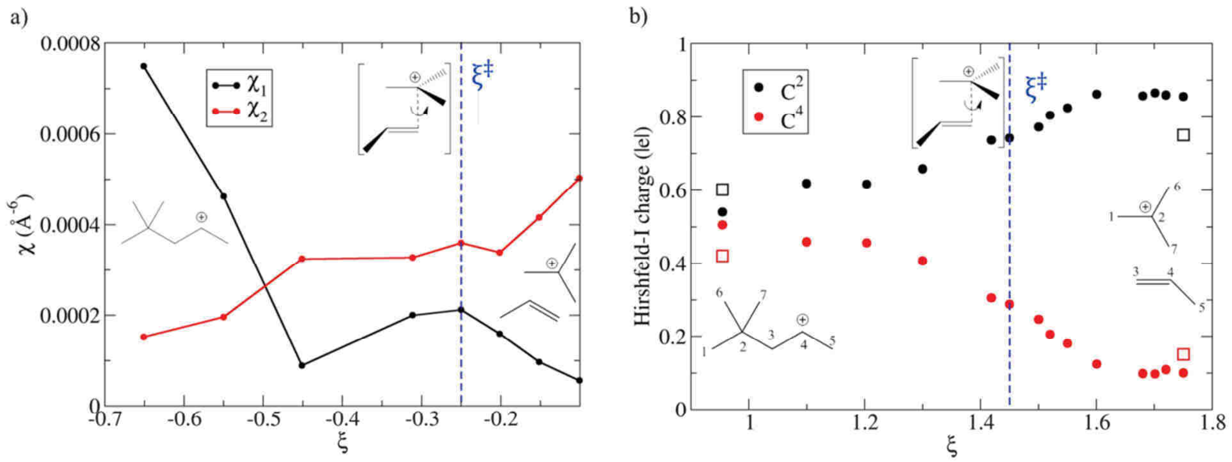

Figure 12. a) Evolution of the χ parameters (defined via Equation (9)) of propene (χ_1) and tert-butylium cation (χ_2) as a function of ξ, for the type B_1 β-scission starting from an alkoxide (Section 3.1.2). b) Hirshfeld-I charges of selected atoms of the C_7 species as a function of the reaction coordinate for the cracking reaction starting from the π-complex. Charges for the corresponding gas phase optimized structures are reported with empty squares. All other carbon atoms have negative charges (around -0.5|e|).

V.3.2. Type B_2 β-scission of 2-4-dimethyl-penten-2-ium

V.3.2.1. Free energy profile

In this reaction, the secondary propenium cation formed in the conventional mechanism (Figure 1.b) is highly reactive. Preliminary slow growth simulations showed that fast and spontaneous proton transfers occurred between the propenium cation and isobutene (giving propene and tert-butylium cation) or between the propenium cation and the zeolite (giving pi-complex of propene and isobutene). Without taking into account these transformations in the approximation to reaction coordinate, discontinuities in the free energy gradient occur and the simulation is not reliable (Section SVI.1). Thus, we investigated the mechanism depicted in Figure 14 by blue moon simulation.

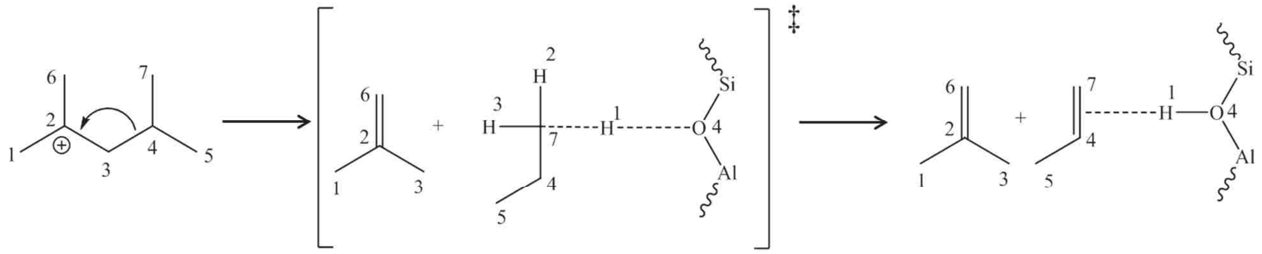

Figure 13. Mechanism of type B_2 cracking of 2-4-dimethyl-penten-2-ium in adsorbed propene and isobutene.

We used for this reaction the following approximation to the reaction coordinate, which involves the C^3-C^4 bond broken in the transformation and the O-H bond in formation (the numbering of atoms is as in Figure 13):

$$\xi = -\eta(C^3 - C^4) + \sum_{\substack{i=5,7 \\ j=1,2,3}} \eta\left(O^4 - H^j_{C^i}\right), \qquad (10)$$

where $\eta(A - B)$ is the coordination number of the $A - B$ bond (Equation (5)), $H^j_{C^i}$ is the hydrogen atom *j* on the carbon atoms *i* of the propenium fragment, and O^4 is the relevant oxygen atom of the zeolitic framework (Figure 2).

No undesirable by-reaction was observed and the blue moon simulation was performed without any restraints. The free energy profile is shown in Figure 14. In the first part of this profile, from $\xi_{ref,R} = -0.70$ to $\xi \approx 0$, isobutene and propenium cation are formed. As shown in Figure S14, the maximum of distribution of C^3-C^4 distances becomes much larger, and its width reduces, when shifting from the point of the simulation $\xi = -0.10$ to $\xi = -0.08$. This evolution demonstrates that most of the C^3-C^4 interaction is lost in this part of process. Meanwhile, the O^4-H^1 bond is not formed yet, nor the C^7-H^1 bond is broken (Figure S14). There is no stationary point on this part of the free energy profile. In the next stage, from $\xi \approx 0$ to $\xi_{ref,P} = 0.75$, a proton from a terminal methyl group of the propenium cation is transferred to zeolite (Figure 15). The transition state ($\xi^* \approx 0.20$) on the free energy profile corresponds to this transfer, and not to the β-scission step itself. The value of the term $\Delta A_{\xi_{ref,R} \rightarrow \xi^*}$ is 86.8 ± 5.3 kJ/mol.

The free energy of activation $\Delta A^\ddagger$ is determined via Equation (1), using $\langle |\dot{\xi}^*| \rangle = 6.5 \cdot 10^{12}$ s^{-1}, and $P(\xi_{ref,R})$ = 5.79 determined as described in Section SV. The computed free energy of activation $\Delta A^\ddagger$ is 84.4 ± 5.3 kJ/mol. Employing Equation (2) together with the probability density for the product state ($P(\xi_{ref,R}) = 6.57$, Section SVI.2), a free energy of reaction of 46.3 ± 5.4 kJ/mol was obtained.

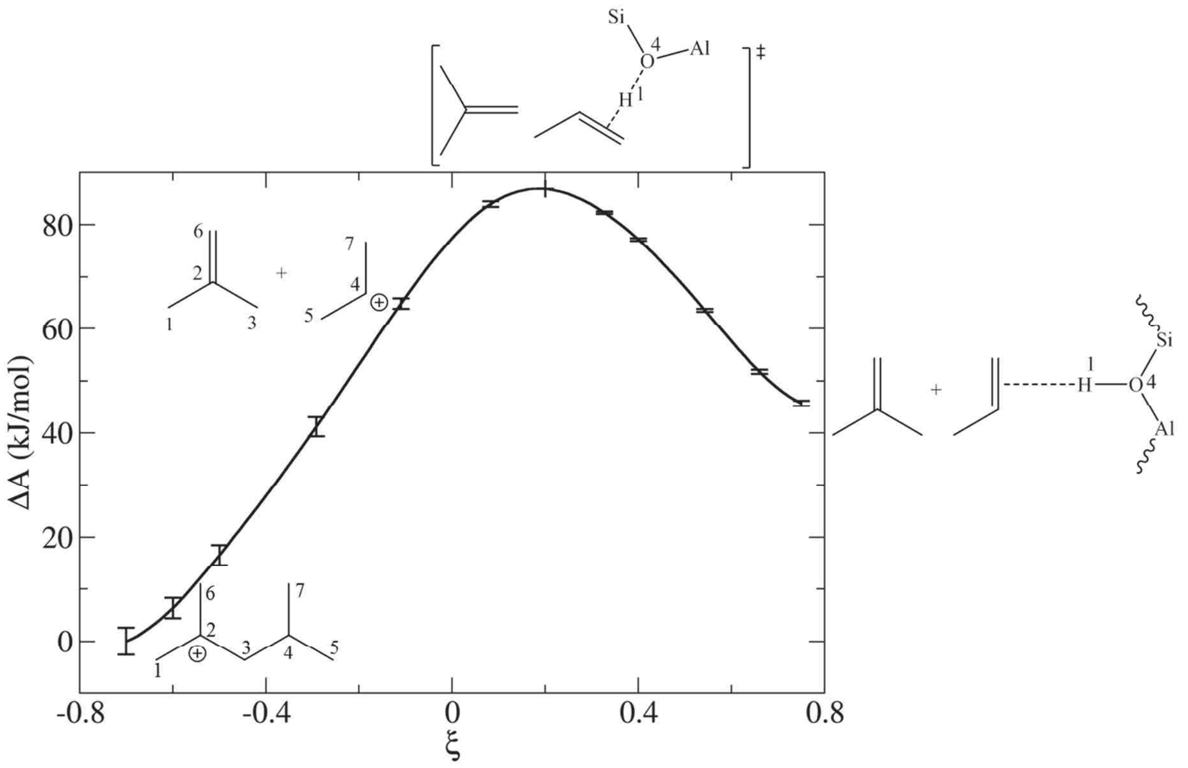

Figure 14. Free energy profile computed using the blue moon ensemble approach for the type B_2 β-scission of 2-4-dimethyl-penten-2-ium in isobutene and π-complex of propene.

Transition path sampling simulations have been performed to verify the stability of the present reaction pathway. In contrast to reactions described in Section 3.1, no new reaction mechanism was identified with 100 trial moves.

As for the previous result on the type B_1 cracking, the free energy barrier obtained for the type B_2 cracking reaction (84.4 kJ/mol) is much lower than the barriers reported previously. In static DFT, a wide range of large barriers, depending on the initial conformation of the reactant, were found (89 to 171 kJ/mol for C_8 in H-ZSM-5,[10] 94 to 151 kJ/mol also for C_8 in H-ZSM-5 in another paper[14] and 127 kJ/mol for C_7 alkenes in H-SAPO34[12]). In kinetic modeling a barrier of 118 kJ/mol for C_{12} cracking in H-BEA was proposed.[19]

The barrier that we found for this type B_2 reaction is higher than that for type B_1 cracking (17 kJ/mol higher considering an initial tertiary cation and 24 kJ/mol higher with an initial a π-complex) and we note that the transition state is of a different nature (associated to the β-scission step in the type B_1 mechanism, and to a proton transfer in the type B_2). This is also about 12 kJ/mol higher than the one proposed in a recent biased MD study for the type B_2 cracking of C_8 alkenes in H-ZSM-5 by Cnudde et al.[14] This difference can possibly be attributed to the proton transfer of the propenium to zeolite which is not described in the paper by Cnudde et al.

V.3.2.2. Structural analysis of the transition state of type B_2 cracking

At the transition state ($\xi^* \approx 0.20$), the large distribution of the C^3-C^4 distance shows that the C^3-C^4 bond is broken and that the two fragments are not in strong interaction any more. Concomitantly, the atom H^1 is tightly constrained between O^4 and C^7 atoms (Figure 15.b). Thus the transition state of the overall process does not correspond to the β-scission itself but to the proton transfer between the highly unstable propenium cation and the zeolite, which is different from the transition state of the type B_1 reaction previously investigated and corresponding to the cracking itself.

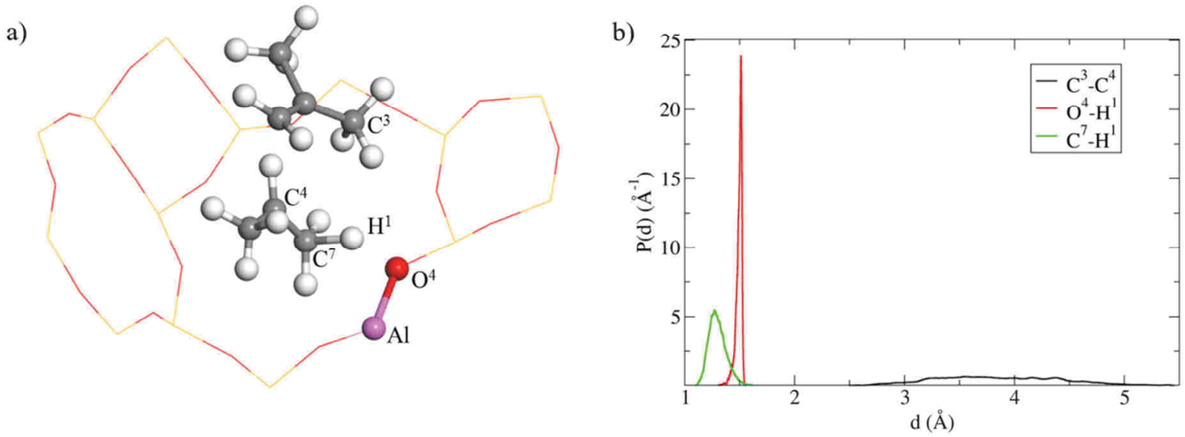

Figure 15. a) Selected structure from the constrained blue moon simulation of the transition state of the type B_2 cracking reaction. b) Probability distributions of selected distances involved in the transition state of the type B_2 cracking reaction determined using MD at 500K.

V.4. Conclusion

In this work, we compared the two different mechanisms giving propane and isobutane by hydrocraking of C_7 alkenes in acid chabazite (Figure 1). Propane and isobutane are indeed the predominant products of n-heptane hydrocracking (obtained after deprotonation of the cations created in the β-scission step and hydrogenation of the subsequent alkenes).[4] To the best of our knowledge, this work is the first theoretical study which identifies the energies and the structures of the transition states involved in the β–scission mechanisms (B_1 and B_2 types). The different reactions involving the reactive secondary cation, the 4,4-dimethyl-penten-2-ium (I) confirmed that secondary cations are very unstable species, involved in many reactions such as type A isomerization, formation of alkoxides or π-complexes, and spontaneous cracking. The stable species with the same carbon skeleton as the secondary cation (I) is a π-complex. We came to a similar conclusion also in our previous work on type B isomerization reaction connecting secondary and tertiary cations.[28] Therefore, the π-complex is the relevant reactant in kinetic modeling of secondary cations in hydrocracking. The free energy barriers computed in this work by biased MD simulations are lower than in previous static calculations or kinetic models and are more consistent with the experimental evidence on the relative rates of type B isomerization and β-scissions,[1] and with the barriers obtained for type A and B_2 β-scissions in MD simulations by Van Speybroeck and coworkers.[14]

We found that the direct type B_2 cracking mechanism (from the dibranched tertiary cation 4,4-dimethyl-penten-2-ium to isobutene and the propenium secondary carbenium ion spontaneously deprotonated in propene), is kinetically slower (free energy barrier 23 kJ/mol higher) than the type B_1 mechanism (producing a tertiary carbenium ion), in its different variants. In the transition state of the type B_1 reaction, the carbon planes of propene and tert-butylium cation in formation are approximately parallel and are virtually free to rotate (Figure S9). The relative position of these two fragments with respect to the conjugated basic site of the zeolite changes during the reaction (the propene fragment is closer at the beginning, the tert-butylium fragment at the end). In contrast, the transition state for the type B_2 cracking is associated with the proton transfer between the newly formed propenium cation and the zeolite. As the free energy difference between C_7 tertiary cations in zeolites is expected to be small (within a few kJ/mol according to our previous work[16,28]), and as they can be connected by fast type A isomerization reactions, we can assume that the type B_1 mechanism via the reactive secondary cation (I) dominates over the type B_2 mechanism. At variance with our results, Cnudde and coworkers concluded that type B_1 cracking of C_8 alkenes in H-ZSM-5 was expected to be less favored than B_2 because the germinal methyl substituted (with a quaternary carbon atom) secondary cation was too unstable.[14] Connecting this kind of highly unstable secondary cations to a more stable species (such as a π-complex with the same carbon skeleton), we find that the type B_1 cracking is easier than the B_2 for C_7 alkenes in chabazite.

The type C cracking reaction is a perspective of this work: it is a difficult case because starting and finishing with secondary cations will certainly give rise to many by-reactions. Indeed, we performed preliminary free runs showing that, depending on its conformation, the 3,4-dimethyl-penten-2-ium can undergo cracking, methyl shifts,1,2 hydride shift, 1,3 hydride shifts and even propyl shift.

This work completes our previous findings on the isomerization reactions[16,28], and opens the way to a complete kinetic model for the network of hydrocracking reactions of C_7 species.

References

(1) Marcilly, C. *Acido-Basic Catalysis. Application to Refining and Petrochemistry;* Technip, 2005.
(2) Weitkamp, J. Catalytic Hydrocracking-Mechanisms and Versatility of the Process. *ChemCatChem* **2012**, *4*, 292–306.
(3) *Catalysis by transition metal sulphides. From molecular theory to industrial application;* Toulhoat, H., Raybaud, P., Eds.; IFP énergies nouvelles publications; Éd. Technip: Paris, 2013.
(4) Raybaud, P.; Patrigeon, A.; Toulhoat, H. The Origin of the C7-Hydroconversion Selectivities on Y, β, ZSM-22, ZSM-23, and EU-1 Zeolites. *J. Catal.* **2001**, *197*, 98–112.
(5) Gutierrez-Acebo, E.; Leroux, C.; Chizallet, C.; Schuurman, Y.; Bouchy, C. Metal/Acid Bifunctional Catalysis and Intimacy Criterion for Ethylcyclohexane Hydroconversion. *ACS Catal.* **2018**, *8*, 6035–6046.
(6) Olsbye, U.; Svelle, S.; Bjørgen, M.; Beato, P.; Janssens, T. V. W.; Joensen, F.; Bordiga, S.; Lillerud, K. P. Conversion of methanol to hydrocarbons. *Angew. Chem. Int. Edit.* **2012**, *51*, 5810–5831.
(7) Brouwer, D. M.; Hogeven H. Electrophilic Substitutions at Alkanes and in Alkylcarbonium Ions. *Prog. Phys. Org. Chem.* **1972**, *9*, 179–240.
(8) Baltanas, M. A.; van Raemdonck, K. K.; Froment, G. F.; Mohedas, S. R. Fundamental Kinetic Modeling of Hydroisomerization and Hydrocracking on Noble Metal-Loaded Faujasites. 1. Rate Parameters for Hydroisomerization. *Ind. Eng. Chem. Res.* **1989**, *28*, 899–910.
(9) Weitkamp, J.; Jacobs, P. A.; Martens, J. A. Isomerization and hydrocracking of C9 through C16 n-alkanes on Pt/HZSM-5 zeolite. *Appl. Catal.* **1983**, *8*, 123–141.
(10) Mazar, M. N.; Al-Hashimi, S.; Cococcioni, M.; Bhan, A. β-Scission of Olefins on Acidic Zeolites: A Periodic PBE-D Study in H-ZSM-5. *J. Phys. Chem. C* **2013**, *117*.
(11) Guo, Y.-H.; Pu, M.; Chen, B.-H.; Cao, F. Theoretical study on the cracking reaction catalyzed by a solid acid with zeolitic structure. *Appl. Catal. A-Gen.* **2013**, *455*, 65–70.
(12) Wang, C.-M.; Wang, Y.-D.; Xie, Z.-K. Insights into the reaction mechanism of methanol-to-olefins conversion in HSAPO-34 from first principles. *J. Catal.* **2013**, *301*, 8–19.
(13) Huang, B.; Bai, P.; Neurock, M.; Davis, R. J. Conversion of n-Hexane and n-Dodecane over H-ZSM-5, H-Y and Al-MCM-41 at Supercritical Conditions. *Appl. Catal. A-Gen.* **2017**, *546*, 149–158.
(14) Cnudde, P.; Wispelaere, K. de; Vanduyfhuys, L.; Demuynck, R.; van der Mynsbrugge, J.; Waroquier, M.; van Speybroeck, V. How Chain Length and Branching Influence the Alkene Cracking Reactivity on H-ZSM-5. *ACS Catal.* **2018**, *8*, 9579–9595.
(15) Bučko, T.; Benco, L.; Hafner, J.; Ángyán, J. G. Monomolecular Cracking of Propane over Acidic Chabazite. *J. Catal.* **2011**, *279*, 220–228.
(16) Rey, J.; Gomez, A.; Raybaud, P.; Chizallet, C.; Bučko, T. On the Origin of the Difference Between Type A and Type B Skeletal Isomerization of Alkenes Catalyzed by Zeolites: The Crucial Input of ab initio Molecular Dynamics. *J. Catal.* **2019**, *373*, 361–373.
(17) Martens, G. G.; Marin, G. B.; Martens, J. A.; Jacobs, P. A.; Baron, G. V. A Fundamental Kinetic Model for Hydrocracking of C8 to C12 Alkanes on Pt/US–Y Zeolites. *J. Catal.* **2000**, *195*, 253–267.
(18) Vandegehuchte, B. D.; Thybaut, J. W.; Marin, G. B. Unraveling Diffusion and Other Shape Selectivity Effects in ZSM5 Using n -Hexane Hydroconversion Single-Event Microkinetics. *Ind. Eng. Chem. Res.* **2014**, *53*, 15333–15347.
(19) Vandegehuchte, B. D.; Thybaut, J. W.; Martínez, A.; Arribas, M. A.; Marin, G. B. n-Hexadecane Hydrocracking Single-Event MicroKinetics on Pt/H-beta. *Appl. Catal. A-Gen.* **2012**, *441-442*, 10–20.
(20) Aretin, T. von; Schallmoser, S.; Standl, S.; Tonigold, M.; Lercher, J. A.; Hinrichsen, O. Single-Event Kinetic Model for 1-Pentene Cracking on ZSM-5. *Ind. Eng. Chem. Res.* **2015**, *54*, 11792–11803.

(21) Thybaut, J. W.; Laxmi Narasimhan, C. S.; Marin, G. B.; Denayer, J. F.M.; Baron, G. V.; Jacobs, P.A.; Martens, J. A. Alkylcarbenium Ion Concentrations in Zeolite Pores During Octane Hydrocracking on Pt/H-USY Zeolite. *Catal. Lett.* **2004**, *94*, 81–88.
(22) Zimmerman, P. M.; Tranca, D. C.; Gomes, J.; Lambrecht, D. S.; Head-Gordon, M.; Bell, A. T. Ab initio simulations reveal that reaction dynamics strongly affect product selectivity for the cracking of alkanes over H-MFI. *J. Am. Chem. Soc.* **2012**, *134*, 19468–19476.
(23) Tranca, D. C.; Zimmerman, P. M.; Gomes, J.; Lambrecht, D.; Keil, F. J.; Head-Gordon, M.; Bell, A. T. Hexane Cracking on ZSM-5 and Faujasite Zeolites. *J. Phys. Chem. C* **2015**, *119*, 28836–28853.
(24) Bouchy, C.; Hastoy, G.; Guillon, E.; Martens, J. A. Fischer-Tropsch Waxes Upgrading via Hydrocracking and Selective Hydroisomerization. *Oil Gas Sci. Technol. – Rev. IFP Energies nouvelles* **2009**, *64*, 91–112.
(25) Marcilly, C. *Catalyse acido-basique. Application au raffinage et à la pétrochimie;* Technip: Paris, 2003.
(26) Hajek, J.; van der Mynsbrugge, J.; Wispelaere, K. de; Cnudde, P.; Vanduyfhuys, L.; Waroquier, M.; van Speybroeck, V. On the Stability and Nature of Adsorbed Pentene in Brønsted Acid Zeolite H-ZSM-5 at 323K. *J. Catal.* **2016**, *340*, 227–235.
(27) Cnudde, P.; Wispelaere, K. de; van der Mynsbrugge, J.; Waroquier, M.; van Speybroeck, V. Effect of Temperature and Branching on the Nature and Stability of Alkene Cracking Intermediates in H-ZSM-5. *J. Catal.* **2017**, *345*, 53–69.
(28) Rey, J.; Raybaud, P.; Chizallet, C.; Bučko, T. Competition of Secondary versus Tertiary Carbenium Routes for the Type B Isomerization of Alkenes over Acid Zeolites Quantified by AIMD Simulations. *Manuscript submitted for publication*, *2019*.
(29) Smith, L. J.; Davidson, A.; Cheetham, A. K. A Neutron Diffraction and Infrared Spectroscopy Study of the Acid Form of the Aluminosilicate Zeolite, Chabazite (H- SSZ-13). *Catal. Lett.* **1997**, *49*, 143–146.
(30) Carter, E. A.; Ciccotti, G.; Hynes, J. T.; Kapral, R. Constrained Reaction Coordinate Dynamics for the Simulation of Rare Events. *Chem. Phys. Lett.* **1989**, *156*, 472–477.
(31) Ciccotti, G.; Sprik, M. Free Energy from Constrained Molecular Dynamics. *J. Chem. Phys.* **1998**, *109*, 7737–7744.
(32) Iannuzzi, M.; Laio, A.; Parrinello, M. Efficient Exploration of Reactive Potential Energy Surfaces Using Car-Parrinello Molecular Dynamics. *Phys. Rev. Lett.* **2003**, *90*, 238302.
(33) Dellago, C.; Bolhuis, P. G.; Geissler, P. L. Transition path sampling. *Adv. Chem. Phys.* **2002**, *123*.
(34) Bultinck, P.; van Alsenoy, C.; Ayers, P. W.; Carbó-Dorca, R. Critical analysis and extension of the Hirshfeld atoms in molecules. *J. Chem. Phys.* **2007**, *126*, 144111.
(35) Bučko, T.; Lebègue, S.; Hafner, J.; Ángyán, J. G. Improved Density Dependent Correction for the Description of London Dispersion Forces. *J. Chem. Theory Comput.* **2013**, *9*, 4293–4299.

Relevant cracking intermediates and transition states for β-scission reactions of alkenes over acid zeolites revealed by AIMD. Supporting information.

Contents

SI. Supercell of chabazite 209
SII. Determination of the velocity term $\boldsymbol{\xi}\ast$ 209
SIII. Type B_1 β-scission from an initial stable tertiary cation 209
  SIII.1 Avoiding the by-reactions during a blue moon simulation 209
  SIII.2. Intrinsic reaction coordinate determination in gas phase 211
  S.III.3 Probability distribution function $P(\xi_{ref})$ 212
  SIII.4. Structural analysis of the transition state 212
  SIII.5 Free MD run of 4,5-dimethyl-penten-2-ium cation (I) in gas phase 213
SIV. Type B_1 β-scission starting from initial π-complex or alkoxide 213
  SIV.1. From π-complex 213
  SIV.2. From alkoxide 214
  SIV.3. Structural analysis of the transition state of cracking 215
SV. Isomerization reaction from tertiary cation to π-complex 215
SVI. Type B_2 β-scission of 2-4-dimethyl-penten-2-ium 217
  SVI.1 Slow growth simulation 217
  SVI.2. Probability distribution function $P(\xi_{ref})$ 218
  SVI.3. Structural analysis 218
References 219

SI. Supercell of chabazite

A primitive rhombohedral cell of purely siliceous chabazite (CHA framework, symmetry group R $\overline{3}$ m), with 12 symmetry equivalent tetrahedral sites, was obtained from International Zeolite Association (IZA) database[1]. The cell was reoptimized yielding the lattice constants a =9.336 Å and α = 94.6°, which are in good agreement with the reference values[1] (a = 9.304 Å and α = 94.6°). The relaxed structure was subsequently used to build a supercell defined by lattice vectors $\mathbf{a}_1'$, $\mathbf{a}_2'$, and $\mathbf{a}_3'$ related to the primitive cell vectors of rhombohedral lattice ($\mathbf{a}_1, \mathbf{a}_2, \mathbf{a}_3$) via the following transformations: $\mathbf{a}_1' = \mathbf{a}_2 + \mathbf{a}_3$, $\mathbf{a}_2' = \mathbf{a}_1 + \mathbf{a}_3$, and $\mathbf{a}_3' = \mathbf{a}_1 + \mathbf{a}_2$. The shortest interatomic separation between the atoms in hydrocarbon and atoms in its periodically repeated images in the supercell was at least 5.5 Å. The supercell is shown in Figure 2, where O^1 and O^4 oxygen atoms (following the labeling introduced in ref.[2]) involved in the transformations considered in this study have been highlighted.

SII. Determination of the velocity term $\langle|\dot{\xi}^*|\rangle$

The term $\langle|\dot{\xi}^*|\rangle$) required in the calculations of free energy of activation (see Equation (1) in the main text) is determined using the constrained MD simulations via the formula[3,4]

$$\langle|\dot{\xi}^*|\rangle = \sqrt{\frac{k_B T}{2\pi}} \frac{1}{\left\langle Z^{-1/2} \right\rangle_{\xi^*}}, \qquad \text{(Eq. S1)}$$

where the term enclosed in $\langle \dots \rangle_{\xi^*}$ is computed as a statistical average for a constrained ensemble with $\xi(\boldsymbol{r}) = \xi^*$, and Z the inverse mass metric tensor is:

$$Z = \sum_{i=1}^{N} \frac{1}{m_i} \sum_{\mu=x,y,z} \left(\frac{\partial \xi}{\partial r_{i,\mu}} \right)^2, \qquad \text{(Eq. S2)}$$

with $r_{i,\mu}$ being the Cartesian component μ of position vector of an atom i and the sums are over all atoms and Cartesian components. We note that the term $\left\langle Z^{-1/2} \right\rangle_{\xi^*}$ is readily available from the constrained MD performed for the state ξ^* within the $\Delta A_{\xi_{ref,X} \to \xi^*}$ calculation.

SIII. Type B₁ β-scission from an initial stable tertiary cation

SIII.1 Avoiding the by-reactions during a blue moon simulation

As in our previous work,[5,6] by reactions that can occur in our free energy calculations have been avoided by the use of restraining potentials.

The addition of a restraining potential of the following form

$$V(R) = \frac{1}{2} K (R - R_0)^2 \qquad \text{(Eq. S3)}$$

reinforced the 12 C-H bonds involving all hydrogen atoms except those which are involved in the reaction (on carbon atoms C^3 and C^4). In (Eq. S3, R stands for the interatomic bonding distance C-H, R_0 =1.1 Å is a constant corresponding approximately to the equilibrium length of the C-H bond, and the force constant K is set to 100 eV.Å^{-2}.

The other possibilities of formation of pi-complexes (with deprotonation of C^3 and C^4 carbon atoms) and the formation of alkoxides between the C^4 atom of the secondary cation 4,4-dimethyl-penten-2-ium (I) and the two accessible oxygen atoms bonded to the aluminium atom of the zeolitic framework were prevented by the use of a smeared step potential. This potential (shown in Figure S1) acts on the distance R between the corresponding atoms. Its form is as follows:

$$V(R) = \frac{A_i}{1 + exp\left(-D\left(\frac{\mathrm{R}}{\mathrm{R}_{0i}} - 1\right)\right)}, \qquad \text{(Eq. S4)}$$

where the parameters were set to the following values: $A = -2$ eV, $D = 20$, $\mathrm{R}_{0,1} = 2.5$ Å for the CO and $\mathrm{R}_{0,2} = 1.5$Å for the OH distance. It follows from the shape of this restraining potential (shown in Figure S3) that it generates extra forces acting on atoms only if a fluctuation attempts to create the C-O or O-H bonds involved.

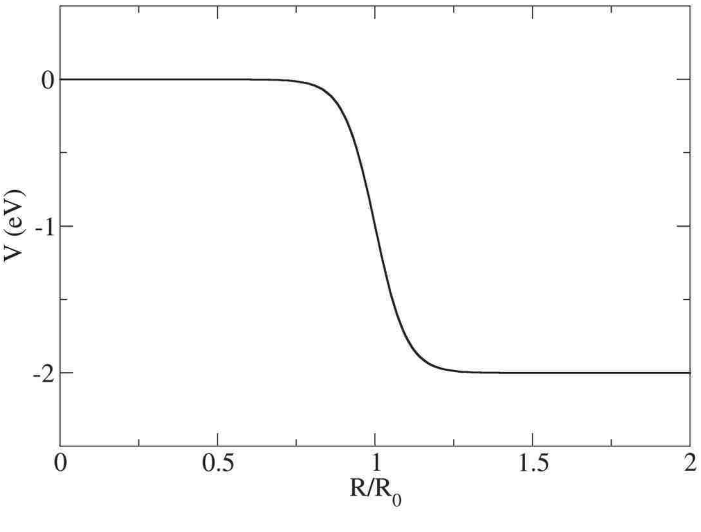

Figure S1. Restraining potential acting on a distance *R* between two atoms.

The initial methyl shift requires a specific conformation of the reactant, corresponding to R(I) (Figure 6 in the main text). At 500 K, undesired rotations occur, causing discontinuities in the free energy gradients. Such uncontrolled rotations were prevented by using a smeared step potential acting on the dihedral angle (τ) between atoms C^6-C^2-C^3-C^7. This restraining potential is shown in Figure S2 and it form was as follows:

$$V(\tau) = \sum_{i=1}^{2} \frac{A_i}{1 + exp\left(-D_i\left(\frac{\tau}{\tau_{0,i}} - 1\right)\right)}, \qquad \text{(Eq. S5)}$$

where the parameters were set to the following values: $A_1 = -2$ eV, $D_1 = 100$, $\tau_{0,1} = 66$ deg., and $A_2 = 2$ eV, $D_2 = 20$, $\tau_{0,2} = 129$ deg.

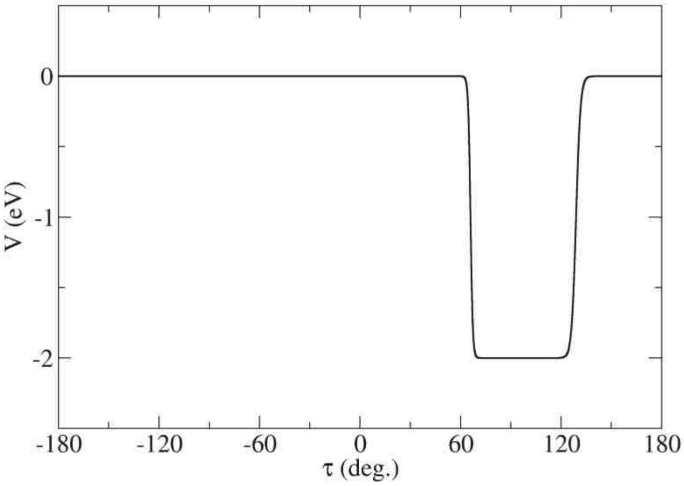

Figure S2. Restraining potential acting on the dihedral angle C^6-C^2-C^3-C^7 (τ).

SIII.2. Intrinsic reaction coordinate determination in gas phase

The intrinsic reaction coordinate (IRC)[7,8] for the forward and backward reaction steps of the isomerization of the 2,3-dimethyl-penten-2-ium (R) into the reactive secondary cation, the 4,4-dimethyl-penten-2-ium (I), was identified using the damped velocity Verlet algorithm.[9] The result is shown in Figure S3.

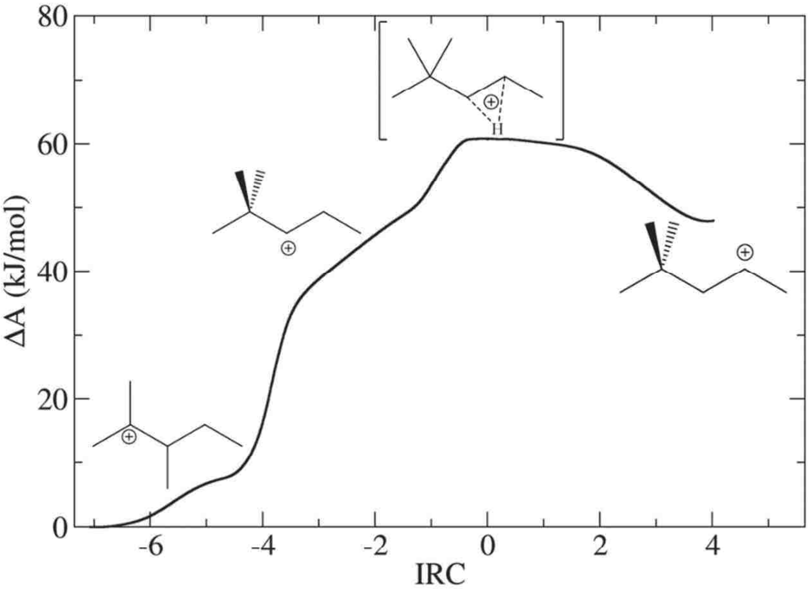

Figure S3. Potential energy profile along intrinsic reaction coordinate (IRC) for the isomerization reaction between 2,3-dimethyl-penten-2-ium cation (R) and 4,5-dimethyl-penten-2-ium cation (I) in gas phase.

S.III.3 Probability distribution function P(ξ_{ref})

Figure S4 shows the probability distribution function $\tilde{P}(\xi_{ref,R})$ for the rotational isomer R(I) of the reactant R. A restraining potential acting on the dihedral angle C^6-C^2-C^3-C^7 (τ) has been used to prevent interconversions between rotational isomers R(I) and R(II) (see section SI.2). The length of production of the run of MD simulations was 175 ps (the initial 5 ps were considered as equilibration and the corresponding data were discarded). The numerical value of $\tilde{P}(\xi_{ref,R})$ for $\xi_{ref,R} = 0.11$ is 4.58.

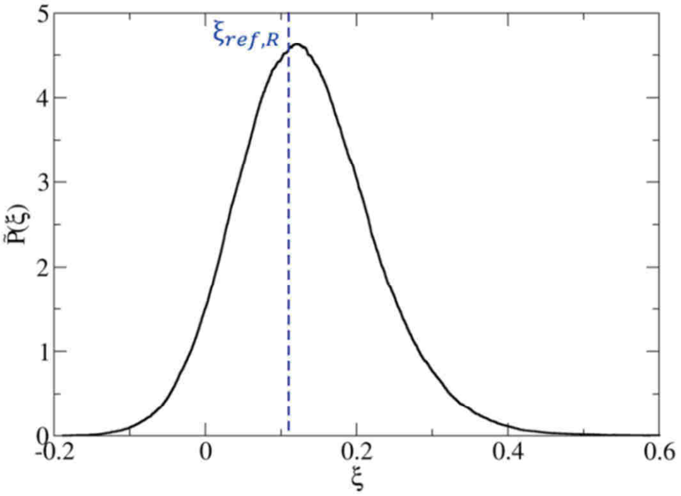

Figure S4. Probability distribution function $\tilde{P}(\xi)$ computed for the reactant state R(I).

SIII.4. Structural analysis of the transition state

In this section, we provide the probability distributions of the C–C and C–H bond involved in the transition state of the isomerization of the stable tertiary cation (the 2,3-dimethyl-penten-2-ium cation R) into the reactive secondary cation (the 4,5-dimethyl-penten-2-ium I).

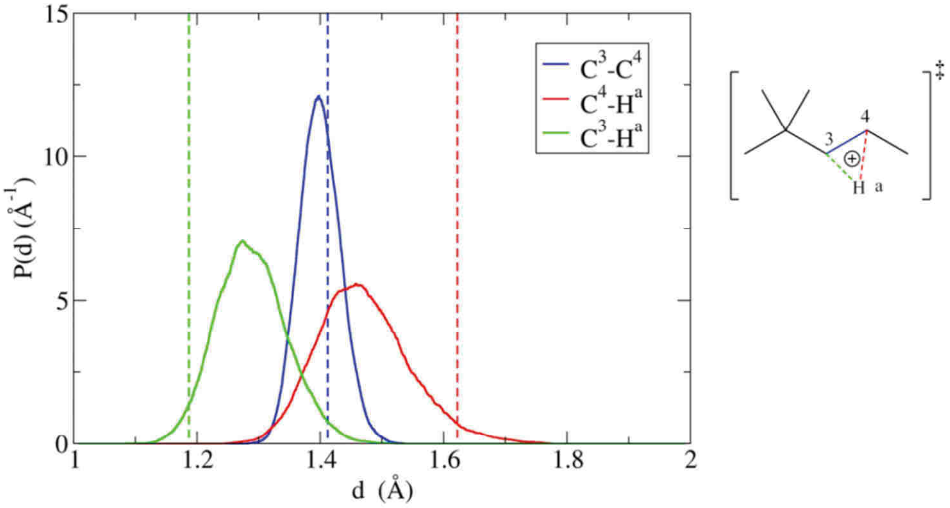

Figure S5. Probability distributions of C–C and C–H bonds involved in the transition state of 1,2 H-shift determined using MD at 500K. The static approach results for the gas phase reaction are indicated by vertical dashed lines.

SIII.5 Free MD run of 4,5-dimethyl-penten-2-ium cation (I) in gas phase

In order to determine if the cracking reaction of the secondary cation 4,4-dimethyl-penten-2-ium (I) is spontaneous, we realized a long (647 ps) free molecular dynamics run. We introduced bias to avoid that the two carbon atoms C^2 and C^3 involved in the broken bond move farther apart than 4 Å, which would prevent reformation of the C^2–C^3 bond. A few tens of separatrix recrossings were observed. The free energy profile computed from probability distribution $P(R)$, with R the C^2–C^3 distance, using $\Delta A = -RTlnP(R)$ is shown in Figure S6.

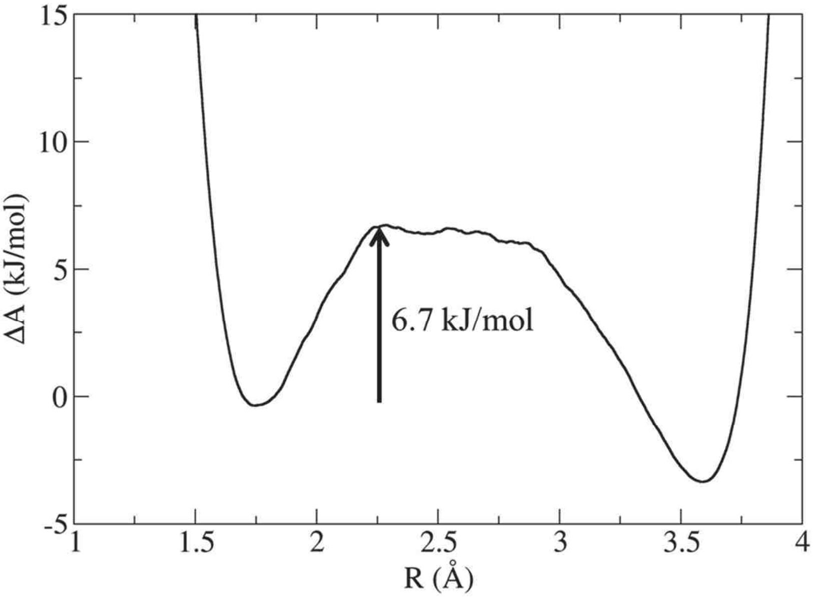

Figure S6. Free energy of the secondary cation 4,4-dimethyl-penten-2-ium (I) in gas phase as a function of the C2–C3 distance (R), obtained with a long (647 ps) free molecular dynamics run.

SIV. Type B_1 β-scission starting from initial π-complex or alkoxide

SIV.1. From π-complex

By-reactions were avoided by addition of a restraining potential reinforcing the 12 C-H bonds not involved in the reaction coordinate (ξ) as described in Section SIII.1. The formation of alkoxides was prevented for the points near the secondary cation ($\xi \approx 1$) by the use of a smeared step potential as described in Section SIII.1.

Figure S7 shows the probability distribution function $P(\xi_{ref,R})$ and $P(\xi_{ref,P})$ for the reactant R and product P of the reaction. The length of the run of MD simulations was 150 ps for the reactant and 130 ps for the product (the first 5 ps were considered as equilibration and the corresponding data were discarded). For the reactant, the numerical value of $P(\xi_{ref,R})$ for $\xi_{ref,R} = 0.16$ is 3.27 and for the product, $P(\xi_{ref,P}) = 4.19$ for $\xi_{ref,P} = 1.70$.

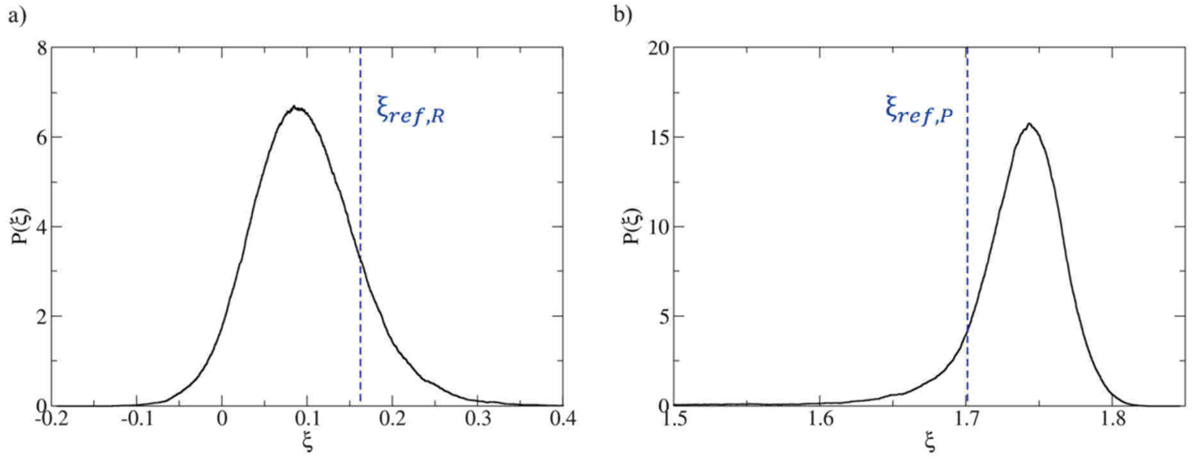

Figure S7. Probability distribution functions $P(\xi)$ for the reactant (a) and product (b) for the cracking mechanism B_1 starting from a π-complex (section 3.2.2).

SIV.2. From alkoxide

By-reactions were avoided by addition of a restraining potential reinforcing the 15 C-H bonds as described in Section SIII.1.

Figure S8 shows the probability distribution function $P(\xi_{ref,R})$ and $P(\xi_{ref,P})$ for the reactant R and product P of the reaction. The length of the run of MD simulations was 148 ps for the reactant and 128 ps for the product (the first 5 ps being considered as equilibration and discarded). For the reactant, the numerical value of $P(\xi_{ref,R})$ for $\xi_{ref,R}$ = -1.52 is 4.44 and for the product, $P(\xi_{ref,P})$ = 7.13 for $\xi_{ref,P}$ = -0.040.

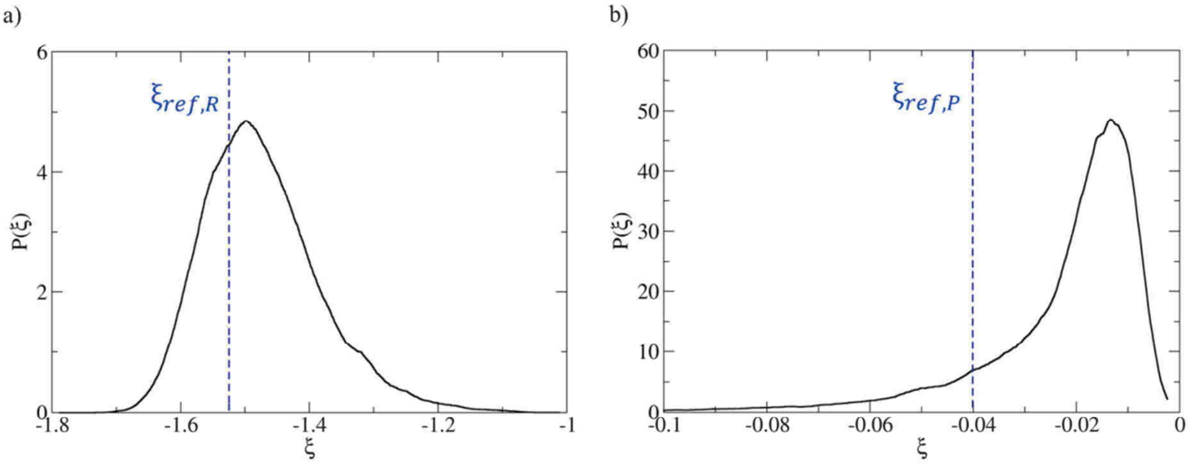

Figure S8. Probability distribution functions $P(\xi_{ref})$ for the reactant (a) and product (b) of the cracking mechanism B_1 starting from an alkoxide (section 3.2.2).

SIV.3. Structural analysis of the transition state of cracking

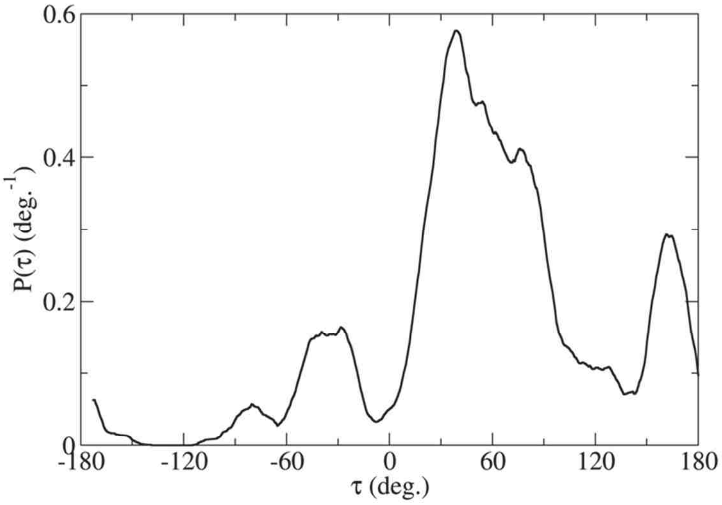

Figure S9. Probability distributions of dihedral angle (τ) defined by the sequence of atoms C^1-C^2-C^3-C^4 involved in the transition state of the type B_1 cracking reaction starting from the π-complex (E)-4,4-dimethyl-pent-2-ene determined using MD at 500 K.

SV. Isomerization reaction from tertiary cation to π-complex

In this section we describe the blue moon simulation performed to connect the initial tertiary cation (2,3-dimethyl-penten-2-ium, Section 3.1.1) to the to the π-complex used as reactant for cracking reaction in ((E)-4,4-dimethyl-pent-2-ene, Section 3.1.2),

The approximation to reaction coordinate must drive smoothly the transformation from the initial tertiary cation (2,3-dimethyl-penten-2-ium, Section 3.1.1) to the π-complex used as reactant for cracking reaction in ((E)-4,4-dimethyl-pent-2-ene, Section 3.1.2), with a methyl shift of C^7H_3 from C^4 to C^3 and a proton transfer from C^4 to an oxygen atom O^4. We used for this reaction the following approximation to reaction coordinate, which is invariant with respect to the interchange of the three methyl groups C^1H_3, C^6H_3, C^7H_3 and of the three hydrogen atoms of C^3 and C^4 (the numbering of atoms is as in Figure 3):

$$\xi = \sum_{j=1,6,7} \eta(C^2 - C^j) - \sum_{j=1,6,7} \eta(C^3 - C^j) - \sum_{j=a,b} \eta(C^4 - H^j) + \sum_{j=a,b} \eta(O^4 - H^j), \qquad \text{(Eq. S6)}$$

where η is the coordination number (Equation (5)) and *a* and *b* are the two hydrogen atoms initially located on C^4.

As described in Section SIII.1, 12 harmonic springs were used to reinforce the C-H bonds of all carbon atoms except C^3 and C^4 which were involved in the reaction coordinate. As discussed in

Section SIII.1, the dihedral angle (τ) between atoms C^6-C^2-C^3-C^7 was restrained on the first points of the simulation to ensure that the required rotamer of the reactant was involved in the methyl shift.

The free energy profile obtained with 16 integration points is shown in Figure S10.

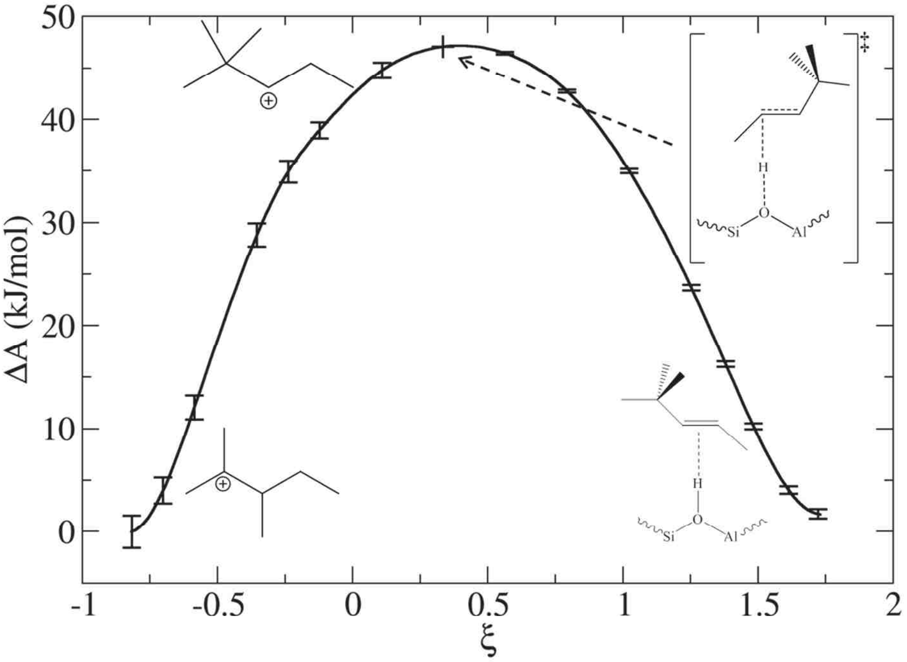

Figure S10. Free energy profile computed using the blue moon ensemble approach for the transformation of the tertiary cation (2,3-dimethyl-penten-2-ium) to the π-complex ((E)-4,4-dimethyl-pent-2-ene).

In the first part of the profile, from $\xi_{ref,R} = -0.82$ to $\xi \approx 0.1$, the methyl shift from C^4 to C^3 occur. The resulting highly unstable secondary cation transfers a proton between the C^4 atom and the O^4 atom of the zeolite. The transition state ($\xi^* \approx 0.33$) corresponds to this proton transfer. The value of the term $\Delta A_{\xi_{ref,R} \to \xi^*}$ is 47.1 ± 3.2 kJ/mol and $\Delta A_{\xi_{ref,R} \to \xi_{ref,P}} =$ 1.7 kJ/mol. The free energy of activation $\Delta A^{\ddagger}$ is determined via Equation (1). The terms $\langle |\dot{\xi}^*| \rangle$ is computed as described in Section SII: its value is $1.82 \cdot 10^{13}$ s^{-1}.

Figure S11 shows the probability distribution function $P(\xi_{ref,R})$ and $P(\xi_{ref,P})$ for the reactant R (2,3-dimethyl-penten-2-ium cation) and product P ((E)-4,4-dimethyl-pent-2-ene) of the reaction. The lengths of the MD runs were 194 ps and 186 ps for the reactant and product, respectively (in both cases, the initial 5 ps were considered as equilibration and the corresponding data were discarded). For the reactant, the numerical value of $\tilde{P}(\xi_{ref,R})$ for $\xi_{ref,R} = -0.82$ is 4.43 and for the product, $P(\xi_{ref,P}) = 3.26$ for $\xi_{ref,P} = 1.72$. The term $P(\xi_{ref,R})$ is computed via Equation (5), as described in Section 3.1.1, using the same value $p(R(I)) = 20.9$ %.

Finally, the computed free energy of activation $\Delta A^{\ddagger}$ is 48.0 ± 3.4 kJ/mol and the free energy of reaction is 7.0 ± 3.4 kJ/mol.

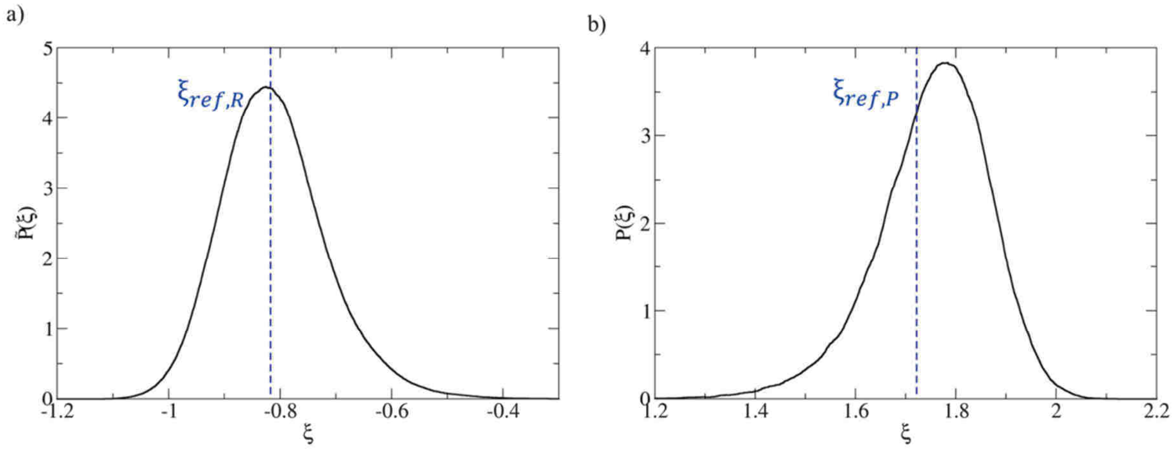

Figure S11. Probability distribution functions $P(\xi_{ref})$ for the reactant (a) and product (b) for the transformation of (section 3.2.2).

SVI. Type B₂ β-scission of 2-4-dimethyl-penten-2-ium

SVI.1 Slow growth simulation

We employed qualitatively a slow growth simulation protocol[10] (MD in which a candidate CV is increased at a constant rate) to check if the candidate CV can drive smoothly the reaction from the reactant to the product state. The results are shown in Figure S12. A modest hysteresis was observed for two different directions of transformation, which is a good indication of reversibility of the process driven by the given CV. We note that no discontinuity occurs owing to the inclusion of the proton transfer between the propenium cation and the zeolite.[11]

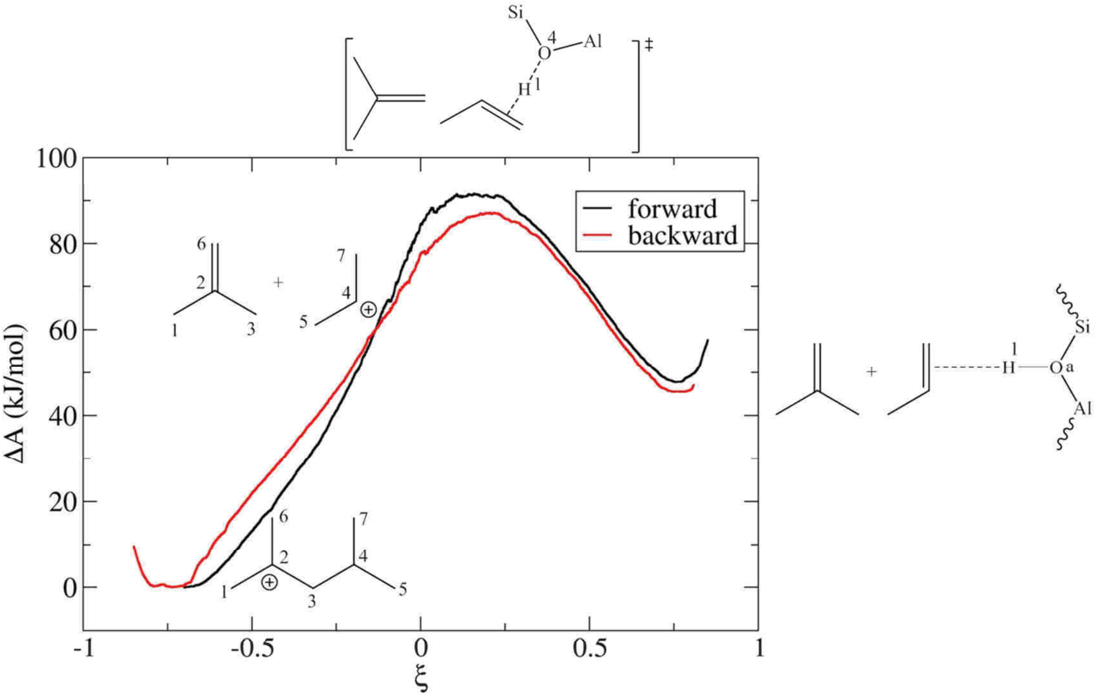

Figure S12. Forward and backward slow growth simulations for the type B₂ β-scission of 2-4-dimethyl-penten-2-ium in isobutene and pi complex of propene. The approximation to reaction coordinate is defined in Equation (9) in the main text.

SVI.2. Probability distribution function P(ξ_{ref})

Figure S13 shows the probability distribution function $P(\xi_{ref,R})$ and $P(\xi_{ref,P})$ for the reactant R and products P of the reaction. The length of the run of MD simulations was 150 ps for the reactant and 200 ps for the products (the first 5 ps being considered as equilibration and discarded). For the reactant, the numerical value of P$(\xi_{ref,R})$ for $\xi_{ref,R}$ = –0.70 is 5.79 and for the product, P$(\xi_{ref,P})$ = 6.57 for $\xi_{ref,P}$ = 0.75.

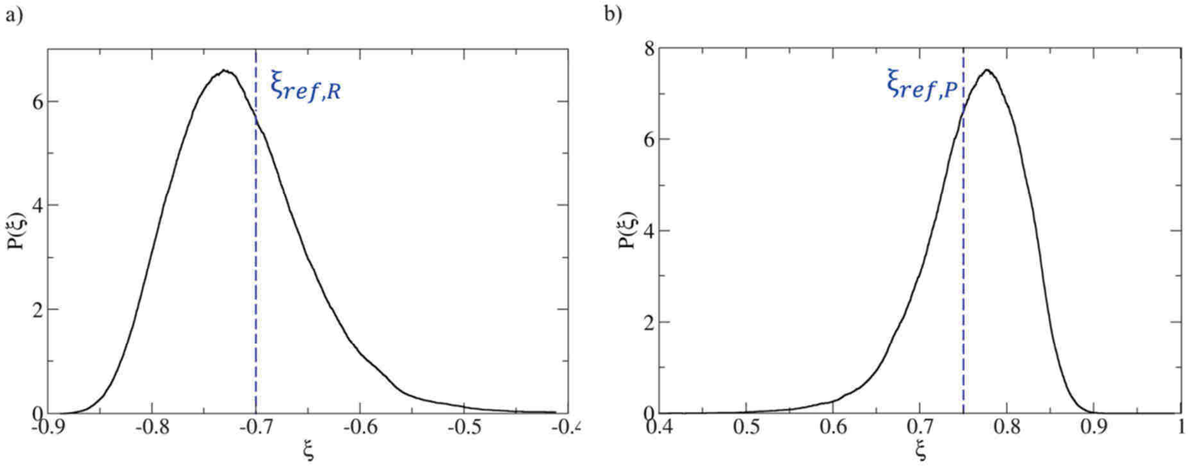

Figure S13. Probability distribution functions $P(\xi)$ for the reactant (a) and product (b) of the B_2 β-scission of 2-4-dimethyl-penten-2-ium reaction.

SVI.3. Structural analysis

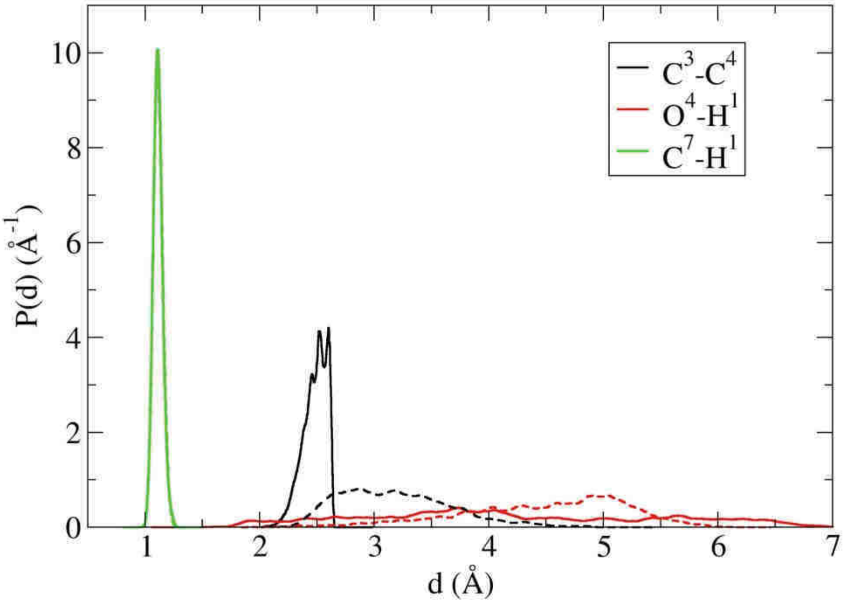

Figure S14. Probability distribution functions of selected distances in two consecutive points along the reaction coordinate of the type B_2 cracking reaction determined using MD at 500 K with ξ = - 0.1 (solid lines) and ξ = -0.08 (dash lines). Note that the green curves for the C^7-H^1 distributions (solid and dash lines) are nearly superimposed.

References

(1) Baerlocher, C., McCusker, J. K. International Zeolite Association. http://www.iza-structure.org/databases/.

(2) Smith, L. J.; Davidson, A.; Cheetham, A. K. A Neutron Diffraction and Infrared Spectroscopy Study of the Acid Form of the Aluminosilicate Zeolite, Chabazite (H- SSZ-13). *Catal. Lett.* **1997**, *49*, 143–146.

(3) Carter, E. A.; Ciccotti, G.; Hynes, J. T.; Kapral, R. Constrained Reaction Coordinate Dynamics for the Simulation of Rare Events. *Chem. Phys. Lett.* **1989**, *156*, 472–477.

(4) Henriksen, N. E.; Hansen, F. Y. *Theories of Molecular Reaction Dynamics: The Microscopic Foundation of Chemical Kinetics;* Oxford University Press, 2008.

(5) Rey, J.; Gomez, A.; Raybaud, P.; Chizallet, C.; Bučko, T. On the Origin of the Difference Between Type A and Type B Skeletal Isomerization of Alkenes Catalyzed by Zeolites: The Crucial Input of ab initio Molecular Dynamics. *J. Catal.* **2019**, *373*, 361–373.

(6) Rey, J.; Raybaud, P.; Chizallet, C.; Bučko, T. Competition of Secondary versus Tertiary Carbenium Routes for the Type B Isomerization of Alkenes over Acid Zeolites Quantified by AIMD Simulations. *Manuscript submitted for publication*, *2019*.

(7) Fukui, K. Formulation of the Reaction Coordinate. *J. Phys. Chem.* **1970**, *74*, 4161–4163.

(8) Fukui, K. The Path of Chemical Reactions - the IRC Approach. *Accounts Chem. Res.* **1981**, *14*, 363–368.

(9) Hratchian, H. P.; Schlegel, H. B. Following Reaction Pathways Using a Damped Classical Trajectory Algorithm. *J. Phys. Chem. A* **2002**, *106*, 165–169.

(10) Woo, T. K.; Magl, Peter M.,Blöchl, Peter E.; Ziegler, T. A Combined Car–Parrinello QM/MM Implementation for ab Initio Molecular Dynamics Simulations of Extended Systems: Application to Transition Metal Catalysis. *J. Phys. Chem. B* **1997**, *101*, 7877–7880.

(11) Cnudde, P.; Wispelaere, K. de; van der Mynsbrugge, J.; Waroquier, M.; van Speybroeck, V. Effect of Temperature and Branching on the Nature and Stability of Alkene Cracking Intermediates in H-ZSM-5. *J. Catal.* **2017**, *345*, 53–69.

Conclusion and perspectives

The present work dealt with the determination of mechanisms for isomerization and cracking reactions of C_7 alkenes in zeolites, in order to provide reliable rate constants and explain the observed products distribution in hydrocracking. In particular, we aimed at determining accurate free energy barriers and detailed structures of transition states for these reactions, with advanced molecular dynamics, beyond the usual static DFT methods. We used the blue moon sampling method as described in Section II. After determination of an approximation to reaction coordinate able to drive reversibly the reaction of interest, this method makes possible an accurate sampling along a discretized path of reaction, with 15 to 20 independent constrained MD runs. The computational cost is high – particularly when a special treatment of the interconversions between rotamers is required – but remains acceptable for a small cell zeolite such as chabazite.

In Section III, type A and B isomerization reactions, starting from a stable dibranched tertiary cation have been investigated. We demonstrated that the static approach is highly problematic for such reactions in zeolites, with a very large uncertainty. The computed free energy barriers allowed to reproduce the empirical difference in kinetic rates of these two types of isomerization reactions. The thermal evolution of the free energy barriers has been unraveled and the differences between the transition state of type A (a loose corner protonated cyclopropane) and type B (a tight edge protonated cyclopropanes) have been established for the first time. The crucial role of slow skeleton motions has also been demonstrated and a method permitting explicit sampling of required rotations for the description of the mechanisms has been developed. This study has been the subject of a publication.[1]

The same AIMD methods have been also used in Section IV for investigating the isomerization of mono- to di-branched C_7 alkenes. The role of intermediate secondary cations has been elucidated: they are not, in general, free energy minima and the kinetically relevant corresponding structures are π-complexes. We found that after a proton transfer from the zeolite, two different isomerization mechanisms can occur, depending on the initial conformation of the π-complex: (i) the direct conventional mechanism consisting in a one-step type B isomerization reaction and (ii) a two steps mechanism, consisting in a 1,3 hydride shift transforming the unstable secondary cation into a more stable tertiary cation, followed by another type B isomerization giving the same product. The two transition states for type B isomerization reactions are edge protonated cyclopropanes with similar stabilities whereas the transition state for the 1,3 hydride shift (a type A isomerization) can also be described as an edge protonated cyclopropane but more stable and with a longer edge C-C bond. Both mechanisms are kinetically relevant. This study is the subject of a submitted publication.[2]

In Section V, two β–scission mechanisms (type B_1 from secondary to tertiary cations and type B_2 from tertiary to secondary cations) have been explored. Once more, all secondary cations proved to be extremely unstable, both as a reactant (type B_1) and as a product (type B_2). The different transformations of the secondary carbenium reactant (the 4,5-dimethyl-penten-2-ium cation) were investigated by transition path sampling, where an ensemble of reactive trajectories is harvested by a Monte Carlo procedure, without an artificial bias nor any a prior knowledge of the mechanism and of a reaction coordinate. We show that it is connected to a π-complex with the same carbon skeleton or to a more stable tertiary cation. For cracking reactions themselves, we found much lower free energy barriers than in the previous static DFT studies or in the kinetic modeling. Our predictions are more consistent with experiment and with a previous biased MD study (dealing only with tertiary cations).[3] However, with a realistic treatment of the transformations involving the secondary cations, we found that the type B_1 mechanism predominates over the type B_2 mechanism for C_7 alkenes in zeolites, unlike what was proposed for C_8 alkenes in H-ZSM-5.[3] We also provide, for the first time, a dynamic description of the transition states of cracking: the transition state of the type B_1 reaction corresponds to the β-scission step, with the molecular planes of propene and tert-butylium cations in formation being approximately parallel and virtually free to rotate. Conversely, the transition state for the type B_2 cracking is associated with the proton transfer between the propenium cation in formation and the zeolitic framework: the β-scission process indeed leads to a highly unstable secondary propenium carbenenium ion that immediately transfers its proton to the framework to form stable products. The overall barrier to be overcome in that case is the sum of the barrier for the β-scission plus proton transfer, without any stable intermediates between these two processes.

As a global summary on the reaction network investigated in the thesis, we provide in Scheme 1 all ab initio rate constants (forward reaction) established by blue moon sampling for different key steps developed in Sections III to V.

In terms of perspectives, the previous results give a basis for a kinetic model for hydrocracking of C7 alkenes in chabazite, in relation with catalytic tests performed at IFPEN on different zeolites, among which also chabazite was considered, to predict selectivity effects. As shown in Scheme 1, some steps are still to be described: the first type B isomerization reaction, between secondary cations, from linear to monobranched species and the type C cracking reaction, from the secondary cation 3,4-dimethyl-penten-2-ium to linear butene and secondary propenium cation. These two kinds of reactions, starting and finishing with secondary cations, are particularly difficult to simulate accurately. Within this context, static gas phase calculations can be useful to build a complete (even if preliminary) network. As demonstrated in Section III, static gas phase calculations offer a reasonable agreement with the advanced MD calculations in chabazite at a much more affordable computational cost: the free energy barriers and the structures of the transition states determined by the static approach in gas phase are close to the ones determined by blue moon sampling, suggesting that for the monomolecular reactions investigated here, in this large pore zeolite, the contribution of the zeolite is modest.

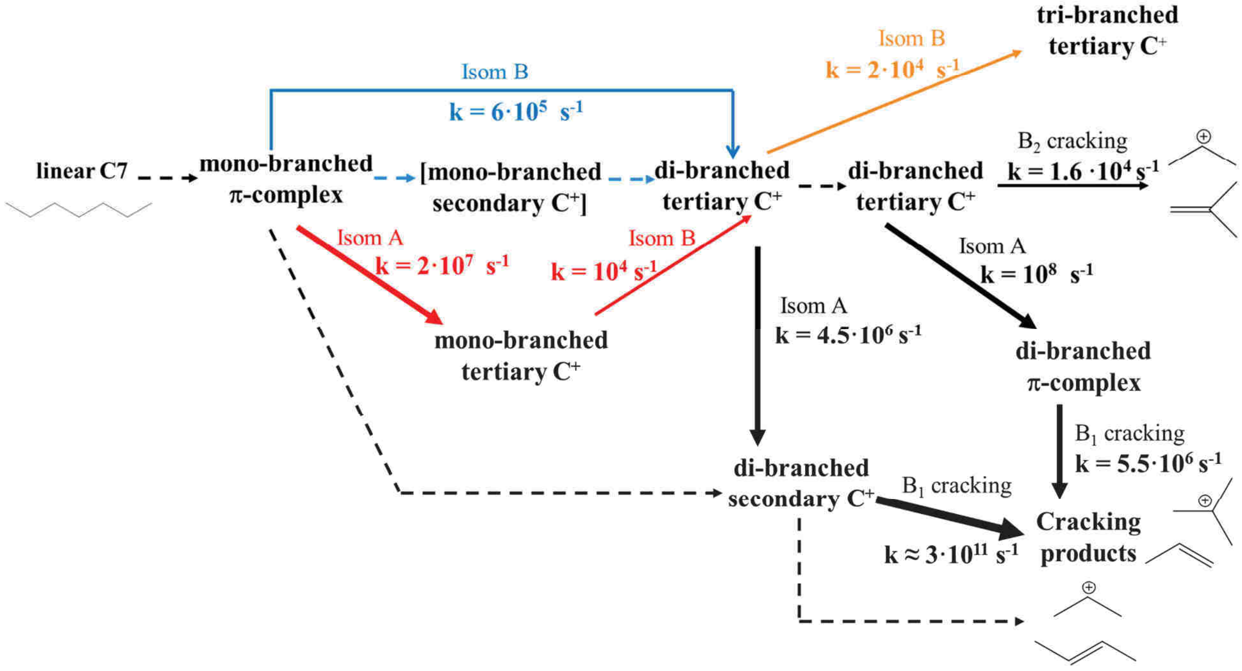

Scheme 1. Rate constants of the forward reaction computed by blue-moon sampling for different steps of the hydrocracking network of C_7 alkenes in chabazite at 500 K (blue arrows: mechanism I, Section IV; red arrows: mechanism II, Section IV; orange arrows: Section III; black arrows: Section V). The steps represented with dashed arrows are still to be described.

High level static calculations (at the MP2 or CCSD(T) level of theory for instance), possibly with an hybrid high level/low level scheme and with anharmonicity corrections, are another perspective of this work, especially for reactions involving secondary cations. These methods were shown to describe several reactions in zeolites with chemical accuracy[4] and could improve the description of secondary cations which are unstable species with non-classical structures at low temperatures.[5] This perspective can be developed in the same time as the kinetic model, to improve the description of gas phase simulations, and later of the influence of the zeolitic framework. However, combining this level of calculation with the MD approach is currently prohibitive, so that the problem of the identification of ensemble of configurations in the zeolite and ensemble of rotamers for each state in the zeolite by static calculations needs to be addressed. In that respect, recent developments using perturbation theory, and combining high level correlated wave-function methods and molecular dynamics at the DFT level are promising:[6] they might help to increase the accuracy of AIMD simulations.

The extension of our mechanistic findings to other zeolites is another perspective, with the objective of studying the shape selectivity of different zeolites, and also taking into account the external surfaces of zeolites, for a better description of realistic experimental conditions. Moving to these bigger cells, zeolites require more computational resources (with an estimation of a computational cost 8 times higher when shifting from chabazite to beta zeolite), or more efficient algorithms. The current developments of the VASP code, with on-the-fly machine learning scheme generating force fields during MD simulations, moreover makes large improvement in computational time possible (possibly of two orders of magnitude) and it also opens up new possibilities for the description of complex systems with AIMD.[7]

References

[1] J. Rey, A. Gomez, P. Raybaud, C. Chizallet, T. Bučko, *J. Catal.* **2019**, *373*, 361–373.

[2] J. Rey, P. Raybaud, C. Chizallet, T. Bučko, *Manuscript submitted for publication*, *2019*.

[3] P. Cnudde, K. de Wispelaere, L. Vanduyfhuys, R. Demuynck, J. van der Mynsbrugge, M. Waroquier, V. van Speybroeck, *ACS Catal.* **2018**, *8*, 9579–9595.

[4] a) G. Piccini, M. Alessio, J. Sauer, *Angew. Chem. Int. Ed.* **2016**, *55*, 5235–5237; b) M. Rybicki, J. Sauer, *J. Am. Chem. Soc.* **2018**, *140*, 18151–18161; c) C. Tuma, T. Kerber, J. Sauer, *Angew. Chem. Int. Edit.* **2010**, *49*, 4678–4680; d) C. Tuma, J. Sauer, *Phys. Chem. Chem. Phys.* **2006**, *8*, 3955–3965;

[5] a) I. V. Vrček, V. Vrček, H.-U. Siehl, *J. Phys. Chem. A* **2002**, *106*, 1604–1611; b) G. Rasul, G. K. S. Prakash, G. A. Olah, *J.Phys.Chem. A* **2015**, *119*, 5762–5769;

[6] a) D. Rocca, A. Dixit, M. Badawi, S. Lebègue, T. Gould, T. Bučko, *Phys. Rev. Materials* **2019**, *3*; b) G. Piccini, M. Parrinello, *J. Phys. Chem. Lett.* **2019**, 3727–3731;

[7] R. Jinnouchi, J. Lahnsteiner, F. Karsai, G. Kresse, M. Bokdam, *Phys. Rev. Lett.* **2019**, *122*, 225701.